

# Numerical Simulation of Pulsating Buoyancy Driven Turbulent Diffusion Flames

by

Mahmud Ashrafzaadeh

A thesis  
presented to the University of Waterloo  
in fulfillment of the  
thesis requirement for the degree of  
Doctor of Philosophy  
in  
Mechanical Engineering

Waterloo, Ontario, Canada, 1998

©Mahmud Ashrafzaadeh, 1998



**National Library  
of Canada**

**Acquisitions and  
Bibliographic Services**

**395 Wellington Street  
Ottawa ON K1A 0N4  
Canada**

**Bibliothèque nationale  
du Canada**

**Acquisitions et  
services bibliographiques**

**395, rue Wellington  
Ottawa ON K1A 0N4  
Canada**

*Your file Votre référence*

*Our file Notre référence*

**The author has granted a non-exclusive licence allowing the National Library of Canada to reproduce, loan, distribute or sell copies of this thesis in microform, paper or electronic formats.**

**The author retains ownership of the copyright in this thesis. Neither the thesis nor substantial extracts from it may be printed or otherwise reproduced without the author's permission.**

**L'auteur a accordé une licence non exclusive permettant à la Bibliothèque nationale du Canada de reproduire, prêter, distribuer ou vendre des copies de cette thèse sous la forme de microfiche/film, de reproduction sur papier ou sur format électronique.**

**L'auteur conserve la propriété du droit d'auteur qui protège cette thèse. Ni la thèse ni des extraits substantiels de celle-ci ne doivent être imprimés ou autrement reproduits sans son autorisation.**

0-612-30585-6

The University of Waterloo requires the signatures of all persons using or photocopying this thesis. Please sign below, and give address and date.

## Abstract

An elliptic fully coupled numerical fire model has been developed and applied to simulate the behavior of different laboratory scale pool fires. The new fire model uses the Eddy Dissipation Concept for combustion, a modified  $k$ - $\epsilon$  model for turbulence and a modified constant fraction model for radiation. The temperature dependency of the physical properties are accounted for and the correlations involving density fluctuations are included in the present fire model. The numerical implementation of the model is such that the strong coupling between the temperature and velocity fields in the physical problem is reflected and preserved in the model. The present fire model is applicable to both 2D planar and axisymmetric fires.

The present fire model has been used to numerically simulate the pulsating behavior of a 30-cm-diameter propane fire. The unique transient results presented in the thesis clearly demonstrate the capability of the present fire model in simulating such complicated phenomena. The quantitative agreement between numerical results and experimental observation is very promising and predicted frequencies for the propane fire agree very well with the reported values in the literature.

A comparison between the predicted results and experimental data for three different laboratory scale pool fires show that the use of a constant  $C_p$  in fire calculations has a rather significant deleterious effect on the accuracy of the results and should be avoided. In addition, it is shown that the use of the standard parameters in the turbulence model produces poor results. To improve the accuracy of the results, new modifications based on an analysis of the University of Waterloo pool fire laboratory data base have been proposed



and tested. The results obtained using the modified turbulence model show significant improvements compared to that of the standard turbulence model and agree very well with experimental data.

## Acknowledgments

I would like to express my sincere appreciation to my supervisors, Professor A.B. Strong and Dr. E. Weckman, for their continuous support, guidance and encouragements throughout this study. I have gratefully benefited from Dr. Strong's excellent course notes on turbulence.

I would also like to thank Dr. G. Stublely, who taught me the control volume method in the first place, and Dr. G. Raithby for their remarkable teaching ability and patiently answering my questions.

I also wish to thank Mr. Colin Campbell from the University of Waterloo Information Systems and Technology department, who patiently helped me with some of the computer softwares that I used to process my results. Many helpful discussions with my former and present colleagues, Dr. S.H. Karimian, Dr. M. Darbandi, P. Zwart and my dear brother Ali should be mentioned, as well.

The scholarship that I received from the Ministry of Culture and Higher Education of Iran and the financial support of the Natural Science and Engineering Research Council of Canada are gratefully acknowledged.

My heartiest appreciation and love is extended to my parents for their pure love, support and encouragements throughout my entire life.

Finally, I would like to dedicate this work to my wife, Neda, who has patiently taken care of me and our sons and lovingly supported me all along the way.

# Contents

|          |   |           |
|----------|---|-----------|
| <b>1</b> | <b>Introduction</b>                                   | <b>1</b>  |
| 1.1      | Zone Models . . . . .                                 | 4         |
| 1.2      | Field Models . . . . .                                | 6         |
| 1.2.1    | Examples of Fire Field Modeling . . . . .             | 7         |
| 1.3      | Laboratory Scale Fire Models . . . . .                | 10        |
| 1.4      | Review of Laboratory Scale Fire Simulations . . . . . | 12        |
| 1.5      | Objectives of the present work . . . . .              | 19        |
| 1.6      | Thesis organization . . . . .                         | 21        |
| <b>2</b> | <b>Background</b>                                     | <b>23</b> |
| 2.1      | Physics of the Phenomenon . . . . .                   | 23        |
| 2.2      | Elements of a Pool Fire Model . . . . .               | 25        |
| 2.3      | Effects of Turbulence on Chemistry . . . . .          | 27        |
| 2.4      | The Averaging Problem . . . . .                       | 30        |
| <b>3</b> | <b>Description of The Fire Model</b>                  | <b>35</b> |
| 3.1      | Introduction . . . . .                                | 35        |
| 3.2      | Basic Definitions . . . . .                           | 36        |
| 3.3      | Instantaneous Conservation Equations . . . . .        | 37        |
| 3.4      | Averaged Conservation Equations . . . . .             | 43        |
| 3.5      | Turbulence Submodel . . . . .                         | 45        |
| 3.6      | Combustion Submodel . . . . .                         | 49        |
| 3.7      | Radiation Submodel . . . . .                          | 53        |
| 3.8      | Thermophysical Properties . . . . .                   | 56        |
| 3.9      | Summary: The Base Fire Model . . . . .                | 57        |
| <b>4</b> | <b>Numerical Implementation</b>                       | <b>59</b> |
| 4.1      | Domain Discretization and Grid Generation . . . . .   | 61        |

|          |  |            |
|----------|--|------------|
| 4.2      | Discretization of the Governing Equations . . . . .                      | 62         |
| 4.2.1    | Integration of the Transient Term . . . . .                              | 63         |
| 4.2.2    | Integration of the Convection Term . . . . .                             | 64         |
| 4.2.3    | Integration of the Diffusion Term . . . . .                              | 67         |
| 4.2.4    | Integration of the Source Term . . . . .                                 | 67         |
| 4.3      | Discretization of the Coupled Equations . . . . .                        | 68         |
| 4.3.1    | Discrete Form of the Mass Equation . . . . .                             | 68         |
| 4.3.2    | Discrete Form of the r-momentum Equation . . . . .                       | 70         |
| 4.3.3    | The Discrete form of the z-momentum Equation . . . . .                   | 72         |
| 4.3.4    | The Discrete Form of the Energy Equation . . . . .                       | 73         |
| 4.4      | Discretization of the Segregated Equations . . . . .                     | 75         |
| 4.4.1    | Source Term Linearization of the $k$ - $\epsilon$ Equations . . . . .    | 76         |
| 4.4.2    | Source Term Linearization for the Species Equation . . . . .             | 77         |
| 4.5      | The Solver . . . . .   | 78         |
| 4.6      | Convergence Criteria . . . . .   | 79         |
| <b>5</b> | <b>Steady State Base Model Results</b>                                   | <b>82</b>  |
| 5.1      | Introduction . . . . .   | 82         |
| 5.2      | Specification of the Rectangular Propane Fire . . . . .                  | 83         |
| 5.2.1    | Computational Domain and Grid Specifications . . . . .                   | 85         |
| 5.3      | The axisymmetric propane fire . . . . .                                  | 86         |
| 5.3.1    | Computational Domain and Grid Specifications . . . . .                   | 86         |
| 5.4      | Boundary Conditions . . . . .  | 89         |
| 5.5      | Mean Flow Results . . . . .  | 93         |
| 5.5.1    | Results for the Rectangular Fire . . . . .                               | 94         |
| 5.5.2    | Results for the axisymmetric fire . . . . .                              | 98         |
| 5.6      | Appropriateness of using a constant $C_p$ for fire simulations . . . . . | 103        |
| <b>6</b> | <b>Simulation of the Fire Puffing Phenomenon</b>                         | <b>108</b> |
| 6.1      | Introduction . . . . .   | 108        |
| 6.2      | Previous Studies on Fire Pulsation . . . . .                             | 111        |
| 6.3      | Transient Fire Simulation . . . . .                                      | 112        |
| 6.4      | Details of the Puffing Mechanism . . . . .                               | 137        |
| <b>7</b> | <b>The Modified Fire Model</b>   | <b>145</b> |
| 7.1      | Introduction . . . . .   | 145        |
| 7.2      | The Methanol Pool Fire . . . . .   | 146        |
| 7.2.1    | Results of the Base Fire Model . . . . .                                 | 147        |

|          |   |            |
|----------|---|------------|
| 7.3      | Results of the Modified Fire Model . . . . .              | 154        |
| 7.3.1    | The Methanol Fire . . . . .                               | 154        |
| 7.3.2    | The Axisymmetric Propane Fire . . . . .                   | 159        |
| 7.3.3    | The Rectangular Propane Fire . . . . .                    | 161        |
| <b>8</b> | <b>Closure</b>  | <b>168</b> |
| 8.1      | Summary and Conclusions . . . . .                         | 168        |
| 8.2      | Recommendation for Future Work . . . . .                  | 170        |
| <b>A</b> | <b>Conserved Variables</b>                                | <b>172</b> |
| <b>B</b> | <b>Functional Form for <math>C_p</math></b>               | <b>175</b> |
| <b>C</b> | <b>The Grid Generator</b>                                 | <b>179</b> |
| <b>D</b> | <b>Code Validation Results</b>                            | <b>182</b> |
| D.1      | Laminar Flow Between Parallel Plates . . . . .            | 183        |
| D.2      | Flow in Circular Pipes . . . . .                          | 190        |
| D.3      | Convection of a step profile . . . . .                    | 194        |
| D.4      | Shear Driven Cavity Flow . . . . .                        | 198        |
| D.5      | Natural Convection in a Square Cavity . . . . .           | 206        |
| D.6      | Simulation of a Turbulent Buoyant Plume . . . . .         | 216        |
| <b>E</b> | <b>An energy balance for the rectangular propane fire</b> | <b>230</b> |

# List of Tables

|      |  |     |
|------|--|-----|
| 1.1  | Summary of field models for pool or pool-like fires . . . . .  | 17  |
| 5.1  | Steady-state operating conditions for the rectangular propane<br>fire . . . . .                                      | 83  |
| 5.2  | Grid specifications for rectangular propane fire . . . . .   | 85  |
| 5.3  | Grid specifications used for the axisymmetric fire . . . . .   | 87  |
| 5.4  | Turbulence model constants . . . . .   | 93  |
| 6.1  | Effects of different geometric and physical conditions on pre-<br>dicted frequencies of the fire pulsation . . . . . | 115 |
| 7.1  | Thermophysical properties of Methanol . . . . .  | 147 |
| 7.2  | Operating conditions for the methanol pool fire . . . . .  | 154 |
| 7.3  | Turbulence model constants . . . . .   | 158 |
| 7.4  | Grid specifications used for the methanol pool fire. . . . .   | 158 |
| B.1  | Polynomial constants to calculate the isobaric heat capacity<br>for different species . . . . .                      | 176 |
| D.1  | Calculated parameters for flow between parallel plates . . . . .   | 189 |
| D.2  | Calculated entrance length for flow between parallel plates,<br>$Re = 50$ . . . . .                                  | 189 |
| D.3  | Calculated results for flow in a circular pipe . . . . .   | 193 |
| D.4  | property values for the heated cavity test case . . . . .  | 207 |
| D.5  | cavity size for different Rayleigh numbers . . . . .   | 208 |
| D.6  | Calculated results for the heated cavity test case, $Ra = 10^4$ . .  | 213 |
| D.7  | Calculated results for the heated cavity test case, $Ra = 10^5$ . .  | 214 |
| D.8  | Calculated results for the heated cavity test case, $Ra = 10^6$ . .  | 215 |
| D.9  | Plume steady-state operating condition . . . . .   | 217 |
| D.10 | Grid specification for the buoyant plume . . . . .   | 217 |

|  |     |
|--|-----|
| D.11 Coefficients for the turbulence model . . . . . | 219 |
|--|-----|

# List of Figures

|      |  |     |
|------|--|-----|
| 2.1  | Differences between time and Favre averaged quantities - a) vertical velocity , b) temperature . . . . .                                       | 32  |
| 4.1  | A typical control volume in a 5-molecule node centered grid . . . . .  | 61  |
| 4.2  | Flowchart of the solution procedure . . . . .  | 80  |
| 5.1  | Schematic of the rectangular propane fire . . . . .  | 84  |
| 5.2  | Schematic of the computational domain for the axisymmetric propane fire. (a) The small computational domain, (b) The extended domain . . . . . | 88  |
| 5.3  | Predicted temperature contours and velocity field for the rectangular propane fire . . . . .   | 95  |
| 5.4  | Lateral distribution of vertical velocity at different heights . . . . .   | 96  |
| 5.5  | Lateral distribution of temperature at different heights . . . . .   | 97  |
| 5.6  | Centerline distribution of velocity and temperature for the axisymmetric propane fire, — present results, o experimental data . . . . .        | 99  |
| 5.7  | Radial profiles of temperature for the axisymmetric propane fire, — present results, o experimental data . . . . .                             | 101 |
| 5.8  | Radial profiles of vertical velocity for the axisymmetric propane fire, — present results, o experimental data . . . . .                       | 102 |
| 5.9  | Energy balance for the rectangular propane fire . . . . .  | 103 |
| 5.10 | variation of radiation heat loss versus presumed $C_p$ . . . . .   | 105 |
| 5.11 | Effect of $C_p$ on centerline velocity and temperature distributions for the rectangular propane fire . . . . .                                | 106 |
| 5.12 | Effect of $C_p$ on centerline velocity and temperature distributions for the axisymmetric propane fire . . . . .                               | 107 |
| 6.1  | Photographs of a 30-cm pulsating acetone pool fire . . . . .   | 110 |



|      |  |     |
|------|--|-----|
| 6.2  | Schematic of the computational domain for the transient fire simulations . . . . .   | 113 |
| 6.3  | Pressure variation in time at the burner surface for case 1 in Table 6.1. The lower plot shows the burner surface pressure, $P_d$ , at two radial location and the upper plot shows the pressure difference across the burner radius, $\Delta P_d = P_{d_{rim}} - P_{d_{cl}}$ . . . . .  | 117 |
| 6.4  | Temperature contours for case 1 in Table 6.1. Contour lines represent $T = 700, 1000, 1400$ and $1700$ (K). . . . .  | 118 |
| 6.5  | Temperature contours for case 1 in Table 6.1. Contour lines represent $T = 700, 1000, 1400$ and $1700$ (K). . . . .  | 119 |
| 6.6  | Burner surface pressure and frequency spectra for a 60 kW propane flame on a 30-cm-diameter burner at three radial locations reported by Cetegen et al. . . . .  | 120 |
| 6.7  | Time sequence photographs of a 60 kW propane flame on a 30-cm-diameter burner reported by Cetegen et al. , time interval between successive frames is $1/6$ s . . . . .  | 121 |
| 6.8  | Pressure variation in time at the burner surface for case 4 in Table 6.1. The lower plot shows the burner surface pressure, $P_d$ , at two radial locations and the upper plot shows the pressure difference across the burner radius, $\Delta P_d = P_{d_{rim}} - P_{d_{cl}}$ . . . . . | 123 |
| 6.9  | Temperature contours for case 4 in Table 6.1 at different times. Contour lines represent $T = 700, 1000, 1400$ and $1700$ (K). . . . .   | 124 |
| 6.10 | Predicted temperature field for case 4 in Table 6.1 at different times. Contour lines represent $T = 700, 1000, 1400$ and $1700$ (K). . . . .  | 125 |
| 6.11 | Pressure variation in time at the burner surface for case 7 in Table 6.1. The lower plot shows the burner surface pressure, $P_d$ , at two radial locations and the upper plot shows the pressure difference across the burner radius, $\Delta P_d = P_{d_{rim}} - P_{d_{cl}}$ . . . . . | 126 |
| 6.12 | Temperature contours for case 7 in Table 6.1 at different times. Contour lines represent $T = 700, 1000, 1400$ and $1700$ (K). . . . .   | 127 |
| 6.13 | Predicted temperature field for case 7 in Table 6.1 at different times. Contour lines represent $T = 700, 1000, 1400$ and $1700$ (K). . . . .  | 128 |
| 6.14 | Pressure variation in time at the burner surface for case 8 in Table 6.1. The lower plot shows the burner surface pressure, $P_d$ , at two radial locations and the upper plot shows the pressure difference across the burner radius, $\Delta P_d = P_{d_{rim}} - P_{d_{cl}}$ . . . . . | 129 |

|      |  |     |
|------|--|-----|
| 6.15 | Temperature contours for case 8 in Table 6.1 at different times. Contour lines represent $T = 700, 1000, 1400$ and $1700$ (K). . .   | 130 |
| 6.16 | Predicted temperature field for case 8 in Table 6.1 at different times. Contour lines represent $T = 700, 1000, 1400$ and $1700$ (K). . . . .  | 131 |
| 6.17 | Pressure variation in time at the burner surface for case 2 . .  | 132 |
| 6.18 | Pressure variation in time at the burner surface for case 3 . .  | 133 |
| 6.19 | Pressure variation in time at the burner surface for case 5 . .  | 134 |
| 6.20 | Pressure variation in time at the burner surface for case 6 . .  | 135 |
| 6.21 | Pressure variation in time at the burner surface for case 9 . .  | 136 |
| 6.22 | Temperature contours and velocity vector plots during a typical cycle of the fire pulsation. . . . .   | 139 |
| 6.23 | Simultaneous plots of velocity vectors, fuel reaction rate contours and shaded maps of the temperature field close to the burner rim of a 30 cm diameter propane fire. The time delay between the subplots is 0.05 (s) . . . . . | 141 |
| 6.24 | Simultaneous plots of velocity vectors, fuel reaction rate contours and shaded maps of the temperature field close to the burner rim of a 30 cm diameter propane fire. The time delay between the subplots is 0.05 (s) . . . . . | 142 |
| 7.1  | Centerline velocity and temperature distributions for the methanol fire and using the base fire model . . . . .  | 149 |
| 7.2  | Radial profiles of temperature at different heights above the burner for the methanol fire and using the base fire model . .   | 150 |
| 7.3  | Variation of $C_\mu$ versus $\frac{P_{uv}}{\epsilon}$ for a methanol pool fire . . . . .   | 152 |
| 7.4  | Contour plot of the distribution of turbulent Prandtl number throughout the methanol fire flow field . . . . .   | 153 |
| 7.5  | Centerline velocity and temperature profiles for the methanol fire and using the modified fire model . . . . .   | 155 |
| 7.6  | Radial profiles of temperature for the methanol fire, using the modified fire model . . . . .  | 156 |
| 7.7  | Radial profiles of velocity for the methanol fire, using the modified fire model. . . . .  | 157 |
| 7.8  | Computational grids used for the methanol pool fire . . . . .  | 160 |

|      |   |     |
|------|---|-----|
| 7.9  | Centerline velocity and temperature distributions for the axisymmetric propane fire using the modified fire model, compared to experimental data and base fire model predictions. . . . . | 162 |
| 7.10 | Radial profiles of temperature for the axisymmetric propane fire using the modified fire model, compared to experimental data and base fire model predictions. . . . .                    | 163 |
| 7.11 | Radial profiles of velocity for the axisymmetric propane fire using the modified fire model, compared to experimental data and base fire model predictions. . . . .                       | 164 |
| 7.12 | Lateral profiles of velocity for the rectangular propane fire using the modified fire model, compared to experimental data and base fire model predictions. . . . .                       | 166 |
| 7.13 | Lateral profiles of velocity for the rectangular propane fire using the modified fire model, compared to experimental data and base fire model predictions. . . . .                       | 167 |
| B.1  | Variation of $C_p$ for different species . . . . .  | 177 |
| B.2  | Variation of $C_p$ for propane and methanol . . . . .   | 178 |
| C.1  | Effect of the blending function on grid node distribution . . . . .   | 181 |
| D.1  | The entrance region of a flow between parallel plates . . . . .   | 184 |
| D.2  | Boundary conditions used for flow between parallel plates . . . . .   | 185 |
| D.3  | Streamwise velocity profiles between parallel plates for different boundary conditions, (-) BC-I, (- -) BC-II, (- ·) BC-III and ⊙ exact . . . . .   | 186 |
| D.4  | Centerline pressure variation along the channel . . . . .   | 187 |
| D.5  | Pressure contours between parallel plates . . . . .   | 188 |
| D.6  | Geometry and variable definitions for the pipe flow test case . . . . .   | 190 |
| D.7  | Calculated and exact velocity profiles for the pipe flow test case . . . . .  | 191 |
| D.8  | Calculated centerline pressure variation for different $Re$ numbers . . . . .   | 192 |
| D.9  | Pressure contours along the pipe . . . . .  | 193 |
| D.10 | Convection of a step profile in a uniform flow oblique to the grid lines . . . . .  | 194 |
| D.11 | $\phi$ distribution along the horizontal mid-plane using UDS . . . . .  | 195 |
| D.12 | $\phi$ distribution along the horizontal mid-plane using HOUDS . . . . .  | 196 |

|   |     |
|---|-----|
| D.13 $\phi$ distribution along the horizontal mid-plane using HOUDS<br>with limiters . . . . .                        | 196 |
| D.14 Comparison of the results obtained from different advection<br>schemes on the $42 \times 42$ node grid . . . . . | 197 |
| D.15 Schematic of a square cavity with a moving lid . . . . .   | 198 |
| D.16 Velocity distribution along the horizontal and vertical cavity<br>centerlines, $Re = 100$ , PEUDS . . . . .      | 199 |
| D.17 Velocity distribution along the horizontal and vertical cavity<br>centerlines, $Re = 1000$ , PEUDS . . . . .     | 200 |
| D.18 Velocity distribution along the horizontal and vertical cavity<br>centerlines, $Re = 100$ , HOUDS . . . . .      | 201 |
| D.19 Velocity distribution along the horizontal and vertical cavity<br>centerlines, $Re = 1000$ , HOUDS . . . . .     | 202 |
| D.20 Predicted stream lines inside the cavity, $Re = 1000$ , HOUDS,<br>$40 \times 40$ grid . . . . .                  | 204 |
| D.21 Velocity vectors inside the cavity, $Re = 1000$ , HOUDS. . . . .   | 205 |
| D.22 Schematic of the heated square cavity and boundary condi-<br>tions used for the calculations . . . . .           | 206 |
| D.23 Velocity vectors for the heated cavity, $Ra = 10^4$ . . . . .  | 209 |
| D.24 Velocity vectors for the heated cavity, $Ra = 10^5$ . . . . .  | 210 |
| D.25 Velocity vectors for the heated cavity, $Ra = 10^6$ . . . . .  | 211 |
| D.26 Schematic of the buoyant plume . . . . .   | 216 |
| D.27 Boundary conditions for the buoyant plume . . . . .  | 218 |
| D.28 Non-dimensional centerline temperature decay for a buoyant<br>plume . . . . .                                    | 221 |
| D.29 Non-dimensional centerline velocity decay for a buoyant plume  | 222 |
| D.30 plume spread rate . . . . .  | 224 |
| D.31 Radial profiles of mean temperature for a buoyant plume . . . . .  | 225 |
| D.32 Radial profiles of mean velocity for a buoyant plume . . . . .   | 226 |
| D.33 Radial distribution of $\overline{u'v'}$ for a buoyant plume . . . . .   | 227 |
| D.34 Radial distribution of $\overline{u'u'}$ for a buoyant plume . . . . .   | 228 |
| D.35 Radial distribution of $\overline{v'v'}$ for a buoyant plume . . . . .   | 229 |

## Nomenclature

|                     |  |
|---------------------|--|
| $\nu_i$             | molar stoichiometric coefficient for species $i$ appearing as a reactant in the reaction |
| $\nu'_i$            | molar stoichiometric coefficient for species $i$ appearing as a product in the reaction  |
| $\rho_i$            | mass of species $i$ per unit volume [kg/m <sup>3</sup> ]                                 |
| $\bar{\rho}, \rho'$ | time averaged and fluctuating density [kg/m <sup>3</sup> ]                               |
| $Y_i$               | instantaneous mass fraction of species $i$   |
| $\bar{Y}_i, Y'_i$   | time averaged and fluctuating mass fractions of species $i$                              |
| $\mathcal{M}_i$     | molecular weight of species $i$ [kg/kmole]   |
| $A$                 | pre-exponential or frequency factor  |
| $E$                 | activation energy [J/mole]   |
| $\mathcal{R}$       | universal gas constant   |
| $\bar{T}, T'$       | time averaged and fluctuating temperature [K]  |
| $f$                 | mixture fraction   |
| $\mathbf{q}_r$      | radiant heat flux vector [W/m <sup>2</sup> ]   |
| $\mathcal{H}_c$     | heat of combustion [J/kg]  |
| $\chi$              | fraction of the volumetric heat generation which is radiated out                         |
| $\chi$              | a fraction of fine structures which can react, in the EDC model                          |
| $\mathfrak{R}_i$    | reaction rate of species $i$ [kg/m <sup>3</sup> /s]                                      |
| $\mathbf{V}_i^S$    | velocity vector of species $i$   |
| $\mathbf{V}_i^d$    | diffusion velocity vector of species $i$   |

|               |   |
|---------------|---|
| $\bar{U}, U'$ | time averaged and fluctuating velocity vectors, mass weighted [m/s]                       |
| $\bar{u}, u'$ | time averaged and fluctuating radial velocity components [m/s]                            |
| $\bar{w}, w'$ | time averaged and fluctuating vertical velocity components [m/s]                          |
| $v'$          | fluctuating circumferential velocity component [m/s]                                      |
| $t$           | time [s]  |
| $k$           | turbulent kinetic energy/mass [m <sup>2</sup> /s <sup>2</sup> ]                           |
| $\epsilon$    | rate of dissipation of turbulent kinetic energy/mass [m <sup>2</sup> /s <sup>3</sup> ]    |
| $\nu_t$       | eddy viscosity [m <sup>2</sup> /s]  |
| $\nu$         | kinematic viscosity [m <sup>2</sup> /s]   |
| $I$           | identity matrix   |
| $h_i$         | specific enthalpy of species $i$ /mass [m <sup>2</sup> /s <sup>2</sup> ]                  |
| $h_i^\circ$   | enthalpy of formation of species $i$ /mass [m <sup>2</sup> /s <sup>2</sup> ]              |
| $H$           | total enthalpy/mass [m <sup>2</sup> /s <sup>2</sup> ]                                     |
| $\sigma$      | total stress tensor (with components $\sigma_{11}, \sigma_{12}, \sigma_{13} \dots$ , etc) |
| $\tau$        | shear stress vector (with components $\tau_{11}, \tau_{12}, \tau_{13} \dots$ , etc)       |
| $\mathcal{N}$ | number of species   |
| $P$           | thermodynamic pressure [pa]   |
| $P_d$         | kinematic pressure [pa]   |
| $g$           | gravitational acceleration [m/s <sup>2</sup> ]  |
| $\mu'$        | bulk or second viscosity  |
| $\mu$         | molecular dynamic viscosity [kg/m/s]  |

|                                  |  |
|----------------------------------|--|
| $\mu_t$                          | turbulent dynamic viscosity [kg/m/s]   |
| $\mu_{\text{eff}}$               | effective viscosity [kg/m/s]   |
| $C_p$                            | mass weighted mixture specific heat at constant pressure [m <sup>2</sup> /s <sup>2</sup> /K] |
| $C_{p_i}$                        | specific heat at constant pressure for species $i$ [m <sup>2</sup> /s <sup>2</sup> /K]       |
| $C_{p_i}^m$                      | mean value of the instantaneous heat capacity of species $i$                                 |
| $T^\circ$                        | reference temperature [K]  |
| $\sigma_t, \sigma_f$             | turbulent Prandtl/Schmidt number   |
| $\sigma_\epsilon, \sigma_k$      | constants in the turbulence model  |
| $C_{\epsilon 1}, C_{\epsilon 2}$ | constants in the turbulence model  |
| $\bar{C}_{\text{min}}$           | mass concentration of the deficient species [kg/m <sup>3</sup> ]                             |
| $a$                              | absorption coefficient [1/m]   |
| $\sigma$                         | Stefan-Boltzmann constant = $5.67051 \times 10^{-8}$ [W/m <sup>2</sup> /K <sup>4</sup> ]     |
| $\forall$                        | volume of a control volume [m <sup>3</sup> ]   |
| $\vec{r}$                        | displacement vector  |
| $C$                              | active coefficient in the discretized equations  |
| $B$                              | source term in the discretized equations   |
| $\mathcal{D}_{T,i}$              | thermal diffusion coefficient for species $i$  |
| $\mathcal{D}_{ij}$               | binary diffusion coefficient for species $i$ and $j$   |
| $\mathcal{D}$                    | binary diffusion coefficient   |
| $Sc$                             | Schmidt number   |
| $\mathbf{f}_i$                   | external force vector per unit mass acting on species $i$                                    |
| $K$                              | gas conductivity   |

|                            |                           |
|----------------------------|---------------------------|
| $C_{g1}, C_{g2}, \sigma_g$ | model constants           |
| A                          | area                      |
| L                          | distance between nodes    |
| P                          | Peclet number             |
| m                          | mass flux                 |
| $\hat{\mathbf{U}}$         | advecting velocity vector |
| $\hat{n}$                  | unit normal vector        |
| l                          | limiter                   |



# Chapter 1

## Introduction

Although *fire* has provided mankind with warmth and power since the early days of its discovery, the *uncontrolled fire* has cost many lives and incurred significant property damage. Even now, with advanced technologies in fire alarm systems and fire fighting techniques and facilities, statistics indicate that damages due to accidental fires are high. For example, the bulletin of the World Fire Statistics Center indicates that the cost of fire losses<sup>1</sup> during the period of 1992 to 1994 was 0.64 and 0.49 percent of the GDP in Canada and the USA, respectively. Therefore, the motivation behind fire research is quite clear.

Despite the public notion of what is meant by *fire*, giving a precise scientific definition for fire, which includes all the intended reacting flows and excludes other types of combustion processes, is not simple [1]. However, fire can be adequately defined as an exothermic reaction of some oxidizable

---

<sup>1</sup>These losses include costs of Direct Fire Losses, costs of Fire Fighting Organization and costs of Fire Insurance Administration

## Introduction

---

structure or material in air [2].

In a typical fire scenario of interest here, pyrolysis of a burning solid or liquid fuel provides volatiles for the fire plume. These generally mix with ambient air and in almost all practical fires burn as *turbulent diffusion flames*.

One of the prominent features of natural fires is the positive heat feedback from the fire plume to the fuel surface. Flame radiation and convective heat transfer from the hot gases enhance the pyrolysis process and consequently more combustible gases become available to the fire which, in turn, increases the heat feedback. This cycle continues until the oxidizer or fuel is expended or the system is cooled sufficiently to thermally quench the reaction.

Many physical and chemical processes such as heat and mass transfer, fluid dynamics, chemical kinetics, turbulence and buoyancy effects are involved in the fire phenomenon. A theoretical fire model should not only incorporate these processes but also account for the very complex interactions between them. However, current knowledge of many of these interactions is still very limited. For example, the interaction between turbulence and chemical kinetics, the effects of buoyancy on turbulence, and the effect of temperature fluctuations on radiation are not well understood. It is the goal of *fire science* to unravel these complex interactions and provide a sound understanding of fire phenomenon such that accurate and reliable predictive methods can be developed to anticipate fire behavior under a wide range of situations.

These predictive tools could then be used to describe for example, structural fire behavior, i.e., fire spread and smoke movement based on material properties, the geometry of the surroundings and ambient conditions. With

## **Introduction**

---

the help of such predictive tools fire engineers will be able to:

- design more effective fire detection-protection systems and develop better fire control techniques for structural fires,
- develop fire suppression attack methodologies in training and practice,
- provide a physical basis for fire postmortem assessment to determine cause and legal responsibility, and
- provide a basis for the design of fire safety codes and fire resistant structures.

Ultimately, they might contribute

- to understanding of environmental issues related to the release of toxic and/or particulate contaminants from a fire to the atmosphere,
- to the design and interpretation of fire test procedures for materials,
- and most importantly, to the (partial) replacement of expensive field fire experiments which, because of the hostile environment for instrumentation and the variable, generally uncontrollable, ambient conditions, can be unreliable and often provide only incomplete results.

Because of the importance and also the immediate need for improving fire safety in buildings, fire scientists and engineers have focused on modeling fire behavior in enclosures and compartments and have developed a number of fire models. A fire model is usually comprised of several modules. One module, which will be referred to as the gas phase module, deals with the

## 1.1 Zone Models

---

gaseous combustion, air entrainment into the fire plume and movement of hot gases from the fire plume. Other modules take care of processes such as heat feed back to the fuel surface, fuel gasification, heat transfer to and from any enclosure boundaries and effects of walls on fire behavior.

For the most part, existing fire models can be divided into two major classes, *zone models* and *field models*. Although the focus of the present work is on a particular aspect of the more general subject of field modeling of fires (i.e. modeling of the gas phase in the vicinity of the fire source), it is instructive to briefly discuss the basics of zone and field models and compare the merits and disadvantages of applying them in the prediction of fire behavior.

### 1.1 Zone Models

In zone modeling, the fire enclosure is divided into several sections or zones each of which are assumed to have uniform properties. Each section describes a recognized component of the overall system. For example, the fire plume, the layer of hot gases below the ceiling, and the cool region near the floor of the compartment, are separate zones commonly considered in these models.

Each zone is described separately by a set of equations, usually for conservation of mass and energy. The interaction between zones is described by global equations which are deduced from semi-empirical laws based on dimensional analysis and/or fire experiments, and heat balance equations are applied to the enclosure walls. Zone models depend heavily on a priori assumptions which are assumed from experience and observation. In addition,

## 1.1 Zone Models

---

they utilize some model constants which are obtained from fire experiments.

There have been many zone models reported in the literature, e.g. [3, 4, 5, 6]; however, the basics of most of these models are similar. For instance, Emmons [3, 4] started the development of a series of fire zone models which can be used not only to calculate the smoke movement in multiple compartment buildings but also allow the user to account for the coupling between radiant heat feedback and the rate of fuel pyrolysis and the spread of flame over the fuel surface. It is beyond the scope of the present section to provide a comprehensive review of fire zone models and interested readers may refer to reviews provided by Friedman [7] and Harmathy and Mehaffey [8].

The main advantages of zone models are that the calculations can be done relatively quickly, and they provide useful information about overall fire behavior and spread of heat and toxic gases. However, because of the treatment of the fire plume as a homogeneous zone, they can not be used to predict the details of the fire behavior in its developing stage. In addition, the applicability of zone models is limited to those cases which lie within the range of experiments used to obtain any empirical parameters included in the model [5, 9]. Finally, since fire behavior strongly depends on the geometry and size of the fire enclosure, different zone components should be used for prediction of different fire scenarios.

For example, the smoke movement in domestic-sized enclosures differs significantly from that inside a very large atrium. In the former case, it may be perfectly reasonable to assume that smoke fills the enclosure from top to bottom. However, such an assumption may not be valid for the latter case and the fire behavior would need to be represented by different zonal compo-

## 1.2 Field Models

---

nents. Therefore, no single zone model should be expected to be applicable to all fire cases [1].

## 1.2 Field Models

A different fire model strategy, i.e. *field modeling*, eliminates many of the a priori assumptions required in zone models by solving the conservation laws governing the fire behavior and smoke movement as described by appropriate partial differential equations subjected to varying degrees of simplification and specified boundary conditions.

In field modeling, techniques of computational fluid dynamics (CFD) are used to discretize and numerically solve the field equations. Because of the heavy computations involved, these models critically depend upon the availability of suitable computational power, which has proven a major obstacle in the development and progress of numerical fire field modeling. However, due to recent advances in computer technology and availability of affordable fast computers with large memory, there is an expanding interest in the use of field modeling for fire simulations, to the extent that their use may surpass that of zone models for fire safety engineering in the near future [10].

Several fire field models have been developed and used to predict fire behavior in two and three dimensional configurations. A short review of the reported results will demonstrate the potential power and also the wide applicability of these models, as well as current deficiencies. The main objective of the following review is to present some evidence indicating the use of field modeling for a wide range of different fire scenarios and to introduce the

## 1.2 Field Models

---

state-of-the-art submodels used in fire field models. A critical discussion on the suitability of these submodels is given in later sections where numerical simulation of laboratory scale pool fires is reviewed.

### 1.2.1 Examples of Fire Field Modeling

Markatos et al. [11] developed a two dimensional model for prediction of buoyancy-induced flows in enclosures using the  $k$ - $\epsilon$  turbulence model. This model was further developed to be used for three dimensional fire simulations and is now known as JASMINE. Cox et al. [12] added a six flux model for radiation to JASMINE and used it to model the fire behavior in several experimental configurations including a fire test cell, a long railway tunnel and a six bed hospital ward.

JASMINE has also been applied by Cox and Kumar [13] for the prediction of conditions in a forced ventilated fire test. Satisfactory agreement between predictions and limited experimental data is reported in all cases [11, 12, 13]; however, the need for further model improvements to enhance the accuracy of the results in the immediate vicinity of the fire source has been emphasized.

Another field model called UNDSAFE was developed by Ku et al. [14]. This two dimensional model solves the field equations in an elliptic formulation and uses an algebraic turbulence model to determine the effective viscosity,  $\mu_{\text{eff}}$ . Ku et al. [14] used this model to predict the fire induced velocity and temperature fields in an enclosure with an exit door and also in a room with a connecting corridor. Either a heat source or experimental floor temperatures were used to simulate the fire source in these cases. Using the same principle, Satoh [15] developed a three dimensional version of UND-

## 1.2 Field Models

---

SAFE and used it to analyze the growth of the hot gas layer and the ceiling jet “T” pattern induced by a flame burning upward along a corner.

Field models are also used to predict fire behavior inside aircraft cabins. Yang et al. [16] used a two dimensional version of UNDSAFE and studied the smoke movement inside the cabin under different seating configurations and several fire locations, whereas Galea and Markatos [17] used a three dimensional model. These authors have also provided a review of mathematical modeling for aircraft cabin fires [18].

Joh et al. [19] have reported transient three dimensional fire simulations of a compartment fire from burn-up to flashover. They have used the  $k$ - $\epsilon$  model for turbulence, a fast chemistry assumption for combustion, simplified formulae to calculate radiation to the walls and experimental relations for one-step gasification of the solid fuel.

KAMELEON, which is another three dimensional field model based on the  $k$ - $\epsilon$  turbulence model, Eddy Dissipation Concept (EDC) for combustion and Discrete Transfer Model for radiation was used by Holen and Magnussen [20, 21] to calculate fire development inside a simplified module of an offshore petroleum production platform as well as for open fires with and without wind.

Fire behavior and smoke filling of single large compartments with forced ventilation are studied by Chandrasekaran et al. [22] using FIRE3D, a model which is again based on the  $k$ - $\epsilon$  model for turbulence. Other field models have been developed by Chow and Leung [23] to study the solid-wall boundary effects in fires and by Hadjisophocleous and Cacambouras [9] to investigate the effects of enclosure opening, fire position and interior objects on fire



## 1.2 Field Models

---

growth and development.

In comparison with zone models, field models should be more universally applicable to the prediction of fire behavior, especially those which incorporate a combustion submodel for the gas phase [12, 13, 19, 20, 22] instead of relying on the simplified approach of treating the fire as a heat source [9, 14, 16]. So far, field models have been used to predict some of the gross features of fire behavior in specific situations, but surprisingly none have been shown to predict accurately the thermal development of the fire plume in the vicinity of its source.

A review of the results generated by fire field models show that the accuracy of the solution for the velocity and temperature fields<sup>2</sup> in the gas phase is of primary concern for fire engineers. This is because the solution for the velocity and temperature fields determines, for instance, how the fire extends in the enclosure and how the hot gases and smoke migrate through the structure. In addition, prediction of other quantities of interest, such as mass flux from the fire, heat transfer to the walls, heat feed back to the fuel surface. etc., all depend on a detailed solution for gas phase fire behavior.

It is clear that the success of any fire model depends on how well the gas phase is modeled. Although the treatment of other processes is also important in a complete simulation of real fire scenarios, they all depend on the solution of the gas phase in the fire. Hence, further development of field models requires closer attention to the accuracy and validity of submodels used to model the gas phase flow development in a fire.

---

<sup>2</sup>and also species concentrations in cases where prediction of toxic gases and smoke concentration is important

### 1.3 Laboratory Scale Fire Models

---

In particular, the accuracy of predictions in the near field region of a fire plays a central role in more accurate fire field modeling. This near field region is of great importance in overall fire behavior for it contains the source of heat and buoyancy. *Development of an appropriate model for this critical region, and validation studies of the different submodels involved, are the main focus of the present work.*

### 1.3 Laboratory Scale Fire Models

In order to evaluate and eventually validate any numerical fire model including the present model, for the gas phase development of a fire, particularly in the vicinity of the fire source where reaction occurs, detailed experimental data must be available for comparison. However, due to practical difficulties involved in making detailed measurements in full scale fires, laboratory scale fire experiments and models are often used for such investigations. The question remains as to the role of laboratory pool fire results as a basis for full scale field/structural fires.

Turbulent diffusion flames stabilized on laboratory scale pools of liquid fuel or on gas burners with very low exit Froude numbers ( $10^{-4} - 10^{-6}$ ), to a large extent, exhibit characteristics similar to the behavior of natural fires of larger scale. Therefore, they can be considered as simplified, yet realistic, models of the fundamental dynamics of field fires in their developing stages. As such, they have been used in theoretical modeling as well as for experimental investigations in fire research.

Small scale fires can be studied under controlled laboratory conditions,

### 1.3 Laboratory Scale Fire Models

---

and so allow detailed measurements of quantities such as gas velocity, temperature and mean species concentration, as well as turbulent shear stresses, turbulent fluxes, etc. Such data provide an excellent resource through which to improve current understanding of the physics of natural fires. Moreover, the performance of theoretical and numerical fire models in accurately predicting the gas phase development of fires can be examined and even to some extent, “tuned” using such data.

A uniqueness of the present work is that physical input and model evaluation is based in large part on the recently published detailed data base measured in medium scale liquid pool fires in the University of Waterloo pool fire facility [24, 25, 26]. This is the first available compilation of data from controlled experiments from which a detailed description of the physical processes controlling the thermal/fluid evolution of pool fires has been proposed [25, 27, 28] and represents a major step forward from that of the pioneering work of McCaffrey [29]. Thus, for the first time it is possible to assess the important physical features that a computational fire code should possess in its submodels and to reliably test its ultimate accuracy.

Having addressed the relevance of laboratory scale fire modeling to full scale fire modeling, the need and importance of validation studies and the availability of a detailed set of laboratory scale pool fire data, it is time to review previous work on the numerical simulation of laboratory scale fires.

## 1.4 Review of Laboratory Scale Fire Simulations

### 1.4 Review of Laboratory Scale Fire Simulations

Fires are essentially turbulent diffusion flames and although there is a rich literature on numerical simulation of turbulent diffusion flames, many of the existing studies are related to jet diffusion flames which lack any significant effect of buoyancy on the structure and development of the flame. Effects of buoyancy on the structure of diffusion flames were shown by Pergament and Fishburne [30]. In their numerical modeling of a wide range of  $H_2$ /air flames with burner diameters of 0.5 to 68 cm, they showed that when buoyancy is neglected, centerline temperature scales with non-dimensional axial distance. But for Froude numbers smaller than  $9 \times 10^5$ , rather substantial departures from the scaled curve is observed if buoyancy is included. This departure is more pronounced downstream of the region of maximum temperature where acceleration due to buoyancy starts to significantly affect the overall entrainment rate. Since buoyancy plays such an important role in determining the structure of diffusion flames, only those laboratory scale fires relevant to fire modeling (i.e. where buoyancy effects are significant) are reviewed in this section.

There are two approaches by which buoyancy driven turbulent diffusion flames have been numerically simulated. In the first approach, time dependent partial differential equations describing the fire dynamics are solved directly in primitive instantaneous form without averaging and thus without incorporating any turbulence model. Davis et al. [31] have reported some preliminary results of their Direct Numerical Simulation, DNS, of a propane/air

## 1.4 Review of Laboratory Scale Fire Simulations

---

buoyant jet diffusion flame, 2.25 cm in diameter. A similar numerical technique is used by Katta et al. [32] to study the effects of non-unity Lewis number and finite rate chemistry on the predictions of  $H_2$ /air flames (1 cm in diameter).

Ghoniem et al. [33] have used a vortex-based model in which the instantaneous vorticity transport equation is solved in Lagrangian form, with a fast chemistry model using Shvab-Zeldovich variables to predict small fire plumes, 10 cm in diameter. Large Eddy Simulation (LES) has also been used to predict the fire behavior and fire induced flows under different geometric configurations. Two dimensional LES results for a multi section corridor and an axisymmetric reacting plume are reported by H.R. Baum [34] and Mell et al. [35], respectively. The same group has also reported three dimensional LES predictions for different fire scenarios, i.e. a 22 cm diameter pool fire and three enclosure fires, [36]. In Large Eddy Simulation the bulk motion of hot gases is calculated directly by solving an approximate form of the Navier-Stokes equations which are specialized to the smoke movement problem. The heat release due to combustion is modeled by inducing a large number Lagrangian thermal elements which are convected by the large eddy structures and release heat. However, the combustion phenomena themselves are not simulated.

Interesting results have been obtained from these models, particularly for the dynamic behavior of the fire<sup>3</sup>, however, no detailed comparison between numerical results and experimental data has been demonstrated. Overall,

---

<sup>3</sup>The dynamic behavior of fires and numerical predictions of such phenomenon are discussed in a later chapter

## 1.4 Review of Laboratory Scale Fire Simulations

the above methods tend to be very computationally intensive and their application for engineering calculation of real fires has yet to be discovered.

In the second approach, which is still the dominant approach in engineering fire calculations, the instantaneous conservation equations are averaged and closure is obtained by a turbulence model which accounts for physical and chemical processes which occur on scales smaller than that of the computational grid. Buoyant diffusion flames over small gas burners, with diameters of 1 cm and smaller, have been numerically simulated by different groups by simplifying the equations to a parabolic form. A Reynolds time-averaged second order closure model is described by Tamanini [37] which accounts for the effects of buoyancy on turbulence properties. Tamanini's model, which is essentially an improved version of the  $k$ - $\epsilon$ - $g$  model of Lockwood and Naguib [38], assumes infinitely fast chemistry and uses a polynomial Probability Distribution Function, PDF, to evaluate mean properties. In  $k$ - $\epsilon$ - $g$  models, a differential equation representing the conservation of scalar temperature intensity,  $g$ , is solved along with conservation equations for  $k$ , turbulent kinetic energy per mass and  $\epsilon$ , the dissipation rate per mass. Radiation losses are assumed to be a fixed fraction of the total heat release and a constant value for the mixture specific heat,  $C_p$ , is assumed in the energy equation.

Three propane flames with different fuel exit velocities and on a 1.27 cm burner were simulated. To obtain better agreement with radiation measurements of Markstien [39], Tamanini used a trial and error method to find an optimum location where initial conditions could be specified for the turbulent calculations. Although flame heights and trends of other calculated parameters were predicted correctly, the calculated effective flame radius was

## 1.4 Review of Laboratory Scale Fire Simulations

---

underestimated. Due to a lack of the necessary detailed measurements for evaluation, the assessment of this code was not completed.

Three versions of the  $k$ - $\epsilon$ - $g$  model were later used by Jeng et al. [40] to simulate methane (0.5 cm diameter burner) and propane (0.119 cm diameter burner) buoyant diffusion flames. These models include the original  $k$ - $\epsilon$ - $g$  model [38] and two other modified versions based on Algebraic Stress Model, ASM, corrections proposed by Chen and Chen [41]. More encouraging predictions of mean velocity and temperature were achieved, mainly due to utilization of better data to describe the initial conditions. However, higher centerline temperatures and lower radial spread of velocity profiles were predicted in comparison with the measurements [40].

In this study, it was found that including the effects of buoyancy on turbulence properties had a relatively minor influence on predictions of the mean flame structure. This conclusion may be partly due to the high Froude number ( $10^4 - 10^5$ ) of the flames studied.

Jeng and Faeth [42] used a Favre averaged formulation of the  $k$ - $\epsilon$ - $g$  model along with a clipped Gaussian PDF to simulate the same methane flames as in [40]. The state relations for the combustion model were found using two methods, (1) *a laminar flamelet method* and (2) *a partial equilibrium method*. Predictions were compared with new measurements of the mean concentration of major species and turbulence quantities in the methane flames. Agreement between predicted and measured turbulence quantities was found less satisfactory than that for the mean quantities. Underestimation of overall flow widths was again reported.

Buoyant diffusion flames on larger burners, with diameters greater than

## 1.4 Review of Laboratory Scale Fire Simulations

---

5 cm and lower Froude numbers, have been simulated using similar computational models. A summary of these models, which are more representative of those required to predict natural fires, is given in Table 1.1.

You and Faeth [43] studied 5.5 cm diameter methane flames with a range of exit Froude numbers between  $10^{-2}$  and  $10^{-3}$ . To numerically simulate the fires, they used Tamanini's  $k-\epsilon-g$  model without including the effects of buoyancy on turbulence quantities. Calculations were started about 2 diameters downstream of the burner exit to avoid potential laminar to turbulent transitions, as well as elliptic effects in the flow close to the burner.

Poor agreement was reported between the predictions and experimental data for mean velocities, temperatures and Reynolds stresses, and especially in predictions of the width of the flow in the upper portions of the flame. The poor performance of the model was attributed to difficulties in defining initial conditions and to the neglect of buoyancy and density fluctuations, but also to inaccuracies in the data due to effects of room disturbances on the fire.

On a larger scale, Gengembre et al. [44] have studied some low Froude number ( $1.2 \times 10^{-5} - 2 \times 10^{-6}$ ) propane flames on a burner of 30 cm diameter. In addition to velocity and temperature profiles, mole fractions of major species were measured. Tamanini's  $k-\epsilon-g$  model was again used to predict the fire behavior. Turbulent computations were started right at the burner exit. Satisfactory agreement was obtained in predictions of centerline velocity but centerline temperatures were overpredicted. As was the case in previous computations, the radial expansion of the fire plume was underestimated.

Later, Crauford et al. [45] simulated the behavior of a methane flame



Table 1.1: Summary of field models for pool or pool-like fires

| Parabolic models   |  |  |                                       |  |                     |
|--|--|--|---------------------------------------|--|---------------------|
| reference study case   | Buoyancy   | Turbulence                                     | Combustion                            | Radiation  | Soot                |
|  |  | averaging                                      |                                       |  | size                |
| You and Faeth (1982)[43] natural gas fire                            | $g(\rho_{\infty} - \rho)$                              | $k-\epsilon$                                   | flamelet model clipped Gaussian PDF   | a) none<br>b) 20% radiative heat loss                                | -                   |
|  |  | $C_{\mu} = 0.09$                               |                                       |  | D=5.5 cm            |
| Gengembre <i>et al.</i> 1984[44] propane gas fire                    | $g(\rho_{\infty} - \rho)$ modification to $k-\epsilon$ | hybrid $k-\epsilon$ using ASM for correlations | flamelet model clipped polynomial PDF | 35% radiative heat loss  | -                   |
|  |  | Time ave.                                      |                                       |  | D=30 cm             |
| Crauford <i>et al.</i> (1985)[45] methane gas fire                   | $g(\rho_{\infty} - \rho)$ modification to $k-\epsilon$ | $k-\epsilon$                                   | flamelet model beta function PDF      | 10% radiative heat loss  | -                   |
|  |  | $C_{\mu} = 0.09$                               |                                       |  | D=25 cm             |
| Adiga <i>et al.</i> (1989)[46] propane gas fire                      | $g(\rho_{\infty} - \rho)$                              | $k-\epsilon$                                   | EDC <sup>4</sup>                      | flux model for gaseous radiation and some percent for soot radiation | -                   |
|  |  | $C_{\mu} = 0.09$                               |                                       |  | D=30 cm             |
| Adiga <i>et al.</i> (1990)[47] methane gas fire                      | $g(\rho_{\infty} - \rho)$                              | $k-\epsilon$                                   | EDC                                   | four flux model  | Tesner <sup>5</sup> |
|  |  | $C_{\mu} = 0.09$                               |                                       |  | D=25 cm             |
| Elliptic models  |  |  |                                       |  |                     |
| Annarumma <i>et al.</i> (1991)[48] propane gas fire & a 2D pool fire | $g(\rho_{\infty} - \rho)$ modification to $k-\epsilon$ | $k-\epsilon$                                   | flamelet model rectangular PDF        | 50% radiative heat loss  | -                   |
|  |  | $C_{\mu} = 0.09$                               |                                       |  | 25 x 40             |
|  |  | Favre ave.                                     |                                       |  |                     |

4- eddy dissipation concept for combustion developed by Magnussen [49]

5- phenomenological method of Tesner [50] for soot modeling

## 1.4 Review of Laboratory Scale Fire Simulations

over a 25-cm-diameter burner. Similar to most of the earlier models, the  $k$ - $\epsilon$  model was used for the turbulence closure. In addition, their Favre-averaged numerical model consisted of a non-equilibrium chemistry model along with an assumed beta function PDF for the mixture fraction. The comparison between their numerical results and measurements of velocity, temperature and turbulent quantities showed good agreement for fire spread but, the flame length was consistently underpredicted. They pointed out that the predictions were sensitive to the form of the probability distribution function and concluded that commonly assumed forms of PDF's (e.g. Gaussian, clipped Gaussian, beta function or polynomials) were probably unsuitable for buoyant fire predictions.

While different variations of the  $k$ - $\epsilon$ - $g$  model were used by other researchers, Adiga et al. [46] developed a different parabolic fire model and reported simulation results for Gengembre's burner [44]. This model was again based on the  $k$ - $\epsilon$  model for turbulence, but included Magnussen's Eddy Dissipation Concept for combustion [49] and a four flux model [51] for gaseous radiation, whereas soot radiation was based on an empirical method. Following Gengembre et al. they started the turbulent calculations at the burner exit, with optimized initial values for  $k$  and  $\epsilon$  based on the burner exit velocity. The optimized  $k$  and  $\epsilon$  values were found through a trial and error procedure used to match predicted results with experimental data along the fire centerline. As one might expect, good agreement for the centerline distribution of velocity, temperature and species mole fractions was reported but, radial distribution of velocity and temperature at lower heights in the combustion zone were significantly underpredicted.

## 1.5 Objectives of the present work

---

The same authors further developed their parabolic fire model [47] by incorporating a phenomenological soot model [50], then validated the model against Crauford's data [45]. Because of the low concentration of soot in the methane flame, the contribution of soot to radiation appears to be very small compared to that of the hot gases. Reasonable agreement for the centerline quantities were reported but the flame width was severely underpredicted near the burner surface. They speculated that the underprediction of the flame spread was related to the neglect of any elliptic flow behavior in the near field region of the fire.

In an attempt to account for elliptic flow behavior, Annarumma et al. [48] developed a Favre averaged fire model which, to the knowledge of the author and at the time of writing this manuscript, is the only elliptic model for which detailed comparisons between predictions and experimental data has been published. This model uses the  $k$ - $\epsilon$  turbulence model, a constant radiative heat loss and a flamelet model for combustion. A rectangular ( $25 \times 40$  cm) propane flame was simulated and numerical results were compared with experimental data [52]. A rather high radiation heat loss fraction (50%) was used to obtain reasonably good agreement for velocities and temperatures along the fire centerline. But, despite the use of an elliptic formulation, the flame width was still significantly underpredicted.

## 1.5 Objectives of the present work

The potential power and general applicability of fire field models were discussed in Section 1.2 and several examples of full scale fire simulations were

## 1.5 Objectives of the present work

noted. But due to lack of detailed measurements, the accuracy and validity of these models have not been demonstrated for the region near the fire source. In the case of laboratory fire models, as discussed in Section 1.4, most existing models have used parabolic formulations which are not valid in the vicinity of the fire source. In all cases, radial spread of the fire is underpredicted.

Considering the need for developing pool fire models and to take advantage of the availability of a new data base [24, 26] consisting of detailed LDA and fine thermocouple measurements of laboratory scale acetone and methanol pool fires, the objective of the present thesis is:

To formulate and validate physically and numerically an elliptic, Reynolds averaged fire model appropriate to the prediction of pool fires.

To achieve this objective, it is proposed to:

- review state of the art models currently in use and define a new BASE level model formulation for the prediction of pool fires,
- test the physical and numerical formulation against several benchmark data and other available numerical simulations for both reacting and non-reacting flows,
- analyze the University of Waterloo pool fire data base to ascertain its implications with respect to some of the currently used physical submodels,

## 1.6 Thesis organization

---

- based on the above, propose, validate and test the impact of new submodels,

and finally

- and finally, critically assess detailed steady-state and transient predictions of the field model in so far as the appropriateness of the BASE model with and without the proposed new submodels, permit.

## 1.6 Thesis organization

Chapter 2 defines the physical problem under investigation and identifies the important submodels required for numerical modeling of pool fires. In addition, some of the commonly used assumptions in existing fire models are critically reviewed.

The mathematical description of the present pool fire model and details of various submodels used are described in Chapter 3. Chapter 4 presents the details of the numerical implementation of the proposed fully coupled elliptic fire model.

Results of the base fire model for two laboratory scale propane pool fires are given and discussed in Chapter 5. Moreover, the implications of using a constant value of the gas heat capacity at constant pressure, as is a common practice in fire modeling, are evaluated in this chapter.

Chapter 6 includes a unique set of transient simulation results which demonstrate the capability of the present fire model in predicting the pulsating behavior of fires.

## **1.6 Thesis organization**

---

New modifications to the turbulence submodel, based on the analysis of the experimental pool fire data base [26], are proposed and their effects on numerical predictions are discussed in Chapter 7.

Finally, Chapter 8 summarizes the findings of this work and concludes with some recommendations for future work.

# Chapter 2

## Background

### 2.1 Physics of the Phenomenon

Pool fires are known as self sustained buoyancy driven diffusion flames. Although some of their characteristics have been identified, the current knowledge of the physics and details of different mechanisms governing their behavior is still very limited. This is mainly due to particular difficulties in experimental studies which form the base of our understanding of the physics of pool fires.

In laboratory experiments, pool fires are often modeled by igniting shallow pans of liquid fuels. From the results of such experiments an overall picture of pool fire behavior emerges [25, 24, 29, 53]. Based on experimental observation, after ignition a diffusion flame rapidly forms above the fuel surface and the gas temperature rises, producing an upward buoyant force. This buoyancy drives the hot gases upward and causes the system to entrain air [24]. Due to lack of initial momentum, the system is highly unstable;

## **2.1 Physics of the Phenomenon**

---

however, there seems to be an ordered series of repetitive cycles of mixing, combustion, expansion and mixing again. There is also a characteristic large scale coherent eddy structure of rising toroidal-shaped vortices which is believed to control the mixing process in pool fires [29].

Experimental results show that the flame structure above a pool fire can be divided into three zones [29].

1. Continuous Flame (CF) zone
2. Intermittent Flame (IF) zone
3. Buoyant Plume

The CF zone is the field near the pool surface, where a persistent flame exists continuously. As the result of buoyant forces, the burning gases accelerate upward through this region. A fuel rich subdomain has also been observed in the lower part of the CF zone adjacent to the liquid surface. Above the CF, zone there is the IF zone where the flame surface shows large irregularities which fluctuate with time (i.e. flame intermittency). At the top of this region where flame is seldom seen, the turbulent plume starts. The motion of combustion products and entrained air in the buoyant plume is governed by the buoyancy generated in the first two zones.

A distinguishing feature of pool fires over momentum driven jet flames is that the flow field and flame structure are dominated by buoyancy in pool fires. In other words, in a pool fire the momentum of the fuel vapor rising from the fuel surface is too small to drive the flow field. In addition, the supply of combustible gases in pool fires is controlled by heat feed back from the flame to the liquid fuel whereas, in jet flames it is controlled by the fuel



## **2.2 Elements of a Pool Fire Model**

---

feed rate to the nozzle and is therefore independent of the flame temperature and/or structure.

## **2.2 Elements of a Pool Fire Model**

Because of the complexity of and interactions between the different phenomena involved in modeling pool fire behavior, accurate prediction of such complicated flow fields is extremely difficult. Therefore, the problem must be reduced to determine those factors which are the most important in pool fire calculations. These have been identified as *buoyancy, turbulence, radiation* and *reaction*.

The roles of each factor and how they interact with one another in the overall modeling of the pool fire are discussed in the following.

### **1- Buoyancy**

Buoyancy is the dominant force driving the development of the pool fire flow field, thus it should be properly accounted for in the mean flow equations. Moreover, production of turbulent kinetic energy through buoyancy effects should be included since it, in turn, affects the accuracy of the prediction of mixing processes and subsequent calculation of reaction rates and chemical effects.

### **2- Turbulence**

The enhanced diffusion of momentum, mass and energy characteristic of turbulent flows is a very important aspect of the pool fire model. Modeling of the turbulent diffusion processes will directly affect prediction of the extent of mixing and therefore the reaction rate. The reaction rate, in turn, determines

## **2.2 Elements of a Pool Fire Model**

---

the fire heat release and consequently the buoyancy production which drives the fluid motion.

### **3- Radiation**

In pool fires, the fuel evaporation rate and hence fire heat release rate is determined by the net heat feed back to the liquid fuel from its surroundings including the flame. In medium and large scale pool fires, the dominant heat transfer mechanism is radiation [54]. As a result, the accuracy of the predicted fuel evaporation and fire spread rates in these fires, depends on how well radiation is modeled.

In addition, radiative heat transfer has a strong contribution to the energy equation. This will again affect the evaluation of the buoyancy production term in the momentum equation. Therefore, it is important to adequately account for the effects of radiation in the overall fire simulation.

Radiation models often require calculation of local radiative properties in the fire. For this, it is necessary to model soot formation and growth (i.e. local soot concentration) as well. This aspect of the modeling becomes more important as the sooting tendency of the fuel increases.

### **4- Reaction**

The importance of an accurate prediction for the reaction rate has been previously discussed. To this end, it is necessary to adequately account for the interaction of turbulence in predicting the reaction rate in the pool fire model. In the next section, the necessity to consider the details of the reaction mechanism for different applications is discussed first, and then different techniques to account for the effects of turbulence on reaction are briefly reviewed.

### 2.3 Effects of Turbulence on Chemistry

In computational combustion there have been two independent approaches in order to include chemical reaction in the analysis.

- In one case, more attention has been paid to detailed chemistry rather than fluid mechanic effects, in order to assess the important elementary reaction paths taken to get from fuel/oxidizer to products of combustion.
- In the second approach, the overall prediction of the flow field quantities, such as velocity and temperature, is given higher priority than the details of the reaction mechanism.

The first approach is more desirable for those cases where determination of the reaction efficiency is important or where environmental issues regarding the production of, for instance, nitrogen based pollutants should be considered. Since fire calculations are usually used in the design of fire detection-protection systems, where prediction of the velocity and temperature fields is the number one priority, it seems that the second approach is more applicable to achieve the current objectives. In the second approach, a one step irreversible reaction is usually assumed and therefore, the effects of turbulence on chemistry will be discussed below only for such reaction mechanisms.

Although the kinetic mechanisms are not always known and kinetic constants are difficult to identify, the major difficulty in accounting for combustion in the flow, lies not in these areas but in estimating the mean reaction rate in the presence of turbulence [55, 56]. Considering the following simple

### 2.3 Effects of Turbulence on Chemistry

---

reaction,



where  $F$  and  $O$  represent the reactants and  $P$  denotes the products, the instantaneous reaction rate of species  $F$  ( $\mathfrak{R}_F$ ), for instance, becomes [57] (variables are defined in the nomenclature)

$$\mathfrak{R}_F = \rho^2 Y_F Y_O \nu'_F \mathcal{M}_F^{-1} A \exp\left(-\frac{E}{\mathcal{R}T}\right). \quad (2.2)$$

Since all practical fires essentially occur in highly turbulent flows, the interactions between the turbulent fluid mechanics and the chemical reaction are crucial in prediction of the overall process. To calculate the mean reaction rate needed for the species equation, after Reynolds decomposition and appropriate simplification, one obtains [57, 58]

$$\begin{aligned} \overline{\mathfrak{R}}_F = & \overline{\rho}^2 \overline{Y}_F \overline{Y}_O \nu'_F \mathcal{M}_F^{-1} A \exp\left(\frac{-E}{\mathcal{R}\overline{T}}\right) \left[ 1 + \frac{\overline{\rho'^2}}{\overline{\rho}^2} + \frac{\overline{Y'_F Y'_O}}{\overline{Y}_F \overline{Y}_O} + 2 \frac{\overline{\rho' Y'_F}}{\overline{\rho} \overline{Y}_F} + 2 \frac{\overline{\rho' Y'_O}}{\overline{\rho} \overline{Y}_O} \right. \\ & \left. + \frac{E}{\mathcal{R}\overline{T}} \left( \frac{\overline{Y'_F T'}}{\overline{Y}_F \overline{T}} + \frac{\overline{Y'_O T'}}{\overline{Y}_O \overline{T}} \right) + \left( \frac{E}{2\mathcal{R}\overline{T}} - 1 \right) \frac{\overline{T'^2}}{\overline{T}^2} + \dots \right]. \quad (2.3) \end{aligned}$$

For slow reactions (i.e. reaction time scale  $\gg$  turbulent time scale) the effect of fluctuations on the reaction rate can be ignored. This means that the sum of all the terms inside the square brackets in Equation (2.3) approaches unity for slow reactions. But, when reaction rates are not sufficiently slow compared to the local turbulence (which is the case in practical pool fires), this approximation may result in appreciable error [56]. On the other hand, accounting for the effects of fluctuations such as those in Equation (2.3), will increase the complexity of the closure problem.

## 2.3 Effects of Turbulence on Chemistry

---

To overcome the problem associated with the nonlinear relations between instantaneous quantities in Equation (2.2), there have been two major proposals. In one approach, the need for calculating the reaction rate is eliminated through introduction of a conserved scalar (i.e. mixture fraction  $f$ ) whose transport equation does not have a source term. Then, instantaneous values of species concentrations and enthalpy may be related to  $f$  under certain assumptions. In this approach, all averaged quantities may be deduced by weighting the instantaneous values with a probability distribution function (PDF) for the mixture fraction [57, 59, 60]. The usual use of PDF techniques, however, prevents a detailed solution for the radiation effects in the energy equation. The reason for this is that in PDF techniques the energy equation is usually written in terms of a conserved quantity whose definition relies on using a simple radiation model.

In the second approach, the reaction rate is related to turbulent quantities (e.g.  $k$  and  $\epsilon$ ) and mean concentrations. One such method is the eddy dissipation concept (EDC) pioneered by Magnussen [49], which is an extension of the eddy break up model of Spalding [61]. The EDC was proposed to model the interaction of turbulence and chemistry for both premixed and diffusion flames. This model has successfully been used for different flames (e.g. [46], [47] and [62]) and is rather easy to implement. In this model, it is assumed that the reaction occurs inside the fine eddy structures and is controlled by the mass transfer rate between these structures and the bulk of the fluid.

## 2.4 The Averaging Problem

---

### 2.4 The Averaging Problem

Experimental evidence shows that the flow in laboratory scale pool fires, as well as in all practical fires is turbulent. The range of time and length scales encompassed in the temporal and spatial variations in the dependent variables is so wide that direct numerical solution of the governing equations becomes prohibitively expensive.

An alternative approach to describe the fire flow is to decompose the dependent variables into mean and fluctuating components. The governing equations are then averaged to convert them into statistical equations describing the evolution of mean flow quantities. For flows where density changes are significant, two types of decomposition are used.

In time or unweighted averaging, the instantaneous value of any dependent variable,  $\phi$ , is decomposed into a mean value,  $\bar{\phi}$ , and its fluctuating component,  $\phi'$ , such that

$$\phi(\mathbf{x}, t) = \bar{\phi}(\mathbf{x}, t) + \phi'(\mathbf{x}, t), \quad (2.4)$$

where

$$\bar{\phi}(\mathbf{x}, t) = \frac{1}{2\delta t} \int_{-\delta t}^{\delta t} \phi(\mathbf{x}, t) dt. \quad (2.5)$$

The time interval,  $\delta t$ , must be chosen to be sufficiently large compared with the largest turbulence time scale but small compared with the smallest mean flow time scale.

On the other hand, in Favre or density weighted averaging the dependent variable is decomposed as

$$\phi(\mathbf{x}, t) = \bar{\phi}(\mathbf{x}, t) + \phi''(\mathbf{x}, t) \quad (2.6)$$

## 2.4 The Averaging Problem

---

where the Favre averaged value of the dependent variable,  $\bar{\phi}$ , is calculated by

$$\bar{\phi}(\mathbf{x}, t) = \frac{\overline{\rho(\mathbf{x}, t)\phi(\mathbf{x}, t)}}{\bar{\rho}(\mathbf{x}, t)} \quad (2.7)$$

and  $\phi''$  is the Favre fluctuating component of  $\phi$ .

If time averaging is used, many extra correlations involving density fluctuation appear in the governing equations, and each needs to be modeled. This, in turn, increases the complexity of the *turbulence closure* problem for variable density flows. The use of Favre averaging eliminates these extra unknown correlations, making Favre averaging very attractive for flow situations where significant density changes occur. The Favre averaged equations look similar to the time averaged equations obtained for turbulent incompressible flows, with the exception that time averaged quantities are now replaced by Favre averaged values.

The use of Favre averaged equations may not always be recognized. Often, time averaging is ostensibly used, but the extra correlations involving density fluctuation are neglected. This essentially reduces the exact time averaged equations to a form identical to the Favre averaged equations. The solution of these equations would then yield density-weighted values of all variables, the validity of which depends on how close the Favre and time averaged values actually are.

It can be shown that for any quantity, say  $\phi$ , the difference between  $\bar{\phi}$  and  $\bar{\phi}$  is

$$\frac{\bar{\phi} - \bar{\phi}}{\bar{\phi}} = -\frac{\overline{\rho'\phi'}}{\bar{\rho}\bar{\phi}}. \quad (2.8)$$

Since experimental data for density is often not available, in order to calculate the right hand side of Equation (2.8), a model is proposed in order to

## 2.4 The Averaging Problem

relate  $\rho'$  to a measured quantity. We have assumed that  $\rho'$  can be approximated by  $-\frac{\bar{\rho}}{\bar{T}}T'$  in the second order correlations involving  $\rho'$ . This model is equivalent to neglecting all third order correlations and second order correlations involving  $\rho'$  and is consistent with the usual assumptions made to derive the averaged governing equations. Using this model for  $\rho'$ , the right hand side of Equation (2.8) can be calculated from *the available data*. For the vertical velocity component, results are shown in Figure (2.1-a). They

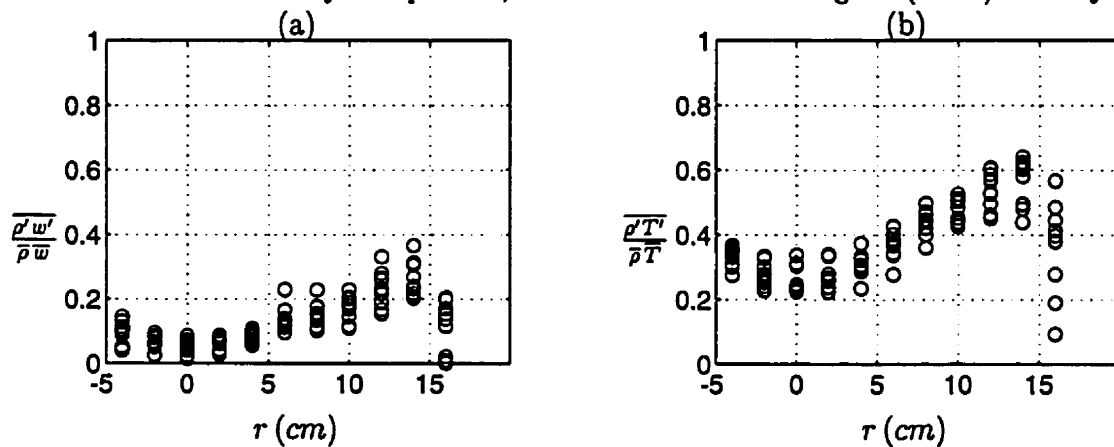


Figure 2.1: Differences between time and Favre averaged quantities - a) vertical velocity , b) temperature

indicate that the differences between time and Favre averaged mean velocities based on the methanol pool fire data of interest are on the order of 10% in the fire core region and increase towards the edge of the fire where the intermittency is higher. To further appreciate the magnitude of these values, it should be noted that measurement uncertainties in the data are also on the order of 5-10%. Measurements made in other turbulent reacting flows indicate similar results. Direct measurements of  $\bar{u}$  and  $\bar{u}$  in round jet diffusion flames yield differences which are on the order of 5% [63] while for other



## 2.4 The Averaging Problem

---

measurements they are estimated to be on the order of 10% [64, 65, 66].

From the results it appears that time and Favre averaged mean velocities are not too much different in turbulent reacting flows; however, it has elsewhere been shown that the difference between time and Favre averaged turbulent quantities and mean temperatures can be significant. From *the available data*, the differences between time and Favre averaged temperatures can be as high as 60%, as depicted in Figure (2.1-b). Experimental results of Starner and Bilger [63] show that differences between  $\sqrt{u'^2}$  and  $\sqrt{u''^2}$  are also much higher, on the order of 40% in their flow. Therefore, Favre and time averaging should not be used interchangeably.

Despite the attractive simpler form of the Favre averaged equations there are two disadvantages with the use of Favre averaging in modeling fire flows.

First, Favre averaged data may not be readily available to validate and compare with the numerical results, and also to set up boundary/initial conditions. This is because most instruments measure unweighted quantities [67]. For instance, an infinitely small thermocouple will detect an unweighted record of instantaneous temperature and it is commonly accepted that thermocouple systems provide measured values of temperature which approach the time averaged values [25, 66]. Although there is some debate on the interpretation of LDA velocity measurements [66], most authors have also considered these as being more representative of time averaged than Favre averaged values.

Second, Favre averaged turbulence models are essentially based on time averaged turbulence closures and it is not clear to what extent the hypotheses developed for incompressible flows may be transferred to Favre averaged

## **2.4 The Averaging Problem**

---

forms of the governing equations [68, 69].

For these reasons, time averaging is chosen for the present study. It should be mentioned that the choice of either averaging technique is still very much a matter of taste, and no definite advantage of one over the other has been shown.

# Chapter 3

## Description of The Fire Model

### 3.1 Introduction

Experimental results suggest that under weak wind conditions and in controlled laboratory conditions, fire plumes over circular burners remain nearly axisymmetric [45, 26]. In this study, a two dimensional numerical model applicable to both planar and axisymmetric fire scenarios is developed and used. In the following sections, the theoretical base for this fire model is discussed and governing equations are presented. For brevity and also generality, governing equations are presented using invariant vector notation and the expanded form of the equations is presented for clarity only when needed.

In order to mathematically describe the basic physics which govern fire behavior including the transport processes involved, one should start with a suitable form of the conservation equations for mass, momentum, energy and species. Since the present study is primarily concerned with gas phase processes, the conservation equations are presented here for a multicomponent,

### 3.2 Basic Definitions

---

reacting, gas mixture. Detailed derivation of these equations based upon continuum theory and the kinetic theory of gases can be found elsewhere [70, 71, 72] and will not be repeated here. However, certain basic definitions and relations which are frequently used will be given as needed for clarity and completeness. All variable definitions can be found in the nomenclature section and are given in the text only where required for clarity.

### 3.2 Basic Definitions

For a mixture of  $\mathcal{N}$  gaseous species, each species is associated with a mass concentration,  $\rho_i$  which is the mass of species  $i$  per unit volume of the mixture. This quantity depends on the species molecular weight,  $\mathcal{M}_i$ , and its molar concentration,  $c_i$ , as given in Equation (3.1)

$$\rho_i = \mathcal{M}_i c_i \quad i = 1, \dots, \mathcal{N} \quad (3.1)$$

The total (local) density of the mixture is then calculated as the sum of the densities of all species

$$\rho = \sum_{i=1}^{\mathcal{N}} \rho_i \quad (3.2)$$

An important quantity which is used to calculate the mass-weighted<sup>1</sup> mixture properties is the species mass fraction,  $Y_i$ , which is defined as

$$Y_i = \frac{\rho_i}{\rho} \quad i = 1, \dots, \mathcal{N} \quad (3.3)$$

---

<sup>1</sup>not to be confused with the mass-averaged or Favre-averaged properties in turbulent flows

### 3.3 Instantaneous Conservation Equations

---

An obvious property of the individual species mass fractions, which is frequently used to simplify other equations, is that they sum up to unity.

$$\sum_{i=1}^{\mathcal{N}} Y_i = 1 \quad (3.4)$$

In a diffusing mixture, each species may move at a different velocity denoted here by  $\mathbf{V}_i^S$ . Thus, the local instantaneous mass-weighted velocity of the mixture,  $\mathbf{U}$ , is defined as

$$\mathbf{U} = \frac{\sum_{i=1}^{\mathcal{N}} \rho_i \mathbf{V}_i^S}{\sum_{i=1}^{\mathcal{N}} \rho_i} = \sum_{i=1}^{\mathcal{N}} Y_i \mathbf{V}_i^S \quad (3.5)$$

The diffusion velocity of each species is then defined as the difference between the species velocity and the mass-weighted velocity

$$\mathbf{V}_i^d = \mathbf{V}_i^S - \mathbf{U} \quad (3.6)$$

### 3.3 Instantaneous Conservation Equations

#### Conservation of Species

The continuity equation for each species can be derived by applying the conservation law for mass of species  $i$  to a fixed volume element in space,  $\Delta V$ . The general form of this equation becomes

$$\frac{\partial}{\partial t}(\rho Y_i) + \nabla \cdot (\rho Y_i (\mathbf{U} + \mathbf{V}_i^d)) = -\mathfrak{R}_i \quad (3.7)$$

where  $\mathfrak{R}_i$  is the mass rate of consumption of species  $i$  in  $\Delta V$ . The diffusion velocity can be eliminated from the species equation, Equation (3.7), by

### 3.3 Instantaneous Conservation Equations

---

invoking Fick's law which states

$$\mathbf{V}_i^d = -\mathcal{D}\nabla \ln Y_i \quad i = 1, \dots, \mathcal{N} \quad (3.8)$$

Implicit in Fick's law is that all species have the same binary diffusion coefficient,  $\mathcal{D}$ , which can then be totally removed from the species equation.

Utilizing a Schmidt number,  $Sc$ , the species equation becomes

$$\frac{\partial \rho Y_i}{\partial t} + \nabla \cdot (\rho Y_i \mathbf{U}) = \nabla \cdot \left( \frac{\mu}{Sc} \nabla Y_i \right) - \mathfrak{R}_i \quad (3.9)$$

where

$$Sc = \frac{\mu}{\rho \mathcal{D}} \quad (3.10)$$

#### Overall Continuity Equation

Summing Equation (3.9) over all species and noting that

$$\sum_{i=1}^{\mathcal{N}} \mathfrak{R}_i = \sum_{i=1}^{\mathcal{N}} Y_i \mathbf{V}_i^d = 0 \quad (3.11)$$

yields the overall continuity equation,

$$\frac{\partial \rho}{\partial t} + \nabla \cdot (\rho \mathbf{U}) = 0 \quad (3.12)$$

#### Conservation of Momentum

The equations which describe the conservation of linear momentum are essentially based upon Newton's second law of motion. If a continuous, isotropic and homogeneous media is considered and the relation between shear stress

### 3.3 Instantaneous Conservation Equations

---

and the rate of fluid deformation is linear (i.e. a Newtonian fluid), the momentum equations can be written in the following vector form

$$\frac{\partial \rho \mathbf{U}}{\partial t} + \nabla \cdot \rho \mathbf{U} \mathbf{U} = \nabla \cdot \boldsymbol{\sigma} + \sum_{i=1}^{\mathcal{N}} \rho_i \mathbf{f}_i \quad (3.13)$$

where  $\mathbf{f}_i$  is the external force per unit mass acting on species  $i$  and  $\boldsymbol{\sigma}$  is the total stress tensor defined by

$$\boldsymbol{\sigma} = -P\mathbf{I} + \boldsymbol{\tau} \quad (3.14)$$

In Equation (3.14)  $P$  is the pressure,  $\mathbf{I}$  is the identity matrix and  $\boldsymbol{\tau}$  is the shear stress tensor given as

$$\boldsymbol{\tau} = \left[ \left( \mu' - \frac{2}{3}\mu \right) \nabla \cdot \mathbf{U} \right] \mathbf{I} + \mu [(\nabla \mathbf{U}) + (\nabla \mathbf{U})^T] \quad (3.15)$$

where  $\mu'$  is the bulk viscosity<sup>2</sup> and  $\mu$  is the molecular viscosity of the mixture.

The local pressure in Equation (3.14) is usually broken into three terms [73] for flows where buoyancy is the main driving force, such as natural convection flows and of course, fires. This yields

$$P = P_{\text{ref}} - \int_{z_{\text{ref}}}^z g \rho_{\infty}(z) dz + P_d \quad (3.16)$$

where  $P_{\text{ref}}$  is a fixed reference pressure, usually the far field ambient pressure,  $g$  is the magnitude of gravitational acceleration,  $\rho_{\infty}$  is the far field ambient density and  $P_d$  is a kinematic pressure associated with the dynamics of the flow.

Substituting Equation (3.16) into (3.13) and assuming that gravity is the only important external force (i.e.  $\mathbf{f}_i = \mathbf{g}$ ) yields

$$\frac{\partial \rho \mathbf{U}}{\partial t} + \nabla \cdot \rho \mathbf{U} \mathbf{U} = -\nabla P_d + \nabla \cdot \boldsymbol{\tau} + (\rho - \rho_{\infty}) \mathbf{g} \quad (3.17)$$

---

<sup>2</sup>sometimes called the second viscosity

### 3.3 Instantaneous Conservation Equations

---

#### Conservation of Energy

The principle of energy conservation for a multicomponent mixture states that [74]

*the rate of change of both internal and kinetic energy within a control volume balances with the net energy influx due to the usual heat transfer modes (i.e. conduction, convection and thermal radiation), the inter-diffusion of species together with the net rate of work done on the mixture by its surroundings (e.g. viscous stresses and body forces) plus the rate of heat added by other heat sources.*

The general form of the energy equation for a reacting system of gases is extremely complex. Using vector notation, the energy equation in terms of total enthalpy,  $H$ , becomes [70, 74]

$$\rho \frac{DH}{Dt} = \frac{Dp}{Dt} - \nabla \cdot \mathbf{q} + \rho \sum_{i=1}^N Y_i \mathbf{f}_i \cdot (\mathbf{U} + \mathbf{V}_i^d) + \mathbf{U} \cdot \nabla \boldsymbol{\sigma} + \boldsymbol{\tau} : \nabla \mathbf{U} \quad (3.18)$$

where

$$\mathbf{q} = -K \nabla T + \rho \sum_{i=1}^N h_i Y_i \mathbf{V}_i^d + \mathcal{R}T \sum_{i=1}^N \sum_{j=1}^N \left( \frac{X_j \mathcal{D}_{T,i}}{\mathcal{M}_i \mathcal{D}_{ij}} \right) (\mathbf{V}_i^d - \mathbf{V}_j^d) + \mathbf{q}_r \quad (3.19)$$

$$H = \sum_{i=1}^N Y_i h_i + \frac{\mathbf{U} \cdot \mathbf{U}}{2} = h + \frac{\mathbf{U} \cdot \mathbf{U}}{2} \quad (3.20)$$

and

$$h_i = h_i^0 + \int_{T^0}^T C_{p_i} dT \quad i = 1, \dots, N \quad (3.21)$$



### 3.3 Instantaneous Conservation Equations

---

Based on Equation (3.21), the specific enthalpy of species  $i$ ,  $h_i$ , consists of its enthalpy of formation,  $h_i^\circ$ , at a reference temperature,  $T^\circ$ , plus a change in enthalpy from  $T^\circ$  to  $T$ . In this form, energy is not explicitly added to a fluid during reaction, instead reaction is accounted for through conversion of chemical energy stored in different species into sensible heat.

For fires where the gas velocity is low and pressure is nearly constant, the general form of the energy equation, Equation (3.18), can be reduced to a simplified form. The total viscous work term and the term describing work due to buoyancy can be neglected, along with the term for work done by pressure. In addition, since the kinetic energy of the mixture is very small compared to the mixture enthalpy, the static enthalpy,  $h$ , is approximately equal to the total enthalpy,  $H$ . Finally, the heat flux caused by concentration gradients of different species, the third term on the RHS of Equation (3.19), can be neglected in comparison with the thermal energy exchange within the mixture for most applications [74, 70]. Under these assumptions, the energy equation reduces to

$$\frac{\partial \rho h}{\partial t} + \nabla \cdot (\rho h \mathbf{U}) = \nabla \cdot (K \nabla T + \rho \sum_{i=1}^N h_i \mathcal{D} \nabla Y_i - \mathbf{q}_r) \quad (3.22)$$

Using Equation (3.9) and assuming that the reference temperature,  $T^\circ$ , for all species is the same, the simplified energy equation can be rearranged into a form in terms of temperature,  $T$ ,

$$\begin{aligned} \frac{\partial \rho C_p (T - T^\circ)}{\partial t} + \nabla \cdot (\rho C_p (T - T^\circ) \mathbf{U}) \\ = \nabla \cdot \left( K \nabla T + \mu \sum_{i=1}^N C_{p_i}^m (T - T^\circ) \nabla Y_i - \mathbf{q}_r \right) + \mathfrak{R}_{fu} \mathcal{H}_c \end{aligned} \quad (3.23)$$

### 3.3 Instantaneous Conservation Equations

---

where  $C_{p_i}^m$  is a mean value of the instantaneous heat capacity of species  $i$  at constant pressure,  $C_p$  is a mass-weighted heat capacity of the mixture at constant pressure and  $\mathcal{H}_c$  is the heat of combustion, as defined below

$$C_{p_i}^m = \frac{\int_{T^\circ}^T C_{p_i} dT}{T - T^\circ} \quad (3.24)$$

$$C_p = \sum_{i=1}^N Y_i C_{p_i}^m \quad (3.25)$$

and

$$\mathcal{H}_c = \frac{-\sum_{i=1}^N h_i^\circ \mathfrak{R}_i}{\mathfrak{R}_{fu}} \quad (3.26)$$

Equation (3.23) is the one which is numerically solved in the present study. The advantages of solving the energy equation in terms of  $T$  rather than  $h$  are twofold. First, it reduces the calculations required to obtain temperature in simulations of reacting flows where  $C_p$  is a function of  $T$  and species mass fraction. Second, it allows more explicit coupling of the energy, mass and momentum equations. Since in natural fires the velocity and temperature fields are strongly coupled, a better coupling in the governing equations improves the overall efficiency of the numerical model.

### Gas State Relation

In natural fires, pressure is nearly atmospheric and temperature is relatively high. Therefore, the gas phase can be treated as an ideal gas for which the

### 3.4 Averaged Conservation Equations

---

state relation is

$$\rho = \frac{P}{\mathcal{R}T \sum_{i=1}^{\mathcal{N}} \frac{Y_i}{\mathcal{M}_i}} \quad (3.27)$$

Equations (3.9), (3.12), (3.17), (3.23) and (3.27) constitute a closed set of equations for  $P$ ,  $\rho$ ,  $T$ ,  $\mathbf{U}$  and  $Y_i$ , provided gas properties and reaction rates of different species are known.

### 3.4 Averaged Conservation Equations

As discussed in Section 2.4, time averaging is preferred for the present study. In this method, exact averaged conservation equations are obtained by using Reynolds decomposition of the variables, and then time averaging the results. To simplify the resultant equations, third and higher order correlations are assumed to be negligible and turbulent fluctuations in thermophysical properties, e.g.  $C_p$ ,  $\mu$  and  $K$  as well as correlations involving both  $\rho'$  and  $Y_i'$  are neglected. This results in the following simplified form of the averaged equations.

**Averaged species equation**

$$\frac{\partial \bar{\rho} \bar{Y}_i}{\partial t} + \nabla \cdot (\bar{\rho} \bar{\mathbf{U}} \bar{Y}_i + \overline{\rho' \mathbf{U}' Y_i}) = \nabla \cdot \left( \frac{\mu}{Sc} \nabla \bar{Y}_i - \bar{\rho} \overline{\mathbf{U}' Y_i'} \right) - \bar{\mathfrak{R}}_i \quad (3.28)$$

**Averaged continuity equation**

$$\frac{\partial \bar{\rho}}{\partial t} + \nabla \cdot (\bar{\rho} \bar{\mathbf{U}} + \overline{\rho' \mathbf{U}'}) = 0 \quad (3.29)$$

**Averaged momentum equation**

Components of the averaged momentum equations are best presented in a

### 3.4 Averaged Conservation Equations

---

semi-expanded vector form as follows. In the following equations  $\hat{r}$  and  $\hat{z}$  are the unit vectors of the coordinate system. For axisymmetric cases, they denote radial and axial directions, respectively.

**Averaged r-momentum equation**

$$\begin{aligned} \frac{\partial}{\partial t} (\bar{\rho} \bar{u} + \overline{\rho' u'}) + \nabla \cdot (\bar{\rho} \bar{u} \bar{U} + \bar{u} \overline{\rho' U'} + \overline{\rho' u'} \bar{U}) + \nabla \cdot (\bar{\rho} \overline{u' u'} \hat{r} + \bar{\rho} \overline{u' w'} \hat{z}) \\ - \mathcal{J} \frac{\bar{\rho} \overline{v' v'}}{r} = - \frac{\partial \bar{P}_d}{\partial r} - \mathcal{J} \frac{\bar{\tau}_{22}}{r} + \nabla \cdot (\bar{\tau}_{11} \hat{r} + \bar{\tau}_{13} \hat{z}) \end{aligned} \quad (3.30)$$

where

$$\mathcal{J} \begin{cases} = 0 & \text{for Cartesian coordinate system} \\ = 1 & \text{for cylindrical coordinate system} \end{cases}$$

**Averaged z-momentum equation**

$$\begin{aligned} \frac{\partial}{\partial t} (\bar{\rho} \bar{w} + \overline{\rho' w'}) + \nabla \cdot (\bar{\rho} \bar{w} \bar{U} + \bar{w} \overline{\rho' U'} + \overline{\rho' w'} \bar{U}) + \nabla \cdot (\bar{\rho} \overline{u' w'} \hat{r} + \bar{\rho} \overline{w' w'} \hat{z}) \\ = (\rho_\infty - \bar{\rho})g - \frac{\partial \bar{P}_d}{\partial z} + \nabla \cdot (\bar{\tau}_{31} \hat{r} + \bar{\tau}_{33} \hat{z}) \end{aligned} \quad (3.31)$$

where

$$\bar{\tau}_{11} = -\frac{2}{3}\mu(\nabla \cdot \bar{U}) + 2\mu \frac{\partial \bar{u}}{\partial r}$$

$$\bar{\tau}_{31} = \bar{\tau}_{13} = \mu \left( \frac{\partial \bar{w}}{\partial r} + \frac{\partial \bar{u}}{\partial z} \right)$$

$$\bar{\tau}_{33} = -\frac{2}{3}\mu(\nabla \cdot \bar{U}) + 2\mu \frac{\partial \bar{w}}{\partial z}$$

### 3.5 Turbulence Submodel

---

and

$$\bar{\tau}_{22} = -\frac{2}{3}\mu(\nabla \cdot \bar{\mathbf{U}}) + 2\mathcal{J}\mu\frac{\bar{u}}{r}$$

**Averaged energy equation**

$$\begin{aligned} & \frac{\partial}{\partial t} \left( \bar{\rho} C_p (\bar{T} - T^\circ) \bar{\rho}' T' C_p \right) \\ & + \nabla \cdot \left( \bar{\rho} C_p (\bar{T} - T^\circ) \bar{\mathbf{U}} + \bar{\rho}' \bar{\mathbf{U}}' C_p (\bar{T} - T^\circ) + \bar{\rho}' T' C_p \bar{\mathbf{U}} \right) \\ & = \nabla \cdot \left( K \nabla \bar{T} - \bar{\rho} C_p \bar{\mathbf{U}}' T' + \mu \sum_{i=1}^N \left( C_{p_i}^m (\bar{T} - T^\circ) \nabla \bar{Y}_i \right) - \mathbf{q}_r \right) + \mathfrak{R}_{fu} \mathcal{H}_c \end{aligned} \quad (3.32)$$

### 3.5 Turbulence Submodel

The unweighted averaged equations given in Section 3.4 involve some unknown correlations (i.e. turbulent shear stresses and turbulence fluxes etc.) which need to be evaluated. This is accomplished through the turbulence model closure. Depending on the complexity of the turbulence closure, different methods are used to estimate the unknown correlations. Turbulence closures could be as simple as using algebraic relations (i.e. Prandtl's mixing length hypothesis) or as complicated as solving full transport equations for each of the unknown correlations.

In fire modeling, where strong buoyancy effects enhance the non-isotropy of turbulence, simplistic algebraic turbulence models are not suitable. On the other hand, second order turbulence closures (i.e. Reynolds Stress Models or Algebraic Stress Models) which seem to account for such turbulence non-isotropy are computationally expensive and often cause instability problems

### 3.5 Turbulence Submodel

---

in numerical computations. Since buoyancy-driven flows tend to be very unstable both physically and numerically, it is hard to obtain a convergent solution [75]. Therefore, it is generally not advisable to utilize turbulence models which may further contribute to instability and/or convergence problems.

The  $k$ - $\epsilon$  model [76] is, by far, the most popular and widely used turbulence model for engineering calculations [77], and for calculations of pool fires as shown in Section 1.4. This two equation turbulence model seems to provide a reasonable compromise between accuracy and efficiency of computation and therefore, is used in the present fire model.

In the standard  $k$ - $\epsilon$  model, the main modeling assumptions for time averaged shear stresses and turbulent fluxes are based on the Boussinesq hypothesis, which may be written as

$$\overline{U'U'} = \frac{2}{3} \left( k + \nu_t (\nabla \cdot \overline{U}) \right) \mathbf{I} - \nu_t \left( \nabla \overline{U} + (\nabla \overline{U})^T \right) \quad (3.33)$$

and

$$\overline{\phi'U'} = -\frac{\nu_t}{\sigma_\phi} \nabla \overline{\phi} \quad (3.34)$$

The eddy viscosity,  $\nu_t$ , is given by

$$\nu_t = C_\mu \frac{k^2}{\epsilon} \quad (3.35)$$

where  $C_\mu$  is assumed to be a constant in the standard  $k$ - $\epsilon$  model.

The turbulent kinetic energy,  $k = \frac{1}{2} \overline{U' \cdot U'}$ , and its dissipation rate,  $\epsilon = \nu \overline{\nabla U' : \nabla U'}$ , are obtained by solving separate transport equations. The  $k$  equation can be obtained by subtracting the averaged momentum equation from the instantaneous one, multiplying the result, *the perturbation equation*, by the fluctuating velocity vector,  $U'$ , and then averaging.

### 3.5 Turbulence Submodel

---

A transport equation for  $\varepsilon$  can be obtained by taking the divergence of the perturbation equation, performing the inner multiplication by  $\nabla \mathbf{U}'$  and then averaging [78, 77, 79].

The exact transport equations for turbulent kinetic energy and its dissipation rate for variable density flows using unweighted averaging involve many unknown third and higher order turbulence correlations, including many involving density fluctuations [80], and for which very little information is available. In practice, many of these correlations are either neglected or modeled using purely empirical proposals and/or arguments involving dimensional analysis. In this way, the exact equations are reduced to a more tractable form.

Without further elaborating on the simplifications and drastic surgeries involved in the derivation of the  $k$  and  $\varepsilon$  equations [77], their final forms including buoyancy production terms, are given as [81, 46]

**The  $k$  equation**

$$\begin{aligned} \frac{\partial}{\partial t}(\bar{\rho}k) + \nabla \cdot ((\bar{\rho}\mathbf{U} + \overline{\rho'\mathbf{U}'})k) = \\ \nabla \cdot \left[ \left( \mu + \frac{\mu_t}{\sigma_k} \right) \nabla k \right] + P_k - \bar{\rho}\varepsilon + B_k \end{aligned} \quad (3.36)$$

**The  $\varepsilon$  equation**

$$\begin{aligned} \frac{\partial}{\partial t}(\bar{\rho}\varepsilon) + \nabla \cdot ((\bar{\rho}\mathbf{U} + \overline{\rho'\mathbf{U}'})\varepsilon) = \\ \nabla \cdot \left[ \left( \mu + \frac{\mu_t}{\sigma_\varepsilon} \right) \nabla \varepsilon \right] + C_{\varepsilon 1} \frac{\varepsilon}{k} (P_k + B_k) - C_{\varepsilon 2} \bar{\rho} \frac{\varepsilon^2}{k} \end{aligned} \quad (3.37)$$

where

$$\begin{aligned} P_k = -\overline{\rho\mathbf{U}'\mathbf{U}'} : \nabla \bar{\mathbf{U}} \approx \\ \mu_t \left[ 2 \left( \frac{\partial \bar{u}}{\partial r} \right)^2 + 2\mathcal{J} \left( \frac{\bar{u}}{r} \right)^2 + 2 \left( \frac{\partial \bar{w}}{\partial z} \right)^2 + \left( \frac{\partial \bar{u}}{\partial z} + \frac{\partial \bar{w}}{\partial r} \right)^2 \right] \end{aligned} \quad (3.38)$$

### 3.5 Turbulence Submodel

---

and

$$B_k = \mathbf{g} \cdot \overline{\rho' \mathbf{U}'} \quad (3.39)$$

These forms of the equations were used in this work.

With known values of  $k$  and  $\varepsilon$ , turbulent Reynolds stresses and turbulent fluxes can be calculated using Equations (3.33) and (3.34). However, the  $\overline{\rho' T'}$  term in the energy equation still remains to be modeled. This term, which represents a turbulent energy flux due to simultaneous fluctuations of density and temperature, appears only when time averaging is used and has simply been neglected in previous models.

Due to the potential importance of the  $\overline{\rho' T'}$  term in determination of the behavior of fires, a first order approximation is used to model this term, which yield

$$\overline{\rho' T'} \approx -\frac{\bar{\rho}}{\bar{T}} \overline{T'^2} \quad (3.40)$$

To evaluate the right hand side of Equation (3.40) a transport equation for  $\overline{T'^2}$  is solved. The modeled form of this equation, which is equivalent to the transport equation for mean square fluctuations of mixture fraction used in other models [37, 43, 82], is

$$\begin{aligned} \frac{\partial}{\partial t} (\bar{\rho} \overline{T'^2}) + \nabla \cdot (\bar{\rho} \overline{\mathbf{U} T'^2}) = \\ \nabla \cdot \left[ \left( \mu + \frac{\mu_t}{\sigma_g} \right) \nabla \overline{T'^2} \right] + C_{g1} \mu_t (\nabla \bar{T})^2 - C_{g2} \bar{\rho} \frac{\varepsilon}{k} \overline{T'^2} \end{aligned} \quad (3.41)$$

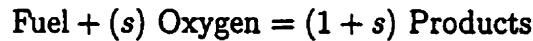
where  $\sigma_g$ ,  $C_{g1}$  and  $C_{g2}$  are additional model constants.



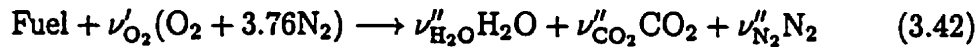
## 3.6 Combustion Submodel

The reaction of fuel and air in fires involves many elementary reactions, even for a simple fuel. For instance, Westbrook and Dryer [83] have postulated that the oxidation of methane, which is the simplest hydrocarbon, occurs through roughly two paths and involves at least 78 important elementary reactions.

Although such detailed reaction models may be important in certain applications, consideration of such complications in fire field modeling, where the global impact of combustion on flow field is of primary concern, is neither necessary nor desired. Besides, detailed reaction mechanisms and the associated rate coefficients for many of the common fuels are not completely known. Therefore, for engineering fire calculations, it is convenient to assume that the fuel oxidation takes place in a one-step irreversible reaction where 1 kg of fuel reacts with  $s$  kg of oxygen to produce  $(1 + s)$  kg of products.



For the fuels considered in the present study, the following general one-step global reaction mechanism is assumed to describe the combustion process for the fuel in air.



where  $\nu'_i$  and  $\nu''_i$  denote the molar stoichiometric coefficients of reactants and of products, respectively.

One of the main difficulties in computations of turbulent reacting flows is the estimation of mean reaction rate,  $\bar{\mathfrak{R}}_i$ , in the species equation, Equation

### 3.6 Combustion Submodel

---

(3.28). Magnussen and his coworkers [84, 85] have developed a model for this purpose which is an extension of the earlier Spalding Eddy Break Up (EBU) model [61] and assumes infinitely fast reaction kinetics. This is the formulation used in the present study. Justification is provided below.

For slow flows such as those occurring in natural fires, the reaction rate is usually limited by the rate at which diffusion processes can bring fuel and oxidizer together. Therefore, for overall calculation of the reaction rate, it is quite reasonable to assume that chemical rates are infinitely fast relative to mixing rates. The fast chemistry assumption can be evaluated by defining a Damköhler number which, in this case, would be the ratio of the time scale associated with the dissipation of turbulent fluctuations,  $\tau_t$ , to a characteristic chemical time scale,  $\tau_c$ . For fires,  $\tau_c$  seems to be 5 to 6 orders of magnitude smaller than  $\tau_t$  [1] which implies very high Damköhler numbers and justifies the fast chemistry assumption.

In a turbulent flow, according to Magnussen's generalized Eddy Dissipation Concept (EDC), reaction occurs in regions where fuel and oxidizer are mixed at the molecular level. These regions, where the molecular mixing associated with the dissipation of turbulence takes place, are believed to occupy only a small fraction of the total volume of the fluid. They also tend to appear in the highly strained regions between the larger eddies in the flow. Further, the Eddy Dissipation Concept postulates that the reaction rate of fuel in a turbulent flame is proportional to the mass transfer between the fine structures and the surrounding fluid and is controlled by the deficient reactant. With an assumption of nearly isotropic turbulence within the fine structures, EDC suggests the following relation for estimating the fuel

### 3.6 Combustion Submodel

---

consumption rate in a turbulent flame [84, 85]

$$\mathfrak{R}_{fu} = 23.6 \left( \frac{\nu \varepsilon}{k^2} \right)^{1/4} \frac{\varepsilon}{k} \frac{\chi}{1 - 9.7\chi \left( \frac{\nu \varepsilon}{k^2} \right)^{3/4}} \bar{C}_{\min} \quad \left( \frac{\text{kg}}{\text{m}^3\text{s}} \right) \quad (3.43)$$

where  $\chi$  is the fraction of the fine structures which react and, for diffusion flames, is usually assumed to be unity.  $\bar{C}_{\min}$  is the mass concentration of the deficient specie defined as

$$\bar{C}_{\min} = \text{Min} \left( \rho \bar{Y}_{fu}, \frac{\rho \bar{Y}_{O_2}}{\nu_{O_2} \frac{\mathcal{M}_{O_2}}{\mathcal{M}_{fu}}} \right) \quad (3.44)$$

Once the fuel reaction rate is calculated from Equation (3.43), the transport equation for the fuel mass fraction can be solved. To calculate the mass fraction of other species, significant savings in computational time are achieved by introducing a new conserved variable, the so called mixture fraction,  $f$ . The transport equation for the mixture fraction does not have a source term and after time averaging, it can be written in the form

$$\frac{\partial}{\partial t} \bar{\rho} \bar{f} + \nabla \cdot (\bar{\rho} \bar{\mathbf{U}} \bar{f} + \overline{\rho' \mathbf{U}' f}) = \nabla \cdot \left( \frac{\mu}{Sc} \nabla \bar{f} - \bar{\rho} \bar{\mathbf{U}}' f' \right) \quad (3.45)$$

There are several scalar variables which are conserved under chemical reaction and can be used to describe the mixing in a non-premixed reacting flow. But for cases where the chemistry is reduced to a one-step reaction, such as the present one, Shvab-Zeldovich variables are the most convenient ones. These variables can be defined by linear combinations of fuel mass fraction and other species mass fractions. To obtain identical transport equations for these conserved variables under identical boundary conditions, they need to be normalized based on their values in the fuel and oxidizer streams. Details

### 3.6 Combustion Submodel

---

of these manipulations can be found in Appendix A, with the pertinent results summarized below.

With known values of  $\bar{Y}_{fu}$  and  $\bar{f}$ , the mass fractions of other species can be calculated as follows

$$\bar{Y}_{O_2} = (\bar{Y}_{fu} - \bar{f}) \left( \frac{\nu'_{O_2} \mathcal{M}_{O_2}}{\mathcal{M}_{fu}} \right) + 0.2321(1 - \bar{f}) \quad (3.46)$$

$$\bar{Y}_{CO_2} = (\bar{f} - \bar{Y}_{fu}) \frac{\nu''_{CO_2} \mathcal{M}_{CO_2}}{\mathcal{M}_{fu}} \quad (3.47)$$

$$\bar{Y}_{H_2O} = (\bar{f} - \bar{Y}_{fu}) \frac{\nu''_{H_2O} \mathcal{M}_{H_2O}}{\mathcal{M}_{fu}} \quad (3.48)$$

and

$$\bar{Y}_{N_2} = 1 - (\bar{Y}_{fu} + \bar{Y}_{O_2} + \bar{Y}_{CO_2} + \bar{Y}_{H_2O}) \quad (3.49)$$

Since numerical values of  $\bar{Y}_{fu}$  at any point are always smaller than or equal to the corresponding values of  $\bar{f}$ , under certain situations and most likely due to numerical round off errors, Equation (3.46) sometimes yields non-physical, negative values for  $\bar{Y}_{O_2}$  before a fully converged solution is obtained. In order to prevent such problems and enhance the robustness of the numerical technique used to solve the governing equations, a separate transport equation for  $\bar{Y}_{O_2}$  can be solved. This is given by

$$\begin{aligned} \frac{\partial}{\partial t} \bar{\rho} \bar{Y}_{O_2} + \nabla \cdot ((\bar{\rho} \bar{U} + \bar{\rho}' \bar{U}') \bar{Y}_{O_2}) = \\ \nabla \cdot \left( \frac{\mu}{Sc} \nabla \bar{Y}_{O_2} - \bar{\rho} \bar{U}' Y'_{O_2} \right) - \mathfrak{R}_{fu} \frac{\mathcal{M}_{fu}}{\nu'_{O_2} \mathcal{M}_{O_2}} \end{aligned} \quad (3.50)$$

The addition of a transport equation for  $\bar{Y}_{O_2}$  is a new feature of the present model which eliminates problems with non-physical values of  $\bar{Y}_{O_2}$

### 3.7 Radiation Submodel

---

and improves the robustness of the numerical model significantly. The above set of equations forms the basis for the combustion submodel in the present fire field model.

## 3.7 Radiation Submodel

Thermal radiation directly affects the energy equation through the divergence of the radiative energy flux,  $\nabla \cdot \mathbf{q}_r$ . The calculation of this term requires a solution for the Radiative Transfer Equation (RTE) which, in general, is extremely difficult to solve and imposes another challenge in fire modeling.

A comprehensive radiation model for fires which are non-homogeneous absorbing-emitting media needs a detailed description of temperature and species scalar fields and also requires accurate methods to calculate soot concentration and radiative properties of the participating species. Including such a detailed model for radiation dramatically increases the complexity of a fire model, as well as increasing computational time required to reach a solution; however, inclusion of a complex radiation submodel may not significantly improve the final predictions of fire behavior for several reasons. First, the angular resolution required to accurately solve the radiative transfer equation and resolve the directional dependency of radiation intensity within the fire may be much finer than those assumed in commonly used radiation models (e.g. flux models). Second, there still exists a large degree of uncertainty in the results of some of the submodels required in radiation calculations, in particular models for soot formation and radiation, mainly due to the very approximate nature of their current formulations.

### 3.7 Radiation Submodel

---

Therefore, in cases where only the properties of the gas phase are solved, many authors have justified the use of a much simpler approach to radiation modeling [48, 43, 44, 45]. This simplified model, *the constant fraction radiation model*, is based on the experimental observation that flames appear to radiate a fixed fraction of their total available heat of combustion. The specific fraction radiated depends on the fuel type [1, 39, 86]. Using this simplification, the divergence of the radiative heat flux can be calculated by

$$\nabla \cdot \mathbf{q}_r \approx \chi \mathcal{H}_c \mathcal{R}_{fu} \quad (3.51)$$

where  $\chi$  is a constant radiation fraction obtained from experiment and is different than the  $\chi$  in the EDC model discussed in Section 3.6. The constant fraction model has the merit of simplicity and also restricting the total radiation loss to a desired level; however, the implied distribution of volumetric radiation loss within the fire flow field is not realistic. Equation (3.51) indicates that the radiation loss distribution depends only on the calculated fuel reaction rate, whereas, in reality, at least the temperature field and local gas emissivities should also be accounted for in determining the distribution of radiation from the fire.

In an attempt to incorporate the effects of local gas temperature and emissivity in the radiation submodel, a new alternative approach to evaluate  $\nabla \cdot \mathbf{q}_r$  has been added to the present fire model.

It can be shown that in the optically thin limit, the divergence of radiative heat flux becomes [87, 88]

$$\nabla \cdot \mathbf{q}_r = 4a\sigma(T^4 - T_\infty^4) \quad (3.52)$$

where  $a$  is the local gas absorption coefficient and  $\sigma$  is the Stefan-Boltzmann

### 3.7 Radiation Submodel

---

coefficient. This expression can be multiplied by an appropriate factor to ensure that even though radiation losses are locally redistributed throughout the fire field, the total radiation loss remains equal to the level obtained from the classical constant fraction radiation model. Therefore, as an alternative to the classical constant fraction approach to radiation, in this work the radiation is postulated to be distributed as

$$(\nabla \cdot \mathbf{q}_r)_n = 4a_n \sigma (T_n^4 - T_\infty^4) \frac{\chi \mathcal{H}_c \dot{m}_{fu}}{\sum_n 4a_n \sigma (T_n^4 - T_\infty^4) \nabla_n} \quad (3.53)$$

where  $\dot{m}_{fu}$  is the total fuel mass flux and the subscript  $n$  refers to the  $n$ th control volume. In the present model,  $a$  is calculated by [46, 47]

$$a = \frac{\epsilon}{\delta} \quad (3.54)$$

where  $\epsilon$  is the total gas emissivity and  $\delta$  is a local cell dimension of the computational grid which is assumed to be equal to the ratio of volume to area for each control volume. The total gas emissivity is calculated by the temperature weighted sum of gray gases model [89] which postulates that total emissivity may be represented by the sum of gray gas emissivities weighted by some temperature dependent factors. According to this model, the total emissivity may be calculated by

$$\epsilon = \sum_{i=0}^I a_{\epsilon,i}(T) (1 - e^{-\kappa_i PS}) \quad (3.55)$$

where  $\kappa_i$  is the absorption coefficient of the  $i$ -th gray gas and  $PS$  is the partial pressure-path length product. The emissivity weighting factors for the  $i$ -th gray gas,  $a_{\epsilon,i}$ , are calculated by

$$a_{\epsilon,i} = \sum_{j=1}^J b_{\epsilon,i,j} T^{j-1} \quad (3.56)$$

### 3.8 Thermophysical Properties

---

where  $b_{\epsilon,i,j}$  are referred to as the emissivity gas temperature polynomial coefficients. Numerical values for  $\kappa_i$  and  $b_{\epsilon,i,j}$  can be found in [89].

## 3.8 Thermophysical Properties

The thermophysical properties of a mixture of ideal gases which undergo a reaction vary significantly due to changes in the gas temperature and composition. In the present model, the gas density is calculated using the state relation, Equation (3.27), where the mixture composition has been accounted for.

The specific heat of the gas mixture at constant pressure,  $C_p$ , which has a direct effect on the energy equation, is calculated using equations (3.24) and (3.25). The heat capacities for each species in Equation (3.24),  $C_{p_i}^m$ , are expressed by third order polynomials [90]; however, some of these polynomial fits fail to give realistic values of the properties at the higher temperatures found in the fire. In such cases, the  $C_{p_i}^m$  curve fit reaches a maximum at some temperature, generally greater than 1000 K, and decreases for higher temperatures. This inconsistency in thermophysical property value can cause serious convergence problems and therefore, for such cases, an adhoc technique is used to estimate values of  $C_p$ . In the present model, the third order polynomial fits are used up to  $T = 1000$  K and for  $T > 1000$  K a linear fit based on values of  $cpim$  obtained from the CRC tables [91] are used (see Appendix B for details).

The molecular viscosity of the mixture as a function of temperature can be calculated by either a third order polynomial fit assuming that the mixture



### 3.9 Summary: The Base Fire Model

---

is largely air, or for a mixture other than air by a species weighted power-law relation [92]

$$\mu = \left( \frac{T}{T^\circ} \right)^n \sum_{i=1}^N Y_i \mu_i^\circ \quad (3.57)$$

where  $\mu_i^\circ$  is the viscosity of specie  $i$  at a reference temperature  $T^\circ$ . A value of 0.75 is used for  $n$  in Equation (3.57) [37]. Due to minimal effects of molecular diffusion, the first method is used for most of the fire simulations in the present work.

### 3.9 Summary: The Base Fire Model

This chapter has discussed and rationalized the various physical assumptions, based on assessment of previous work, that form the theoretical Base Fire Model (BFM) which was developed in this thesis. This includes the formulations of the transport equations, the various turbulence, radiation and other submodels, property values, and geometric considerations. As the BFM comprises a considerable number of such assumptions, the following will summarize, in point form, the main elements of the model so as to clearly distinguish the BFM from any further extensions to be discussed later.

The base fire model is based on:

- a two dimensional (rectangular or axisymmetric) geometry with the transport equations of motion formulated in invariant vector notation,
- incorporation of a multicomponent reacting gas mixture formulation,
- uniquely solving a temperature formulation of the energy conservation equation rather than the enthalpy formulation more commonly used,

### 3.9 Summary: The Base Fire Model

---

- the equations of mass, momentum and energy, solved simultaneously using a strong coupled formulation,
- the assumption of the  $k$ - $\epsilon$  turbulence model which includes buoyancy production terms, but with the diffusion coefficient  $C_\mu$  taken as a constant,
- special treatment of the scalar fluxes including the density temperature correlation,  $\overline{\rho' T'}$ , formulated in terms of a transport equation for the scalar intensity  $\overline{T'^2}$ ,
- a single one-step irreversible combustion submodel assuming infinitely fast chemistry and which incorporates the Eddy Dissipation Concept for the estimation of the reaction rates,
- a transport equation for the mixture fraction  $f$  so as to facilitate calculation of the species mass fractions,
- special treatment for the conservation of oxygen mass fraction by invoking a separate transport equation, for  $\overline{Y_{O_2}}$
- a new but simplified radiation model, and
- retaining the temperature dependence of the thermodynamic properties  $C_p$  and  $\mu$ .

## Chapter 4

# Numerical Implementation

The partial differential equations given in Chapter 3 describe the theoretical basis for the present fire model. Because of the strong interaction between the fluid flow and temperature fields, these equations are strongly coupled. The additional temperature dependency of the thermophysical properties further contributes to the nonlinearity of the equation set. Finally, the range of time scales associated with the physical phenomena occurring in the fire causes the governing equations to become stiff and hence, it is difficult to obtain a converged solution to this coupled equation set.

Robust and efficient numerical methods are needed to solve these highly non-linear, coupled equations. The essence of all methods in CFD is to convert the continuous partial differential equations to a set of algebraic linear equations in terms of the unknown values at discrete locations in time and space. A solution to these algebraic equations provides a discrete representation of the unknown fields over the computational domain. Because of the wide variety of numerical methods in use and their associated merits and

## Numerical Implementation

---

disadvantages, it is necessary to describe the details of the present model so that the numerical results can be interpreted properly, and also so that possible sources of numerical errors are recognized.

In this chapter, the numerical model developed during the course of this research is described. This model is based on a fully implicit pressure based control volume method and primitive variables are used. The governing equations are discretized using a *colocated variable arrangement*. Mass, momentum and energy equations are solved simultaneously, whereas other equations are solved in a segregated manner. The present model can be used to solve a variety of two dimensional flows including:

- planar and axisymmetric flows,
- laminar and turbulent flows,
- reacting and non-reacting flows, and
- isothermal and non-isothermal flows with strong buoyancy effects.

Although many of the different techniques and submodels used in the present model have been used separately in models for different flow situations, this is the first time that all these techniques have been combined into a strongly coupled CFD model applicable to both steady-state and transient fire simulations.

### 4.1 Domain Discretization and Grid Generation

In control volume methods, a grid is first generated over the computational domain to define either the boundaries of each control volume (node centered) or the node locations themselves (face centered). In the present model a node centered grid is used, where grid points determine the corners of each control volume and computational nodes are located at the center of each control volume, as shown in Figure 4.1.

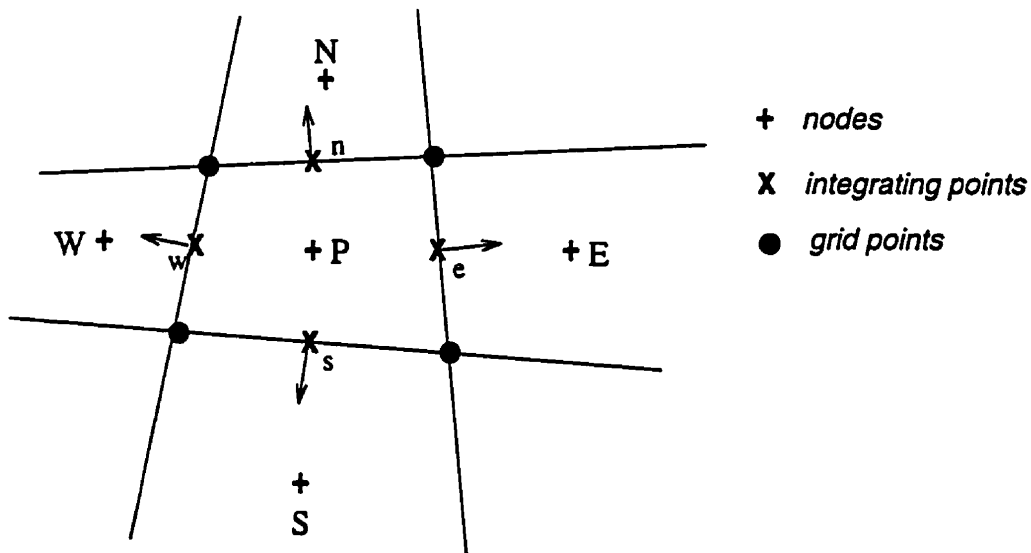


Figure 4.1: A typical control volume in a 5-molecule node centered grid

The grid itself is generated using an *algebraic grid generator* which is described in more detail in Appendix C. As shown in Figure 4.1, each face of a control volume contains one integrating point, *ip*, in the middle where different fluxes are calculated. To generate axisymmetric grids, a Cartesian

## 4.2 Discretization of the Governing Equations

---

grid is first created, and then rotated about an axis to generate the required axisymmetric grid.

## 4.2 Discretization of the Governing Equations

After discretizing the computational domain, the general approach in a control volume method is to integrate the partial differential equations over each control volume [93, 94]. The resulting volume and surface integrals are then approximated to obtain a set of algebraic equations in terms of the nodal values of the unknown variables. Since a five-molecule grid is used here, each equation should only contain the unknown values at the associated node (i.e.  $P$ ) and its immediate neighboring nodes (i.e.  $E$ ,  $N$ ,  $W$  and  $S$ ). Therefore, the algebraic equation for a variable  $\phi$  at node  $P$ , for instance, will have the form

$$C_P^{\phi\phi} \phi_P + C_E^{\phi\phi} \phi_E + C_N^{\phi\phi} \phi_N + C_W^{\phi\phi} \phi_W + C_S^{\phi\phi} \phi_S = B_P^\phi \quad (4.1)$$

or simply

$$\sum_i^{\text{nodes}} C_i^{\phi\phi} \phi_i = B_P^\phi \quad (\text{nodes} = P, E, N, W, S) \quad (4.2)$$

where  $C_i^{\phi\phi}$  is the coefficient of  $\phi$  at node  $i$  and  $B_P^\phi$  is a constant value which includes all the terms which do not implicitly depend on nodal values of  $\phi$  at the five-molecule nodes. This set of algebraic equations is then solved for the nodal values of the primitive variables.

It can be shown that all of the transport equations in the theoretical model can be rearranged and cast into a generic transport equation for a

## 4.2 Discretization of the Governing Equations

---

variable denoted here by  $\phi$ . This generic transport equation can be written as

$$\frac{\partial \rho \phi}{\partial t} + \nabla \cdot (\rho \mathbf{U} \phi) = \nabla \cdot (\Gamma \nabla \phi) + S_\phi''' \quad (4.3)$$

where  $\Gamma$  is the total diffusivity and  $S_\phi'''$  denotes the volumetric source of  $\phi$ . To describe the main approximations used in the present model for discretizing the governing equations, it is illuminating to briefly describe the integration of equation (4.3) over a typical control volume. Further detail can be found in [95].

### 4.2.1 Integration of the Transient Term

The transient term of Equation (4.3) is integrated over volume  $\forall$  using an average value of the time derivative in space which yields

$$\iint_{\forall} \frac{\partial \rho \phi}{\partial t} d\forall \approx \left( \frac{\partial \rho \phi}{\partial t} \right)_{\forall} \approx \frac{\rho \phi - (\rho \phi)^{old}}{\Delta t} \forall \quad (4.4)$$

where  $\Delta t$  is the time step and the superscript  $old$  denotes the value of  $\rho \phi$  at the previous time step. The backward differencing scheme used in Equation (4.4) implies that the present model is first order accurate in time for the solution to transient problems. For steady state problems, the final solution is approached by marching in time and the time step is used as a relaxation parameter.

## 4.2 Discretization of the Governing Equations

---

### 4.2.2 Integration of the Convection Term

For the generic transport equation here, integration of the convection term over the volume yields

$$\iiint_{\mathcal{V}} (\rho \mathbf{U} \phi) d\mathcal{V} = \int_{\mathbf{A}} (\rho \phi \hat{\mathbf{U}} \cdot \hat{\mathbf{n}}) dA = \sum_{ip=1}^4 (\rho \phi \hat{\mathbf{U}} \cdot \hat{\mathbf{n}} A)_{ip} = \sum_{ip=1}^4 m_{ip} \phi_{ip} \quad (4.5)$$

where  $A$  denotes the area of the control volume surface,  $\hat{\mathbf{U}}$  is the advecting velocity and  $\hat{\mathbf{n}}$  is the unit vector normal to  $A$  as shown in Figure 4.1.

Therefore, one needs to evaluate the integrating point values of  $\phi$ , velocity and some other variables. These have been the subject of much research and numerous approaches have been proposed [93, 94, 96]. In summary, the first order accurate upwind difference schemes are very robust and efficient but are well known for their associated numerical or false diffusion effects, particularly in regions where convection is strong and the flow is oblique to the grid lines. On the other hand, higher order accurate schemes generally produce more accurate results providing the grid is sufficiently fine, but they may cause oscillatory solutions or even convergence problems for some flow situations.

The performance of different advection schemes is generally dependent on the application. Since there is no clear evidence indicating the superiority of a particular advection scheme for fire simulations, the numerical implementation in the present model is such that any one of three advection schemes can be selected. These are

- pure Upwind Differencing Scheme (UDS)
- PEclet weighted Upwind Differencing Scheme (PEUDS), and



## 4.2 Discretization of the Governing Equations

---

- Higher Order (2nd) Upwind Differencing Scheme (HOUDS)

In UDS, the integrating point values are evaluated based on the nodal value in the upstream direction. For example, at the east integrating point of a control volume,  $\phi_e$  is calculated by

$$\phi_e = \begin{cases} \phi_P & \text{if } m_e > 0 \\ \phi_E & \text{if } m_e < 0 \end{cases} \quad (4.6)$$

where  $m_e$  is the mass flux through the east face of the control volume.

According to the Peclet weighted upwind differencing scheme (PEUDS)  $\phi_e$ , for instance, can be evaluated by[97]

$$\phi_e = \left( \frac{1}{2} + \text{sign}(m_e)\alpha_e \right) \phi_P + \left( \frac{1}{2} - \text{sign}(m_e)\alpha_e \right) \phi_E \quad (4.7)$$

where  $\alpha_e$  is a function of the local Peclet number,  $P$ , as follows

$$\alpha_e = \frac{P_e^2}{10 + 2P_e^2} \quad , \quad P_e = \frac{m_e}{D_e}. \quad (4.8)$$

Here,  $D_e = \frac{\Gamma_e A_e}{L_e}$  relates to the strength of the total diffusion flux through the east control volume face,  $\Gamma_e$  denotes the total diffusion coefficient,  $A_e$  is the area of the east face and  $L_e$  is the distance between the  $P$  and  $E$  nodes.

In HOUDS, integrating point variables are calculated based on their upwind values and a second order correction term. At the east integrating point, for example, HOUDS yields

$$\phi_e = \begin{cases} \phi_P + l_P \nabla \phi_P \cdot \vec{r}_{P-e} & \text{if } m_e > 0 \\ \phi_E + l_E \nabla \phi_E \cdot \vec{r}_{E-e} & \text{if } m_e < 0 \end{cases} \quad (4.9)$$

## 4.2 Discretization of the Governing Equations

---

where  $l$  denotes the nodal value of the limiter,  $\nabla\phi$  is the nodal averaged gradient of  $\phi$  and  $\vec{r}$  represents the displacement vector from the upwind node location to the integrating point. Central differencing is used to calculate the gradient terms and the limiters, which are introduced to prevent oscillatory solutions and are calculated based on reference [98].

The relative performance of these advection schemes for different flow situations is shown in test case results presented in Appendix D.

The advecting velocities,  $\hat{\mathbf{U}}$ , are calculated quite differently from the convection terms, using the Rhie and Chow [99] pressure weighted interpolation method. According to this method, the advecting velocities are calculated based on the average of the neighboring nodal velocities corrected by a pressure redistribution term and a history term to prevent pressure velocity decoupling. The advecting velocity at the east integrating point, for example, would be

$$\hat{\mathbf{U}}_e = \overline{ave}(\mathbf{U}_P, \mathbf{U}_E) - \hat{d}_e \cdot [\nabla P_e - \overline{ave}(\nabla P_P, \nabla P_E)] + \frac{\rho_e \hat{d}_e}{\Delta t} \cdot [\hat{\mathbf{U}}_e^t - \overline{ave}(\mathbf{U}_P^t, \mathbf{U}_E^t)] \quad (4.10)$$

where the  $\overline{ave}()$  operator takes the geometric average of its two arguments (i.e. mean averaging for a uniformly spaced grid) and  $\hat{d}_e = \hat{d}_e^u \hat{r} + \hat{d}_e^w \hat{z}$ . The components of  $\hat{d}_e$  (i.e.  $\hat{d}_e^u$  and  $\hat{d}_e^w$ ) are calculated based on active coefficients of the corresponding velocity component (see [95] for details).

## 4.2 Discretization of the Governing Equations

---

### 4.2.3 Integration of the Diffusion Term

After integrating the diffusion term over the volume, the equation

$$\iint_{\mathcal{V}} \nabla \cdot (\Gamma \nabla \phi) d\mathcal{V} = \int_{\mathbf{A}} \Gamma \nabla \phi \cdot \hat{n} dA \approx \sum_{ip} \left( A_{ip} \Gamma_{ip} \frac{\partial \phi}{\partial n} \right)_{ip} \quad (4.11)$$

is obtained. To calculate this term, the gradient of  $\phi$  must be evaluated at each integrating point. Due to the elliptic nature of diffusion, central differencing appears to be a suitable choice to represent the gradient, and is adopted here. A second order central differencing scheme is also used to evaluate the integrating point diffusion coefficient,  $\Gamma_{ip}$ . Calculation of  $\Gamma_{ip}$  at each integrating point is critical to preserve the fully conservative properties of the present model.

### 4.2.4 Integration of the Source Term

In general, the source term is linearized such that there is a part  $S_{\phi}^r$ , which implicitly depends on the nodal value of  $\phi_P$  and another part,  $S_{\phi}^q$ , which is calculated explicitly. This yields

$$S_{\phi}''' = S_{\phi}^r \phi_P + S_{\phi}^q \quad (4.12)$$

After integrating the source term over the volume and discretizing the result, the implicit part is added to  $C_P^{\phi\phi}$  whereas the explicit part is added to  $B_P^{\phi}$ , in Equation (4.1).

The linearization of the source term depends on the nature of the source term in the original equation and its dependency on the variable being sought. Therefore source terms are discussed separately for each equation later in this chapter.

### 4.3 Discretization of the Coupled Equations

---

## 4.3 Discretization of the Coupled Equations

As stated earlier the conservation equations for mass, momentum and energy are solved simultaneously in the present model. This requires that the discrete form of each equation include active coefficients for the dominant variables in other equations as well.

Since  $u$ ,  $w$ ,  $P_d$  and  $T$  may not explicitly appear in every one of the coupled equations, special care must be taken to reflect the strong coupling between the transport equations for these variables in their counterpart linearized discrete equations. Such issues are addressed in the following sections.

### 4.3.1 Discrete Form of the Mass Equation

The continuity equation is used to find the pressure even though pressure does not explicitly appear in this equation. The continuity equation integrated over the volume becomes

$$\iiint_{\mathcal{V}} \frac{\partial \bar{\rho}}{\partial t} d\mathcal{V} + \iiint_{\mathcal{V}} \nabla \cdot (\bar{\rho} \bar{\mathbf{U}}) d\mathcal{V} + \iiint_{\mathcal{V}} \nabla \cdot (\bar{\rho}' \bar{\mathbf{U}}') d\mathcal{V} = 0 \quad (4.13)$$

The first term of Equation (4.13) shows the rate of change of mass inside the control volume and is approximated by

$$\iiint_{\mathcal{V}} \frac{\partial \bar{\rho}}{\partial t} d\mathcal{V} \approx \frac{\bar{\rho} - \bar{\rho}^{old}}{\Delta t} \mathcal{V} \quad (4.14)$$

For the variable density flows considered here, density changes mainly due to changes in temperature. Therefore, it is desired to express  $\bar{\rho}$  in Equation (4.14) as a function of  $T$  to create a coupling between the continuity equation and the energy equation. This is accomplished by taking the first two terms

### 4.3 Discretization of the Coupled Equations

---

of the Taylor series expansion of  $\bar{\rho}$  about its lagged value, which yields

$$\bar{\rho} \approx \bar{\rho}^l + \left( \frac{\partial \bar{\rho}}{\partial \bar{T}} \right)^l (\bar{T} - \bar{T}^l) \quad (4.15)$$

From the state equation we obtain

$$\frac{\partial \bar{\rho}}{\partial \bar{T}} = - \frac{P}{\mathcal{R} \sum_{i=1}^{\mathcal{N}} \frac{Y_i}{\mathcal{M}_i} \bar{T}} = - \frac{\bar{\rho}}{\bar{T}} \quad (4.16)$$

Substituting Equation (4.16) into (4.15) yields an expression for  $\bar{\rho}$

$$\bar{\rho} \approx 2\bar{\rho}^l - \frac{\bar{\rho}^l}{\bar{T}^l} \bar{T} \quad (4.17)$$

Equation (4.17) is valid only if  $(\bar{T} - \bar{T}^l)$  is small enough that any higher order terms in Equation (4.15) can be neglected. This condition is usually met if the temperature variation is small (e.g. weak buoyant flows) or a small enough time step is used in the solution. Since highly buoyant flows, including pool fires, are themselves numerically unstable, small time steps are required anyway. Therefore, the above condition is likely to be valid.

The second term of Equation (4.13) is approximated as

$$\iiint_{\mathcal{V}} \nabla \cdot (\bar{\rho} \bar{\mathbf{U}}) d\mathcal{V} = \int_{\mathbf{A}} \bar{\rho} \hat{\mathbf{U}} \cdot \hat{\mathbf{n}} dA \approx \sum_{ip} (\bar{\rho} \hat{\mathbf{U}} \cdot \hat{\mathbf{n}} \mathbf{A})_{ip} \quad (ip = e, n, w, s) \quad (4.18)$$

To discretize this term, Equation (4.10), is substituted into the RHS of Equation (4.18) and then the equation is rearranged to obtain active coefficients for nodal velocities and pressures. In obtaining the pressure coefficients, only the pressure gradient terms at the integrating point,  $\nabla P_{ip}$ , are implicitly included. Other pressure redistribution terms are lagged and included in the source term for the mass continuity equation.

### 4.3 Discretization of the Coupled Equations

---

For turbulent flows, the third term of Equation (4.13) is present when time averaging is used. Based on the gradient diffusion hypothesis, it can be approximated as

$$\iint_{\mathbf{V}} \nabla \cdot (\overline{\rho' \mathbf{U}'}) d\mathbf{V} = \int_{\mathbf{A}} \overline{\rho' \mathbf{U}'} \cdot \hat{n} dA \approx \int_{\mathbf{A}} -\frac{\nu_t}{\sigma_\rho} \nabla \bar{\rho} \cdot \hat{n} dA \approx \sum_{ip} \left( -\frac{\nu_t}{\sigma_\rho} \frac{\partial \bar{\rho}}{\partial \hat{n}} \mathbf{A} \right)_{ip} \quad (4.19)$$

To discretize this term, central differencing is used to evaluate the density gradients at each integration point and all these terms are added to the source term in the mass equation. The final form of the discretized continuity equation is

$$\mathcal{C}_P^{TP} T_P + \sum_i^{\text{nodes}} \mathcal{C}_i^{uP} u_i + \sum_i^{\text{nodes}} \mathcal{C}_i^{wP} w_i + \sum_i^{\text{nodes}} \mathcal{C}_i^{PP} = \mathcal{B}_P^P \quad (4.20)$$

The convention for writing the coefficients  $\mathcal{C}$  is that the subscripts indicate the corresponding node (i.e. P, E, N, W, S), the first letter of the superscript denotes the variable that the coefficient is multiplied by (i.e.  $P$ ,  $T$ ,  $u$  etc ...) and the second letter of the superscript indicates the equation in which it appears (e.g.  $P$  for mass,  $T$  for energy etc ...).

#### 4.3.2 Discrete Form of the r-momentum Equation

To discretize the r-momentum equation, Equation (3.30), we first present the modeled form of that equation which can be derived using Equations (3.33) and (3.34). After substituting for the turbulent correlations and rearranging

### 4.3 Discretization of the Coupled Equations

---

some of the terms, the equation becomes

$$\begin{aligned}
 \frac{\partial}{\partial t}(\bar{\rho}\bar{u}) + \nabla \cdot (\bar{\rho}\bar{u}\bar{\mathbf{U}}) &= -\frac{\partial \bar{P}_d^*}{\partial r} + \nabla \cdot (\mu_{\text{eff}} \nabla \bar{u}) + \\
 &\underbrace{\frac{\partial}{\partial t} \left( \frac{\nu_t}{\sigma_\rho} \frac{\partial \bar{\rho}}{\partial r} \right) + \nabla \cdot \left[ \frac{\nu_t}{\sigma_\rho} \left( \bar{u} \nabla \bar{\rho} + \frac{\partial \bar{\rho}}{\partial r} \bar{\mathbf{U}} \right) \right]}_{\text{u-I}} - \underbrace{\mathcal{J} \left[ \frac{2}{r} \mu_{\text{eff}} \left( -\frac{\nabla \cdot \bar{\mathbf{U}}}{3} + \frac{\bar{u}}{r} \right) \right]}_{\text{u-II}} + \\
 &\underbrace{\nabla \cdot \left[ \mu_{\text{eff}} \left( -\frac{2 \nabla \cdot \bar{\mathbf{U}}}{3} + \frac{\partial \bar{u}}{\partial r} \right) \hat{r} + \mu_{\text{eff}} \frac{\partial \bar{w}}{\partial r} \hat{z} \right]}_{\text{u-III}}
 \end{aligned} \tag{4.21}$$

where  $\mu_{\text{eff}} = \mu + \mu_t$  and  $\bar{P}_d^* = \bar{P}_d + \frac{2}{3} \bar{\rho} k$ .

As can be seen in Equation (4.21) a modified pressure,  $\bar{P}_d^*$ , replaces  $\bar{P}_d$  in the momentum equation for turbulent flows. This modified pressure is also used in the definition for the advecting velocities and therefore, it is this pressure which is obtained by solving the governing equations.

The discretization of the transient, convection and diffusion terms follows the procedure described earlier for the generic transport equation. The pressure gradient term is discretized using central differencing and therefore, the pressure coefficients,  $C_{ip}^{P_u}$ , depend purely on the geometry of the grid.

The last three terms in Equation (4.21) are grouped terms because each term is active only for certain situations. Term u-II represents the effects of correlations involving  $\rho'$ . Term u-II exists only for axisymmetric flow solutions and term u-III is nonzero only if density is variable.

Terms u-I and u-III are explicitly accounted for using lagged values of all variables involved and using central differencing to discretize any gradient

### 4.3 Discretization of the Coupled Equations

---

terms. Term u-II in Equation (4.21), is discretized as follows

$$\iint_{\mathcal{V}} \frac{2}{r} \mu_{\text{eff}} \left( \frac{\nabla \cdot \bar{\mathbf{U}}}{3} + \frac{\bar{u}}{r} \right) d\mathcal{V} \approx \frac{-2\mu_{\text{eff}}}{3r_P} \int_{\mathbf{A}} \bar{\mathbf{U}} \cdot \hat{\mathbf{n}} dA + \frac{2\mu_{\text{eff}}}{r_P^2} \sqrt{\bar{u}}_P \quad (4.22)$$

where  $r_P$  is the  $r$  coordinate of the node itself and advecting velocities are used to evaluate the first term on the RHS of Equation (4.22) which yields

$$\int_{\mathbf{A}} \bar{\mathbf{U}} \cdot \hat{\mathbf{n}} dA \approx \sum_{ip} \left( \hat{\bar{\mathbf{U}}} \cdot \hat{\mathbf{n}} A \right)_{ip} \quad (4.23)$$

In this term advecting velocities are used to ensure that  $\nabla \cdot \bar{\mathbf{U}}$  goes to zero for constant density flows. After discretizing and rearranging different terms, the final form of the discretized r-momentum equation can be written as

$$\sum_i^{\text{nodes}} C_i^{uu} u_i + \sum_i^{\text{nodes}} C_i^{wu} w_i + \sum_i^{\text{nodes}} C_i^{Pu} P_i = B_P^u \quad (4.24)$$

#### 4.3.3 The Discrete form of the z-momentum Equation

Following similar method as was used for Equation (4.21), the modeled form of the z-momentum equation may be rearranged as

$$\begin{aligned} \frac{\partial}{\partial t} (\bar{\rho} \bar{w}) + \nabla \cdot (\bar{\rho} \bar{w} \bar{\mathbf{U}}) &= -\frac{\partial \bar{P}_d^*}{\partial z} + \nabla \cdot (\mu_{\text{eff}} \nabla \bar{w}) + \\ &\underbrace{\frac{\partial}{\partial t} \left( \frac{\nu_t}{\sigma_\rho} \frac{\partial \bar{\rho}}{\partial r} \right) + \nabla \cdot \left[ \frac{\nu_t}{\sigma_\rho} \left( \bar{w} \nabla \bar{\rho} + \frac{\partial \bar{\rho}}{\partial z} \bar{\mathbf{U}} \right) \right]}_{\text{w-I}} + \\ &\underbrace{\nabla \cdot \left[ \mu_{\text{eff}} \frac{\partial \bar{u}}{\partial z} \hat{\mathbf{r}} + \mu_{\text{eff}} \left( \frac{-2\nabla \cdot \bar{\mathbf{U}}}{3} + \frac{\partial \bar{w}}{\partial z} \hat{\mathbf{z}} \right) \right]}_{\text{w-II}} + (\rho_\infty - \bar{\rho})g \quad (4.25) \end{aligned}$$

The discretization of all terms follows similar procedures to those described earlier, except for the buoyancy term,  $(\rho_\infty - \bar{\rho})g$ , which has no counterpart in the r-momentum equation. The buoyancy term is integrated over the volume and discretized as follows



### 4.3 Discretization of the Coupled Equations

---

$$\iint_{\mathcal{V}} (\rho_{\infty} - \bar{\rho}) g d\mathcal{V} \approx (\rho_{\infty} - \bar{\rho}) g \mathcal{V} \quad (4.26)$$

To create a coupling between the z-momentum and the energy equations Equation (4.17) is used to relate density to temperature which yields

$$\begin{aligned} (\rho_{\infty} - \bar{\rho}) g \mathcal{V} &\approx \left( \rho_{\infty} - \left( 2\bar{\rho}^t - \frac{\bar{\rho}^t}{\bar{T}^t} \bar{T} \right) \right) g \mathcal{V} \\ &\approx (\rho_{\infty} - 2\bar{\rho}^t) g \mathcal{V} + \left( \frac{\bar{\rho}^t}{\bar{T}^t} \right) g \mathcal{V} T \end{aligned} \quad (4.27)$$

As can be seen in Equation (4.27) this discretization produces an active coefficient for  $T$  in the z-momentum equation which reflects the strong interaction between temperature and velocity fields. The resultant algebraic equation which represents the discretized z-momentum equation is

$$\sum_i^{\text{nodes}} C_i^{uw} u_i + \sum_i^{\text{nodes}} C_i^{ww} w_i + \sum_i^{\text{nodes}} C_i^{Pw} P_i + C_P^{Tw} T_P = \mathcal{B}_P^w \quad (4.28)$$

#### 4.3.4 The Discrete Form of the Energy Equation

The modeled form of the energy equation can be written with different terms grouped together such that each group is active for particular applications.

### 4.3 Discretization of the Coupled Equations

---

This form is

$$\begin{aligned}
 \frac{\partial}{\partial t}(\bar{\rho}C_p\bar{T}) + \nabla \cdot (\bar{\rho}C_p\bar{T}\bar{\mathbf{U}}) &= \nabla \cdot \left( \left( K + \frac{\bar{\rho}\nu_t C_p}{\sigma_t} \right) \nabla T \right) + \\
 \underbrace{\frac{\partial}{\partial t} \left( \frac{\bar{\rho}'}{\bar{T}'} \bar{T}'^2 C_p \right) + \nabla \cdot \left( \frac{\bar{\rho}'}{\bar{T}'} \bar{T}'^2 C_p \bar{\mathbf{U}} + \frac{\nu_t}{\sigma_p} \nabla \bar{\rho} C_p \bar{T} \right)}_{\text{T-I}} &+ \\
 \underbrace{\frac{\partial}{\partial t}(\bar{\rho}C_p T^o) + \nabla \cdot \left( \bar{\rho}C_p T^o \bar{\mathbf{U}} - \frac{\nu_t}{\sigma_p} \nabla \bar{\rho} C_p T^o + \mu \sum_{i=1}^N (C_{p_i}^m (\bar{T} - T^o) \nabla \bar{Y}_i) \right)}_{\text{T-II}} &+ \\
 \underbrace{\mathfrak{R}_{fu} \mathcal{H}_c - \nabla \cdot \mathbf{q}_r}_{\text{T-III}} &
 \end{aligned} \tag{4.29}$$

The discretization of the transient, convection and diffusion terms closely follows the procedure described for the generic transport equation, with the exception that in the transient and convection terms  $\bar{\phi}$  is replaced by  $C_p \bar{T}$ . In addition, since the usual linearization of the convection term does not create a coupling between the energy and momentum equations (T-V coupling), it is beneficial in a fire model to use an alternative linearization method for this term.

Following Galpin and Raithby [75], Newton-Raphson linearization is applied to the  $\bar{\mathbf{U}}\bar{T}$  product in the convection term to yield

$$\bar{\mathbf{U}}\bar{T} \approx \bar{\mathbf{U}}'\bar{T} + \bar{\mathbf{U}}\bar{T}' - \bar{\mathbf{U}}'\bar{T}' \tag{4.30}$$

Equation (4.30) is then substituted into the convection term in Equation

#### 4.4 Discretization of the Segregated Equations

---

(4.29) and integrated over the volume, giving

$$\iint_{\mathcal{V}} \nabla \cdot (\bar{\rho} C_p (\bar{\mathbf{U}}^t \bar{T} + \bar{\mathbf{U}} \bar{T}^t - \bar{\mathbf{U}}^t \bar{T}^t)) d\mathcal{V} \approx \sum_{ip} (\bar{\rho} C_p \bar{T})_{ip} + \sum_{ip} (\bar{\rho} C_p \bar{T}^t \hat{\mathbf{U}} \cdot \hat{\mathbf{n}} \mathbf{A})_{ip} - \sum_{ip} (\bar{\rho} C_p \bar{T}^t \hat{\mathbf{U}}^t \cdot \hat{\mathbf{n}} \mathbf{A})_{ip} \quad (4.31)$$

Equation (4.10) is used to define  $\hat{\mathbf{U}}$  in the last two terms of Equation (4.31) in terms of nodal velocities which, in turn, produces active coefficients for the velocity component, and provides a coupled equation set.

All other terms in Equation (4.29) (i.e. T-I, T-II and T-III) are explicitly accounted for using the most updated values of the variables. Term T-I in Equation (4.29) is active only if turbulent correlations involving density fluctuations are accounted for and terms T-II and T-III are present only for reacting flows, despite the fact that  $\nabla \cdot \mathbf{q}_r$  may still be present in some high temperature non-reacting flows.

The final form of the discretized energy equation is

$$\sum_i^{\text{nodes}} C_i^{TT} T_i + \sum_i^{\text{nodes}} C_i^{uT} u_i + \sum_i^{\text{nodes}} C_i^{wT} w_i = B_P^T \quad (4.32)$$

#### 4.4 Discretization of the Segregated Equations

The mass, momentum and energy equations described above are solved simultaneously. All other equations are solved individually. Therefore, the discretization of the transient, convection and diffusion terms for these equations follows exactly the same procedure as that described earlier for the generic transport equation; however, the linearization of the source term should be discussed further for each equation.

## 4.4 Discretization of the Segregated Equations

---

### 4.4.1 Source Term Linearization of the $k$ - $\epsilon$ Equations

Physical realizability requires that both  $k$  and  $\epsilon$  should remain positive, thus care should be taken in linearizing the source terms in the  $k$  and  $\epsilon$  transport equations such that positive solutions are guaranteed. This means that a negative source term, which could lead to a negative solution, could be a potential threat to the realizability of the solution. For the  $k$  equation, the source term can be written

$$S_k''' = P_k - \bar{\rho}\epsilon + B_k \quad (4.33)$$

where  $P_k$  and  $B_k$  are defined in Equations (3.38) and (3.39) respectively. In the present model, the following linearization is used

$$S_k''' = \underbrace{\left(\bar{\rho}\frac{\epsilon}{k}\right)}_{s_k^r} k + \underbrace{(P_k + B_k)}_{s_k^q} \quad (4.34)$$

To evaluate an average value of  $P_k$  for each control volume, the velocity gradients in Equation (3.38) must be approximated. In this case, central differencing is used and advecting velocities are utilized for the calculation of nodal velocity gradients.

The buoyancy production term in the  $k$  equation is approximated by two different methods. One is based on the Gradient Diffusion Hypothesis (GDH) given in Equation (3.34) and the other is based on the Generalized Gradient Diffusion Hypothesis (GGDH) [100] which yields

$$\mathbf{g} \cdot \overline{\rho' \mathbf{U}'} = \overline{g \rho' w'} \approx -C_\rho \frac{k}{\epsilon} \left( \overline{u' w'} \frac{\partial \bar{\rho}}{\partial r} + \overline{w' w'} \frac{\partial \bar{\rho}}{\partial z} \right) \quad (4.35)$$

#### 4.4 Discretization of the Segregated Equations

---

and which can be further expanded as

$$\mathbf{g} \cdot \overline{\rho \mathbf{U}'} \approx -C_\rho \frac{k}{\varepsilon} \left[ -\nu_t \left( \frac{\partial \bar{u}}{\partial z} + \frac{\partial \bar{w}}{\partial r} \right) \frac{\partial \bar{\rho}}{\partial r} + \left( \frac{2}{3}k - \nu_t \left( \frac{\partial \bar{w}}{\partial z} + \frac{\partial \bar{w}}{\partial z} \right) \right) \frac{\partial \bar{\rho}}{\partial z} \right] \quad (4.36)$$

where  $C_\rho = \frac{3}{2} \left( \frac{C_\mu}{\sigma_\rho} \right)$ . The advantage of the second method over the first is that the gradient of both  $\rho$  and  $\mathbf{U}$  are accounted for in the turbulent correlation. In both methods, central differencing is used to discretize the gradient terms.

In a similar fashion, the source term in the  $\varepsilon$  equation may be expressed as

$$S_\varepsilon''' = C_{\varepsilon 1} \frac{\varepsilon}{k} (P_k + B_k) - C_{\varepsilon 2} \bar{\rho} \frac{\varepsilon^2}{k} \quad (4.37)$$

and linearized as

$$S_\varepsilon''' \approx \underbrace{- \left( C_{\varepsilon 2} \bar{\rho} \frac{\varepsilon}{k} \right)}_{S_\varepsilon^{\ddagger}} \varepsilon + \underbrace{C_{\varepsilon 1} \frac{\varepsilon}{k} (P_k + B_k)}_{S_\varepsilon^{\ddagger}} \quad (4.38)$$

The values of  $P_k$  and  $B_k$  used in the  $k$  equation are used in this formulation of the  $\varepsilon$  equation.

#### 4.4.2 Source Term Linearization for the Species Equation

In reacting flows, the combustion source terms in the species and the energy equations are usually the dominant terms and therefore have a significant influence on the solution of these equations. At the same time, the sum of the mass fractions of all species in a reacting flow has to remain bounded between

## 4.5 The Solver

---

0 and 1. Hence, it is important to carefully treat the combustion source terms to obtain robust convergence of all the equations while maintaining the solution of the species equation within a physically realistic range.

To accomplish this, the following linearizations are used

$$S_{Y_{fu}}''' = -\mathfrak{R}_{fu} = \underbrace{\left(-\frac{\mathfrak{R}_{fu}}{Y_{fu}^i}\right)}_{Y_{fu}^r} Y_{fu} \quad (4.39)$$

and

$$S_{Y_{O_2}}''' = -\mathfrak{R}_{fu} \frac{\mathcal{M}_{fu}}{\nu'_{O_2} \mathcal{M}_{O_2}} = \underbrace{\left(-\frac{\mathfrak{R}_{fu} \mathcal{M}_{fu}}{\nu'_{O_2} \mathcal{M}_{O_2} Y_{O_2}^i}\right)}_{s_{Y_{O_2}}^i} Y_{O_2} \quad (4.40)$$

As shown in Equations (4.39) and (4.40), only the implicit part of the source term has remained and it inversely depends on the solution itself. This ensures that the solution remains bounded between the physical limits of  $Y_{fu}$  and  $Y_{O_2}$  which are applied through the boundary conditions on the solution.

## 4.5 The Solver

Once the governing equations are discretized, the resultant set of algebraic linear equations needs to be solved. In the present model, two solver options are provided, a direct solver and an iterative solver.

The direct solver is a sparse matrix package which is designed to efficiently solve large sparse systems of linear equations [101]. The iterative solver is again a sparse matrix solver package based on the conjugate gradient stabilized acceleration method and uses right preconditioning [102].

## 4.6 Convergence Criteria

---

### 4.6 Convergence Criteria

As was discussed in previous sections, the solution procedure involves different steps which are schematically presented in the flowchart shown in Figure 4.2. Because of the nonlinearity of the governing equations, the solution procedure is iterative and a convergence criterion must be set to stop each iteration loop. In the present method, three parameters are monitored for this purpose. One is an averaged normalized difference between two consecutive solutions as calculated using Equation (4.41) for a typical variable  $\phi$ .

$$\left( \frac{\sum_i^{\text{all nodes}} \left| \frac{\phi_i - \phi_i^{\text{old}}}{\Phi} \right|^2}{\text{no. of nodes}} \right)^{1/2} \leq \xi \quad (4.41)$$

where

$$\Phi = \left( \frac{\sum_i^{\text{all nodes}} \phi_i^2}{\text{no. of nodes}} \right)^{1/2} \quad (4.42)$$

and  $\xi$  is the convergence criterion, chosen here to be  $1.0 \times 10^{-3}$ .

This criterion is appropriate if the steady state solution is desired and if a large time step is used. However, for cases where small time steps are used, this criterion may not be appropriate. Hence, the maximum residual and the ratio of consecutive residuals are also monitored. The nodal value of the normalized residual for a variable  $\phi$  is calculated as

$$\text{Residual}_\phi = \frac{\left( \sum_i^{\text{all nodes}} C_i^{\phi\phi} \phi_i \right) - B_P^\phi}{C_P^{\phi\phi} \Phi} \quad \text{nodes=P, E, N, W, S} \quad (4.43)$$

## 4.6 Convergence Criteria

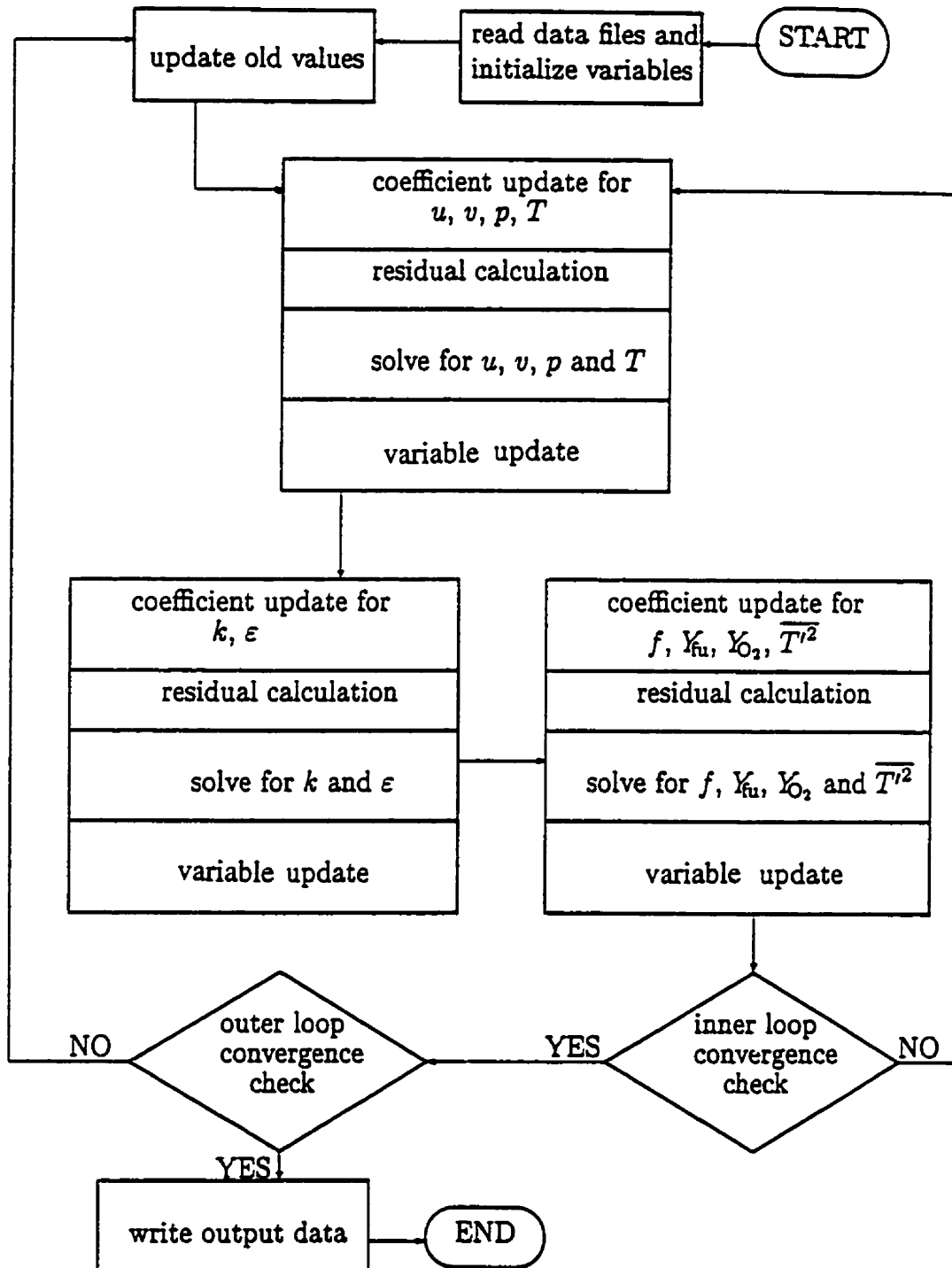


Figure 4.2: Flowchart of the solution procedure



## 4.6 Convergence Criteria

---

For all the cases presented in this thesis, the maximum residual for all variables is set to be smaller than or equal to  $1.0 \times 10^{-3}$  at convergence and the ratio of the consecutive residuals must remain smaller than unity.

In order to validate the implementation of the computer program and the numerical model, several test cases were run at different stages. The results of these test cases are presented in Appendix D and demonstrate the validity of each module in the final fire field model.

# Chapter 5

## Steady State Base Model

### Results

#### 5.1 Introduction

Mathematical description and details of numerical implementation of the present model were introduced in Chapters 3 and 4, respectively. Several validation tests for non-reacting flows have also been conducted to establish the proper implementation of the numerical algorithm structure and physical consistency of the model. These results are contained in Appendix D.

In this chapter, results for two reacting flow test cases, a 2D rectangular propane fire and an axisymmetric propane fire, simulated using the base model formulation will be presented, and some issues regarding appropriate boundary conditions for such simulations will be addressed. In addition, some weaknesses inherent in commonly assumed model assumptions will be identified as requiring further work for fire simulations.

### 5.2 Specification of the Rectangular Propane Fire

The first reacting flow test case considered here is a rectangular propane fire for which experimental data are reported by Annarumma [48, 52]. As stated in Chapter 1, this is the only medium scale pool fire for which elliptic simulation results have been reported in the literature [48]. Hence, it is possible to compare the present numerical results not only with experimental data, but also with other numerical results obtained using a different elliptic fire model.

The experimental setup, shown schematically in Figure 5.1, consisted of a  $25 \times 40$  cm gas burner which was held between two insulated horizontal plates. To keep the flame as nearly two dimensional as possible, two large insulated vertical walls were used on the front and back sides of the fire. Small openings in these vertical walls permitted thermocouple wires and laser beams to access the fire for measurements. To take the measurements at different locations inside the fire, the burner was moved along with the two side floors. For more information regarding details of the experimental setup, reference [52] should be consulted.

The steady-state operating conditions for the fire are listed in Table 5.1.

Table 5.1: Steady-state operating conditions for the rectangular propane fire

| $P_\infty$ (Pa) | $T_\infty$ (K) | $\dot{m}_{fu}$ (kg/s/m <sup>2</sup> ) |
|-----------------|----------------|---------------------------------------|
| 101325          | 300            | $5.3 \times 10^{-3}$                  |

## 5.2 Specification of the Rectangular Propane Fire

---

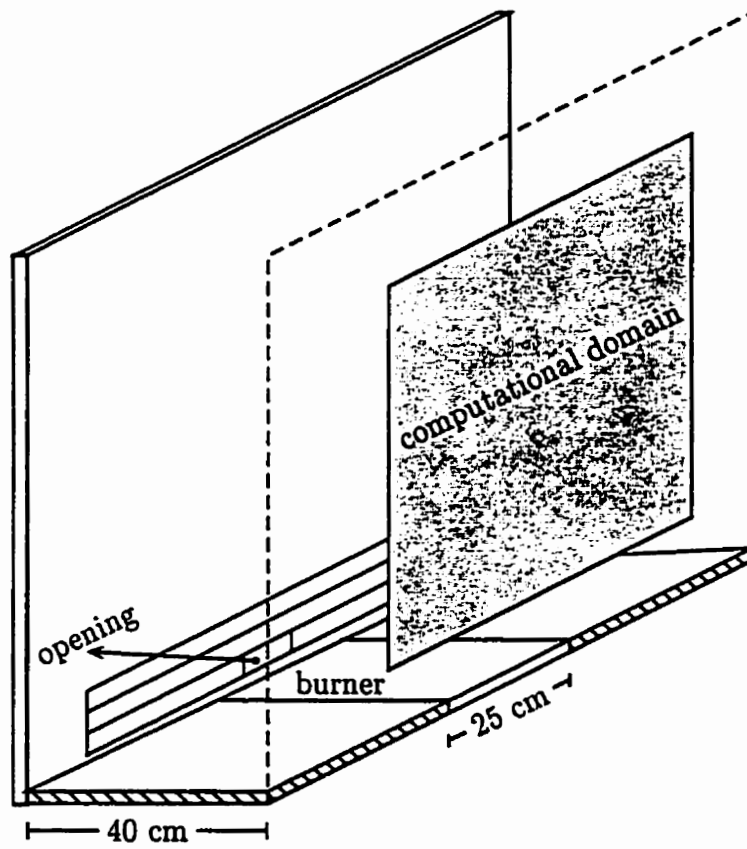


Figure 5.1: Schematic of the rectangular propane fire [52]

## 5.2 Specification of the Rectangular Propane Fire

---

### 5.2.1 Computational Domain and Grid Specifications

To isolate the effect of domain size and grid resolution when comparing numerical results with those of reference [48], the size of the computational domain and grid node distribution are chosen according to [48]. The computational domain, shown in Figure 5.1, is  $7W_b$  wide and  $9W_b$  high, where  $W_b = 25$  cm is the burner width. The results presented in this chapter are obtained using two grids whose specifications are listed in Table 5.2, with grid I-2 being similar to the one used in [48].

Table 5.2: Grid specifications for rectangular propane fire

|          | no. of nodes<br>$N_r \times N_z$ | nodes in half<br>burner width | grid spacing expansion factor |       |
|----------|----------------------------------|-------------------------------|-------------------------------|-------|
|          |                                  |                               | $E_r$                         | $E_z$ |
| grid I-1 | $52 \times 52$                   | 19                            | 1.13                          | 1.08  |
| grid I-2 | $71 \times 72$                   | 31                            | 1.1                           | 1.05  |

The computational domain covers only half of the burner width, as shown in Figure 5.1. This implies that the flow is two dimensional and symmetric about the burner mid-plane.

### 5.3 The axisymmetric propane fire

---

## 5.3 The axisymmetric propane fire

The second test case considered here is an axisymmetric propane fire on a 30cm-diameter burner ( $D = 30$  cm) [44]. The details of the experimental setup can be found in [44] and a short description is provided below for clarity and completeness.

The burner was held above the ground and set in the center of a square 4 m  $\times$  4 m enclosure, 3.6 m in height. To allow the required fresh air to flow into the enclosure, openings were made at the base of the enclosure walls [44]. The calorific power,  $Q$ , of the fire was 37.9 kW which corresponds to a fuel mass flux of  $\dot{m}_{fu} = 8.164 \times 10^{-4}$  kg/s, when a heat of combustion equal to  $4.64 \times 10^7$  J/kg is used.

### 5.3.1 Computational Domain and Grid Specifications

Since the burner is held above the ground, two choices for the placement of the lower boundary of the computational domain were investigated. These are depicted in Figure 5.2.

To reduce the computational time, several attempts were first made to use a smaller computational domain by placing the lower boundary of the solution domain at the same height as the burner exit, Figure 5.2-a. However, no robust open boundary condition was found to describe a lower boundary of this form. Therefore, it was decided to extend the computational domain to cover the area below the burner exit, as shown in Figure 5.2-b. In this case, the region underneath the burner itself is blocked out.

Table 5.3 shows the specifications for the grid used to obtain the numerical

### 5.3 The axisymmetric propane fire

---

results reported in this chapter for the axisymmetric propane fire.

Table 5.3: Grid specifications used for the axisymmetric fire

|                                     |                |
|-------------------------------------|----------------|
| no. of nodes, $N_r \times N_z$      | 52 $\times$ 89 |
| domain size, $W_d \times H_d/R$     | 4 $\times$ 14  |
| depth of the section below, $H_b/R$ | 3              |
| no. of nodes in burner radius       | 26             |

The size of the computational domain was selected based upon the observed extent of the fire spread in the first test case. The width of the domain was chosen such that higher grid resolution could be obtained without setting the far field boundary condition too close to the fire centerline. Effects of the domain size, grid resolution and modified turbulence parameters on predicted results for this case are presented and discussed further in Chapter 7.

### 5.3 The axisymmetric propane fire

---

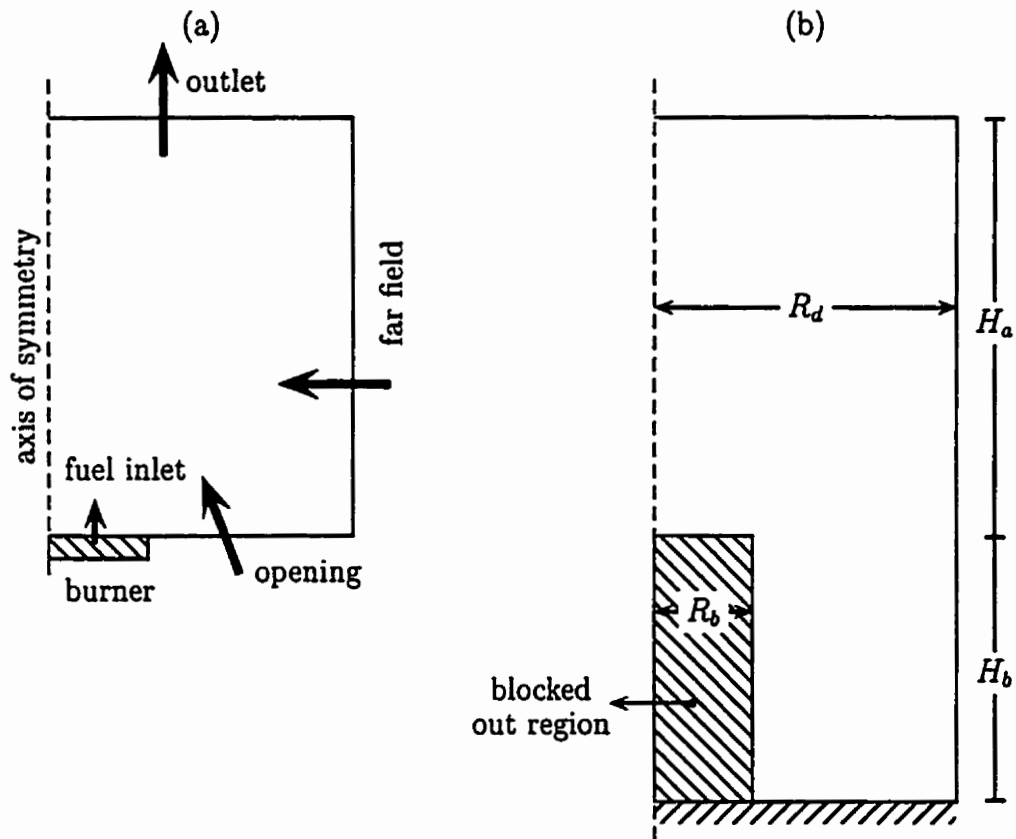


Figure 5.2: Schematic of the computational domain for the axisymmetric propane fire. (a) The small computational domain, (b) The extended domain



## 5.4 Boundary Conditions

---

### 5.4 Boundary Conditions

The boundary of the computational domain for all fire simulations considered in this thesis, can be broken into five sections which represent different physical boundaries. In this section, details of each of these boundary conditions are given.

#### Symmetry Boundary Condition

The assumption of symmetry along the fire centerline dictates the following conditions

$$u = 0, \quad \frac{\partial \phi}{\partial x} = 0 \quad (\phi = P_d, w, T, k, \varepsilon, f, Y_{O_2}, Y_{fu}, \overline{T'^2}) \quad (5.1)$$

where  $x$  represents the direction normal to the axis of symmetry.

#### Solid Wall Boundary Condition

A no-slip adiabatic wall boundary condition is used along all solid walls, which yields

$$u = w = 0, \quad \frac{\partial \phi}{\partial n} = 0 \quad (\phi = P_d, T, k, \varepsilon, f, Y_{O_2}, Y_{fu}, \overline{T'^2}) \quad (5.2)$$

where  $n$  represents the direction normal to the wall.

The boundary conditions for  $k$  and  $\varepsilon$  follow the recommendation of Annarumma [52]. After trying a low Reynolds number version of the  $k$ - $\varepsilon$  model and also standard wall functions in his numerical simulations, he concluded that such complications are unsuitable for fire modeling due to the transitional character of the flow near the floor. Therefore, these boundary conditions are set as given in Equation (5.2).

## 5.4 Boundary Conditions

---

### Far Field Boundary Condition

The side boundary condition is located some diameters away from the fire centerline, where there is hardly any ambient motion. Since laboratory pool fire measurements are usually taken in quiescent neutrally stratified environments, conditions which represent such room condition can be easily justified along this boundary. These are

$$\begin{aligned} w = Y_{fu} = f = P_d = 0 \quad , \quad k \approx \varepsilon \approx \overline{T'^2} \approx 0 \\ \frac{\partial u}{\partial x} = 0 \quad T = T_\infty \quad Y_{O_2} = 0.2321 \end{aligned} \quad (5.3)$$

### Outlet Boundary Condition

At the top of the computational domain where hot gases exit, a pressure specified outlet is used. Along this boundary the following conditions are applied.

$$u = P_d = 0 \quad \frac{\partial \phi}{\partial z} = 0 \quad (\phi = w, T, k, \varepsilon, f, Y_{O_2}, Y_{fu}, \overline{T'^2}) \quad (5.4)$$

### Boundary Condition at the Burner Exit

To set appropriate boundary conditions at the burner exit, it should be noted that it is the reaction heat release in natural fires which essentially creates buoyancy and drives the flow. This consequently causes other scalar fields (e.g. pressure, turbulence etc...) to develop. This physical behavior presents itself in mathematical formulation through the effect of source terms in different transport equations. Therefore, solution of the governing equations is

## 5.4 Boundary Conditions

---

primarily source driven in these simulations in contrast to other flow situations where boundary conditions dictate the behavior.

Bearing this in mind, it is noticed that the most critical criteria in specifying boundary conditions at the burner exit is to ensure that the net fuel input ( $\dot{m}_{fu}$ ) to the domain is equal to the desired value (usually obtained from experimental data). To accomplish this, the following boundary conditions are used at the burner exit

$$w_o = \frac{\dot{m}_{fu}}{\rho_o A_{burner}} \quad \frac{\partial P_d}{\partial z} = u_o = Y_{O_2o} = 0 \quad Y_{fuo} = 1 \quad (5.5)$$

where subscript “o” denotes the condition at the burner exit.

These boundary conditions ensure that the convective fuel mass flux into the domain is equal to  $\dot{m}_{fu}$ ; however, the diffusion flux at this boundary may alter the net fuel mass flux into the domain. To prevent such a problem, total diffusion coefficients of  $f$ ,  $Y_{fu}$  and  $Y_{O_2}$  at the burner exit are set to zero.

Boundary condition specification for the energy equation presents its own challenge in pool fire simulations, particularly in cases where liquid fuels are used. Satisfying the energy equation and performing an exact heat balance at the burner (or fuel) surface requires a detailed knowledge of the radiation heat feed back to the burner and also conditions below the burner surface (or inside the liquid pool of fuel). Due to a lack of such information and also lack of detailed temperature measurements at the burner exit in the data for the propane fires considered here, a uniform temperature boundary condition,  $T = T_o$ , is assumed for the present calculations. The specified temperature value,  $T_o$ , fixes the burner exit velocity,  $w_o$ , through the gas density,  $\rho_o$ .

## 5.4 Boundary Conditions

---

The present numerical experiments show that the actual value of  $T_o$  assumed at the burner exit does not noticeably change the solution as long as the diffusion heat loss at the burner surface is kept within a reasonable range. Since the molecular heat diffusion is very small, it is the turbulent heat flux which plays the key role. This creates a strong connection between boundary conditions for turbulence quantities and temperature.

Despite the laminar nature of the fuel flow at the burner exit, in parabolic fire simulations [44, 45, 37, 46] the levels of  $k$  and  $\epsilon$  are usually “tuned” to improve the results and obtain better overall agreement with experimental data. Although this practice may be justifiable for parabolic models, where streamwise diffusion is neglected and only the crosswise velocity gradient contributes to turbulent shear production, it could cause unrealistically high heat losses at the burner exit due to high streamwise gradients close to the burner surface. In addition, in elliptic models it is the total turbulent shear production and buoyancy generation source terms in the  $k$  and  $\epsilon$  equations which determine the turbulence field. Thus in these simulations, the boundary values of  $k$  and  $\epsilon$  chosen for the burner exit are found to have negligible effects on the overall solution.

Considering the above discussion, the following conditions for temperature and turbulence quantities are used at the burner exit

$$T_o = 600(K), \quad k_o \approx \epsilon_o \approx \overline{T'^2}_o \approx 0 \quad (5.6)$$

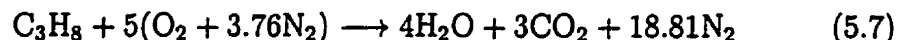
## 5.5 Mean Flow Results

---

### 5.5 Mean Flow Results

The base model results reported here are obtained by neglecting the terms involving  $\rho'$  and using standard coefficients in the  $k$ - $\epsilon$  turbulence model. The neglect of terms involving  $\rho'$  converts the present time averaged formulation into a form which becomes essentially Favre averaged, a similar form to that used in [48].

Propane is assumed to react with air through a one step reaction



and Table 5.4 lists the numerical values of turbulence model coefficients used.

Table 5.4: Turbulence model constants

| $C_\mu$ | $C_{\epsilon 1}$ | $C_{\epsilon 2}$ | $\sigma_t$ | $\sigma_f$ | $\sigma_\epsilon$ | $\sigma_k$ |
|---------|------------------|------------------|------------|------------|-------------------|------------|
| 0.09    | 1.44             | 1.92             | 0.7        | 0.7        | 1.3               | 1.0        |

Calculations for both fires were started from a uniform initial guess for all variables based on their values in the quiescent surrounding. A small time step, of the order of milliseconds, was used at the beginning of the simulation and held at that value but after some iterations the time step was increased by one or two orders of magnitude until steady-state solutions were obtained. The convergence criteria for the maximum non-dimensional residual was set to  $10^{-3}$ .

## 5.5 Mean Flow Results

---

### 5.5.1 Results for the Rectangular Fire

Figure 5.3 shows the predicted velocity and temperature fields when a constant value for the heat capacity at constant pressure<sup>1</sup>, i.e.  $C_p = 1300$  (J/kg/K), and 20% radiation heat loss is used.

As shown in this figure, the general features of the flow field are reasonably well predicted. For instance, the strong entrainment of fresh air into the reaction core, the length of visible flame height (marked by  $T=600$  K temperature contour) and location of maximum temperature close to the burner rim, agree with experimental observations [48]. For a more quantitative evaluation of the results, radial profiles of velocity and temperature at different heights above the fuel surface are plotted against both experimental and numerical results of reference [48] in Figures 5.4 and 5.5.

The lateral spreads of predicted velocity and temperature profiles are both improved in comparison with those of the previous model; however, they are still underpredicted compared to experimental data for  $z \geq 13$  cm. Moreover, values of centerline temperature are over predicted close to the burner surface. It should be noted that 50% radiation heat loss was used in reference [48], whereas only 20% radiation loss is assumed for the present calculations. Nevertheless, both velocity and temperature values at  $z = 46$  cm, which is above the reported visible flame tip at  $z = 37$  cm, are still lower than experimental data.

---

<sup>1</sup>it is a common practice in fire simulations [48, 46, 47] to use a constant value for  $C_p$  to reduce the non-linearity of the governing equations and improve the efficiency of the numerical model. However, this practice has a drawback which will be discussed later in this chapter.

## 5.5 Mean Flow Results

---

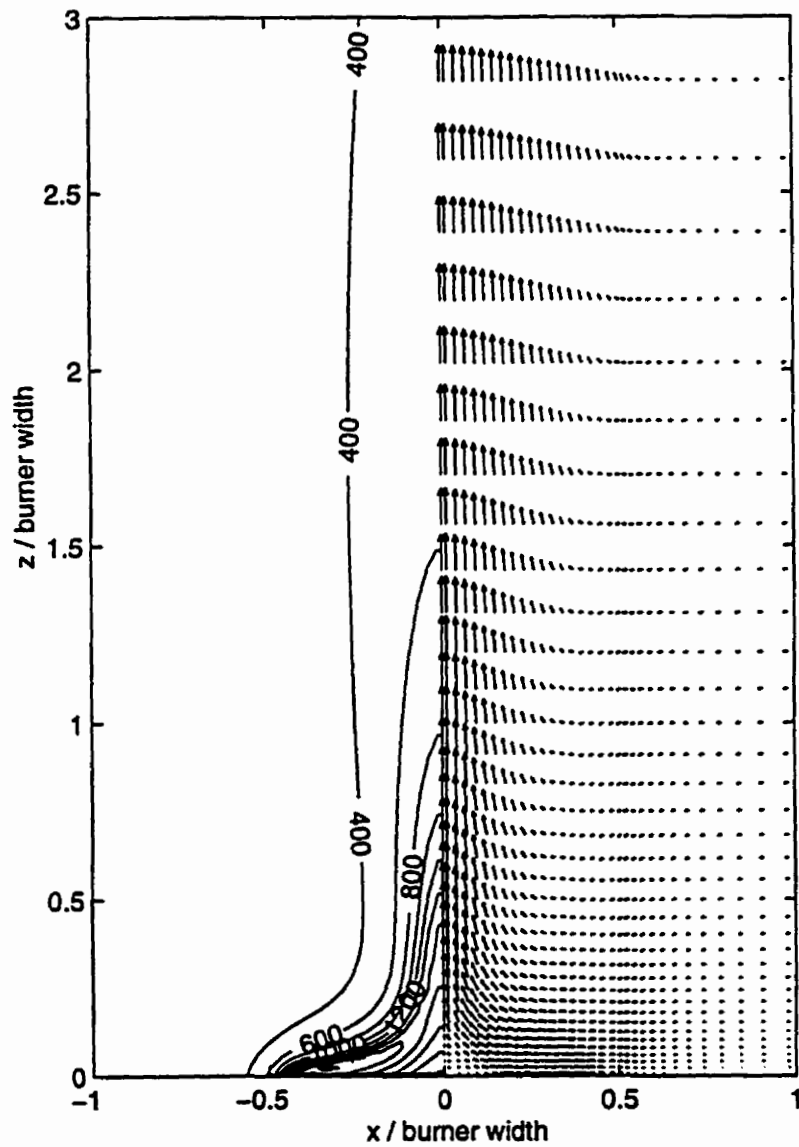


Figure 5.3: Predicted temperature contours and velocity field for the rectangular propane fire [48]

## 5.5 Mean Flow Results

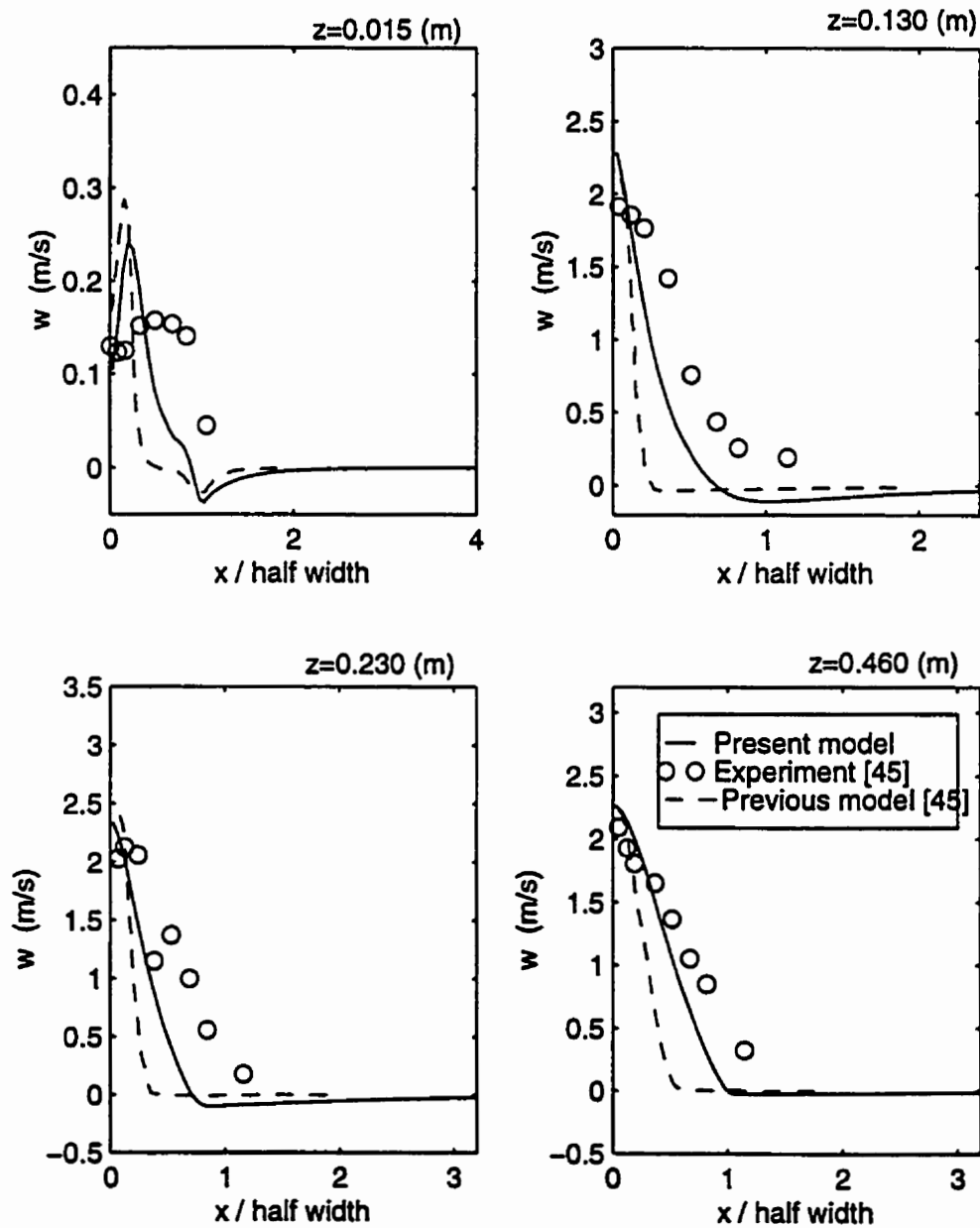


Figure 5.4: Lateral distribution of vertical velocity at different heights



## 5.5 Mean Flow Results

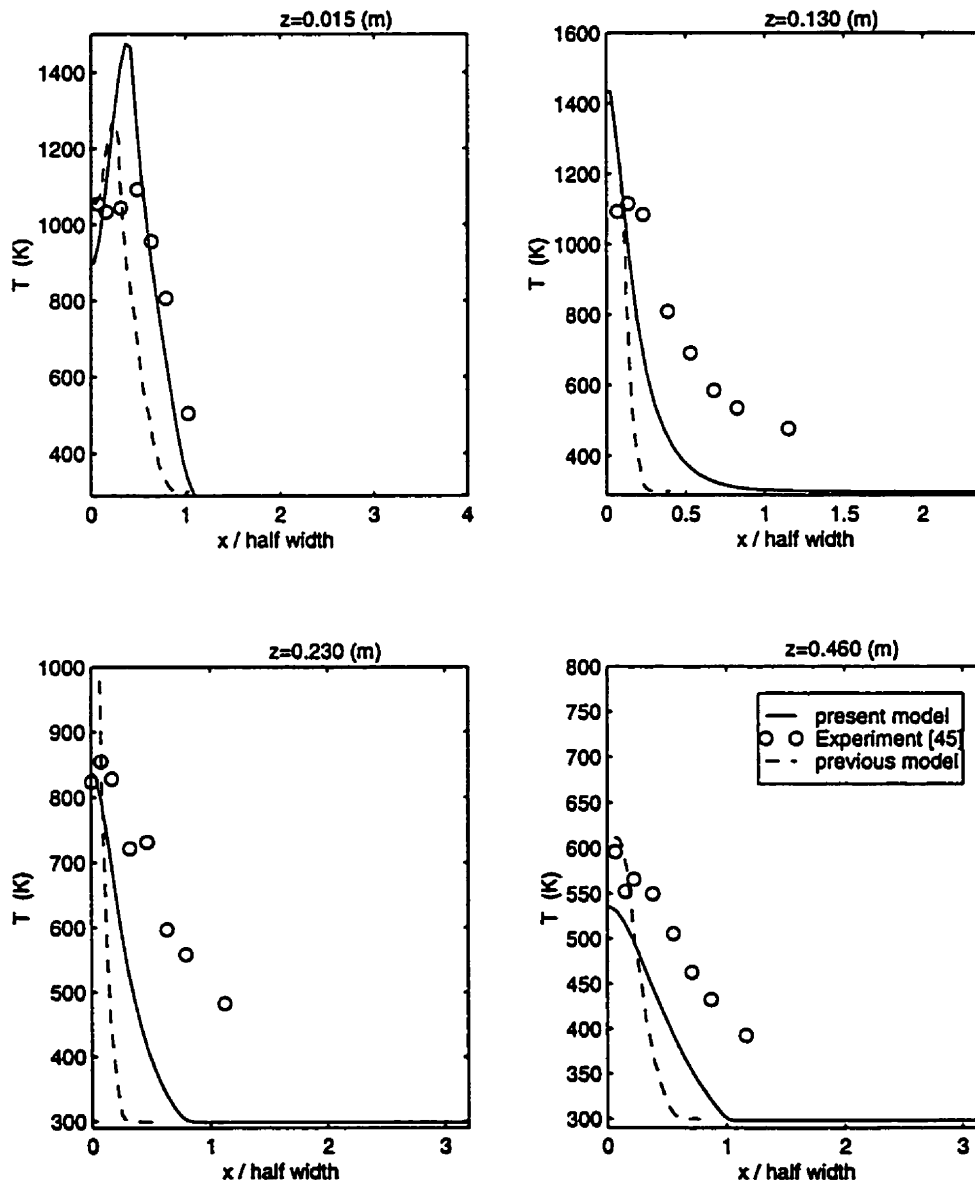


Figure 5.5: Lateral distribution of temperature at different heights

## 5.5 Mean Flow Results

---

The use of 50% radiation heat loss in the present model aggravated these results and reduced the already underpredicted velocity and temperature profiles. Surprisingly, calculations with a radiation loss fraction as low as even 5% did not increase the velocity and temperature profiles to the levels indicated by the experimental data. To investigate the source of this disagreement and to determine the impact of using a constant value for  $C_p$  on the accuracy of the numerical results, an overall energy balance based on the experimental data [48] was performed around the fire. Detailed calculations from this analysis can be found in Appendix E and a summary of the findings is given in Section 5.6. But first, the base model results for the axisymmetric propane fire are presented.

### 5.5.2 Results for the axisymmetric fire

For the axisymmetric fire, computations are done using the same constant value for  $C_p$  as was used for the rectangular fire, i.e.  $C_p = 1300$  J/kg/K, but, a higher value for  $C_\mu$ , i.e.  $C_\mu = 0.11$ , as recommended for axisymmetric plumes [79] with the  $k$ - $\epsilon$  turbulence submodel.

Centerline variations of predicted velocity and temperature are depicted and compared with experimental data [44] in Figure 5.6. The general trends in the predicted results agree reasonably well with the experimental data. In particular, the locations of the maximum velocity and temperature along the centerline are predicted reasonably well, but the overall accuracy of the predictions is still not very good.

Figure 5.7 shows the predicted radial profiles of temperature versus the experimental data reported in [44]. As shown, radial spread of the temper-

## 5.5 Mean Flow Results

---

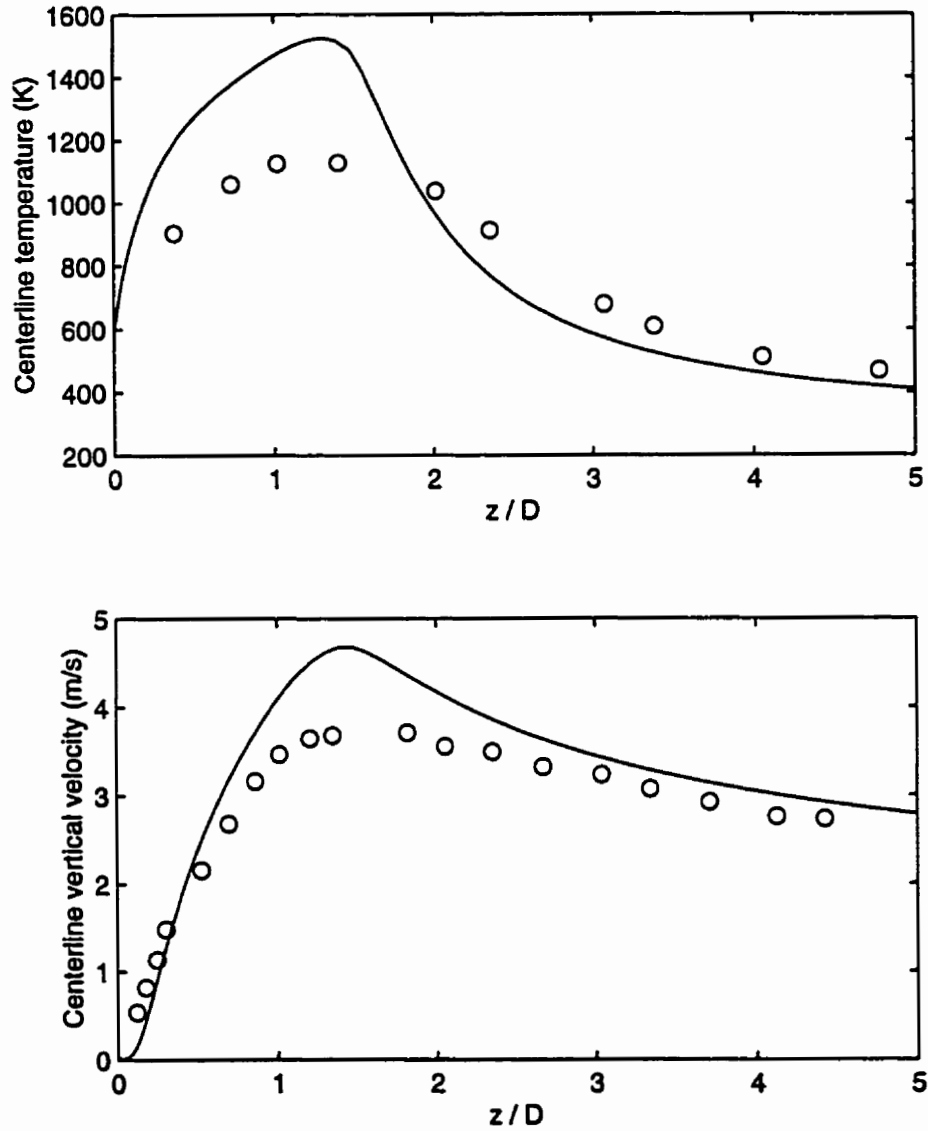


Figure 5.6: Centerline distribution of velocity and temperature for the axisymmetric propane fire, — present results,  $\circ$  experimental data

## 5.5 Mean Flow Results

---

ature profiles is consistently underestimated. Similar comparisons between predictions and experimental data for vertical velocity are shown in Figure 5.8. Although the agreement between predicted velocity profiles and experimental data is better than that observed for the temperature profiles, the relative spread of vertical velocity is still under-predicted. Similar discrepancies between parabolic simulation results and experimental data were observed by other researchers [46, 47], where they speculated that better agreement between numerical results and experimental data could be obtained if elliptic formulations are used. But, the present elliptic results clearly show that the use of an elliptic formulation alone is not enough to reduce the observed discrepancies between predictions and experimental data.

In the next section, the effects of using a constant  $C_p$  on predicted results is discussed and the effects of some new proposed modifications to the BASE fire model, which result in obtaining better agreement between predictions and experimental data, will be presented discussed in Chapter 7.

## 5.5 Mean Flow Results

---

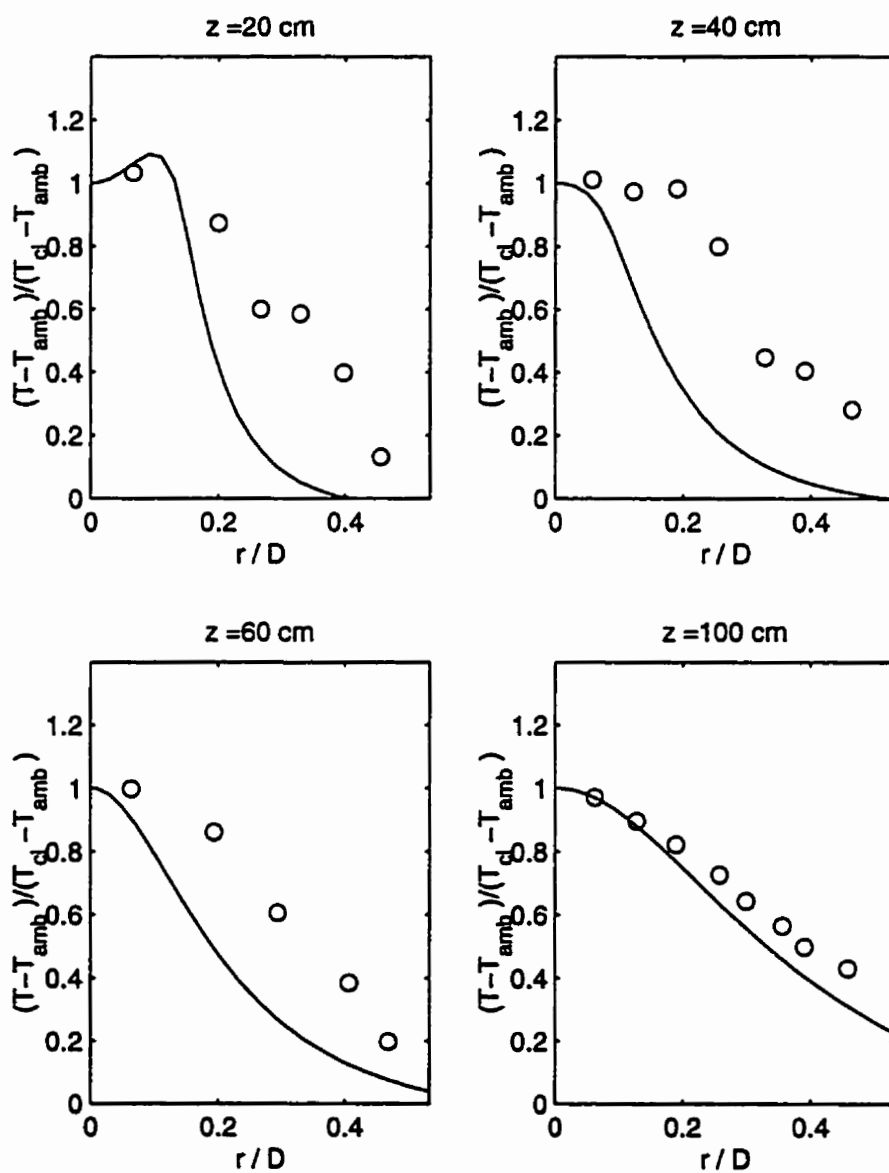


Figure 5.7: Radial profiles of temperature for the axisymmetric propane fire, — present results,  $\circ$  experimental data

## 5.5 Mean Flow Results

---

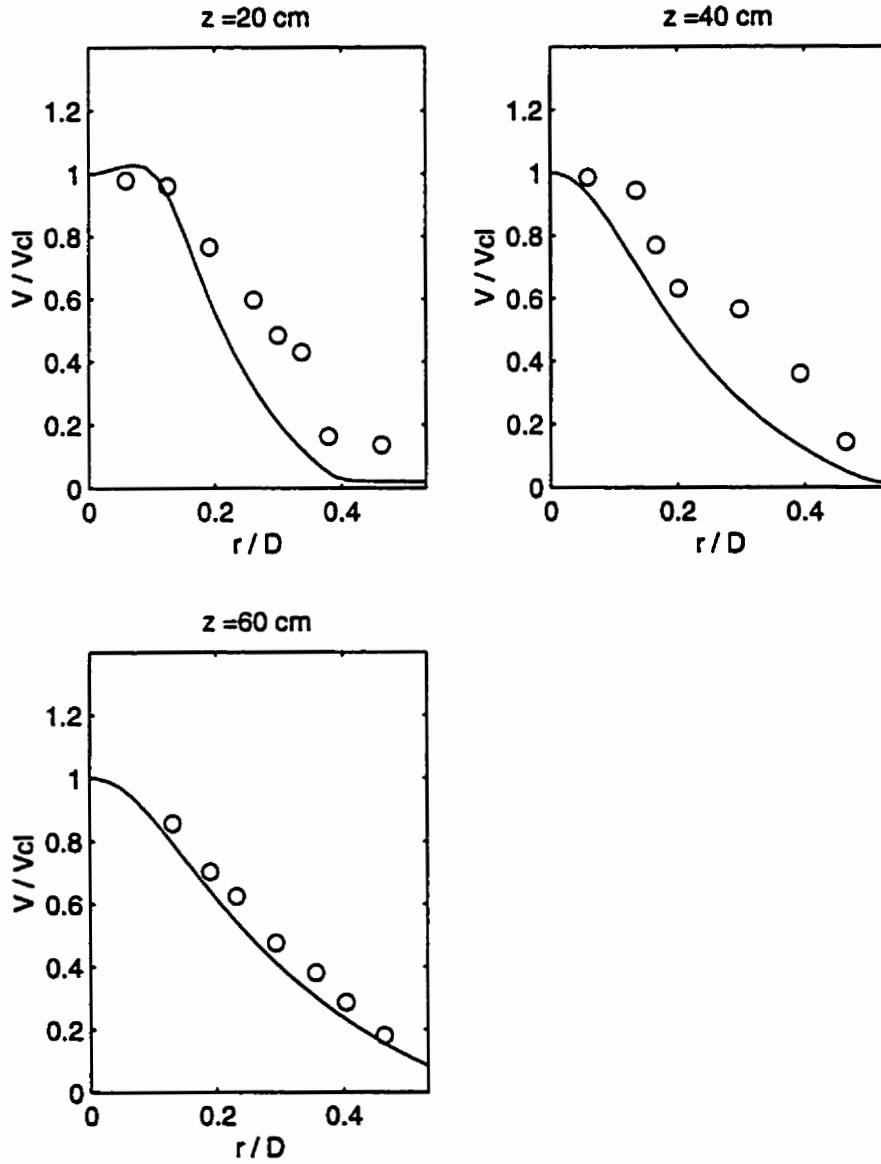


Figure 5.8: Radial profiles of vertical velocity for the axisymmetric propane fire, — present results,  $\circ$  experimental data

## 5.6 Appropriateness of using a constant $C_p$ for fire simulations

### 5.6 Appropriateness of using a constant $C_p$ for fire simulations

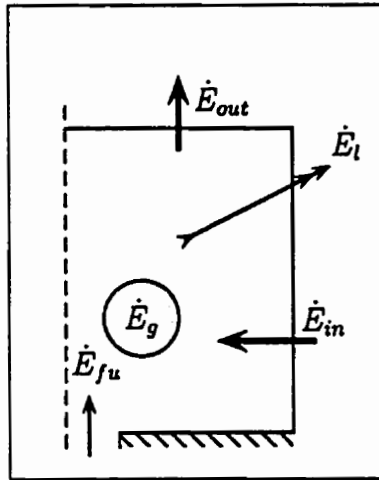


Figure 5.9: Energy balance for the rectangular propane fire

Experimental data can be used to perform an overall energy balance around the fire. Assuming that most of the heat release due to reaction occurs below a certain height and considering the steady-state conservation of energy for a control volume surrounding the fire, as shown in Figure 5.9, the maximum possible radiation heat loss<sup>2</sup>,  $\dot{E}_l$ , can be calculated using

$$\dot{E}_l = \dot{E}_g - (\dot{E}_{out} - \dot{E}_{in} - \dot{E}_{fu}) \quad (5.8)$$

where

•  $\dot{E}_g = \dot{m}_{fu} \cdot \mathcal{H}_c$  is the heat generated due to combustion

<sup>2</sup>One should note that the actual radiation heat loss will be lower due to incomplete reaction and diffusion heat losses.

## 5.6 Appropriateness of using a constant $C_p$ for fire simulations

---

- $\dot{E}_{\text{out}}$  is the heat flow leaving the control volume and can be calculated using experimental data for  $v$  and  $T$  as follows

$$\dot{E}_{\text{out}} = \int_{\text{out}} \rho C_p T v dA \quad (5.9)$$

- $\dot{E}_{\text{in}}$  is the heat flow into the control volume due to entrainment, and
- $\dot{E}_{\text{fu}} = \dot{m}_{\text{fu}} C_p T_{\text{fu}}$  is the energy convected into the control volume at the burner surface.

It can be easily shown that if  $C_p$  is treated as a constant,  $\dot{E}_l$  becomes a linear function of  $C_p$  in Equation (5.8). Assuming different values for  $C_p$ , the right hand side of Equation (5.8) is calculated using the experimental data for the rectangular fire. The result is plotted in Figure 5.10 in a non-dimensional form (see Appendix E for sample calculations).

It is interesting to note that for  $C_p \gtrsim 1160$  J/kg/K the calculated radiation loss becomes negative. This indicates that *if a value of  $C_p = 1300$  J/kg/K is used in a numerical model, even for complete reaction the generated heat is not enough to raise the velocity and temperature profiles high enough to match the experimental data.*

Knowing that  $C_p = 1300$  J/kg/K is inappropriate for the rectangular propane fire simulation, computations were repeated but this time values of  $C_p$  were calculated using the techniques described in Section 3.8. Figure 5.11 shows the effect of variable  $C_p$  on predicted centerline velocity and temperature distributions for the rectangular fire. Similar comparison has also been done for the axisymmetric propane fire [44] and results are shown in Figure 5.12.



## 5.6 Appropriateness of using a constant $C_p$ for fire simulations

---

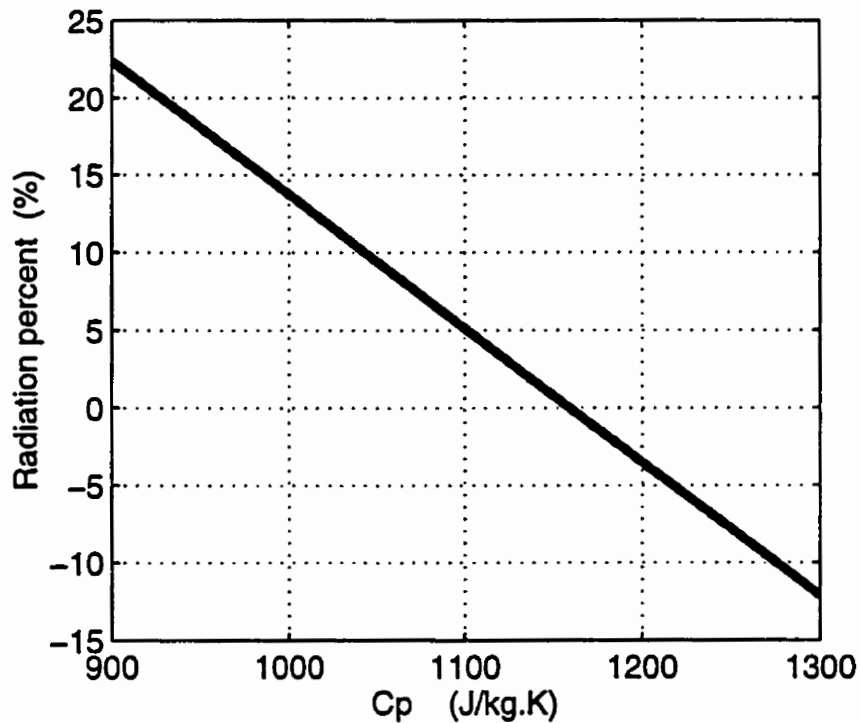


Figure 5.10: variation of radiation heat loss versus presumed  $C_p$

As one might expect, and as shown in Figures 5.11 and 5.12, varying the value of  $C_p$  has rather significant effects on predicted velocity and temperature fields. Use of physical values of  $C_p$  results in higher predicted velocity and temperature values for both rectangular and axisymmetric propane fires.

Since other adjustable parameters are involved in numerical fire modeling, particularly in the turbulence model where these parameters have at most been optimized for non-reacting flows, it is concluded that values of physical properties such as  $C_p$  should be calculated as accurately as possible before other unknown parameters are “tuned” to improve the overall accuracy of the fire model.

## 5.6 Appropriateness of using a constant $C_p$ for fire simulations

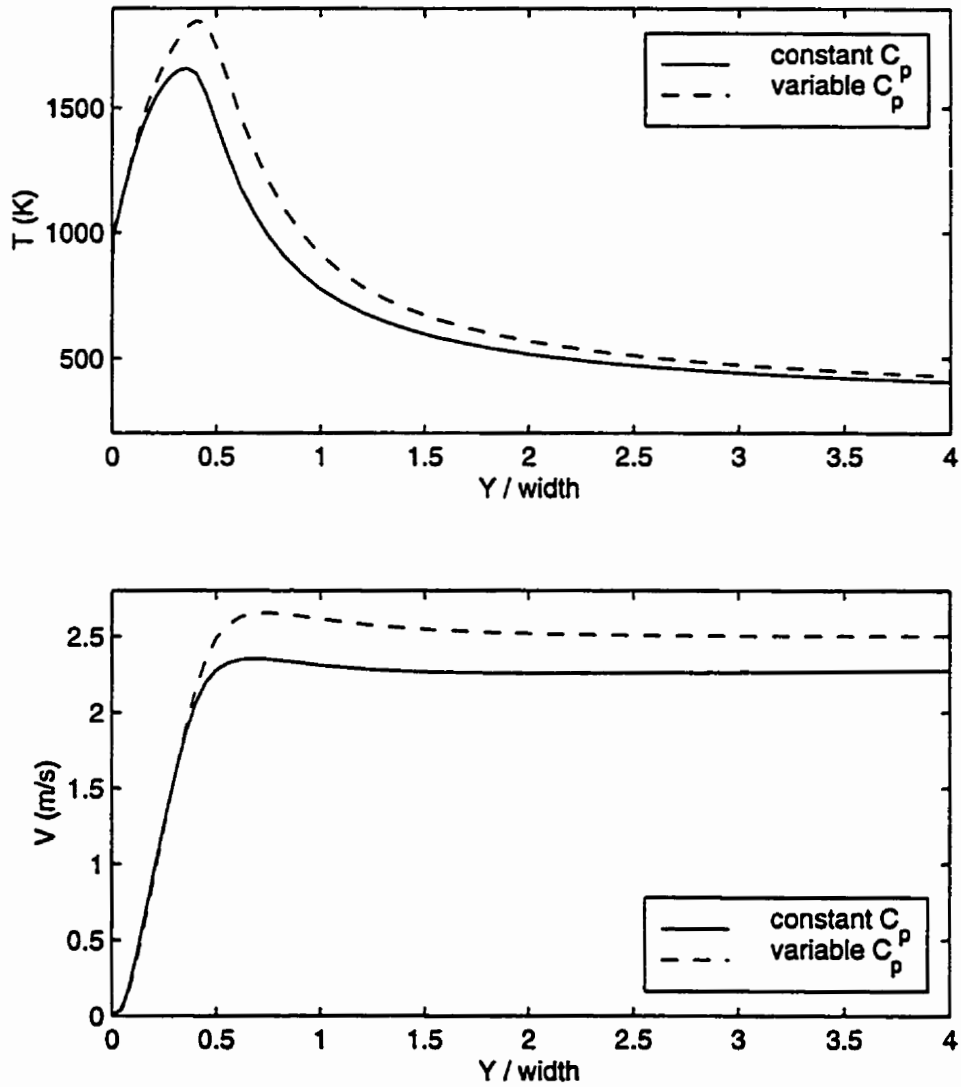


Figure 5.11: Effect of  $C_p$  on centerline velocity and temperature distributions for the rectangular propane fire

## 5.6 Appropriateness of using a constant $C_p$ for fire simulations

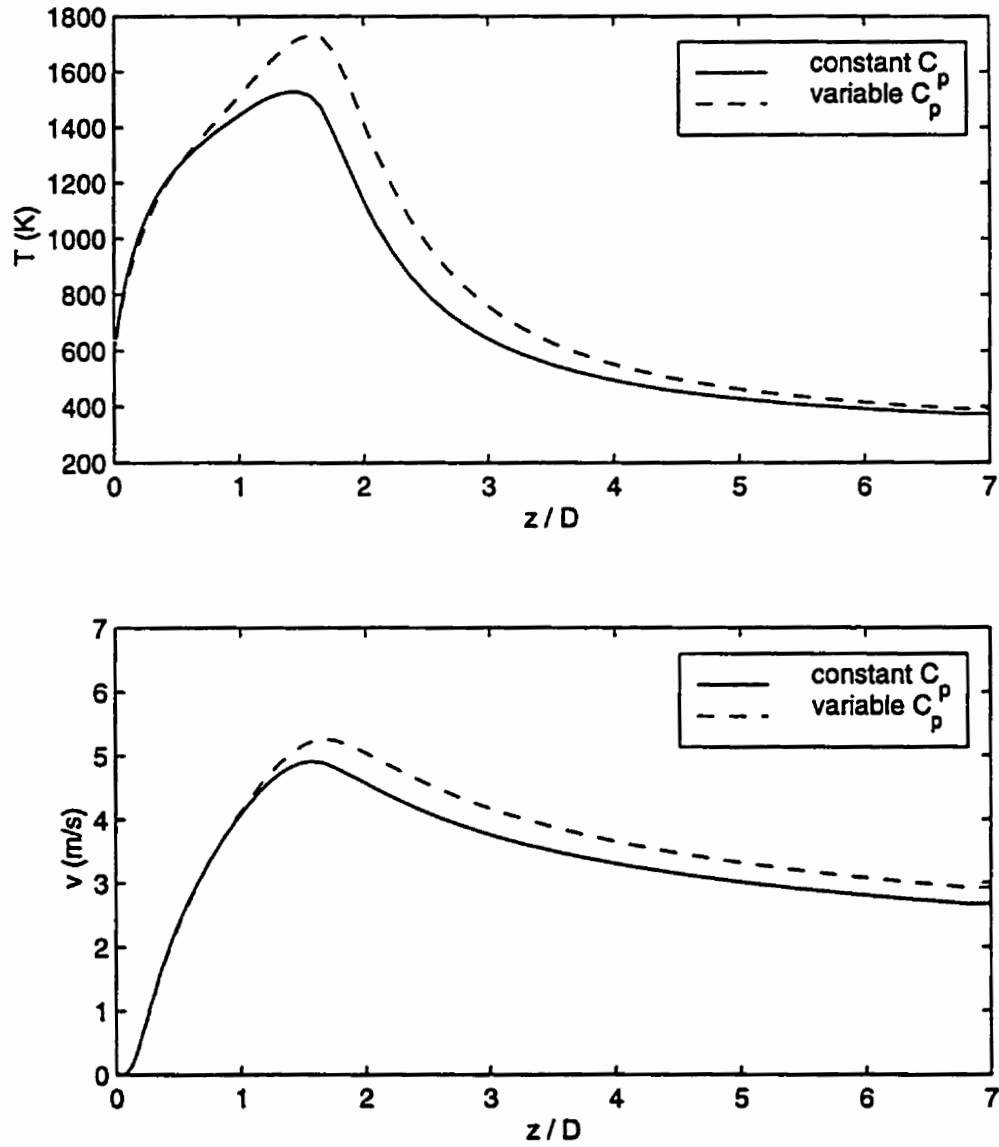


Figure 5.12: Effect of  $C_p$  on centerline velocity and temperature distributions for the axisymmetric propane fire

# Chapter 6

## Simulation of the Fire Puffing Phenomenon

### 6.1 Introduction

One of the prominent features of pool fires is the puffing phenomenon, or the fire pulsation, which appears to be most pronounced in liquid pool fires having a regular circular shape [1]. The fire pulsation is observed to be a periodic formation and shedding of large-scale vortical structures. These structures are known to significantly affect the entrainment process, and consequently the burning rate of the fuel, and thereby to modify the downstream flame behavior. The pulsation frequency appears to correlate with pool diameter and is not dependent on type of fuel [1, 103].

A typical sequence of formation and shedding of large scale structures is shown in Figure 6.1 which includes photographs of a 30 cm diameter acetone pool fire taken in the University of Waterloo pool fire laboratory. As shown in

## 6.1 Introduction

---

these photos, vortical structures with a diameter of approximately one pool diameter, form near the pool surface and shed upward. As these structures move upward, the flame narrows and necks inward behind the structure. The vortical reacting structures grow in size as they move until they disappear near the tip of the visible flame.

Understanding the origin and also the mechanisms of fire pulsation is of great theoretical importance to fire scientists. The pulsating characteristics of fires have been also exploited to practical advantage in design of some infrared fire detection sensors [1, 53].

In this chapter, previous studies on fire pulsation are briefly reviewed, and then the applicability of the present elliptic fire model to numerical simulation of such transient behavior of fires will be demonstrated. Finally, the predicted sequence of formation and shedding of large-scale vortical structures will be compared with experimental observations.

The results presented in this chapter contribute to numerical simulation of pulsating pool fires using the full solution of the Reynolds averaged Navier-Stokes equations for buoyancy driven turbulent diffusion flames. It should be highlighted that, for the first time a turbulent fire model is shown to be capable of simulating the fire pulsation without using an artificial triggering mechanism to start the puffing, such as a periodic boundary condition. This may indicate the advantages of the new elliptic fire model in terms of incorporation of appropriate physical submodels and a strongly coupled numerical implementation.

## 6.1 Introduction

---

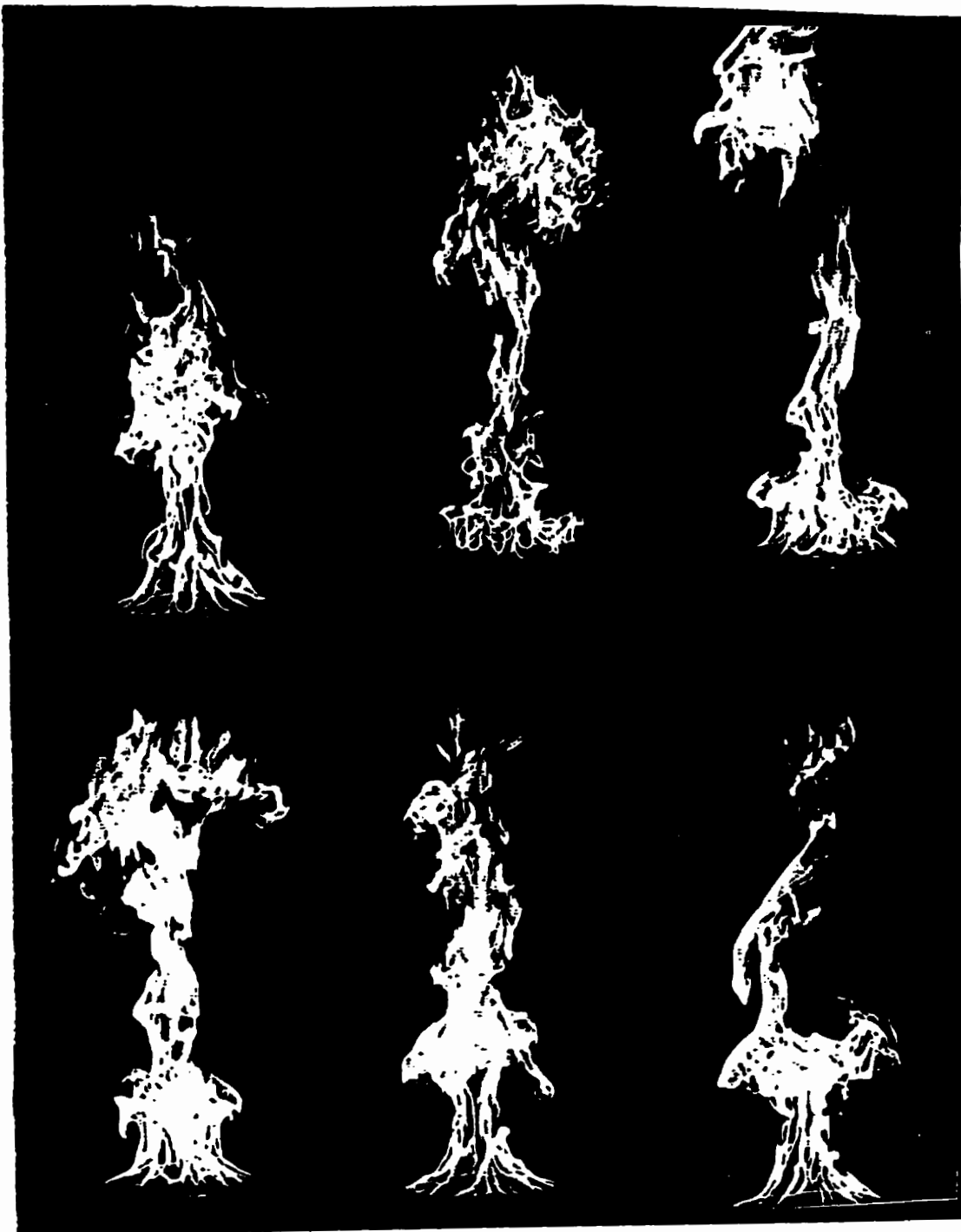


Figure 6.1: Photographs of a 30-cm pulsating acetone pool fire

## 6.2 Previous Studies on Fire Pulsation

Practical and theoretical significance of pool fires has motivated many researchers to study their behavior. These studies have been, mostly, based on experimental observation and cover a wide range of fuels (gaseous, liquid and solid), burner diameters, heat releases and Reynolds numbers [53, 104, 105, 106, 107, 108, 109].

Qualitative descriptions of the characteristics of large-scale flame structures and details of the puffing phenomenon are provided by Zukoski et al. [105], Weckman [24, 106], Cetegen et al. [110] and Chen et al. [108], among others, using visualization techniques. Weckman and Sobiesiak have also studied the effect on the pulsation of applying different boundary conditions around the fire [27].

The pulsation frequency of pool fires has been measured using various techniques. These include video recording and fast photography, acoustic detection, pressure and temperature measurements, hot wire anemometry and LDA velocity measurements. The pulsation frequency is reported to strongly depend on the pool diameter. For example, Pagni [103] has plotted a large number of available data for pulsation frequency versus burner diameter and raised the question as to why the frequency of fire oscillation over a wide range of flame base diameters (0.03 – 60 m) and irrespective of fuel type, is proportional to  $D^{-1/2}$ , where  $D$  denotes the pool diameter. He suggested a best fit to the available data for the pulsation frequency,  $f$ , which yielded  $f \approx 1.5/\sqrt{D}$ .

Although not conclusively understood, there have been several attempts to describe the origin and cause of the fire pulsation. These studies suggest

### 6.3 Transient Fire Simulation

---

that the origin of the puffing phenomenon is related to fluid dynamic and buoyant instability [27, 110], laminar shear layer instability [107] and periodic propagation of a premixed flame into the flammable volume [53]. The puffing frequency has also been approximately predicted using the buckling theory of inviscid streams [111] and dimensional analysis [112]. Although, experimental studies provide invaluable information for fire scientists, reliable and accurate numerical fire models should be able to produce more quantitative and detailed data to aid in understanding of the cause of fire pulsation and the mechanisms involved in that phenomenon.

Recently, the transport element method along with a Shvab-Zeldovich variable formulation [33] has been used to numerically simulate the puffing phenomenon of pool fires and isothermal plumes. The numerical results suggest that a Kelvin-Helmholtz type instability mechanism in the vortex sleeve is the origin of instability in pool fires. Clearly, more research is required to clarify the cause and results of the fire pulsation.

### 6.3 Transient Fire Simulation

In order to simulate the puffing phenomenon, a series of long time transient simulations have been carried out for the axisymmetric propane fire described in Section 5.3. A difference between the transient and the pseudo steady-state simulations performed in Chapter 5 is that a smaller computational domain (i.e. without the extended lower part of the domain) is used here and a floor surrounding the pool and level with the pool rim is assumed, as shown in Figure 6.2. According to experimental evidence [27, 113], this



### 6.3 Transient Fire Simulation

---

change in the boundary condition does not alter the sequence of formation of large-scale structures.

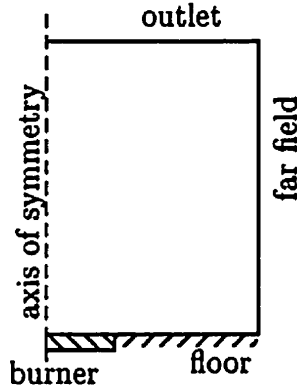


Figure 6.2: Schematic of the computational domain for the transient fire simulations

Computations are started from uniform ambient conditions and continued without obtaining converged solutions for each time step until an approximate flow field is established throughout the computational domain. Then, full transient solutions are obtained at each time step. For most of the simulations performed here a time step of 0.01 s is used, which seems to be small enough compared to the resident time step based on the pulsation frequency. Numerical results after every 0.1 s are saved for post processing. Because of the high cost of computations required to obtain a series of transient solutions, a medium size grid with  $52 \times 72$  nodes in radial and axial directions, respectively, is used for most of the cases presented in this chapter. A summary of the various cases run is contained in Table 6.1.

Figure 6.3 shows the time trace of predicted pressures at two radial lo-

### 6.3 Transient Fire Simulation

---

cations at the burner surface. These results are obtained using the base fire model described in Chapter 5. As shown in this figure, after about one second from the start of the transient simulation (marked with  $t_o$  in Figure 6.3), the burner surface pressure starts to oscillate with a frequency of about 2.63 Hz. The same periodic variation is obtained for the pressure difference across the burner radius ( $\Delta P_d = P_{drim} - P_{dcl}$ ) and shown in the upper half of Figure 6.3. This pressure difference is the main driving force in radial direction which controls the entrainment close to the fire base. The corresponding contour plots of temperature for this transient simulation are shown in Figures 6.4 and (6.5). These figures clearly demonstrate a pulsating flame behavior which is qualitatively very similar to that of the real fire, as shown in the photographs in Figure 6.1.

The pulsating frequency obtained from Figures 6.4 and 6.5 matches that obtained from the oscillating pressure field. The close connection between the oscillating pressure field and the periodic formation of visible large-scale structures in pool fires was experimentally confirmed by Cetegen et al. [110] who reported oscillating pressure measurements for a 30 cm diameter propane fire. Their data and photos of the pulsating flame appeared to correlate very closely and showed that the frequency of the oscillating pressure field corresponds to the frequency of the formation of the large scale structures. A photocopy of their published data from [110] is included here as Figures 6.6 and 6.7 for comparison with the above results. As shown in these figures, at instants 'a', 'c', 'e', 'g' and 'i' the surface pressure reaches its minimum value whereas, at instants 'b', 'd', 'f', 'g' and 'h' the pressure drops to its maximum level. Cetegen et al. [110] argued that the pressure rises as the

| case no. | no. nodes | W×H/R    | $C_p$    | $C_\mu$  | $\chi$ | $\Delta t$ (s) | $Q$ (kW) | $f$ (Hz) | no. of cycles     |
|----------|-----------|----------|----------|----------|--------|----------------|----------|----------|-------------------|
| 1        | 52 × 72   | 4 × 14   | 1300     | 0.11     | 30%    | 0.01           | 39.7     | 2.63     | 5 cycles in 1.9 s |
| 2        | 52 × 72   | 4 × 14   | variable | variable | 30%    | 0.01           | 52.28    | 2.94     | 5 cycles in 1.7 s |
| 3        | 52 × 72   | 4 × 14   | variable | variable | 30%    | 0.005          | 52.28    | 2.86     | 4 cycles in 1.4 s |
| 4        | 52 × 72   | 4 × 14   | variable | variable | 30%    | 0.01           | 39.7     | 2.63     | 5 cycles in 1.9 s |
| 5        | 57 × 72   | 6 × 14   | variable | variable | 30%    | 0.01           | 39.7     | 2.78     | 5 cycles in 1.8 s |
| 6        | 52 × 77   | 4 × 16   | variable | variable | 30%    | 0.01           | 39.7     | 2.76     | 8 cycles in 2.9 s |
| 7        | 62 × 80   | 6.7 × 20 | variable | variable | 30%    | 0.01           | 39.7     | 2.63     | 5 cycles in 1.9 s |
| 8        | 72 × 112  | 4 × 16   | 1300     | 0.11     | 30%    | 0.01           | 39.7     | 2.61     | 6 cycles in 2.3 s |
| 9        | 72 × 112  | 4 × 16   | 1300     | 0.11     | 30%    | 0.005          | 39.7     | 2.5      | 2.5 cycles in 1 s |

Table 6.1: Effects of different geometric and physical conditions on predicted frequencies of the fire pulsation

### 6.3 Transient Fire Simulation

---

flame necks inward, and when the flame envelope opens outward the pressure diminishes.

Identical trends in the pressure variation within the fire and its correlation with the visible flame envelope are seen in the present numerical results as shown in Figures 6.3 through 6.5. However, the present detailed numerical results further reveal that the maximum surface pressure actually corresponds to the early stage of the formation of a vortical structure. The observed close connection between the burner surface pressure and the formation of large scale structures is discussed in more detail in the next section.

To further study the pulsating behavior of fires and validate the present transient numerical results, similar transient computations have been repeated for several cases. The specification of these cases and the predicted pulsation frequencies for each case are summarized in Table 6.1. The predicted pressure variation and temperature contour plots for cases 4, 7 and 8 are shown in Figures 6.8 through 6.16, whereas the pressure variations for other cases are presented in Figures 6.17 through 6.21.

In all cases listed in Table 6.1, a 30% radiation heat loss is assumed. Except for cases 1, 8 and 9, in which the base model constant values for  $C_p$  and  $C_\mu$  are used, for all other cases functional forms of  $C_p$  and a variable  $C_\mu$  are utilized. The functional forms of  $C_p$  used here were discussed in Section 3.8. Local values of  $C_\mu$  are calculated based on a functional form which varies linearly in radial direction from 0.3 at the centerline to 0.11 at the burner rim,  $r = R$ , and remains constant at 0.11 for  $r > R$ , that is

$$C_\mu = \text{MAX} \left( 0.11, 0.3 - 0.19 \frac{r}{R} \right) \quad (6.1)$$

The justification for Equation (6.1) and its effect on the solution are further

### 6.3 Transient Fire Simulation

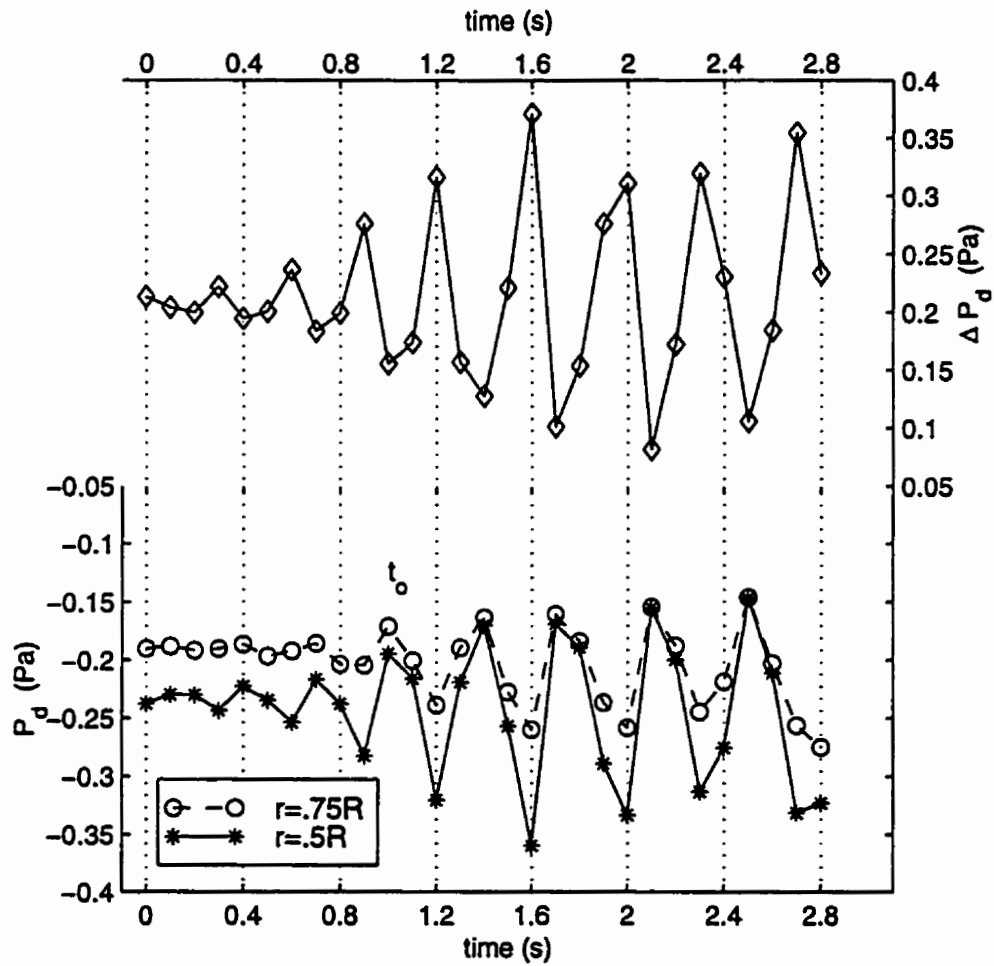


Figure 6.3: Pressure variation in time at the burner surface for case 1 in Table 6.1. The lower plot shows the burner surface pressure,  $P_d$ , at two radial location and the upper plot shows the pressure difference across the burner radius,  $\Delta P_d = P_{drim} - P_{dcl}$

### 6.3 Transient Fire Simulation

---

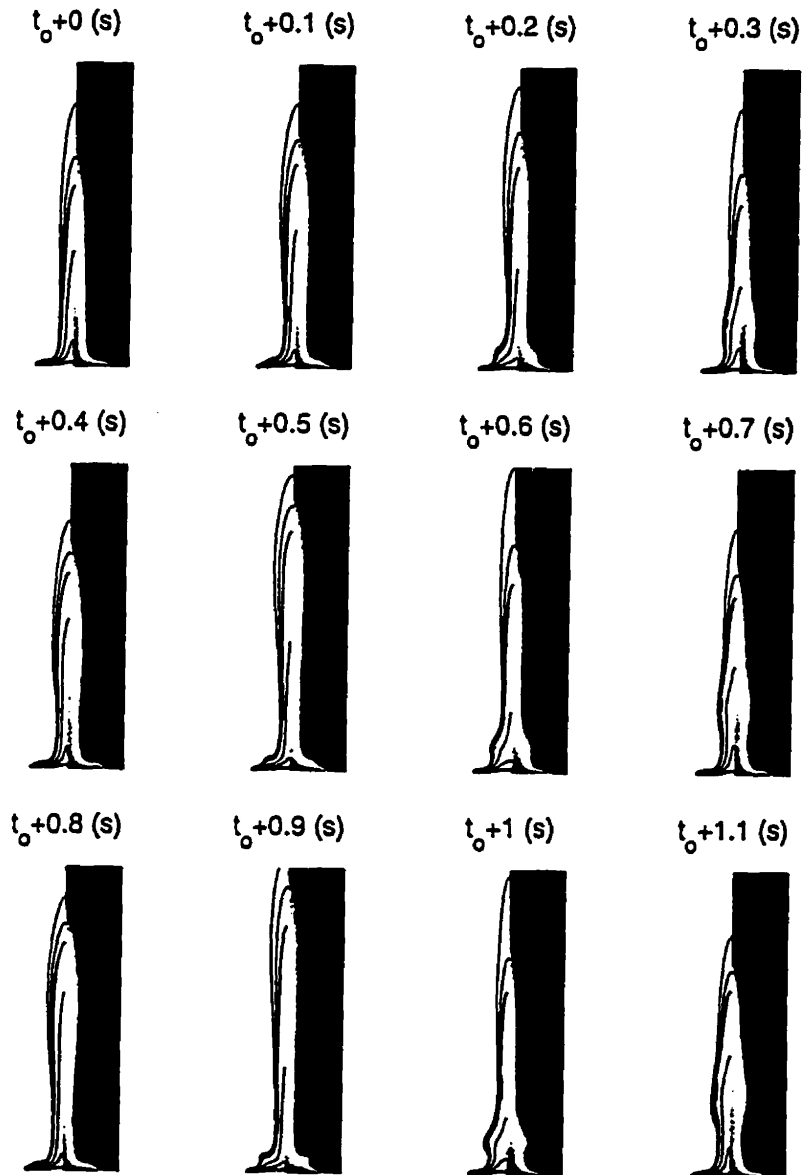


Figure 6.4: Temperature contours for case 1 in Table 6.1. Contour lines represent  $T = 700, 1000, 1400$  and  $1700$  (K).

### 6.3 Transient Fire Simulation

---

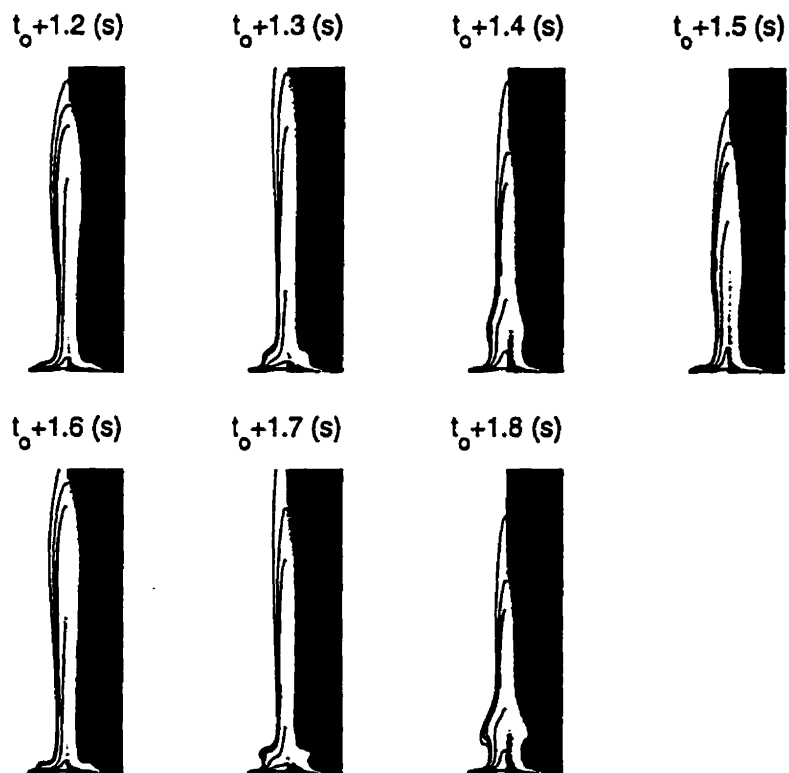


Figure 6.5: Temperature contours for case 1 in Table 6.1. Contour lines represent  $T = 700, 1000, 1400$  and  $1700$  (K).

### 6.3 Transient Fire Simulation

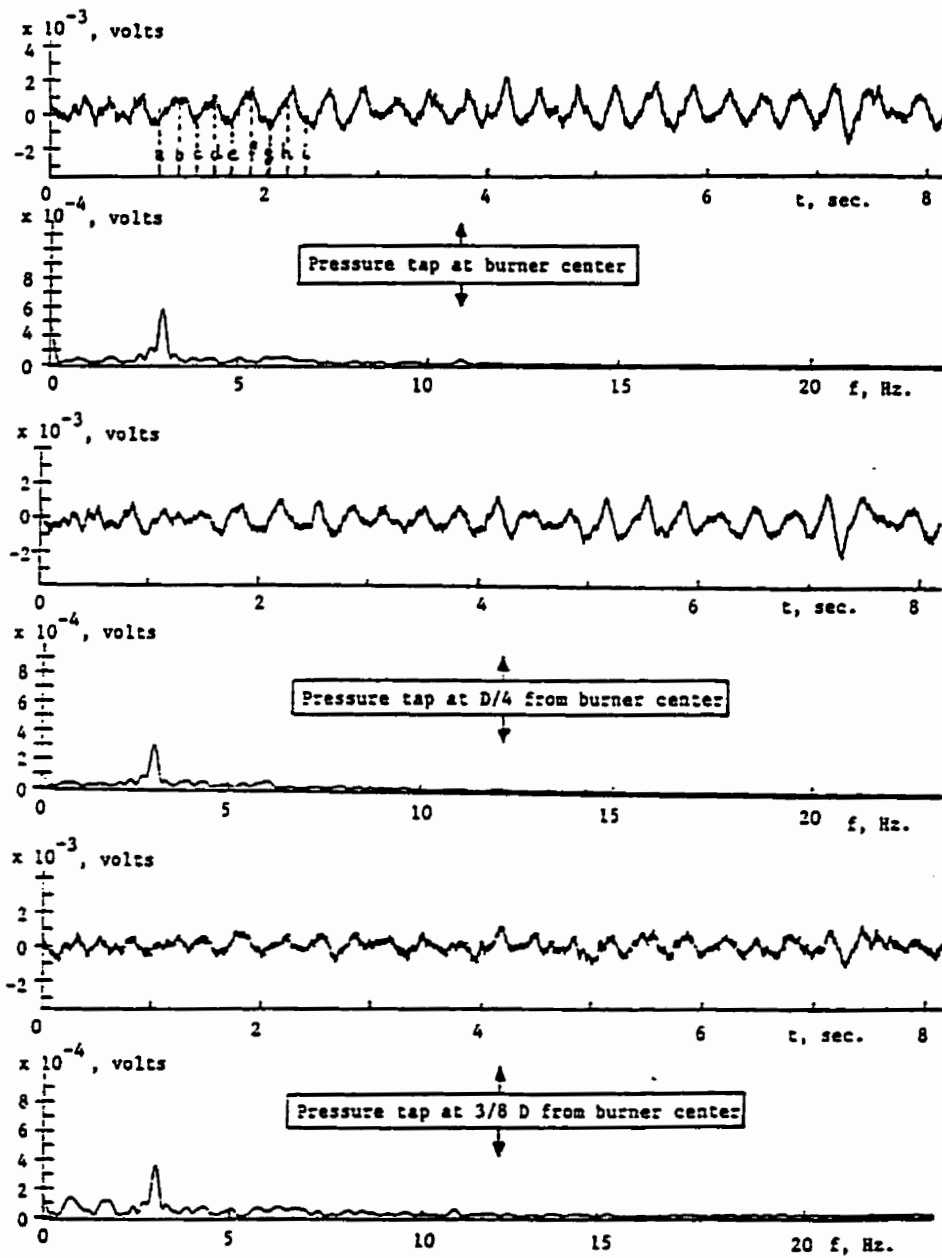


Figure 6.6: Burner surface pressure and frequency spectra for a 60 kW propane flame on a 30-cm-diameter burner at three radial locations reported by Cetegen et al. in ([110])



### 6.3 Transient Fire Simulation

---

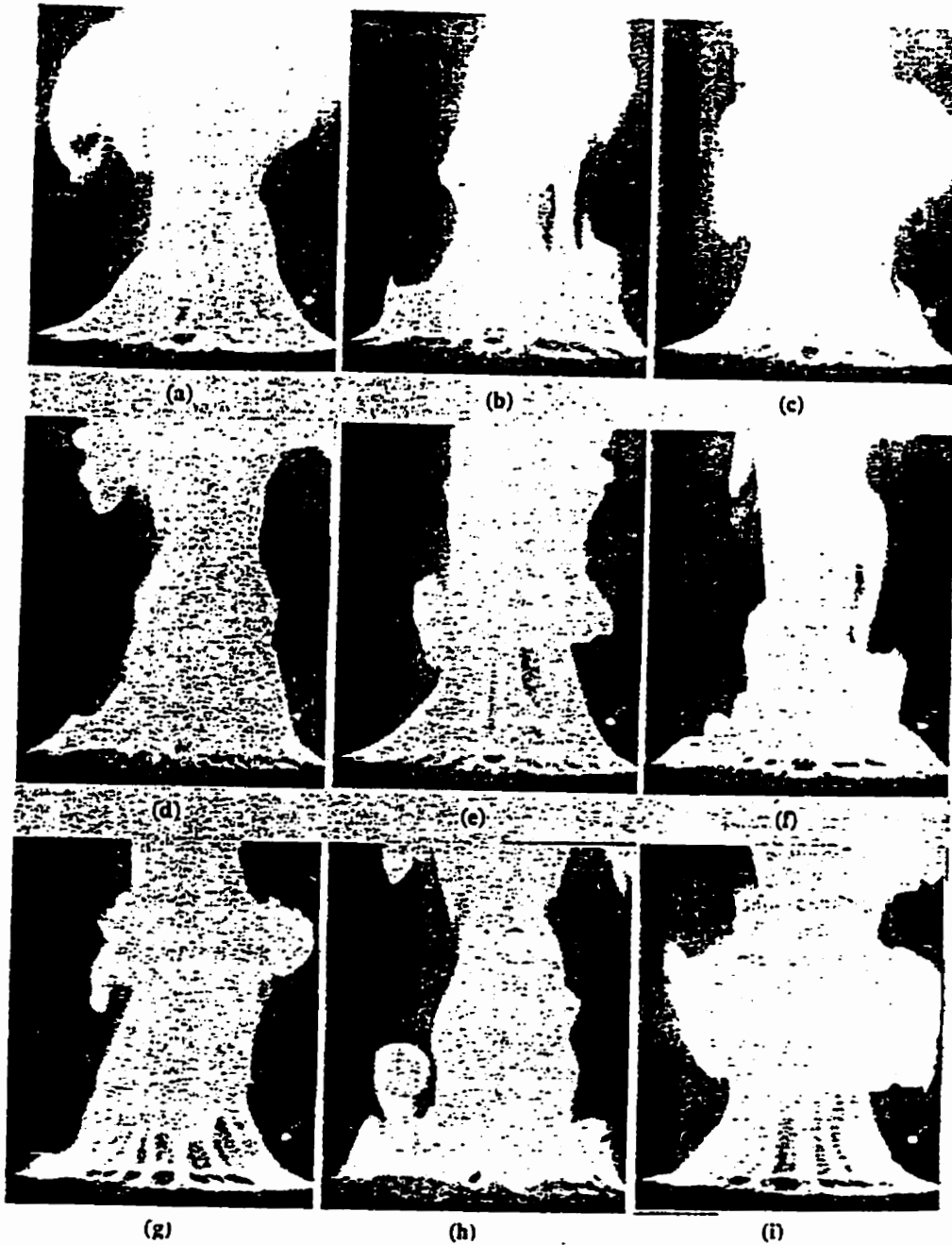


Figure 6.7: Time sequence photographs of a 60 kW propane flame on a 30-cm-diameter burner reported by Cetegen et al. in [110], the time interval between successive frames is  $1/6$  s

### 6.3 Transient Fire Simulation

---

discussed in Chapter 7; however, it should be mentioned here that the use of variable  $C_p$  and  $C_\mu$  does not cause any noticeable change in either the sequence of the fire pulsation or in its frequency, as shown by comparison of cases 1 and 4 in Table 6.1. Therefore, the results and discussions presented in this chapter are equally valid irrespective of the choices for  $C_p$  and  $C_\mu$ .

The predicted frequencies in Table 6.1 are calculated based on the frequency of the oscillating pressure field. They are in very good agreement with experimental data from fires with the same burner size. The curve fit suggested by Pagni [103] yields  $f = 2.7$  Hz for  $D = 30$  cm and other experimental data [27, 110] suggest  $f \approx 3.0$  for pool fires over 30 cm burners. Neither changes in the total heat release,  $Q$ , (case 2) nor temporal refinement in the numerical simulation (case 3 and 9) seemed to alter the predicted puffing frequency by a significant amount. Cases 4 to 7 indicate the effects of domain size on predicted results. Extending the computational domain width and height by as much as 50% , case 7, shows almost no change in the predicted puffing frequency. The slight change in the predicted frequencies for cases 5 and 6 could be attributed to the accompanying change in the spatial grid resolution, though no reason for this is immediately evident. Plots in Figures 6.8 through 6.16 support the similarity in flow development for the various cases in Table 6.1.

To examine the effect of grid resolution and also to obtain a better picture of the puffing cycle, a finer grid with  $72 \times 112$  nodes has been used, see the specifications for case 8 and 9 in Table 6.1. The predicted periodic formation of large scale structures is clearly shown in Figures 6.15 and 6.16 for case 8 and is consistent with that observed for other cases listed in Table 6.1;

### 6.3 Transient Fire Simulation

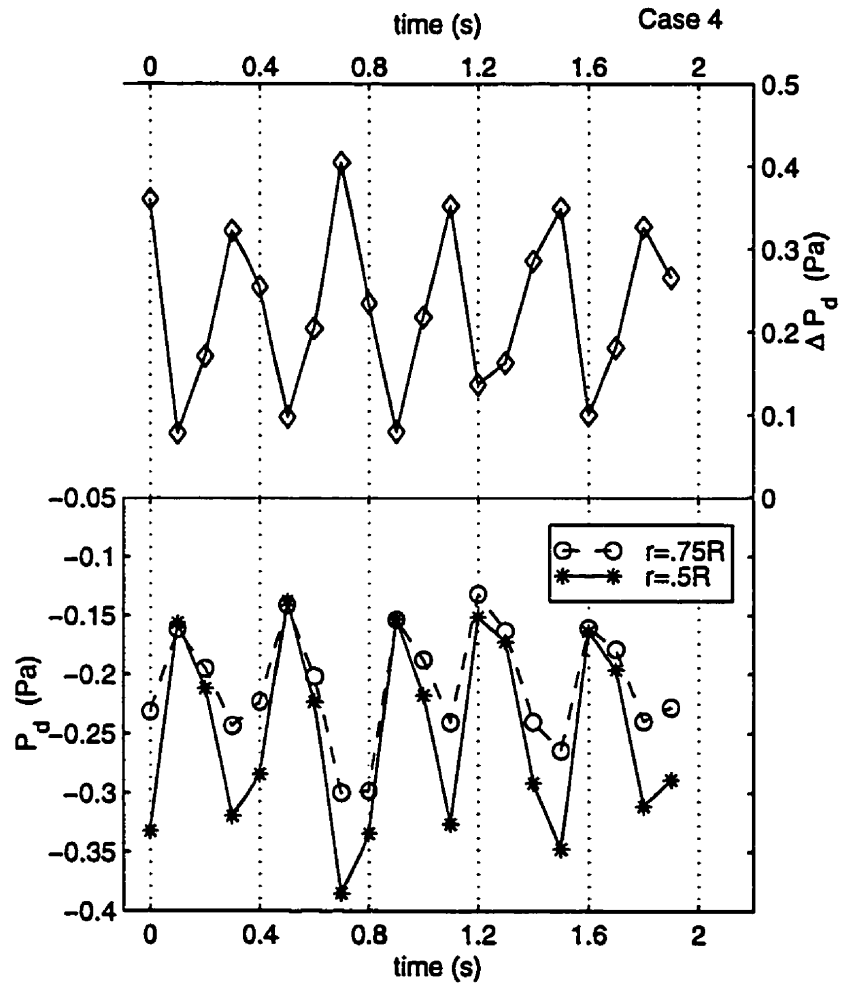


Figure 6.8: Pressure variation in time at the burner surface for case 4 in Table 6.1. The lower plot shows the burner surface pressure,  $P_d$ , at two radial locations and the upper plot shows the pressure difference across the burner radius,  $\Delta P_d = P_{drim} - P_{ddl}$

### 6.3 Transient Fire Simulation

---

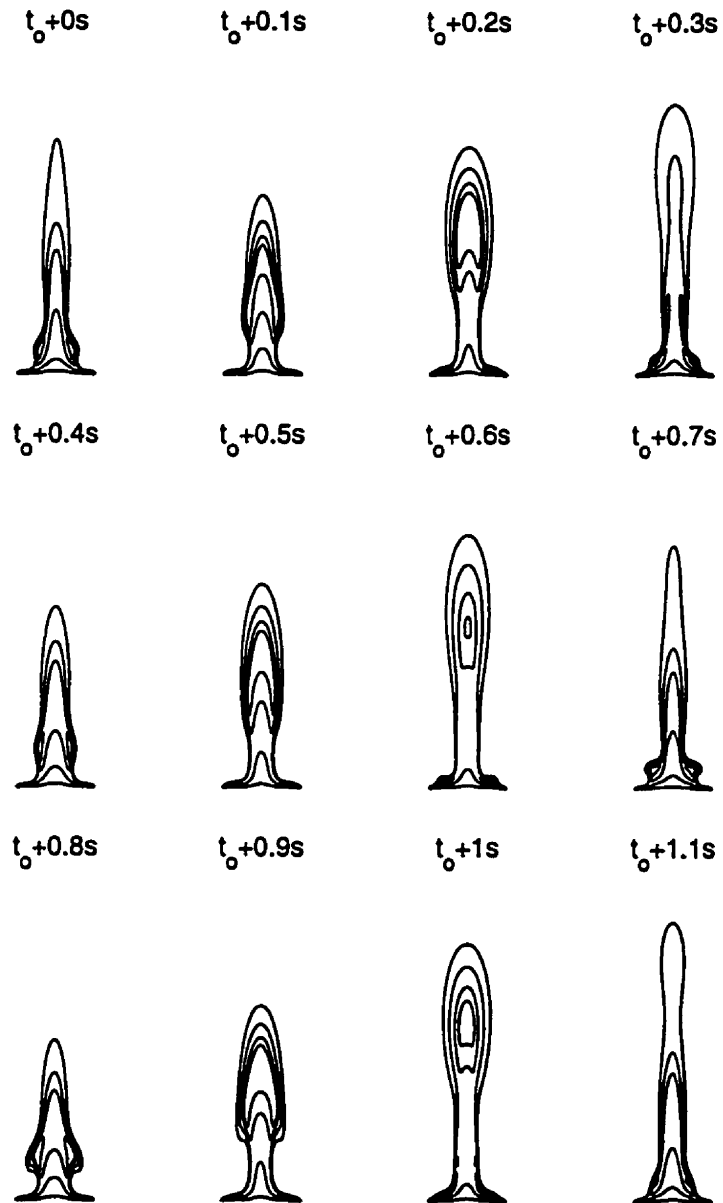


Figure 6.9: Temperature contours for case 4 in Table 6.1 at different times. Contour lines represent  $T = 700, 1000, 1400$  and  $1700$  (K).

### 6.3 Transient Fire Simulation

---

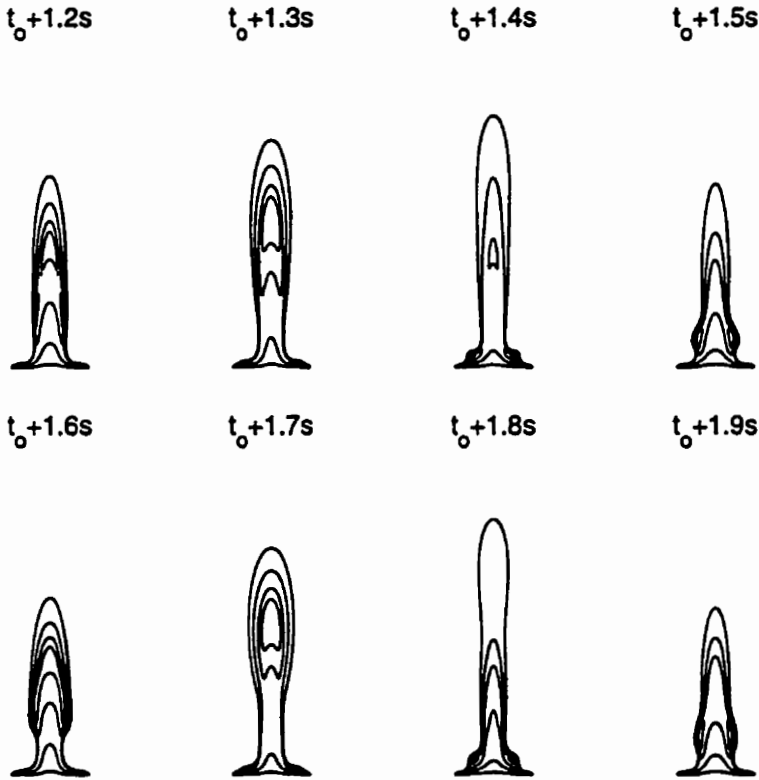


Figure 6.10: Predicted temperature field for case 4 in Table 6.1 at different times. Contour lines represent  $T = 700, 1000, 1400$  and  $1700$  (K).



### 6.3 Transient Fire Simulation

---

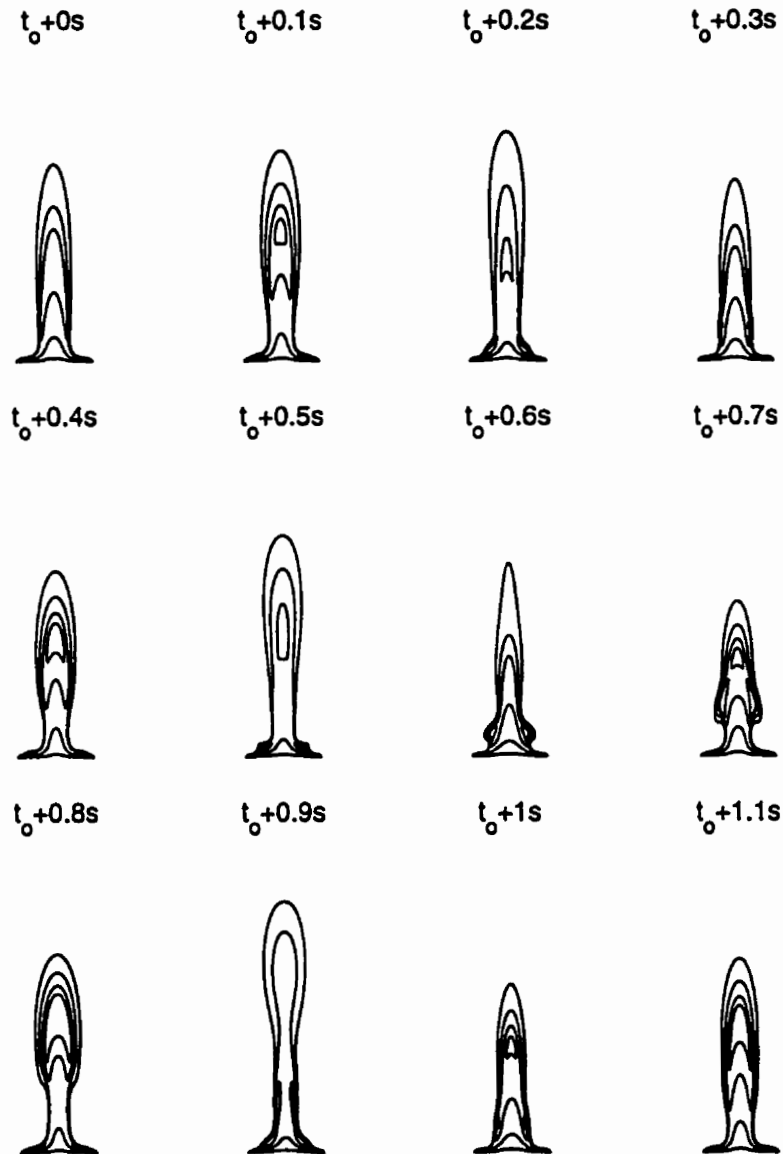


Figure 6.12: Temperature contours for case 7 in Table 6.1 at different times. Contour lines represent  $T = 700, 1000, 1400$  and  $1700$  (K).

### 6.3 Transient Fire Simulation

---

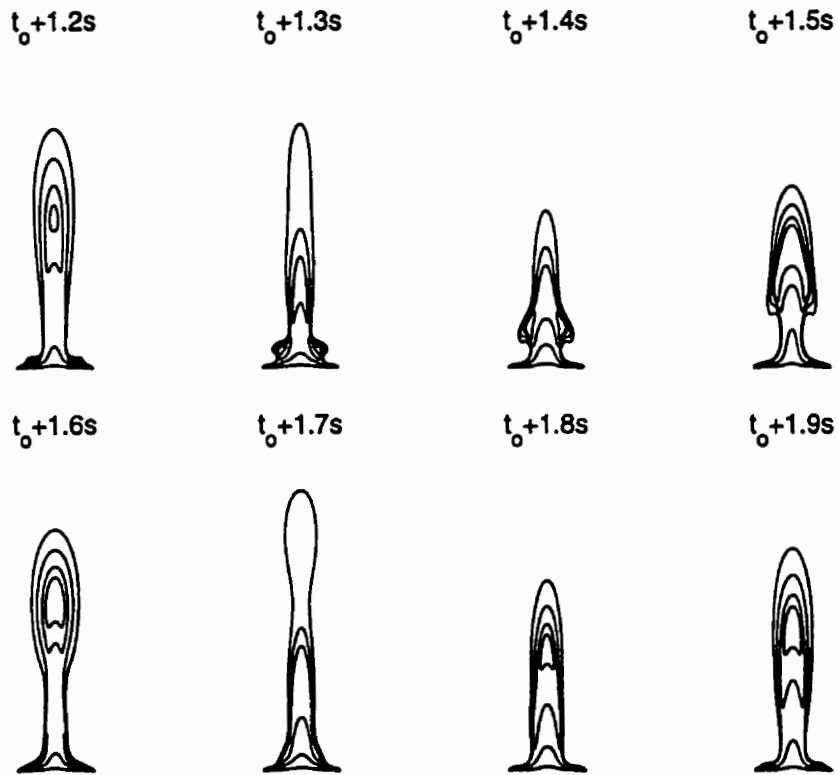


Figure 6.13: Predicted temperature field for case 7 in Table 6.1 at different times. Contour lines represent  $T = 700, 1000, 1400$  and  $1700$  (K).



### 6.3 Transient Fire Simulation

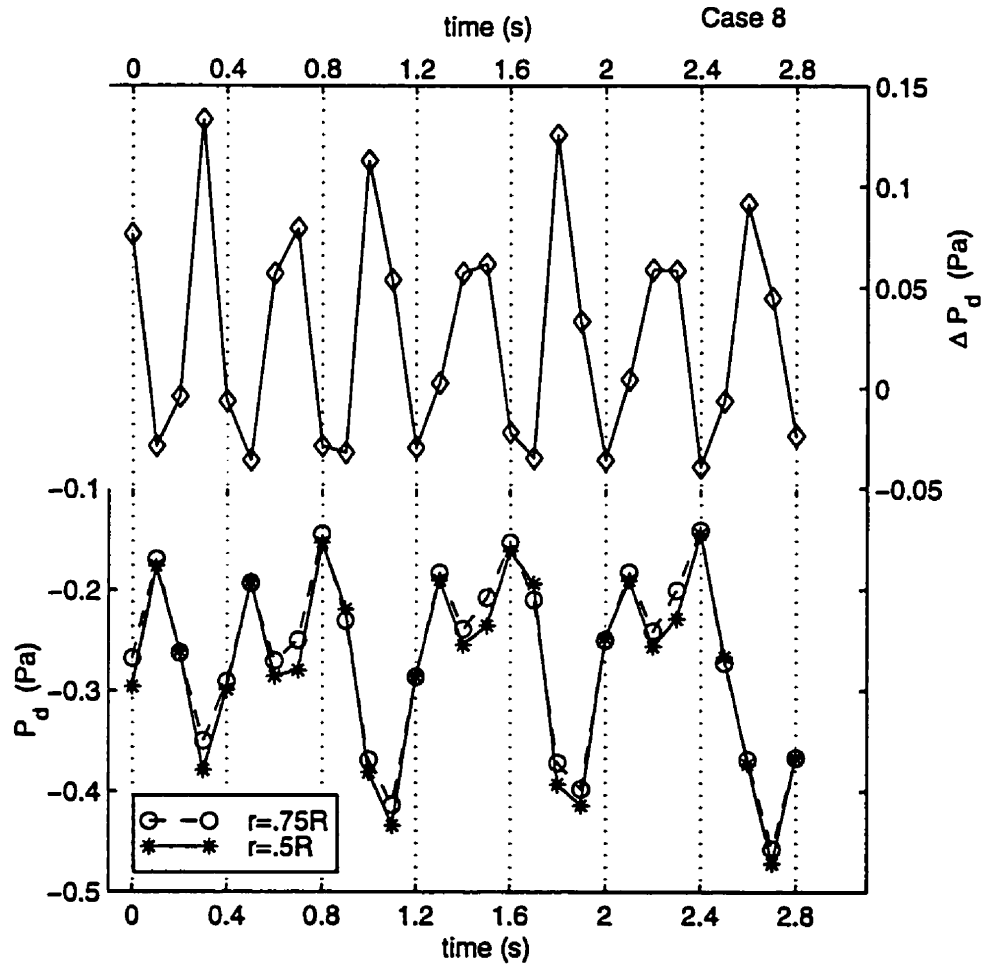


Figure 6.14: Pressure variation in time at the burner surface for case 8 in Table 6.1. The lower plot shows the burner surface pressure,  $P_d$ , at two radial locations and the upper plot shows the pressure difference across the burner radius,  $\Delta P_d = P_{drim} - P_{dcl}$

6.3 Transient Fire Simulation

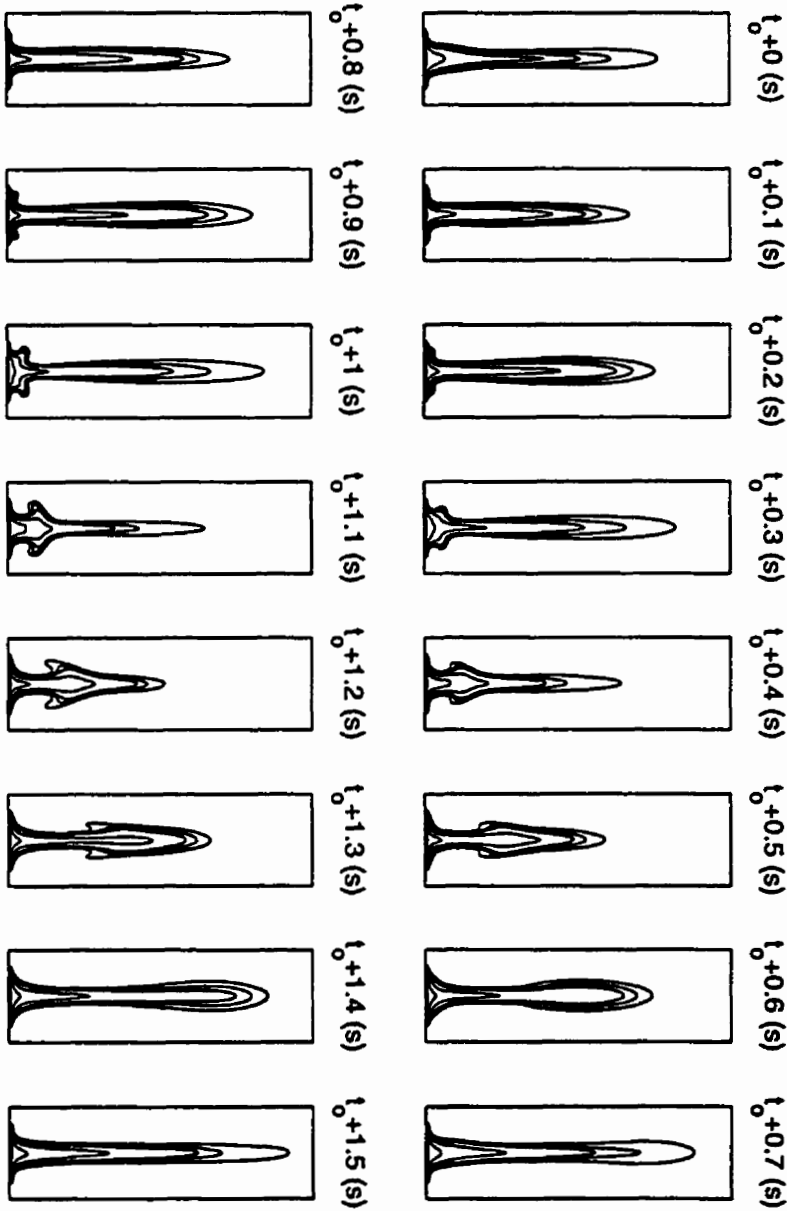


Figure 6.15: Temperature contours for case 8 in Table 6.1 at different times. Contour lines represent  $T = 700, 1000, 1400$  and  $1700$  (K).

6.3 Transient Fire Simulation

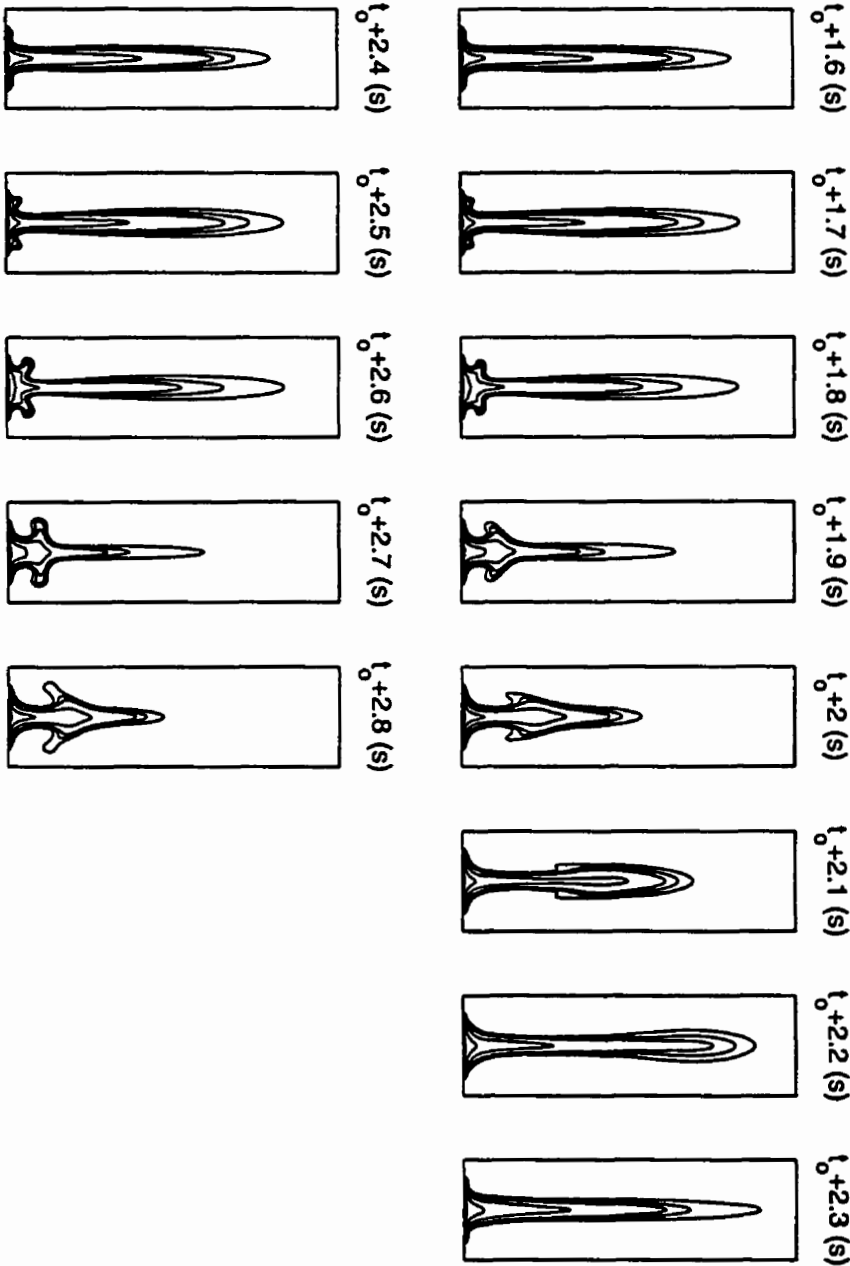


Figure 6.16: Predicted temperature field for case 8 in Table 6.1 at different times. Contour lines represent  $T = 700, 1000, 1400$  and  $1700$  (K).

### 6.3 Transient Fire Simulation

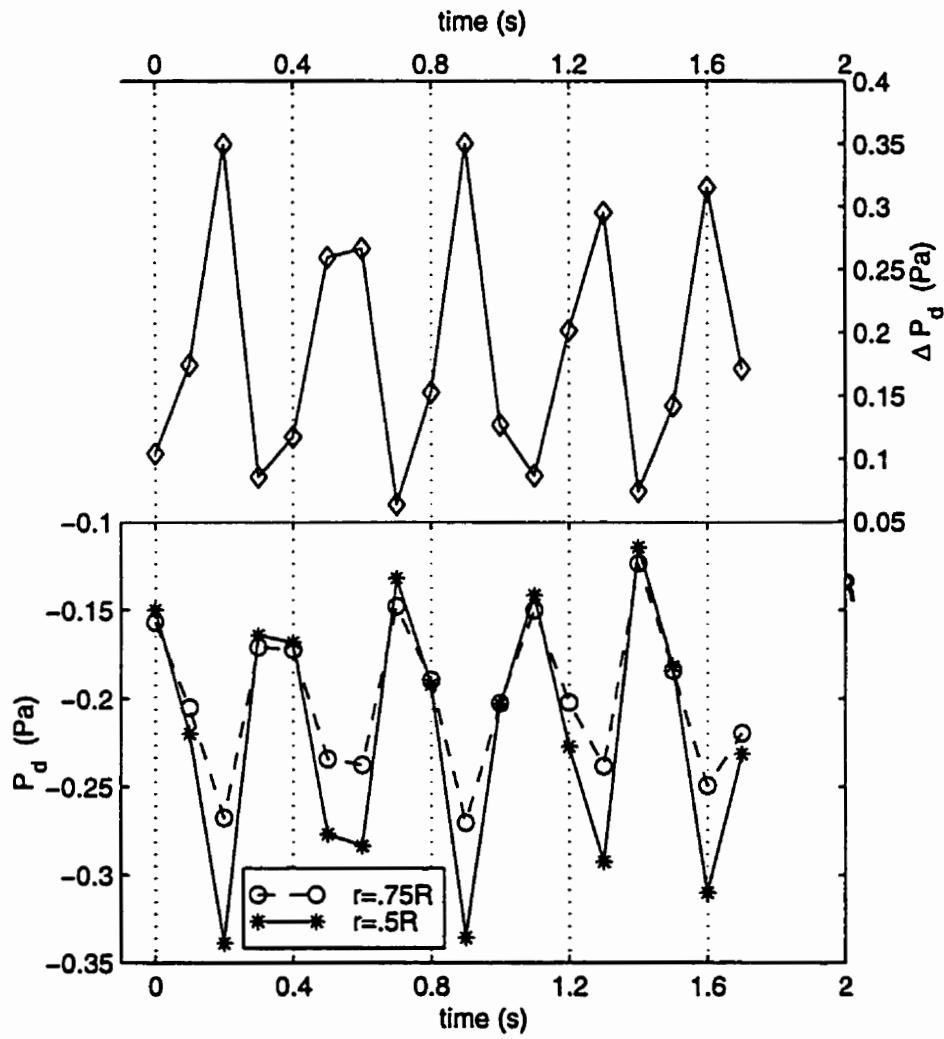


Figure 6.17: Pressure variation in time at the burner surface for case 2 in Table 6.1. The lower plot shows the burner surface pressure,  $P_d$ , at two radial locations and the upper plot shows the pressure difference across the burner radius,  $\Delta P_d = P_{drim} - P_{dcl}$

### 6.3 Transient Fire Simulation

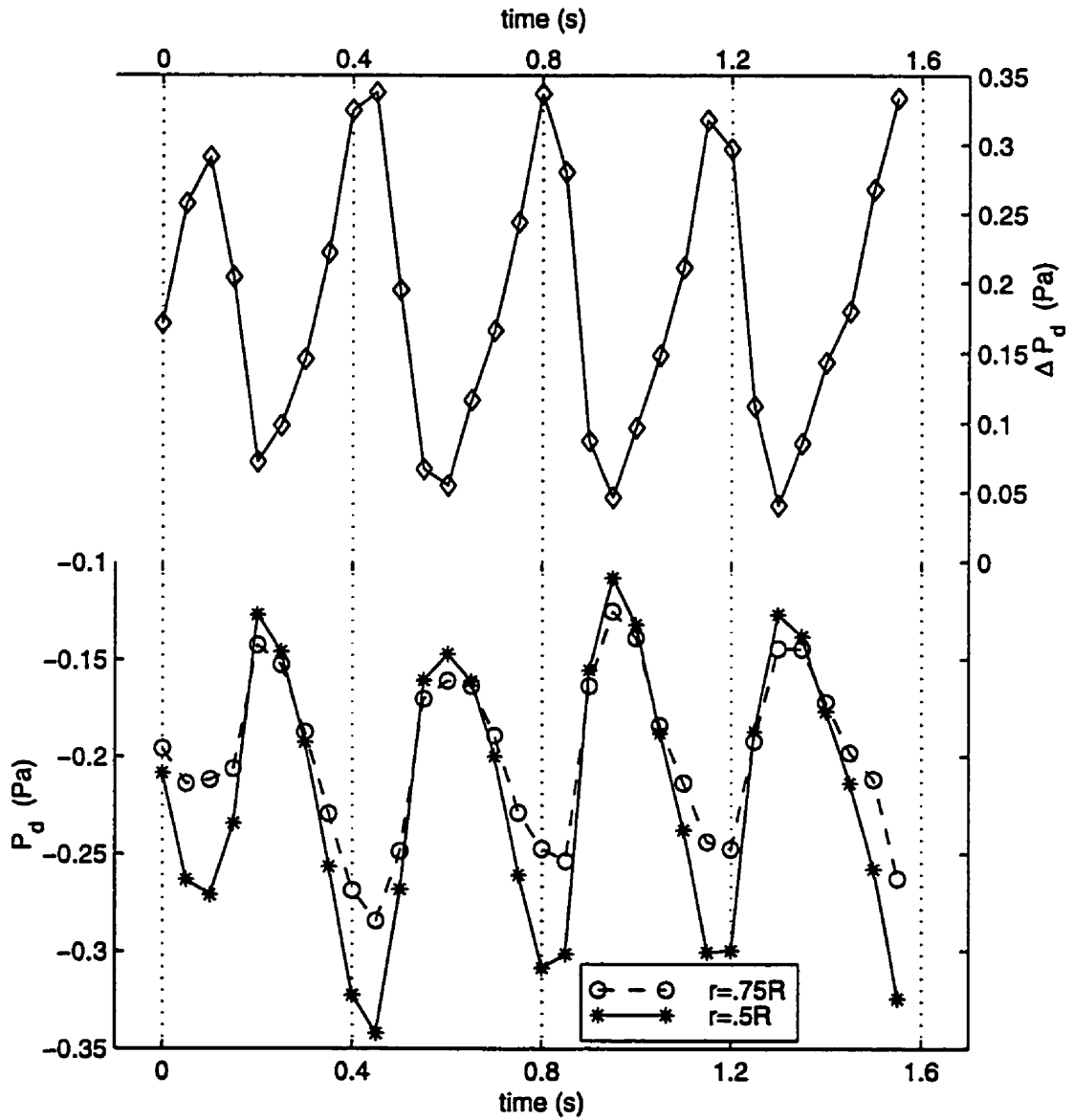


Figure 6.18: Pressure variation in time at the burner surface for case 3 in Table 6.1. The lower plot shows the burner surface pressure,  $P_d$ , at two radial locations and the upper plot shows the pressure difference across the burner radius,  $\Delta P_d = P_{d_{rim}} - P_{d_{cl}}$

### 6.3 Transient Fire Simulation

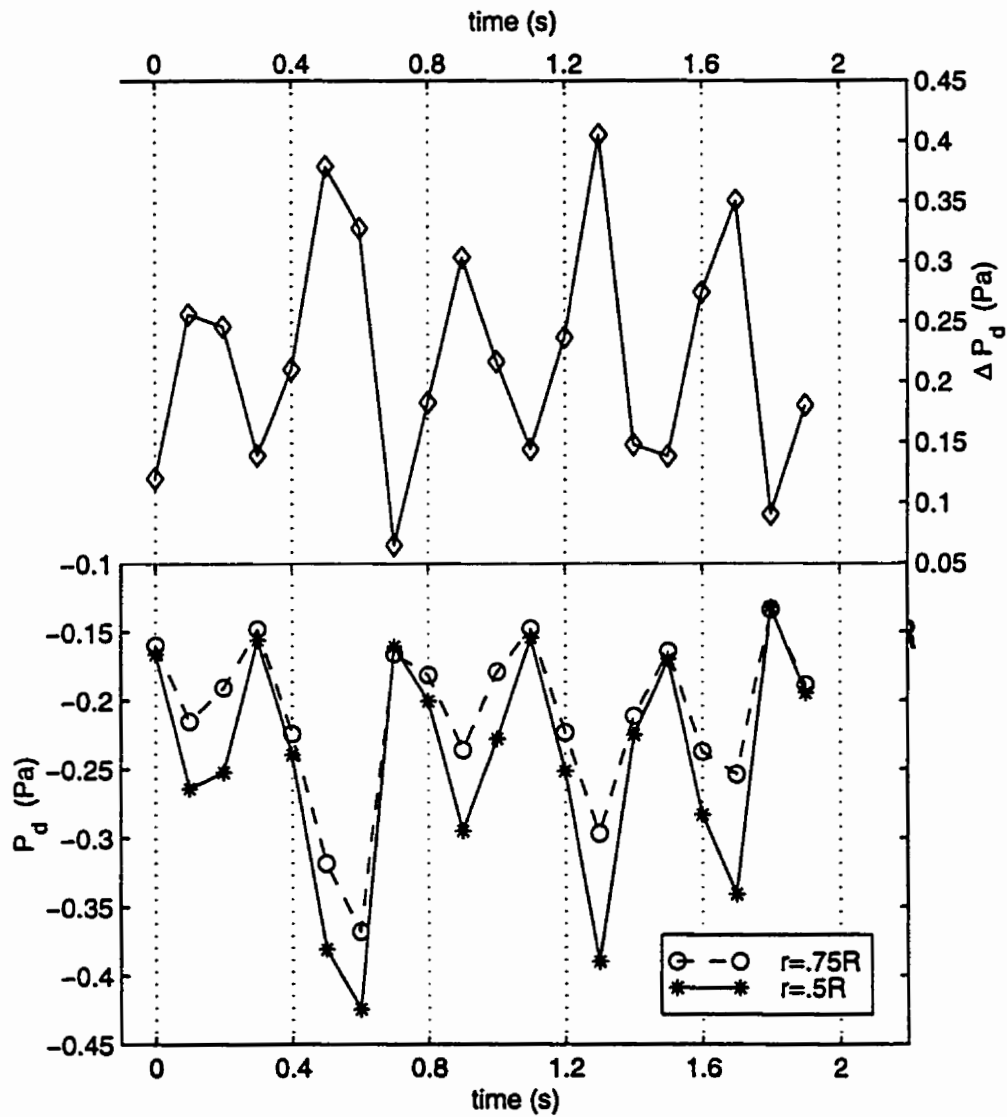


Figure 6.19: Pressure variation in time at the burner surface for case 5 in Table 6.1. The lower plot shows the burner surface pressure,  $P_d$ , at two radial locations and the upper plot shows the pressure difference across the burner radius,  $\Delta P_d = P_{d_{rim}} - P_{d_{cl}}$

### 6.3 Transient Fire Simulation

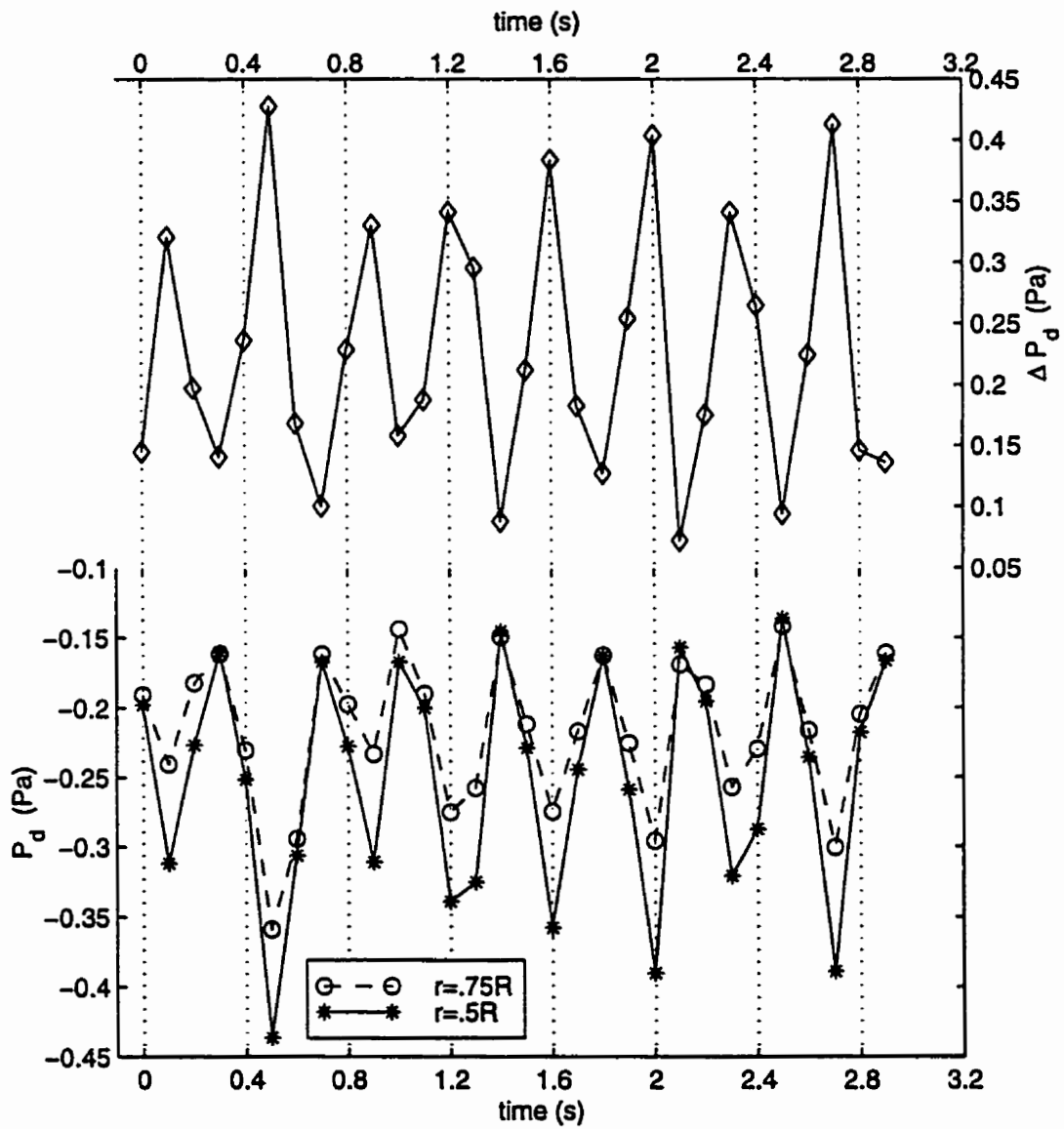


Figure 6.20: Pressure variation in time at the burner surface for case 6 in Table 6.1. The lower plot shows the burner surface pressure,  $P_d$ , at two radial locations and the upper plot shows the pressure difference across the burner radius,  $\Delta P_d = P_{d_{rim}} - P_{d_{cl}}$

### 6.3 Transient Fire Simulation

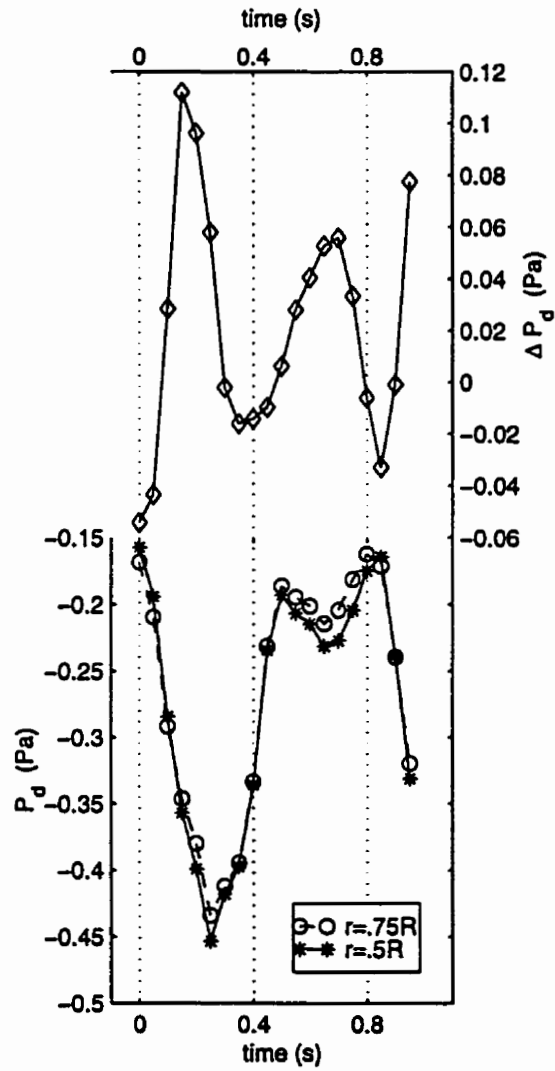


Figure 6.21: Pressure variation in time at the burner surface for case 9 in Table 6.1. The lower plot shows the burner surface pressure,  $P_d$ , at two radial locations and the upper plot shows the pressure difference across the burner radius,  $\Delta P_d = P_{d_{rim}} - P_{d_{cl}}$



## 6.4 Details of the Puffing Mechanism

---

however, the predicted vortical structures are now stronger and much more pronounced, as would be expected with improved spatial resolution.

Overall, the predicted sequence of the fire pulsation is in excellent qualitative agreement with experimental observations and the present transient results suggest that a quantitative insight into the puffing mechanism in pool fires is possible using the present fire model.

## 6.4 Details of the Puffing Mechanism

The transient results shown in the previous section indicate consistent synchronized oscillations in pressure and temperature fields of a 30 cm-diameter propane fire. A close look at these results reveals that at the very beginning of the formation of a large scale structure, which can be detected through examination of the temperature contours and velocity vectors close to the burner rim, the burner surface pressure reaches its maximum value, which corresponds to a minimum pressure difference across the burner radius,  $\Delta P_d$ . For instance, the peak pressures in Figure 6.3 correspond to temperature contours at  $t_o + 0$ ,  $t_o + 0.4$ ,  $t_o + 0.8$ ,  $t_o + 1.2$  and  $t_o + 1.6$  in Figures 6.4 and 6.5, or for the finer grid of case 8 in Table 6.1, the peak pressures in Figure 6.14 correspond to temperature contour plots at  $t_o + 0.1$ ,  $t_o + 0.5$ ,  $t_o + 0.8$ ,  $t_o + 1.3$ ,  $t_o + 1.6$ ,  $t_o + 2.1$  and  $t_o + 2.4$  in Figures 6.15 and 6.16. The quoted temperature contour plots indicate that these peak pressures occur at an early stage of the formation of a vortical structure near the burner rim. The observed connection between the pressure oscillations and the formation of vortical structures agrees very well with the experimental observations of

## 6.4 Details of the Puffing Mechanism

---

Cetegen et al. [110] shown in Figures 6.6 and 6.7.

Although the results obtained for all cases in Table 6.1 present the same sequence for the puffing phenomenon, the results of case 9 are used in this section to describe the details of the fire pulsation. This is due to the high temporal and spatial resolution used in the computations for this case. Figure 6.22 shows a closer look at a complete puffing cycle of the fire. It shows the corresponding vector plots of the region close to the burner rim where a buoyant instability causes a vortical structure to form. As shown in this figure, the vortical structure which forms near the burner rim (b) grows within one diameter above the burner, moves upward (c) and finally disappears at a height approximately two to three diameters above the burner.

The existence of a periodic fire pulsation in the present transient results and consideration of the fact that the present model is based on a combustion submodel which assumes an infinitely fast one step reaction and essentially overlooks the details of the chemical kinetics, suggest that the cause of the fire pulsation must stem from a fluid dynamic or buoyant flow instability rather than a combustion related phenomenon such as the propagation of a premixed flame through a flammable mixture extending from the burner rim to the center of the fire [53]. The presence of similar, although weaker, puffing behavior in non-reacting buoyant plumes, as well as the strong dependency of the fire pulsation frequency on the burner size rather than the fuel type, further support this argument for the cause of the fire pulsation.

Details of the stages which occur during the formation of large-scale structures in the fire are best illustrated through subplots (a) to (g) shown in Figures 6.23 and 6.24, which show simultaneous plots of velocity vectors,

## 6.4 Details of the Puffing Mechanism

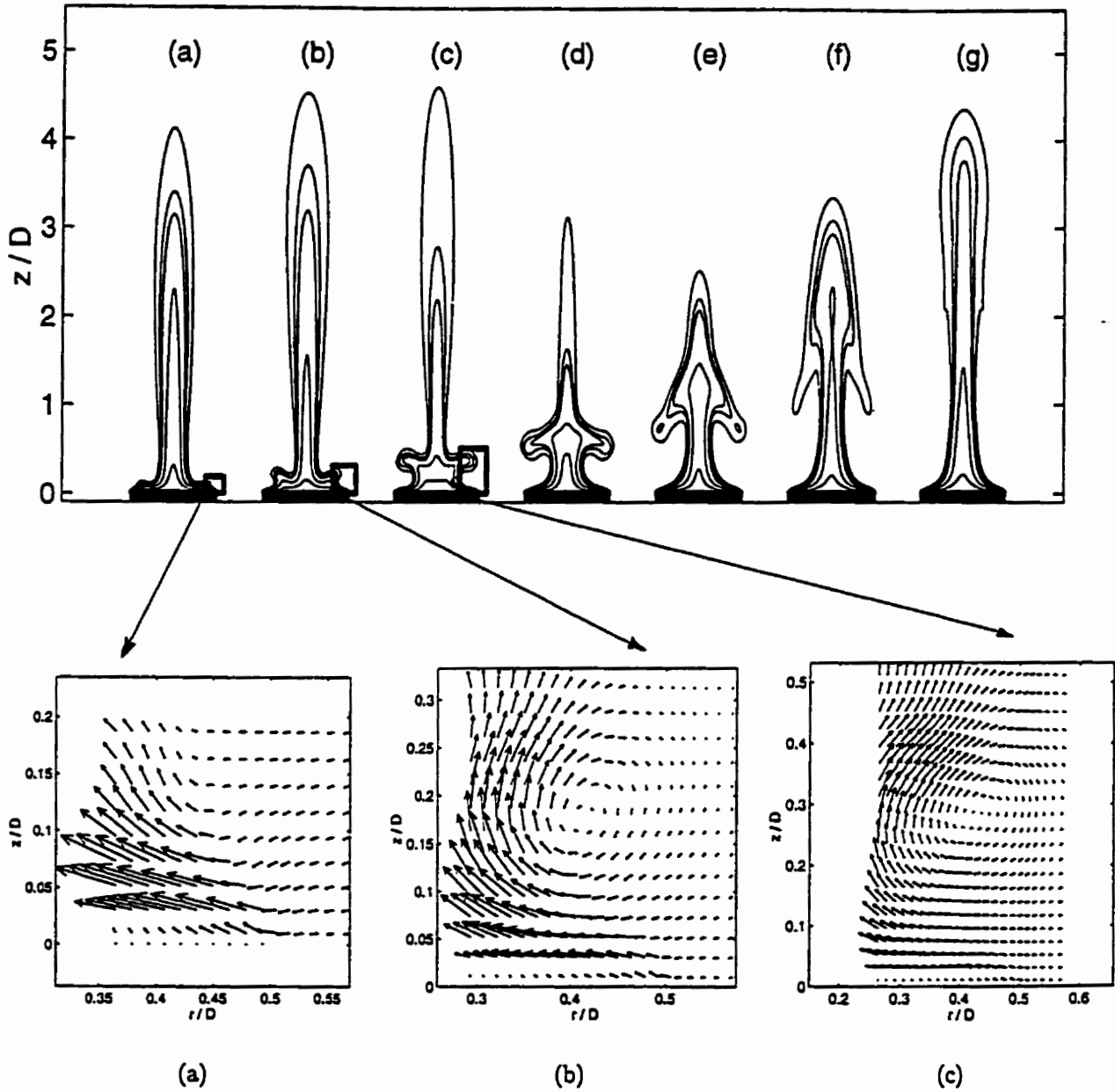


Figure 6.22: Temperature contours and velocity vector plots during a typical cycle of the fire pulsation.

## 6.4 Details of the Puffing Mechanism

---

fuel reaction rate contours and shaded maps of the temperature field in the vicinity of the burner rim. Figure 6.23-a and 6.23-b show that the flow is oriented mainly in the radial inward direction close to the burner rim before a buoyant instability pushes the flow upward and raises the flame sheet with it, shown in Figures 6.23-c and 6.23-d. It should be noted that Figure 6.23-c corresponds to the maximum predicted surface pressure at the burner surface. Therefore, the pressure force which drives the entrainment must be at its minimum strength at this instant.

The upward movement of hot gases and the reaction zone towards the fresh ambient air increases the buoyant forces and further extends the upward expansion of the buoyant instability, Figure 6.24-e. This instability reaches a point where the gas expansion is strong enough to overcome the incoming entrained air and push the flow outward as seen in Figure 6.24-f. The outward flowing hot gases mix with colder ambient air and recirculate to join the incoming entrained air at a lower height. This action produces a vortex close to the interface between the entrained air and the fuel stream, which is located outside the visible flame region. During the formation of the vortical structure, the burner surface pressure decreases which translates to an increase in the pressure force which in turn, drives the entrainment. The increased inward pressure force along with the induced velocity due to the vortex, cause the flame to neck inward behind the vortical structure, as shown in Figures 6.24-f and 6.24-g.

The strong radial entrainment behind the vortical structure tends to contract the buoyant effect in the region near the rim. As the vortex convects upwards, its effect on the gases in that region becomes less and less and with

## 6.4 Details of the Puffing Mechanism

---

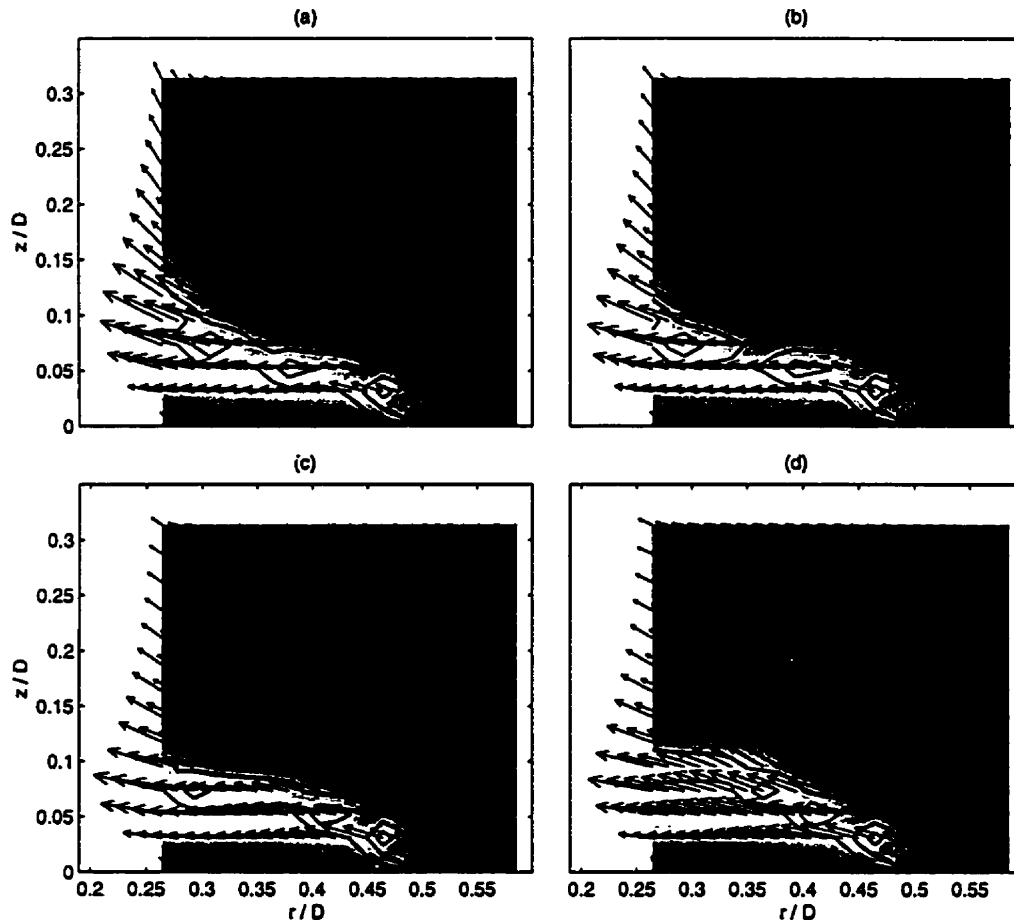


Figure 6.23: Simultaneous plots of velocity vectors, fuel reaction rate contours and shaded maps of the temperature field close to the burner rim of a 30 cm diameter propane fire. The time delay between the subplots is 0.05 (s)

## 6.4 Details of the Puffing Mechanism

---

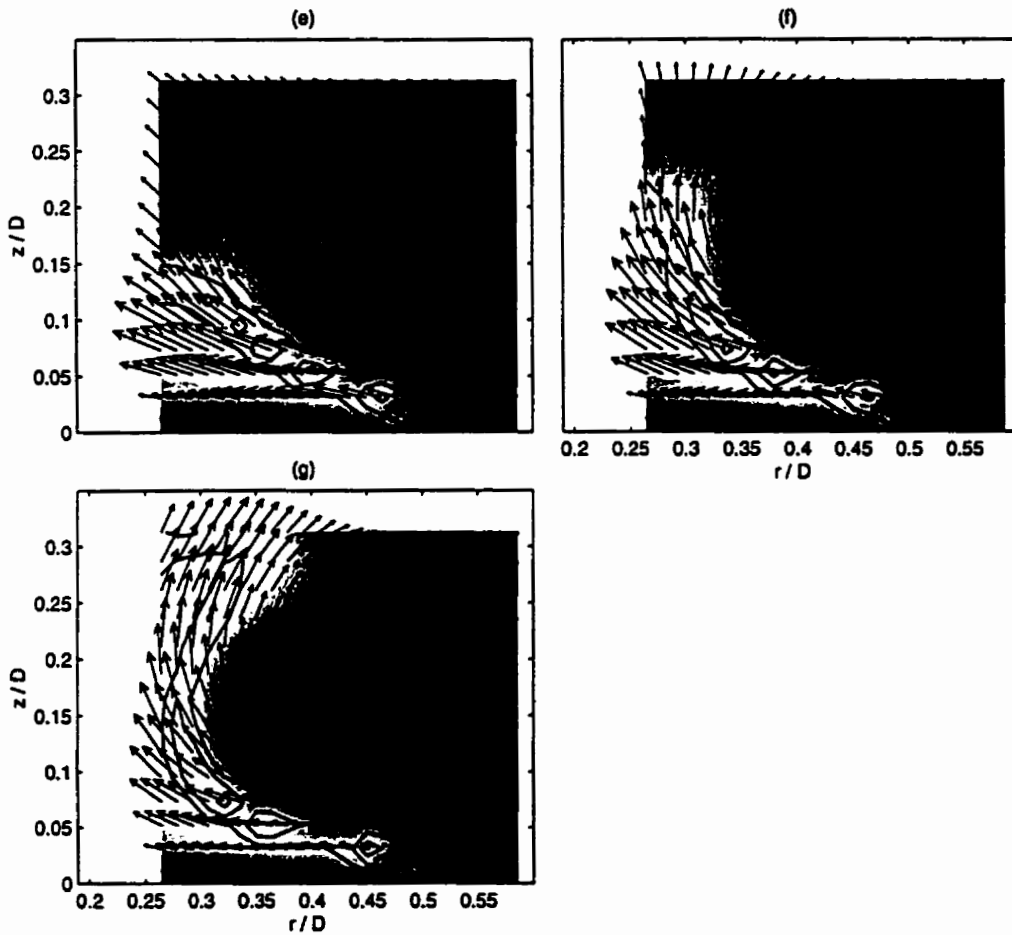


Figure 6.24: Simultaneous plots of velocity vectors, fuel reaction rate contours and shaded maps of the temperature field close to the burner rim of a 30 cm diameter propane fire. The time delay between the subplots is 0.05 (s)

## 6.4 Details of the Puffing Mechanism

---

an increase in the burner surface pressure, another buoyant instability finds a chance to initiate a new structure.

The present description of the fire puffing mechanism suggests that the fire pulsation is more the result of a fluid dynamic instability which interrupts the balance between pressure and buoyant forces close to the burner rim. This instability initiates a vortical structure which grows in size and convects upward due to buoyancy until it disappears at some distance above the fire source. Since the present description of the puffing mechanism is based upon a fluid dynamic instability, it is consistent with experimental observation of the puffing phenomenon in non-reacting buoyant plumes and therefore, equally applicable to such cases. However, the observed strength of the pulsation is higher in reacting flows. Experimental data [110] shows that the puffing intensity is always stronger in fires. This has been attributed to the strength of buoyancy in the fires [110]. The present numerical results show that the more pronounced puffing in fires is not only due to the strength of buoyancy but also due to oscillations in highly reacting zones as well. As shown in Figure 6.23-b, a low reaction rate region appears in the contour plots of fuel reaction rate before a buoyant instability starts to interrupt the balance between the pressure and buoyant forces. This low reaction rate region disappears in Figure 6.23-c where the very first indication of a buoyant instability shows up. The movement of the higher reaction rate zone, which conforms with the interior side of the vortical structure, Figures 6.24-d to g, further increases the buoyancy along one side of the vortical structure as it forms. This is the mechanism which increases the puffing intensity in fires as compared to non-reacting plumes in which the strength of buoyancy dies

## 6.4 Details of the Puffing Mechanism

---

out as the flow convects upward.

The unique transient results shown in this Chapter have clearly demonstrated the capability of the present elliptic fire model in simulating the complicated phenomenon of fire pulsation. The qualitative agreement between numerical results and experimental data is very promising and the predicted frequency for a 30-cm-diameter propane fire agrees very well with the reported values in the literature. In addition, the present transient numerical results have led to a detailed description of the mechanisms involved in the puffing phenomenon and provided new evidence to determine the morphology of the fire pulsation.

In the next chapter, the quantitative accuracy of the present fire model results are discussed further. Moreover, some new modifications, which are based on an analysis of the University of Waterloo pool fire data base, will be introduced and their effects on the overall accuracy of the results will be presented.



# Chapter 7

## The Modified Fire Model

### 7.1 Introduction

Pool fires represent one of the more important complex physical problems of practical interest and it is therefore not unexpected that the solution of their mathematical/theoretical representation should give rise to a large number of modeling and discretization issues. Some of these issues have been identified in previous chapters and it is the purpose of this chapter to report on progress in addressing some of the more important issues which affect the quantitative accuracy of the numerical predictions of fire flow field behavior.

In particular, an examination of the extensive in-house data base taken from methanol pool fires can be used to assess implications regarding the assumption of constant  $C_\mu$  and turbulent Schmidt number,  $\sigma_t$ , in a fire model. Virtually all existing numerical models, including our base case, make these assumptions.

In addition, two of the modeling issues arising from the time averaging

## **7.2 The Methanol Pool Fire**

---

process, namely, the inclusion of density fluctuations and the appropriateness of the buoyancy production term in the turbulence equations will be examined.

In summary, it will be shown that some of the proposed model improvements have significant effects on the accuracy of the results for engineering fire calculations. In addition, they are often more justifiable than previous assumptions from a purely physical perspective.

Many of the potential modeling and computational issues remain unresolved, but can not be resolved in this thesis which of necessity requires its own closure. Therefore, some of these will be identified as future work.

The aforesaid notwithstanding, the numerical solution of even the simplified model examined in this thesis requires considerable computer CPU effort, beyond that available to the writer at this University. Ultimately, the uncontested numerical prediction of pool fires will come when some future generation of computers can deal with Direct Numerical Simulation (DNS) of the instantaneous (unmodeled) equations of motion along with detailed chemical kinetics for the fuel-air reaction.

## **7.2 The Methanol Pool Fire**

In order to take advantage of the available data obtained from the University of Waterloo methanol pool fire [26], and assess the implications of some of the modeling assumptions encompassed in the present fire model, a series of computations has been carried out to predict the behavior of a 30 cm diameter methanol pool fire.

## 7.2 The Methanol Pool Fire

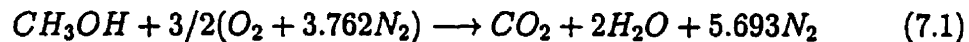
---

Table 7.1: Thermophysical properties of Methanol

|                                      |        |
|--------------------------------------|--------|
| Molecular weight, kg/kmole           | 32.043 |
| Heat of formation at 25 C, kcal/mole | -48.08 |
| Density at 25 C, kg/m <sup>3</sup>   | 795.77 |

The experimental facility consists of a 30.5-cm-diameter pan burner which is attached to a traversing mechanism and is moved to take the measurements at different locations inside and around the continuous flame zone. Details of the experimental apparatus and measurement techniques can be found in [26]. For the reported data in that reference, the methanol feed rate was held constant at 1.35  $cm^3/s$ .

According to the combustion submodel used here, methanol is assumed to react with standard air in a one step reaction mechanism.



The thermophysical properties of methanol which are used in the numerical simulations are given in Table 7.1.

### 7.2.1 Results of the Base Fire Model

The base fire model described in Section 3.9 is first used to simulate the methanol pool fire. The predicted results then serve as a reference solution to demonstrate certain shortcomings of the standard submodels used in the

## 7.2 The Methanol Pool Fire

---

base fire model. The computational domain for the methanol fire predictions is similar to the extended domain shown in Figure 5.2-b.

The boundary conditions used for this case, for the most part, are similar to those used for the axisymmetric propane fire in Chapter 5, except for the specified temperature at the burner exit which is assumed to be  $T_{\text{exit}} = 450$  C. With the specified exit temperature and the given methanol feed rate, the burner exit velocity becomes  $V_{\text{exit}} = 0.0164$  m/s. As discussed earlier in Section 5.4, the value of  $T_{\text{exit}}$  specified at the burner surface has little effect on the solution of the interior points and is mainly used to calculate a gas density at this boundary. Due to lack of experimental data for the radiation fraction heat loss,  $\chi$ , and knowing that the radiation heat loss for a methanol fire is less than that of a comparable propane fire, a 20% radiation heat loss is assumed for the methanol fire predictions.

Predicted centerline velocity and temperature distributions are compared with the experimental data in Figure 7.1. As shown in this figure, the calculated centerline velocity and temperature values are significantly over predicted. In addition, the radial spread of the temperature profiles generally is underpredicted as illustrated in Figure 7.2.

As will be discussed later, further grid refinement aggravated the discrepancy between the predictions and the experimental data and resulted in even higher centerline values and lower spread in radial profiles.

Similar discrepancies between numerical results and experimental data were observed in simulating the axisymmetric propane flame in Chapter 5 and have been reported by other researchers (see the review given in Section 1.4). Those who have used the parabolic formulation in their fire model

## 7.2 The Methanol Pool Fire

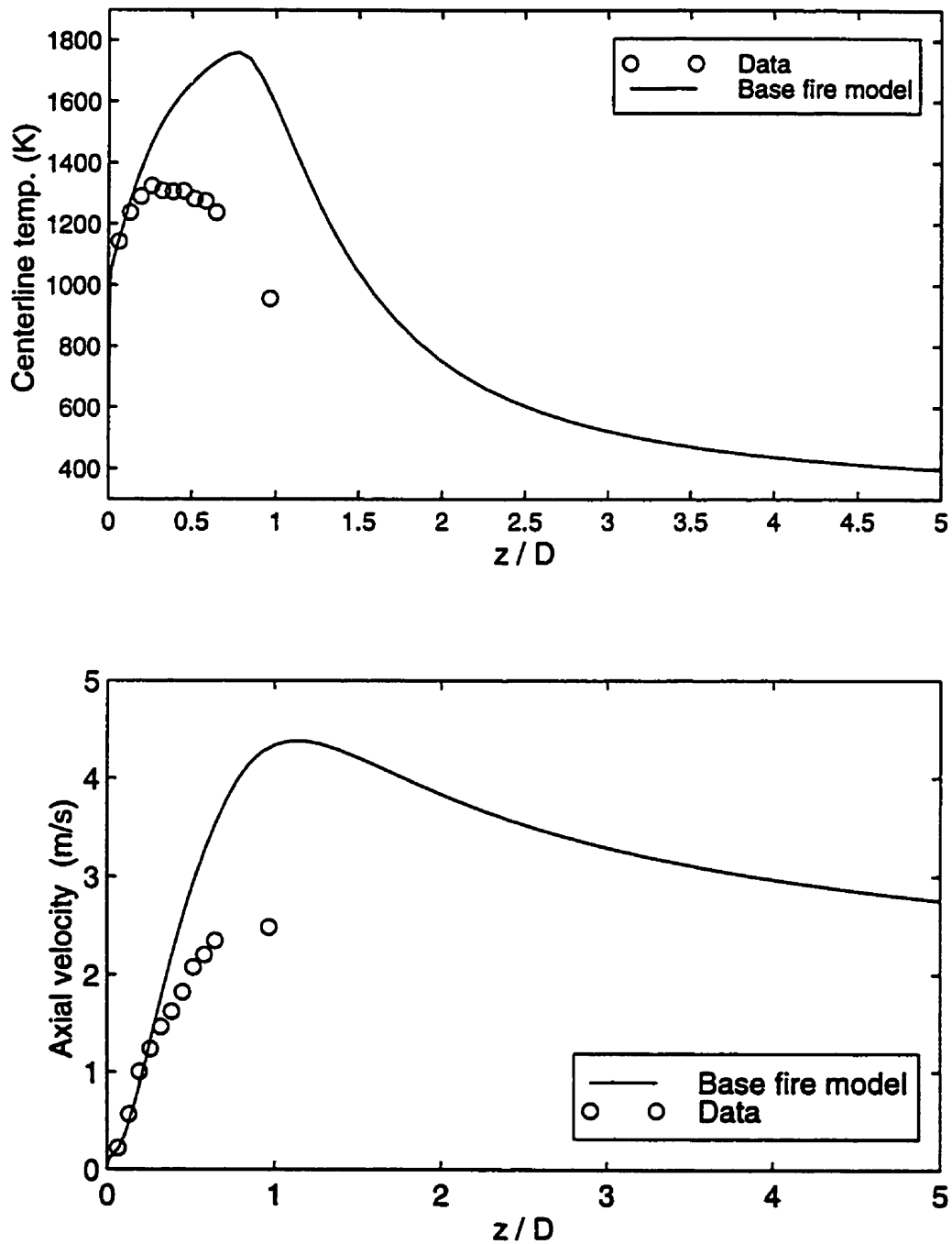


Figure 7.1: Centerline velocity and temperature distributions for the methanol fire and using the base fire model

## 7.2 The Methanol Pool Fire

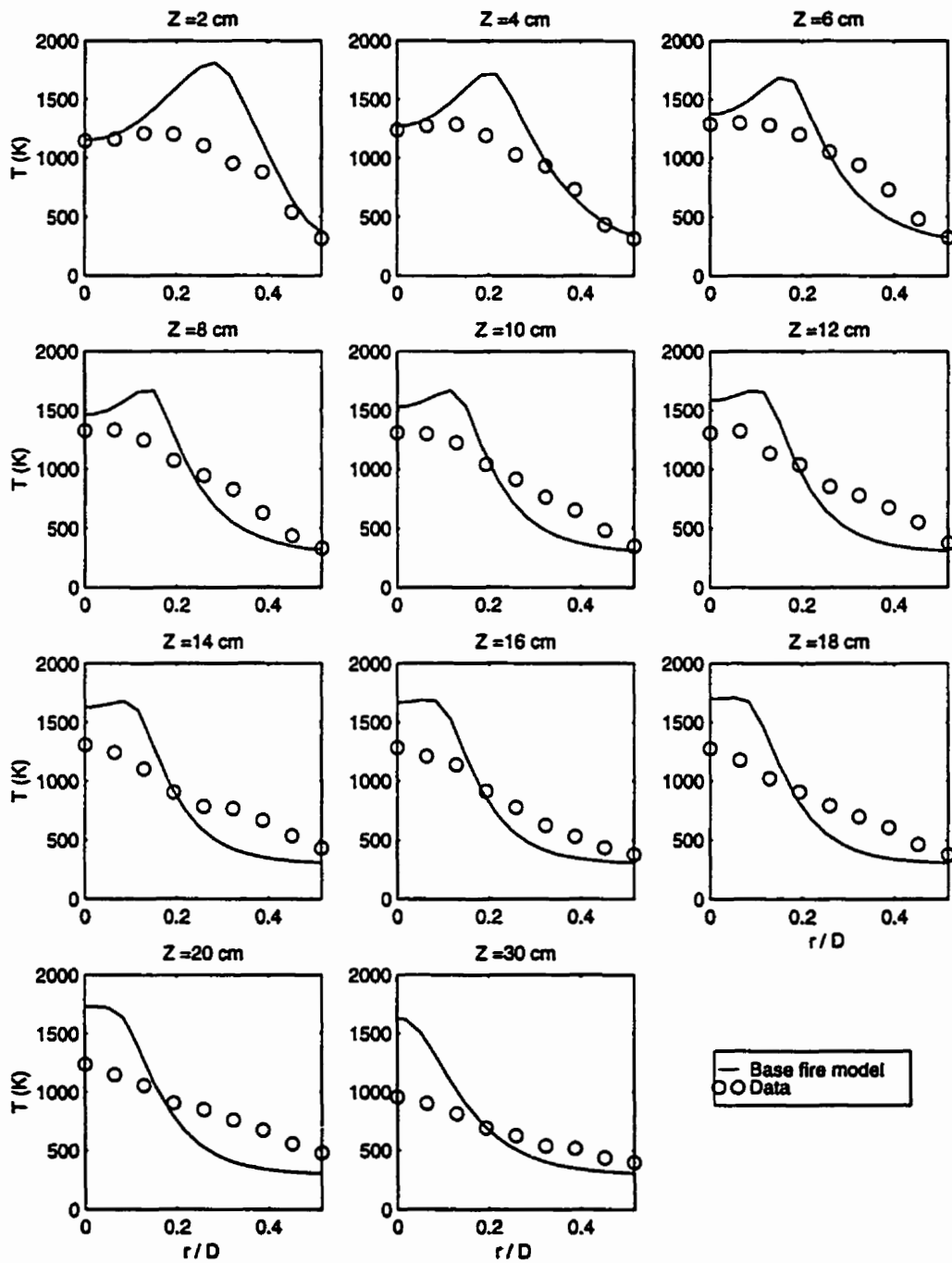


Figure 7.2: Radial profiles of temperature at different heights above the burner for the methanol fire and using the base fire model

## 7.2 The Methanol Pool Fire

---

have blamed the neglect of the elliptic nature of the fire in the near field region for the discrepancy between their predictions and experimental data [46, 47]. The present results, which are to the knowledge of the writer the only available elliptic solutions for the near field region of axisymmetric pool fires, clearly show that it is not the elliptic versus parabolic formulation of the model which causes the above mentioned discrepancies between numerical results and experimental data. Rather, the remedy should be sought in other assumptions involved in the fire model.

Both over prediction of the centerline quantities and underprediction of the fire spread imply that the overall rate of diffusion processes in the fire is underpredicted. The University of Waterloo pool fire data base was studied to obtain approximate values of the parameters which affect the diffusion rates. In particular, estimates for  $C_\mu$  and  $\sigma_t$ , which directly affect the turbulence fluxes, were considered.

Strong and Weckman have suggested that account should be made for variations in  $C_\mu$  based on its dependency on  $\frac{P_{uv}}{\epsilon}$  shown in Figure 7.3, where  $P_{uv}$  is the shear production of turbulent kinetic energy [114]. As indicated in the figure, the calculated values for  $C_\mu$  based on experimental data are generally higher than the standard value of 0.09 used in the  $k-\epsilon$  model formulation. Inclusion of a modified form of  $C_\mu$  into the standard model will increase the turbulent mixing process through diffusion, and as a result, may improve the predictions.

Figure 7.4 shows the distribution of  $\sigma_t$  for the methanol pool fire estimated using the experimental data [26]. These values for  $\sigma_t$  are generally lower than the standard value of 0.7 commonly used in numerical simulations.

## 7.2 The Methanol Pool Fire

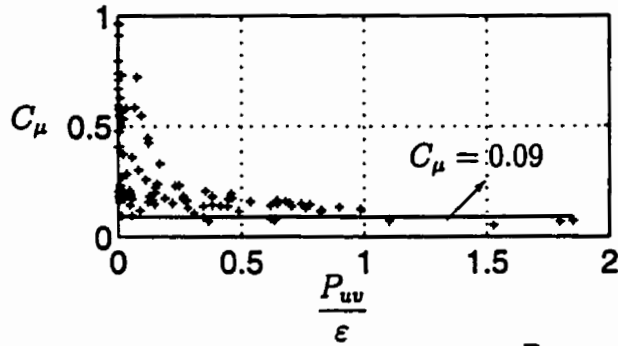


Figure 7.3: Variation of  $C_\mu$  versus  $\frac{P_{uv}}{\epsilon}$  for a methanol pool fire

Once again, inclusion of lower values of  $\sigma_t$  into the present base fire model is expected to improve the accuracy of the results.

Several attempts were made to incorporate into the model functional forms of  $C_\mu$  based on local values of  $\frac{P_{uv}}{\epsilon}$  [115]. In addition, use of constant values of  $C_\mu$  higher than the standard value of 0.09 were examined. However, no satisfactory results were obtained. Since the variation of  $C_\mu$  versus  $\frac{P_{uv}}{\epsilon}$  shown in Figure 7.3 suggests that at lower  $\frac{P_{uv}}{\epsilon}$  values  $C_\mu$  should be higher and it should approach an asymptotic value in the surrounding ambient, the following linear function for  $C_\mu$  is proposed in this thesis.

$$C_\mu = \text{MAX}\left(0.11, 0.3 - 0.19\frac{r}{R}\right) \quad (7.2)$$

where the MAX function takes the larger value of its two arguments. According to the proposed linear variation in Equation (7.2),  $C_\mu$  reaches a maximum value of 0.3 at the centerline where  $P_{uv}$  is zero and decreases linearly to 0.11 for regions where the radius,  $r$ , is greater than the burner radius,  $R$ .



## 7.2 The Methanol Pool Fire

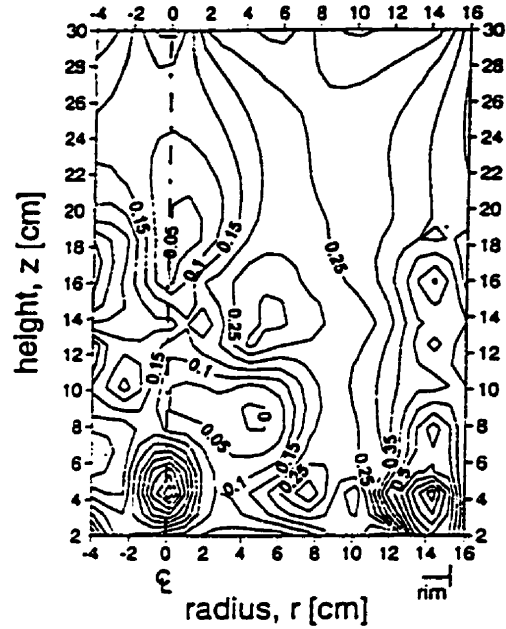


Figure 7.4: Contour plot of the distribution of turbulent Prandtl number throughout the methanol fire flow field

To account for the variation of  $\sigma_t$  shown in Figure 7.4, it is assumed that the turbulent Prandtl number decreases to a minimum of 0.1 where the local temperature is maximum and returns to its standard value of 0.7 if the local temperature is equal to the ambient temperature. That is turbulent Prandtl number is modeled as

$$\sigma_t = 0.7 - 0.6 \frac{T - T_{amb}}{T_{max} - T_{amb}} \quad (7.3)$$

## 7.3 Results of the Modified Fire Model

The proposed modifications for  $C_\mu$  and  $\sigma_t$ , Equations (7.2) and (7.3), discussed in the previous section are added to the base fire model. The Modified Fire Model (MFM) which includes the temperature dependency of  $C_p$ , the correlations involving  $\rho'$  and uses the higher order advection scheme is applied to simulate all three fires studied in this thesis (i.e., the rectangular and axisymmetric propane fires and the methanol fire). Selected results for each case along with a description of the numerical configurations used (i.e., specification of the grid, boundary conditions, steady state operating conditions, etc.) are given in the following subsections.

### 7.3.1 The Methanol Fire

The simulation results for the methanol fire using the modified fire model are shown in Figures 7.5 through 7.7.

The model constants  $\sigma_g$ ,  $C_{g1}$  and  $C_{g2}$  are chosen according to [38]. Model specifications are given in Tables 7.2 and 7.3, and grid III-a, described in Table 7.4, is used for these results.

Table 7.2: Operating conditions for the methanol pool fire

| $T_{amb}$ | $P_{amb}$ | $T_o$ | $\chi$ | fuel feed rate          |
|-----------|-----------|-------|--------|-------------------------|
| 25 C      | 101325 Pa | 450 C | 20%    | 1.35 cm <sup>3</sup> /s |

A comparison between the results plotted in Figures 7.5 to 7.7 show that the proposed modification for  $\sigma_t$  significantly affects the temperature field in

### 7.3 Results of the Modified Fire Model

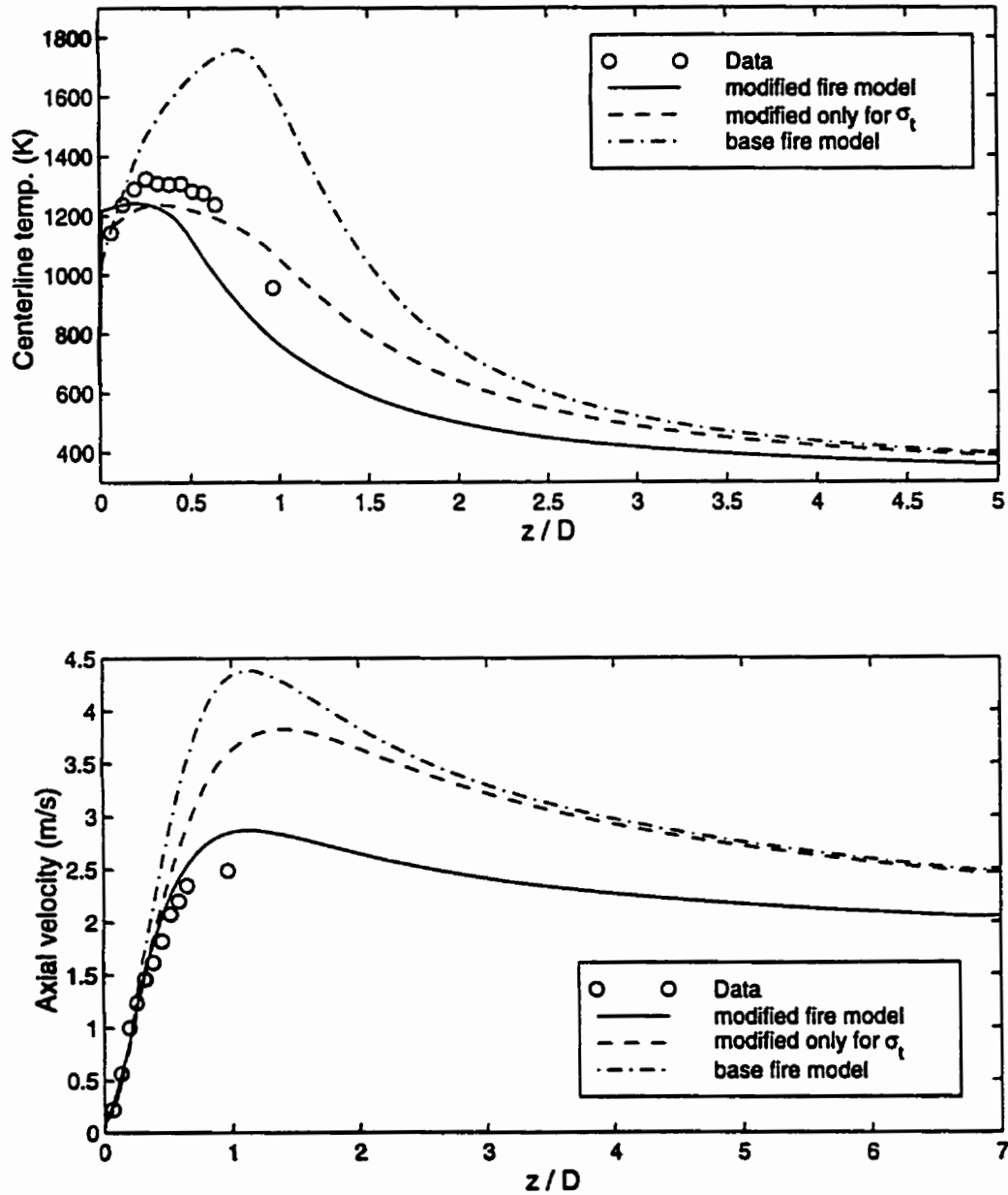


Figure 7.5: Centerline velocity and temperature profiles for the methanol fire and using the modified fire model

### 7.3 Results of the Modified Fire Model

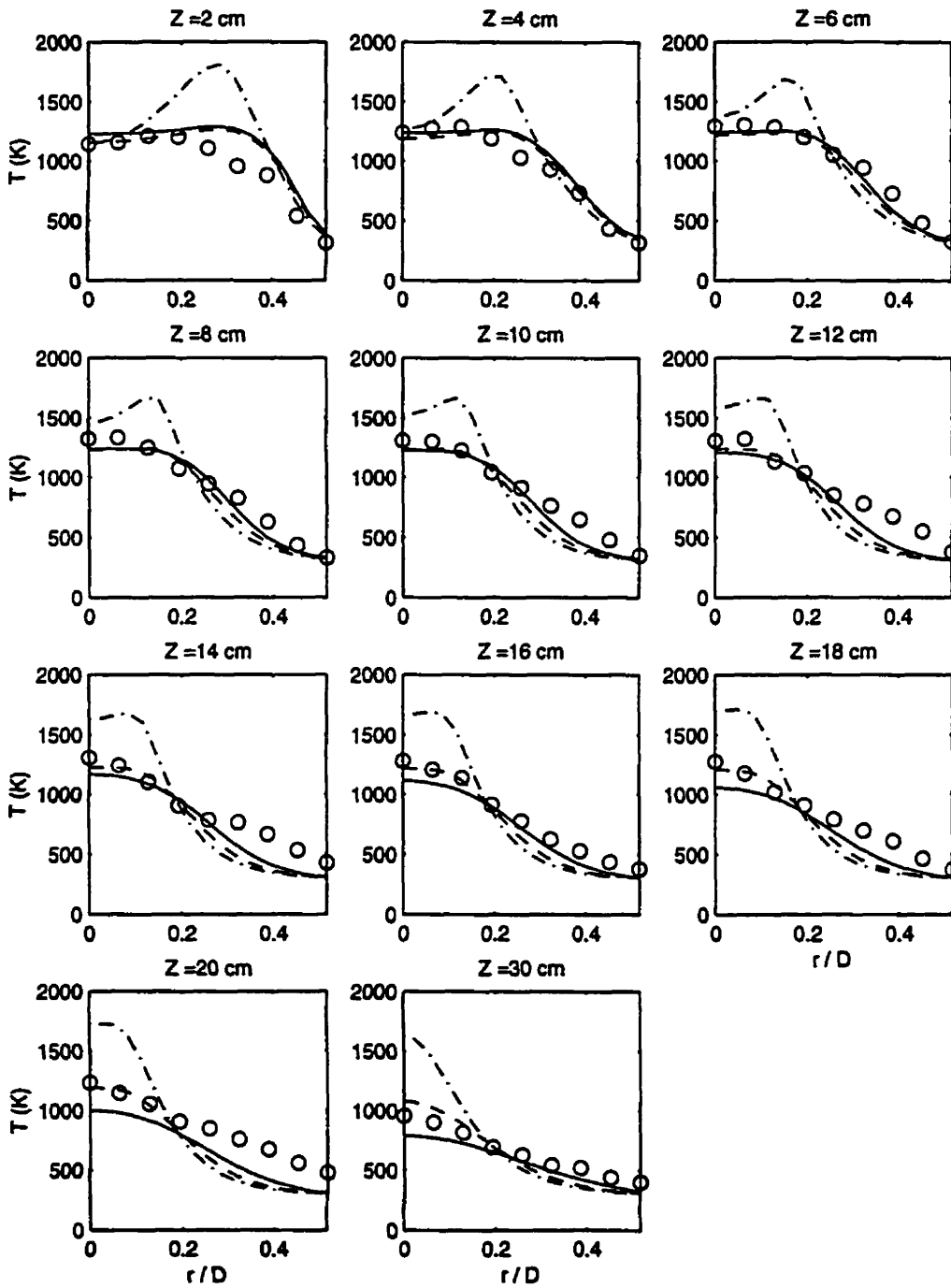


Figure 7.6: Radial profiles of temperature for the methanol fire, using the modified fire model. See Figure 7.5 for the legend.

### 7.3 Results of the Modified Fire Model

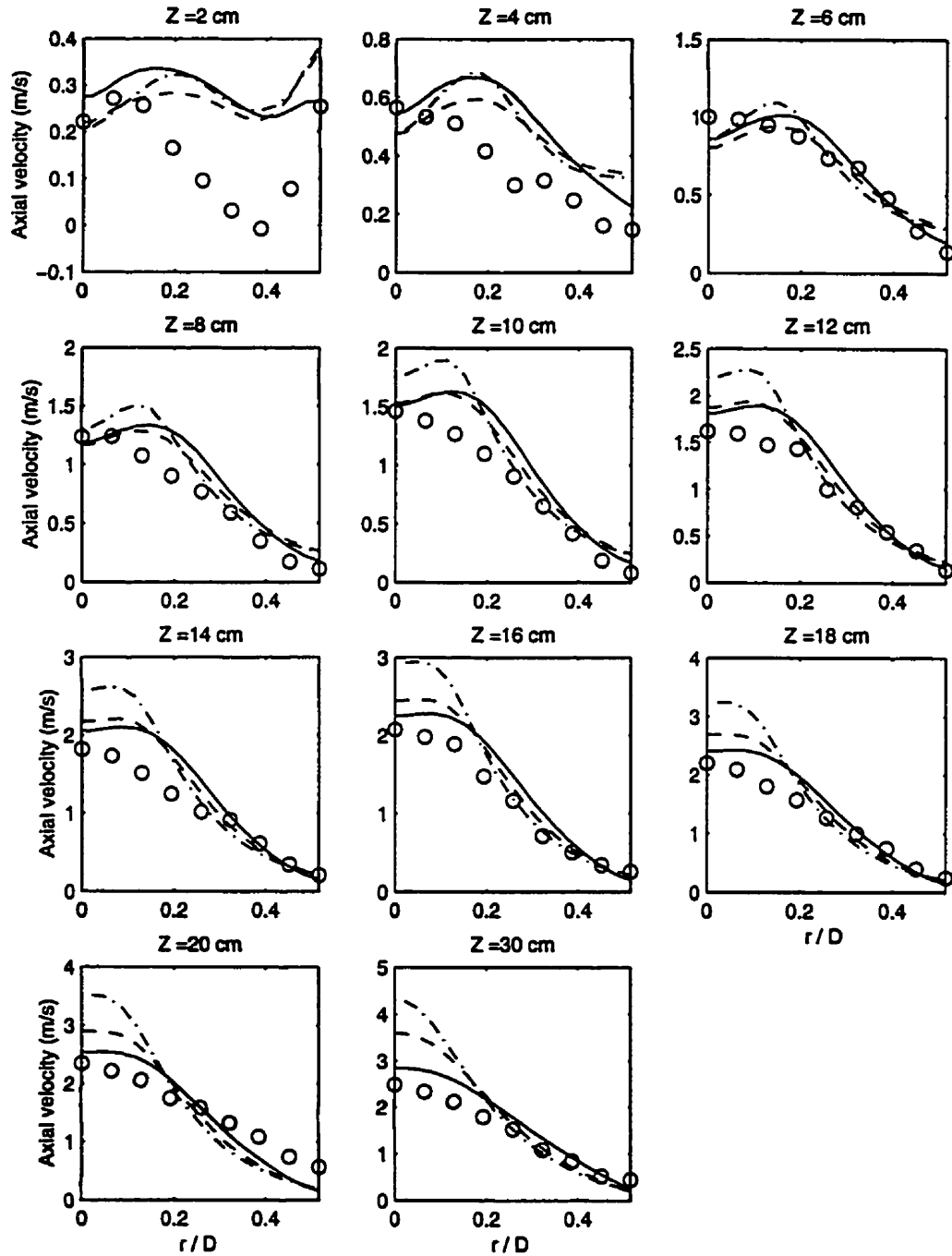


Figure 7.7: Radial profiles of velocity for the methanol fire, using the modified fire model. See Figure 7.5 for the legend

### 7.3 Results of the Modified Fire Model

Table 7.3: Turbulence model constants

| $C_\mu$   | $C_{\epsilon 1}$ | $C_{\epsilon 2}$ | $\sigma_t$ | $\sigma_f$ | $\sigma_\epsilon$ | $\sigma_k$ | $\sigma_g$ | $C_{g1}$ | $C_{g2}$ |
|-----------|------------------|------------------|------------|------------|-------------------|------------|------------|----------|----------|
| Eq. (7.2) | 1.44             | 1.92             | Eq. (7.3)  | 1.0        | 1.3               | 1.0        | 0.7        | 2.8      | 1.61     |

Table 7.4: Grid specifications used for the methanol pool fire (see Figure 5.2 for the nomenclature).

|                                     | grid III-a     | grid III-b     | grid III-c        |
|-------------------------------------|----------------|----------------|-------------------|
| no. of nodes, $N_r \times N_z$      | $31 \times 64$ | $31 \times 77$ | $39 \times 74$    |
| domain size, $W_d \times H_d/R$     | $4 \times 14$  | $4 \times 14$  | $8.5 \times 28.7$ |
| depth of the section below, $H_b/R$ | 3              | 6              | 3                 |
| no. of nodes in burner radius       | 16             | 16             | 16                |

a favorable manner, i.e., lowering the centerline temperature and improving the radial spread of the temperature profiles. The additional modification for  $C_\mu$  further improves the radial spread of both temperature and velocity fields and reduces the centerline velocities such that they agree reasonably well with the experimental data. However, it is noticed that the proposed modification for  $C_\mu$  causes the centerline temperature profile to shift towards the burner surface without affecting the maximum temperature significantly.

Several other test cases with different constant values for  $C_\mu$  and  $\sigma_t$  showed the same trends in changes to the velocity and temperature fields; however, none was found to provide more satisfactory results compared to those from these proposed modifications.

### **7.3 Results of the Modified Fire Model**

---

To study the effect of the size of the computational domain on the numerical results, three grids are used. The specification of these grids is given in Table 7.4 and the grids are shown in Figure 7.8.

These grids are created such that the effects of spatial grid resolution can be minimized while studying the effects of the overall size of the computational domain.

For instance, grid III-a and III-b are identical for the region above the burner and are different only for the lower part which has been doubled in length in grid III-b. To create grid III-c, additional grid points are added to the side and also to the top of grid III-a. Therefore, the spatial grid resolution for the interior part of grid III-c is identical to that of grid III-a.

The results obtained from these different grids did not show noticeable differences and therefore, the smaller grid (i.e. grid III-a) was selected for further computations.

#### **7.3.2 The Axisymmetric Propane Fire**

The axisymmetric propane fire described in Section 5.3 has been simulated using the modified fire model. For the new simulations, the same configurations are used as for the base fire model computations in Chapter 5. For the turbulence model parameters, the values given in Table 7.3 are used.

Centerline variations and radial profiles of velocity and temperature at different heights above the burner are compared with the experimental data in Figures 7.9, 7.10 and 7.11, respectively. In these figures, previous results obtained from the base fire model are also shown for comparison. Clearly, the new modifications provide better agreement between predicted centerline

### 7.3 Results of the Modified Fire Model

---

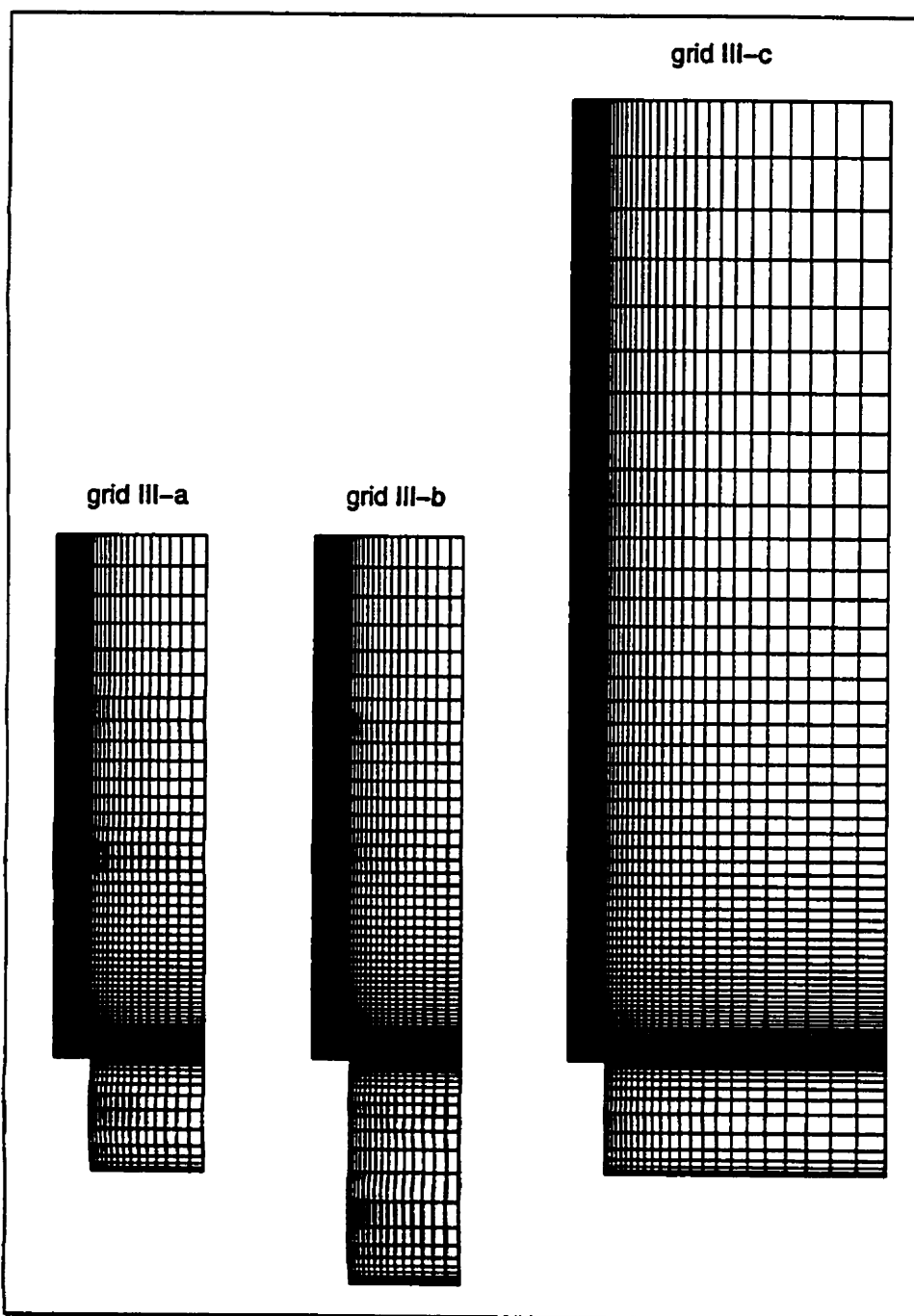


Figure 7.8: Computational grids used for the methanol pool fire



### **7.3 Results of the Modified Fire Model**

---

velocities and experimental data. They also improve the radial spread of the fire.

#### **7.3.3 The Rectangular Propane Fire**

To further determine the performance of the new modified fire model, it has also been applied to the rectangular propane fire described in Section 5.2.

For the new simulations, grid I-1 described in Table 5.2 is used. The boundary conditions and steady state operating conditions are the same as those used in Chapter 5, except that a 10% radiation heat loss is assumed in these simulations. Although experimental data suggests 30% radiation heat loss for propane flames over a wide range of diameters and heat releases [116], due to the radiation blockage caused by the vertical walls on the front and back sides of the rectangular flame (see Figure 5.1) it is expected that the radiation heat loss to the surrounding ambient is much smaller than that reported for fires burning in an open configuration. It can be shown that the radiation view factor between the burner surface and the surrounding ambient for this particular geometry becomes 0.3182 assuming the height of the side walls is about one meter. Therefore, it is quite justifiable to use a 10% radiation heat loss for this rectangular propane fire instead of the 30% suggested for open flames.

The new predicted results are shown in Figures 7.12 and 7.13 as compared with experimental data [48] as well as other numerical results. As shown in these figures, the predicted results using the new modified fire model show significant improvement over those predicted by other models and agree very well with the experimental data. The less satisfactory results at  $Z = 0.015m$

### 7.3 Results of the Modified Fire Model

---

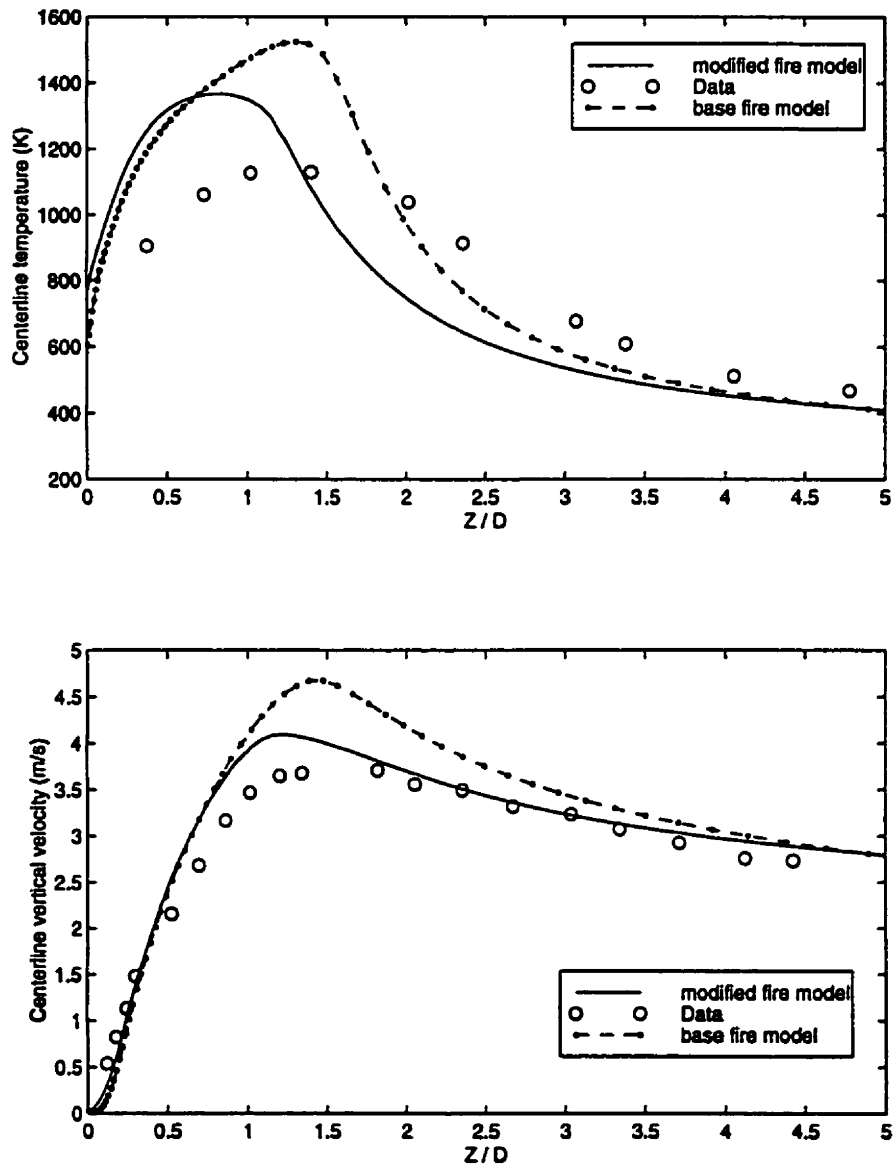


Figure 7.9: Centerline velocity and temperature distributions for the axisymmetric propane fire using the modified fire model, compared to experimental data and base fire model predictions.

### 7.3 Results of the Modified Fire Model

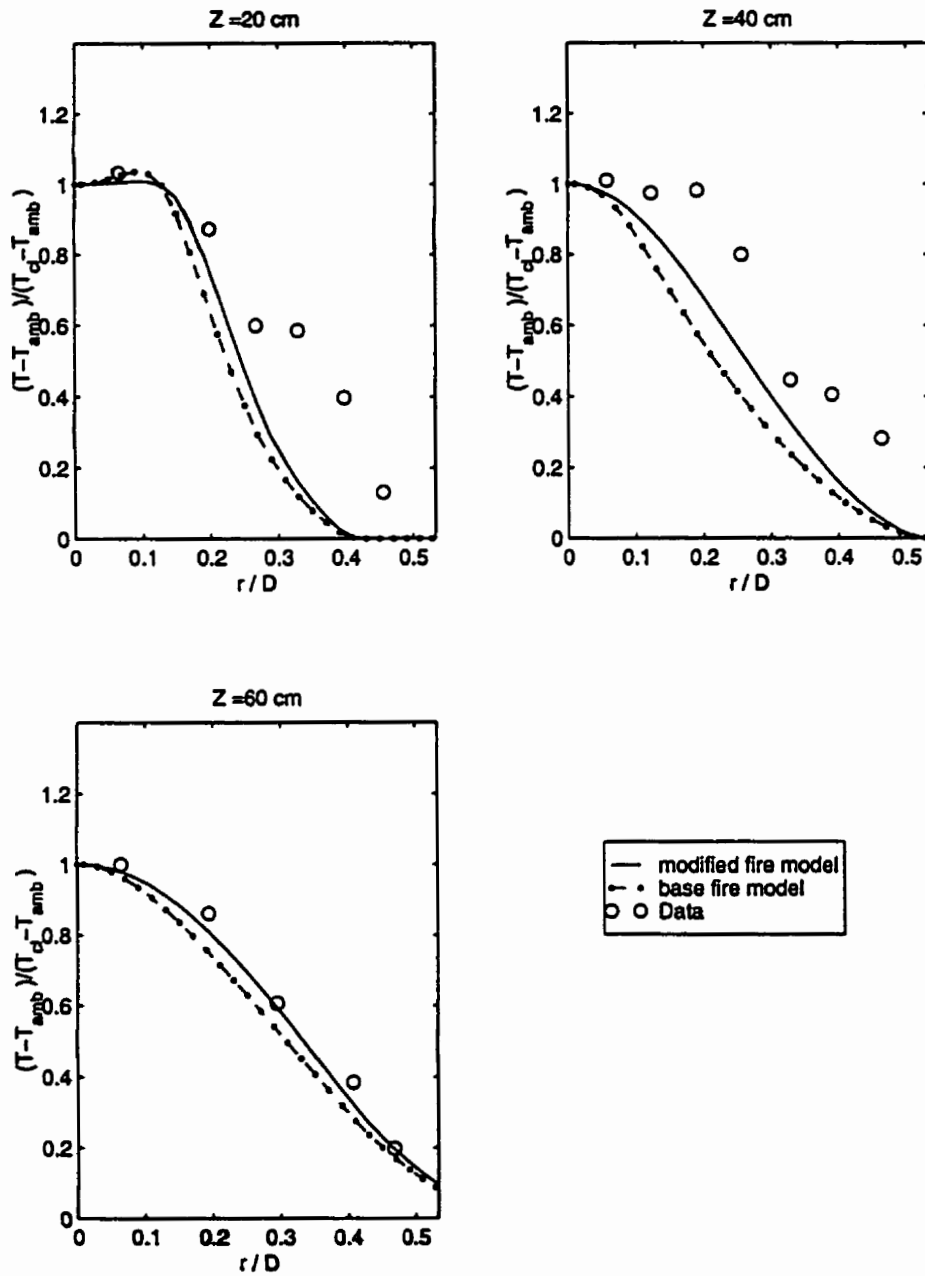


Figure 7.10: Radial profiles of temperature for the axisymmetric propane fire using the modified fire model, compared to experimental data and base fire model predictions.

### 7.3 Results of the Modified Fire Model

---

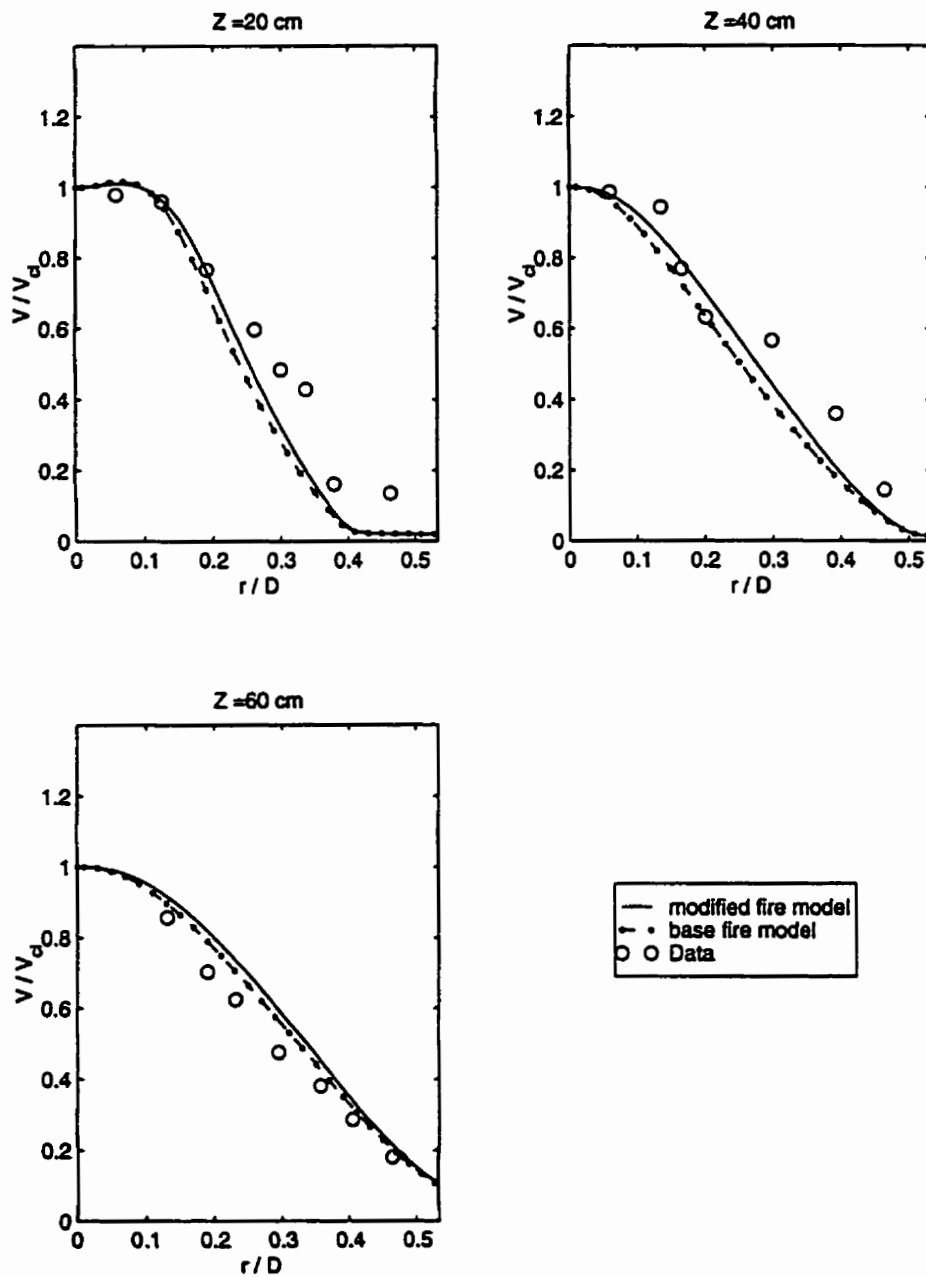


Figure 7.11: Radial profiles of velocity for the axisymmetric propane fire using the modified fire model, compared to experimental data and base fire model predictions.

### **7.3 Results of the Modified Fire Model**

---

above the burner, could be attributed to the simplified boundary conditions used at the burner exit, as well as neglect of any radiation feed back to the fuel surface.

### 7.3 Results of the Modified Fire Model

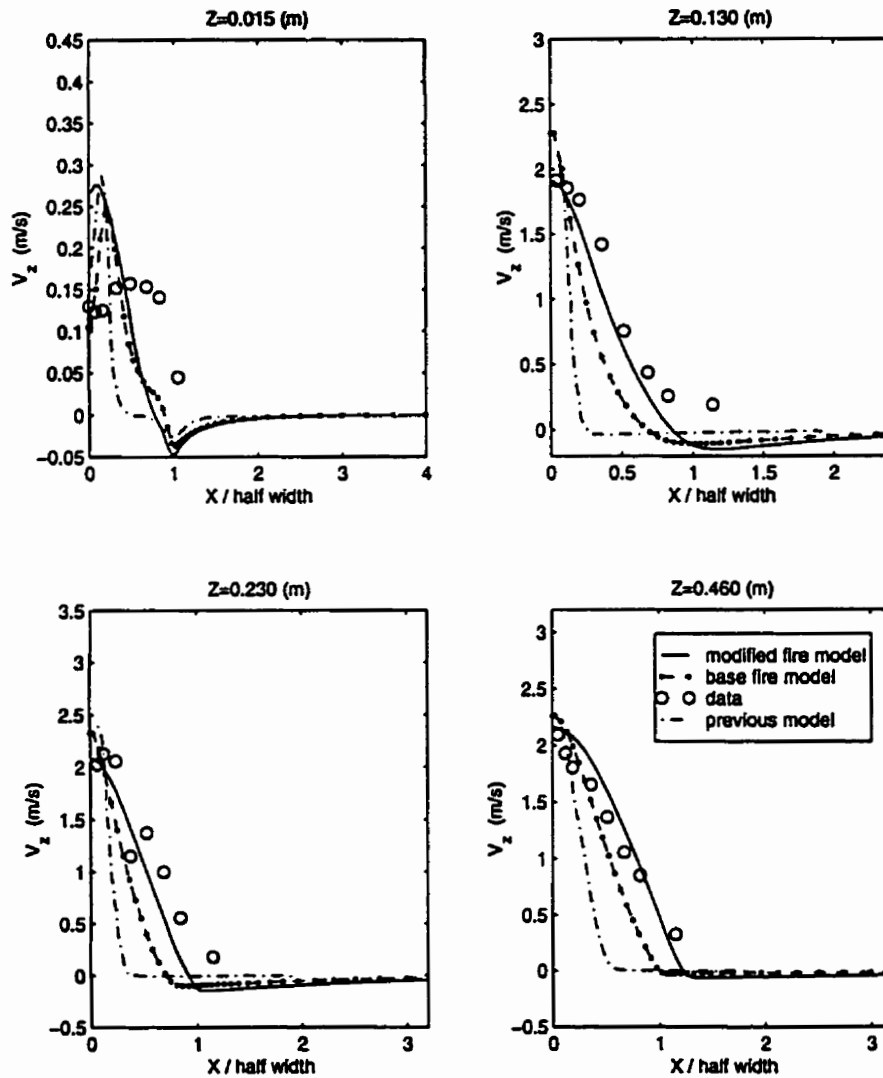


Figure 7.12: Lateral profiles of velocity for the rectangular propane fire using the modified fire model, compared to experimental data and base fire model predictions.

### 7.3 Results of the Modified Fire Model

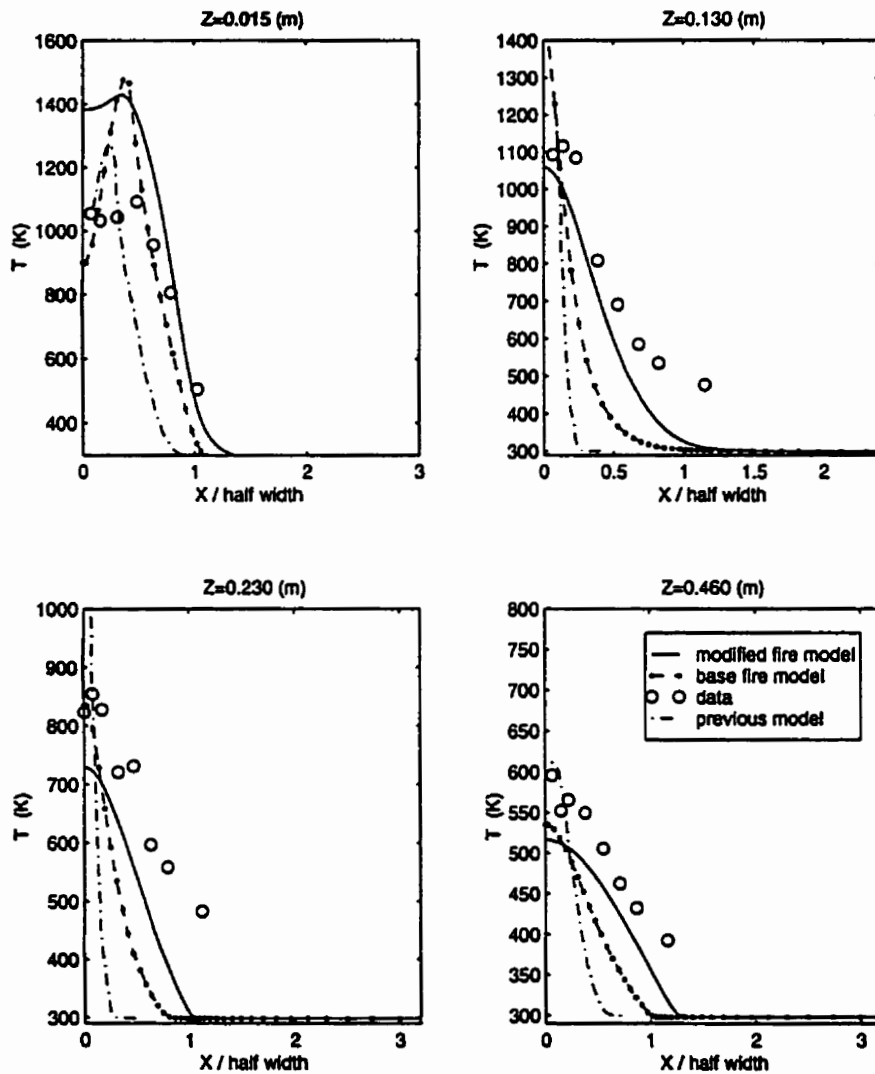


Figure 7.13: Lateral profiles of velocity for the rectangular propane fire using the modified fire model, compared to experimental data and base fire model predictions.

# Chapter 8

## Closure

### 8.1 Summary and Conclusions

It is now common practice to use elliptic formulations of field models when attempting to predict real fire scenarios in buildings. However, the various submodels that are used in these elliptic field models have only been evaluated in codes which are based on parabolic formulations. In the near field region of pool fires or structural fires, the thermal-fluid dynamics is strongly elliptic and the accuracy of using submodels validated mostly in the far field parabolic regions of fires is very much in question. One of the primary purposes of the present work has been the development of a physically based elliptic fire model which can then be used to more realistically examine the accuracy and performance of the existing submodels involved in such larger fire models.

In addition, the availability of the University of Waterloo laboratory pool fire data base has further motivated the present research, for it provides



## 8.1 Summary and Conclusions

---

the detailed measurements needed to validate a fire model in the near field region of a pool fire. The thesis presents the details of the development of an improved pressure based fully coupled elliptic fire model. The new model is based on the Eddy Dissipation Concept for combustion, an improved  $k-\epsilon$  model for turbulence and an improved constant fraction model for radiation. It also accounts for temperature dependency of thermophysical properties, in particular, the heat capacity at constant pressure,  $C_p$ , and incorporates the effects of the terms involving density fluctuations in the governing equations.

The new elliptic fire model has been applied to simulate the fire behavior in the near field region of a range of laboratory scale pool fires. It also has been applied to numerically simulate the very complicated fire pulsation behavior. The qualitative agreement between the numerical results and experimental observations of the puffing phenomenon is very promising. The unique transient results presented in this thesis provide new evidence to determine the morphology of the fire pulsation. These transient results have also led to a detailed description of the mechanisms involved in the puffing phenomenon.

The averaged pseudo steady-state behavior of a range of laboratory scale pool fires has been studied using the present fire model. The accuracy and performance of both the commonly used standard  $k-\epsilon$  turbulence submodel and a new modified version have been demonstrated and compared with one another.

The following conclusions can be drawn from the numerical results presented in this thesis.

- The use of a constant  $C_p$  in numerical fire simulations has a rather sig-

## 8.2 Recommendation for Future Work

---

nificant effect on the results and should be avoided. The use of accurate temperature dependent values of  $C_p$  permit more realistic evaluations of other submodels, for which the use of adjustable parameters is currently unavoidable (i.e. the turbulence submodel).

- The shortcomings of the existing fire models reported when parabolic formulations are used cannot be improved by using an elliptic formulation alone, and other modifications are necessary to improve the accuracy of the results.
- The standard model parameters in the  $k$ - $\epsilon$  turbulence model (i.e.  $C_\mu$  and  $\sigma_t$ ) are not suitable for fire simulations and should be appropriately modified to obtain more accurate results.
- According to the transient results obtained in this study, the origin of the fire pulsation is found to be the result of a fluid dynamic instability; however, the enhanced intensity of the puffing phenomenon in fires compared to that in non-reacting plumes may be partly caused by the oscillations in the reaction zone itself.

## 8.2 Recommendation for Future Work

There are still many unresolved issues remaining with respect to the numerical simulation of fires. Further work is required in a wide range of different areas to improve the predictions and obtain the ultimate fire model, which can realistically predict all aspects of the complicated fire phenomenon. But, as is the case for all branches of science, progress has to be made step by

## 8.2 Recommendation for Future Work

---

step. In what follows, some recommendations are made to further improve the present fire model.

- **Numerical techniques:** For most of the results presented in this thesis, a direct solver is used which is not very efficient. More efficient solvers should be incorporated into the model to reduce the cost of the computations, particularly for the transient simulations.
- **Treatment of density fluctuations:** The present model for the correlations involving  $\rho'$  should either be reformulated or the parameters in the transport equation for  $\overline{T'^2}$  should be customized such that better agreement with experimental data can be obtained.
- **Boundary conditions:** Presently, the radiation heat feed back to the burner surface is totally neglected and a simplified boundary condition is used at the burner exit. Methods of estimating the radiation feed back to the burner surface are required such that more realistic boundary conditions can be used for the energy equation at the burner exit.
- **Application to pool fires with different pool diameter:** Although the predicted pulsation frequency for the 30-cm-diameter pool fire simulated in this thesis agrees very well with experimental data, the present model should be applied to other pool fires with different pool diameters to determine whether results follow the relation between fire pulsation frequency and pool diameter.

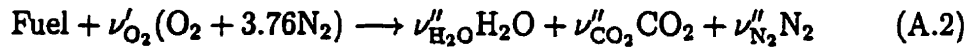
# Appendix A

## Conserved Variables

The derivation of the transport equation for the conserved variable,  $f$ , is explained in detail in this appendix and follows the derivation of equations for coupling functions [70]. The derivation starts with considering the transport equation for the mass fraction of species  $i$ ,  $Y_i$ , that is

$$\frac{\partial \rho Y_i}{\partial t} + \nabla \cdot (\rho Y_i \mathbf{U}) = \nabla \cdot \left( \frac{\mu}{Sc} \nabla Y_i \right) - \mathfrak{R}_i \quad (\text{A.1})$$

Considering a one step complete reaction for combustion as given below



the relation between fuel reaction rate and other species reaction rates be-

## Conserved Variables

---

comes

$$\mathfrak{R}_{\text{fu}} = \frac{\mathcal{M}_{\text{fu}}}{\nu_{\text{O}_2} \mathcal{M}_{\text{O}_2}} \mathfrak{R}_{\text{O}_2} = \mathcal{K}_{\text{O}_2} \mathfrak{R}_{\text{O}_2} \quad \text{where} \quad \mathcal{K}_{\text{O}_2} = \frac{\mathcal{M}_{\text{fu}}}{\nu_{\text{O}_2} \mathcal{M}_{\text{O}_2}} \quad (\text{A.3})$$

$$\mathfrak{R}_{\text{fu}} = -\frac{\mathcal{M}_{\text{fu}}}{\nu'_{\text{CO}_2} \mathcal{M}_{\text{CO}_2}} \mathfrak{R}_{\text{CO}_2} = -\mathcal{K}_{\text{CO}_2} \mathfrak{R}_{\text{CO}_2} \quad \text{where} \quad \mathcal{K}_{\text{CO}_2} = \frac{\mathcal{M}_{\text{fu}}}{\nu'_{\text{CO}_2} \mathcal{M}_{\text{CO}_2}} \quad (\text{A.4})$$

$$\mathfrak{R}_{\text{fu}} = -\frac{\mathcal{M}_{\text{fu}}}{\nu'_{\text{H}_2\text{O}} \mathcal{M}_{\text{H}_2\text{O}}} \mathfrak{R}_{\text{H}_2\text{O}} = -\mathcal{K}_{\text{H}_2\text{O}} \mathfrak{R}_{\text{H}_2\text{O}} \quad \text{where} \quad \mathcal{K}_{\text{H}_2\text{O}} = \frac{\mathcal{M}_{\text{fu}}}{\nu'_{\text{H}_2\text{O}} \mathcal{M}_{\text{H}_2\text{O}}} \quad (\text{A.5})$$

Now, to obtain a conserved scalar one needs to multiply the oxygen mass fraction equation by  $\mathcal{K}_{\text{O}_2}$  and subtract it from the fuel mass fraction equation which yields

$$\frac{\partial \rho(Y_{\text{fu}} - \mathcal{K}_{\text{O}_2} Y_{\text{O}_2})}{\partial t} + \nabla \cdot (\rho \mathbf{U}(Y_{\text{fu}} - \mathcal{K}_{\text{O}_2} Y_{\text{O}_2})) = \nabla \cdot \left( \frac{\mu}{S_c} \nabla (Y_{\text{fu}} - \mathcal{K}_{\text{O}_2} Y_{\text{O}_2}) \right) \quad (\text{A.6})$$

Equation A.6 introduces a conserved variable,  $(Y_{\text{fu}} - \mathcal{K}_{\text{O}_2} Y_{\text{O}_2})$ , whose transport equation doesn't have a source term. Similar equations can be derived by multiplying species equations for  $\text{CO}_2$  and  $\text{H}_2\text{O}$  by  $\mathcal{K}_{\text{CO}_2}$  and  $\mathcal{K}_{\text{H}_2\text{O}}$ , respectively, and adding the results to the fuel mass fraction equation. In order to have similar boundary conditions for these equations it is necessary to define normalized conserved variables as follows

$$f_1 = \frac{(Y_{\text{fu}} - \mathcal{K}_{\text{O}_2} Y_{\text{O}_2}) - (Y_{\text{fu}} - \mathcal{K}_{\text{O}_2} Y_{\text{O}_2})_{\infty}}{(Y_{\text{fu}} - \mathcal{K}_{\text{O}_2} Y_{\text{O}_2})_o - (Y_{\text{fu}} - \mathcal{K}_{\text{O}_2} Y_{\text{O}_2})_{\infty}} \quad (\text{A.7})$$

where  $f_1$  is a normalized conserved variable and subscripts “ $o$ ” and “ $\infty$ ” indicate the value of the variable in the fuel stream and the surrounding

## Conserved Variables

---

ambient, respectively. The other normalized conserved variables are

$$f_2 = \frac{(Y_{fu} + \mathcal{K}_{CO_2} Y_{CO_2}) - (Y_{fu} + \mathcal{K}_{CO_2} Y_{CO_2})_\infty}{(Y_{fu} + \mathcal{K}_{CO_2} Y_{CO_2})_o - (Y_{fu} + \mathcal{K}_{CO_2} Y_{CO_2})_\infty} \quad (\text{A.8})$$

and

$$f_3 = \frac{(Y_{fu} + \mathcal{K}_{H_2O} Y_{H_2O}) - (Y_{fu} + \mathcal{K}_{H_2O} Y_{H_2O})_\infty}{(Y_{fu} + \mathcal{K}_{H_2O} Y_{H_2O})_o - (Y_{fu} + \mathcal{K}_{H_2O} Y_{H_2O})_\infty} \quad (\text{A.9})$$

Since all the normalized conserved variables vary between 0 and 1 and satisfy the same transport equation, one needs to only solve for one of them, which is usually called the mixture fraction,  $f$ , whose transport equation is

$$\frac{\partial \rho f}{\partial t} + \nabla \cdot (\rho f \mathbf{U}) = \nabla \cdot \left( \frac{\mu}{Sc} \nabla f \right) \quad (\text{A.10})$$

After solving for  $Y_{fu}$  and  $f$ , other species mass fractions can be obtained from the definitions of different conserved variables introduced in this appendix.

# Appendix B

## Functional Form for $C_p$

In order to calculate the heat capacity at constant pressure for each species,  $C_{p_i}$  (see Equation 3.24), third order polynomial curve fits are used which yield [90]

$$C_{p_i} = A_i + B_i T + C_i T^2 + D_i T^3 \quad (\text{B.1})$$

where  $C_{p_i}$  is the heat capacity of species  $i$  at temperature  $T$  and  $A_i$ ,  $B_i$ ,  $C_i$  and  $D_i$  are the curve fit constants. Numerical values of these constants for different species are given in Table B.1.

In this table, values of the molecular weight for each species,  $\mathcal{M}_i$ , are in kg/kmole and the calculated  $C_{p_i}$  will be in J/(kg.K). Although, these curve fits are reasonably accurate up to around  $T = 1000$  K, for  $T > 1000$  K they may not be as valid and care should be taken in using these relations. Particularly, for cases when the curve fit for  $C_p$  decreases with increasing temperature (see Figures B.1 and B.2).

To alleviate this problem which could cause significant numerical error or even numerical divergence, for  $T > 1000$  K, linear interpolations based on

## Functional Form for $C_p$

---

Table B.1: Polynomial constants to calculate the isobaric heat capacity for different species

|                               | $A_i/\mathcal{M}_i$  | $B_i/\mathcal{M}_i$    | $C_i/\mathcal{M}_i$     | $D_i/\mathcal{M}_i$     |
|-------------------------------|----------------------|------------------------|-------------------------|-------------------------|
| H <sub>2</sub> O              | $3.224 \times 10^4$  | 1.924                  | $1.055 \times 10^{-2}$  | $-3.596 \times 10^{-6}$ |
| CO <sub>2</sub>               | $1.98 \times 10^4$   | $7.344 \times 10$      | $-5.602 \times 10^{-2}$ | $1.715 \times 10^{-5}$  |
| O <sub>2</sub>                | $2.811 \times 10^4$  | $-3.86 \times 10^{-3}$ | $1.746 \times 10^{-2}$  | $-1.065 \times 10^{-5}$ |
| N <sub>2</sub>                | $3.115 \times 10^4$  | $-1.357 \times 10$     | $2.68 \times 10^{-2}$   | $-1.168 \times 10^{-5}$ |
| C <sub>3</sub> H <sub>8</sub> | $-4.224 \times 10^3$ | $3.063 \times 10^2$    | $-1.586 \times 10$      | $3.215 \times 10^{-5}$  |
| CH <sub>3</sub> OH            | $2.115 \times 10$    | $7.092 \times 10$      | $2.587 \times 10^{-2}$  | $-2.852 \times 10^{-5}$ |

available values of  $C_p$  for H<sub>2</sub>O, CO<sub>2</sub>, N<sub>2</sub> and O<sub>2</sub> at  $T = 1000$  K and  $T = 2000$  K are used. Figure B.1 shows the cubic polynomial fit (solid line), the linear fit (dashed line) and experimental values (\*) of  $C_{p_i}$  for H<sub>2</sub>O, CO<sub>2</sub>, N<sub>2</sub> and O<sub>2</sub>.

Due to lack of available accurate values of  $C_p$  at higher temperatures for propane and methanol, the following approximations are used. For propane, the cubic polynomial is used without any modification, on the ground that the smooth monotonic behavior of the cubic function up to  $T = 2000$  K does not introduce any unphysical trend in variation of  $C_p$  with temperature (see Figure B.2). For methanol, however, as shown in Figure B.2, a linear extrapolation is used for  $T > 1000$  K to discard the descending part of the cubic polynomial fit. This linear extrapolation is based on the predicted values at  $T = 1000$  K and  $T = 1250$  K using the cubic curve fit.



## Functional Form for $C_p$

---

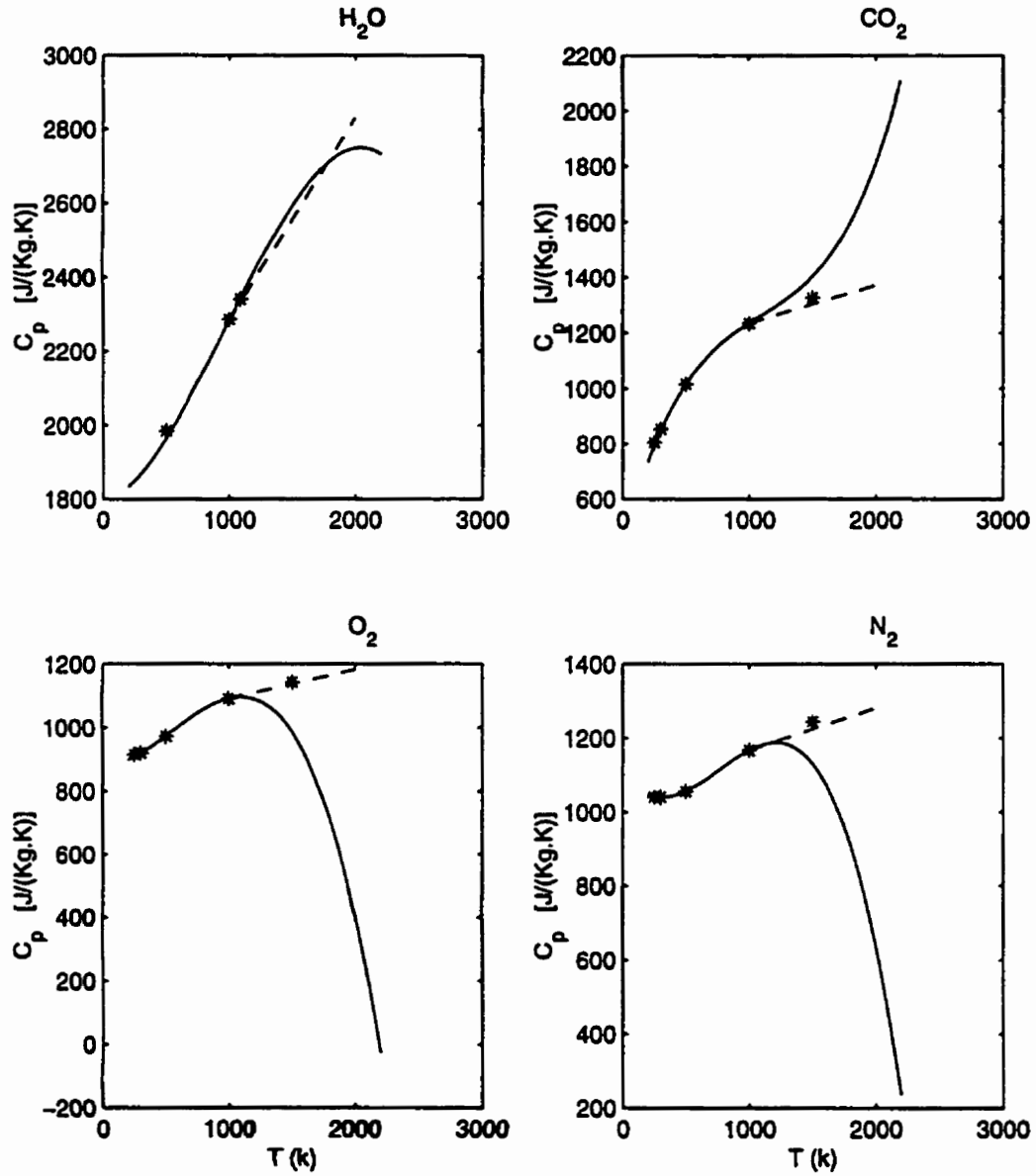


Figure B.1: Variation of  $C_p$  for different species, cubic polynomial (solid line), linear interpolation (dashed line) and experimental values (\*) [91]

## Functional Form for $C_p$

---

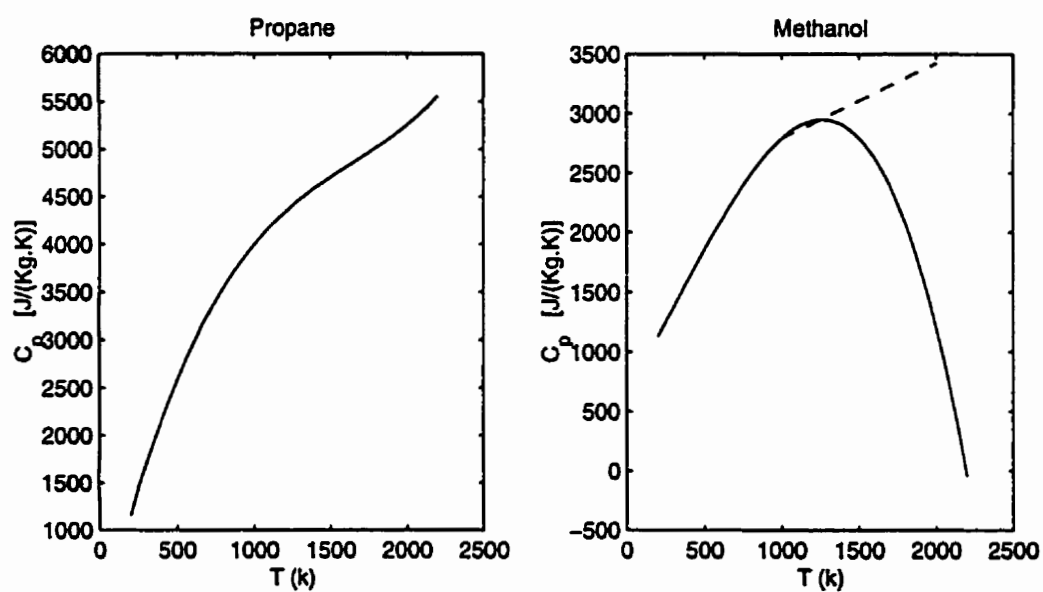


Figure B.2: Variation of  $C_p$  for propane and methanol, cubic polynomial (solid line), linear extrapolation (dashed line)

# Appendix C

## The Grid Generator

To create a computational grid, an algebraic system has been developed and used in this thesis. In this method the grid points of the structured mesh are first distributed along the boundaries of the computational domain according to a desired grid density pattern. The grid points are numbered by two indices,  $i$  and  $j$ , which vary from 1 to  $I$  and 1 to  $J$ , respectively. To determine the coordinate of the interior grid points,  $r_{ij}$ , the general technique is to use interpolation from the boundary coordinates,  $r_{1j}$ ,  $r_{Ij}$ ,  $r_{i1}$  and  $r_{iJ}$ .

An effective structure is provided by transfinite interpolation which, for a two dimensional case, is

$$r_{ij} = \mathfrak{P}^i + \mathfrak{P}^j - \mathfrak{P}^i \mathfrak{P}^j \quad (\text{C.1})$$

where  $\mathfrak{P}^i$  and  $\mathfrak{P}^j$  are called projectors and are defined below

$$\mathfrak{P}^i = f_i r_{Ij} + (1 - f_i) r_{1j} \quad (\text{C.2})$$

$$\mathfrak{P}^j = g_i r_{iJ} + (1 - g_i) r_{i1} \quad (\text{C.3})$$

## The Grid Generator

---

and

$$\Psi^i \Psi^j = f_i g_i r_{IJ} + f_i (1 - g_j) r_{I1} + (1 - f_i) g_j r_{1J} + (1 - f_i) (1 - g_j) r_{11} \quad (\text{C.4})$$

the blending functions,  $f_i$  and  $g_j$ , can be defined differently to provide different grid density. The simplest blending functions are linear functions given by

$$f_i = \frac{i-1}{I-1} \quad \text{and} \quad g_j = \frac{j-1}{J-1} \quad (\text{C.5})$$

However, to provide a concentration of grid lines in certain regions of the grid, one may use exponential blending functions which can be written as

$$f_i = \frac{e^{\alpha \frac{i-1}{I-1}} - 1}{e^\alpha - 1} \quad \text{and} \quad g_j = \frac{e^{\beta \frac{j-1}{J-1}} - 1}{e^\beta - 1} \quad (\text{C.6})$$

The effects of different  $\alpha$  and  $\beta$  values on the grid density for a rectangular computational domain with non-uniform node distribution along its boundaries are shown in Figure C.1. This figure demonstrates the benefit of using exponential blending functions in cases where concentration of grid nodes in a particular region is desired.

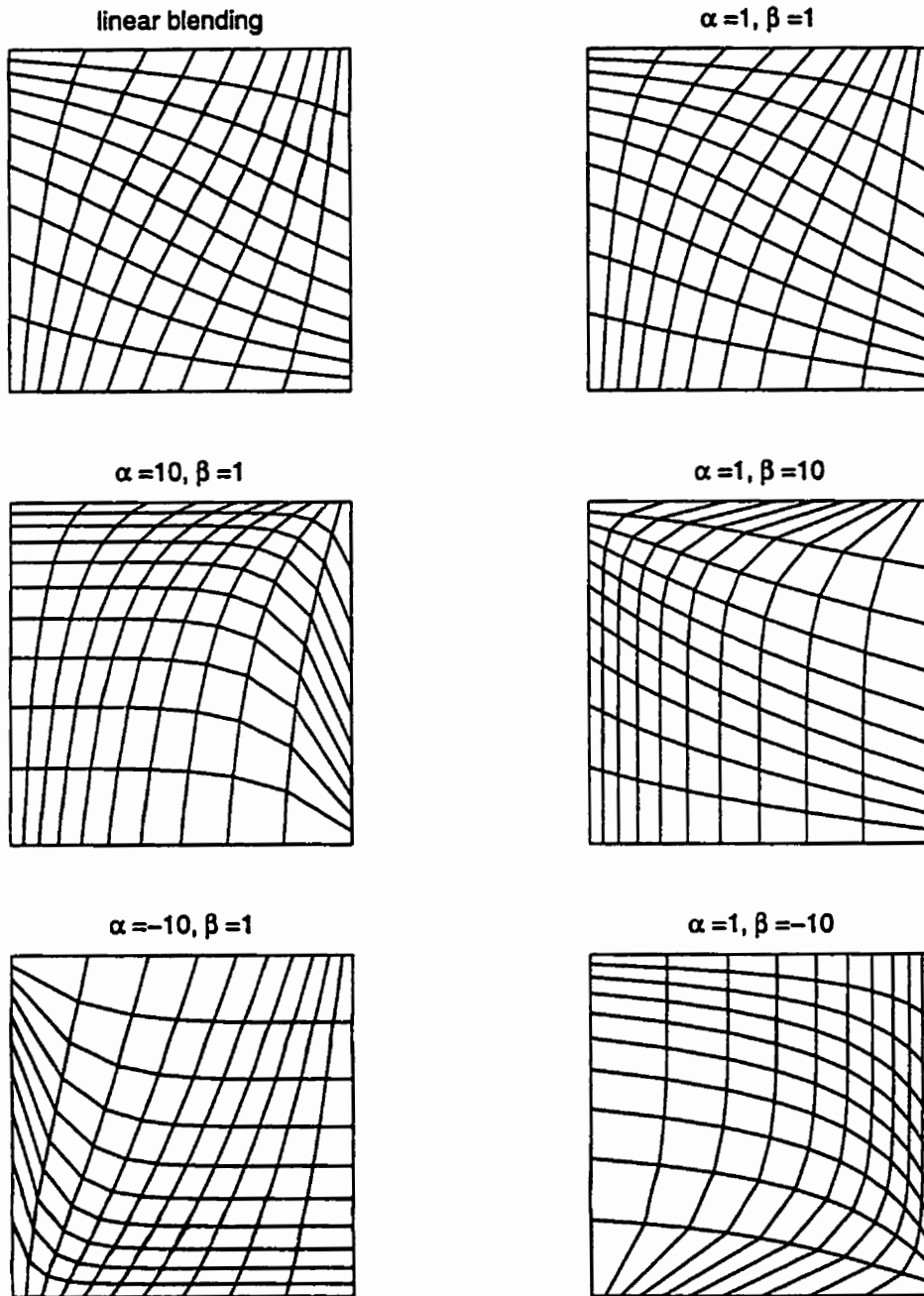


Figure C.1: Effect of the blending function on grid node distribution

# Appendix D

## Code Validation Results

In order to validate the implementation of the numerical model, which has been developed from scratch, several tests have been performed. These tests demonstrate the validity of different modules used in the numerical model. In addition, they examine and compare the performance of different numerical schemes and boundary conditions used for different flow situations. The results of these examinations and comparisons are used to ensure the correct implementation of the numerical model and also to choose an appropriate combination for simulating complicated flow situations such as those which occur in fires.

The validation tests are chosen such that the results of the present model can be compared with either theoretical results, available bench mark solutions or experimental data. These test cases include

- flow between parallel plates,
- flow in circular pipes,

## **D.1 Laminar Flow Between Parallel Plates**

---

- convection of a step profile,
- shear driven cavity flow,
- natural convection flow in a square cavity, and
- an axisymmetric turbulent buoyant plume.

In the following sections, each problem is briefly described and then the numerical setup used to perform the simulation is discussed. Finally, the present numerical results are compared with other numerical, analytical or experimental data.

## **D.1 Laminar Flow Between Parallel Plates**

When a uniform flow enters a 2-dimensional straight channel, the initial uniform velocity profile changes until a fully developed velocity distribution is established. As shown in Figure D.1, the entrance length,  $L_e$ , over which the velocity distribution transforms to its fully-developed distribution is composed of two zones

1. the inviscid-core length,  $L_i$ , which comprises an initial zone with two growing wall boundary layers and an inviscid core region between them, and
2. the profile-development length,  $L_d$ , a developing region over which the streamwise velocity profile gradually approaches the fully developed distribution.

## D.1 Laminar Flow Between Parallel Plates

---

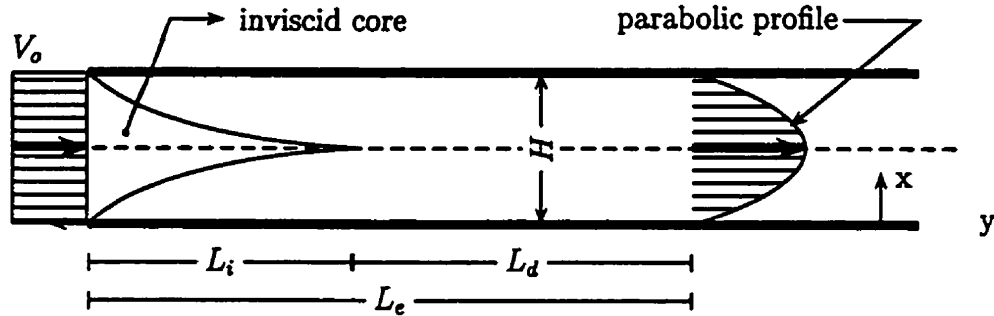


Figure D.1: The entrance region of a flow between parallel plates

The non-dimensional fully-developed velocity distribution for a laminar, incompressible flow can be obtained through an exact solution of the two dimensional Navier-Stokes equations and is given by

$$\frac{v(x)}{V_o} = 6 \frac{x}{H} \left( 1 - \frac{x}{H} \right) \quad (\text{D.1})$$

where  $V_o$  is the average velocity (=the uniform entrance velocity) and  $H$  is the distance between the plates. The maximum velocity occurs at the centerline and is 1.5 times the average velocity ( $V_{max} = 1.5V_o$ ). Due to the flow symmetry about the centerline only half of the physical domain is simulated. Numerical simulations are done for three different Reynolds number (i.e.  $Re = 20, 50$  and  $100$ ) and the effect of different boundary conditions on the solution are studied. The first two sets of boundary conditions used for this problem are described in Figure D.2.



## D.1 Laminar Flow Between Parallel Plates

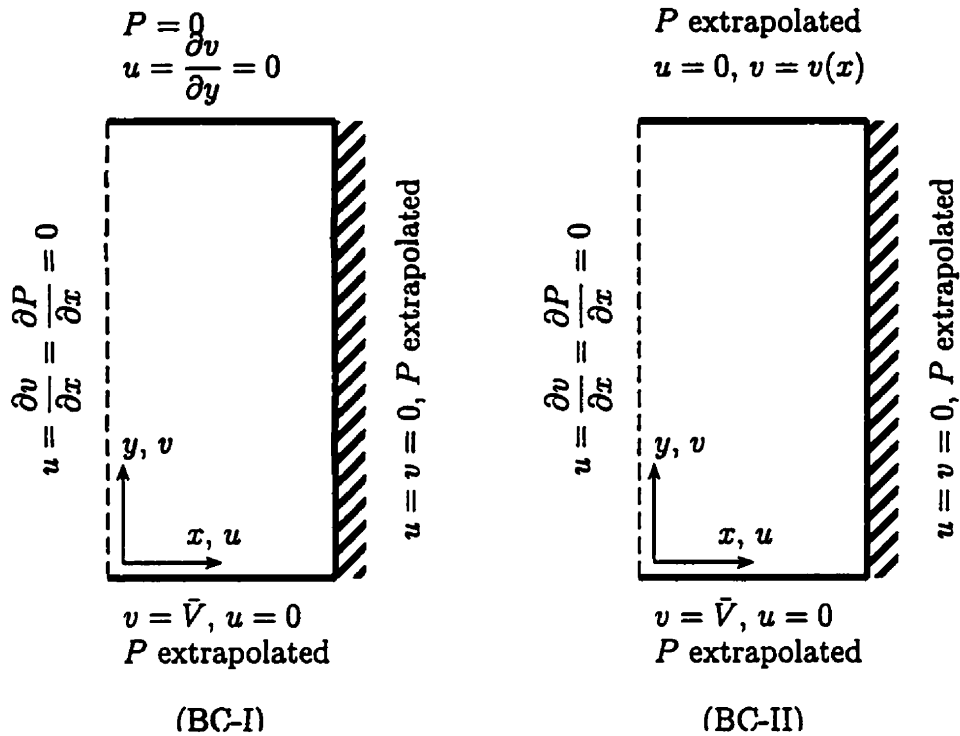


Figure D.2: Boundary conditions used for flow between parallel plates

The third boundary condition, BC-III, is the same as BC-I except that  $\frac{\partial P}{\partial y} = 0$  is applied at the inlet instead of extrapolating the pressure.

Among several grids tested a uniform  $30 \times 60$  node grid (30 nodes across half width of the channel and 60 nodes along the channel) is chosen for the results shown here. Figure D.3 shows the calculated velocity profiles at different streamwise locations along the channel for different Reynolds numbers. The exact solution is also shown at the first streamwise location where the calculated centerline velocity is equal to or greater than 99% of

## D.1 Laminar Flow Between Parallel Plates

---

the exact centerline velocity ( $V_{max}$ ). This point also determines the entrance length,  $L_e$ , of the channel.

As shown in this figure, the uniform inlet velocity develops into the exact fully developed profile for all different boundary conditions and Reynolds numbers.

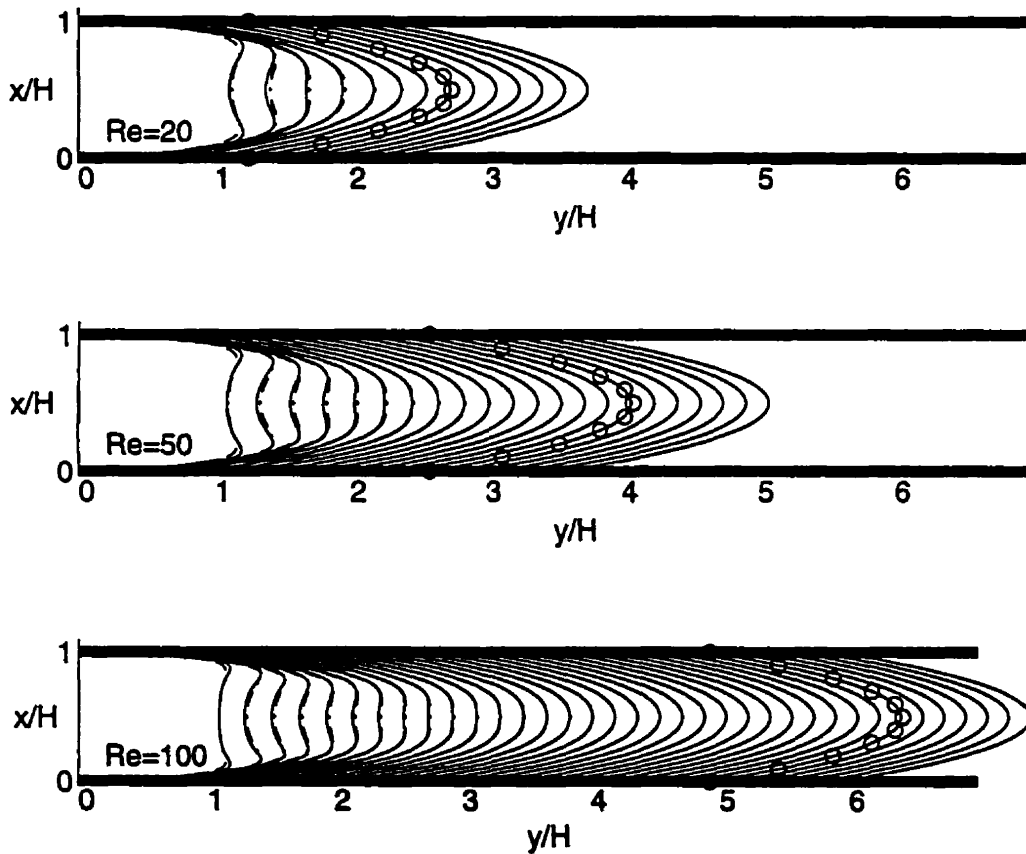


Figure D.3: Streamwise velocity profiles between parallel plates for different boundary conditions, (-) BC-I, (- -) BC-II, (- ·) BC-III and  $\odot$  exact

The pressure field also develops to a uniform pressure across the channel and drops linearly with length in the fully developed region, as expected.

## D.1 Laminar Flow Between Parallel Plates

---

The variation of the centerline pressure for different  $Re$ 's is shown in Figure D.4, whereas, Figure D.5 depicts the isobars within the channel.

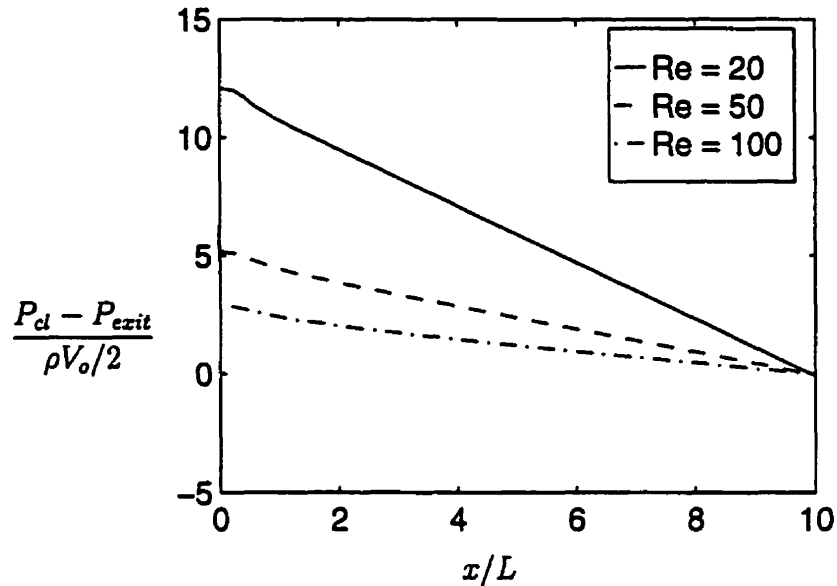


Figure D.4: Centerline pressure variation along the channel

As shown in Figure D.4, after a short distance from the inlet the centerline pressure drops linearly with length as predicted by the exact solution. The slope of the linear pressure variation depends inversely on the Reynolds number and determines the friction coefficient, which is discussed below.

The pressure contours shown in Figure D.5 are typical of those predicted using similar models. They show a pressure buildup at the entrance corners where flow is brought to a stop due to the no-slip wall boundary condition. In addition, velocity profiles in the developing region show some velocity overshoots which have also been observed by others.

As a next test of the integrity of the model, the friction coefficient was calculated and compared to theoretical values. The theoretical friction coef-

## D.1 Laminar Flow Between Parallel Plates

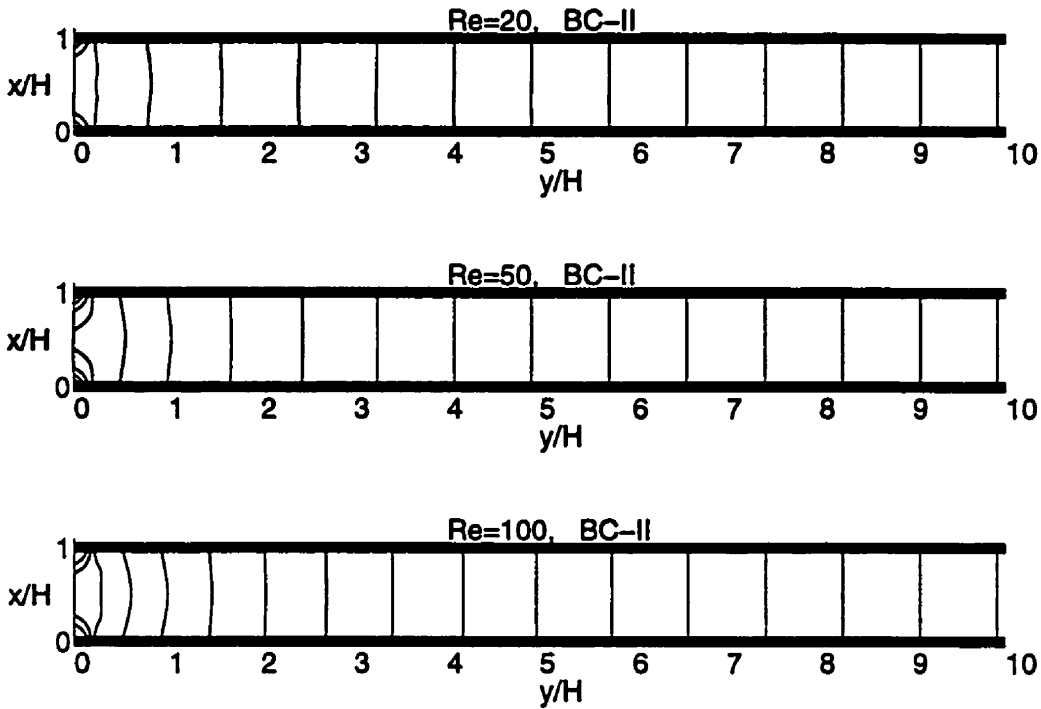


Figure D.5: Pressure contours between parallel plates

friction coefficient,  $\lambda_{th}$ , for the fully developed region is a function of Reynolds number as given by [92]

$$\lambda = \frac{\Delta P}{\frac{\rho V_o^2}{2}} \cdot \frac{H}{x} = \frac{24}{Re} \quad (D.2)$$

Table D.1 summarizes the calculated non-dimensional entrance length,  $L_e/H$ , inviscid core length,  $L_i/H$ , and friction coefficient for the different cases which were modeled. As shown in the Table, the friction coefficient is predicted very accurately, however, the accuracy of the calculated entrance length depends strongly on the grid resolution in that region. To obtain more accurate results, three grids with different node spacings are used for the flow

## D.1 Laminar Flow Between Parallel Plates

---

Table D.1: Calculated parameters for flow between parallel plates

|                | $Re = 20$ |       |        | $Re = 50$ |       |        | $Re = 100$ |       |        |
|----------------|-----------|-------|--------|-----------|-------|--------|------------|-------|--------|
|                | BC-I      | BC-II | BC-III | BC-I      | BC-II | BC-III | BC-I       | BC-II | BC-III |
| $L_e/H$        | 1.25      | 1.25  | 1.25   | 2.583     | 2.583 | 2.417  | 4.917      | 4.917 | 4.75   |
| $L_i/H$        | 0.42-0.58 |       |        | 0.75-0.92 |       |        | 1.42-1.58  |       |        |
| $\lambda$      | 1.2       | 1.2   | 1.2    | .4816     | .4816 | .4818  | .2438      | .2426 | .2426  |
| $\lambda_{th}$ | 1.2       | 1.2   | 1.2    | .48       | .48   | .48    | .24        | .24   | 2.4    |

with  $Re = 50$ . Table D.2 summarizes the calculated results and describes the grid specifications used. The calculated entrance length, as given in Table

Table D.2: Calculated entrance length for flow between parallel plates,  $Re = 50$

| no. of nodes    | channel length | $\Delta x/H$ | $\Delta y/H$ | $L_e/H$ |
|-----------------|----------------|--------------|--------------|---------|
| $30 \times 60$  | $10H$          | 1/6          | 1/30         | 2.6     |
| $30 \times 60$  | $5H$           | 1/12         | 1/30         | 2.5     |
| $60 \times 120$ | $5H$           | 1/24         | 1/60         | 2.5     |

D.2, compares very well with the empirical value of 2.5 for  $Re = 50$  [92].

## D.2 Flow in Circular Pipes

Flow behavior in the entrance region of a pipe is very similar to that of flow between parallel plates. However, the entrance length is longer and the fully developed velocity profile,  $v(r)$ , maximum velocity,  $v_{max}$ , and friction coefficient,  $\lambda$ , are different for this case due to differences in flow geometry. The exact solution for fully developed pipe flow yields [92]

$$v(r) = 2V_o \left(1 - \frac{r^2}{R^2}\right)$$

$$\lambda = \frac{-\Delta P}{\frac{\rho V_o^2}{a}} \cdot \frac{2R}{z} = \frac{64}{Re_D}$$

and

$$v_{max} = v_{(r=0)} = 2V_o$$

where some of the variables are shown in Figure D.6.

The numerical flow simulations are done over half of the physical domain with the axisymmetric flow option turned on. The same  $30 \times 60$  node grid used previously for the parallel plate test case, with a length to diameter aspect ratio of 10 is used for the computations and boundary conditions are specified according to BC-II illustrated in Figure D.2.

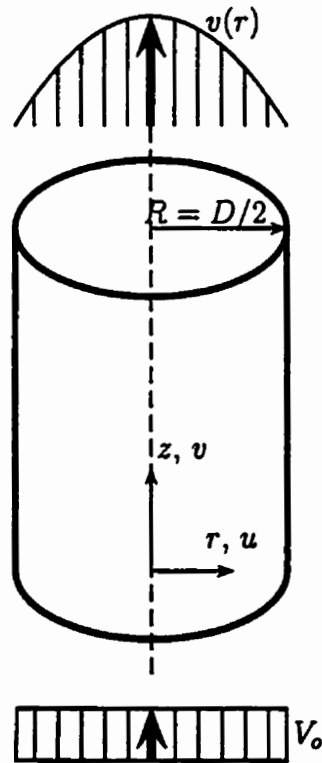


Figure D.6: Geometry and variable definitions for the pipe flow test case

## D.2 Flow in Circular Pipes

---

Figure D.7 shows the predicted velocity profiles along the pipe for the same three Reynolds numbers as were used in the parallel plate test case. The exact fully developed velocity profile is also shown at the beginning of the fully developed region. As evident in this figure the calculated velocity profiles approach the exact solution very accurately. In the entrance region, the expected velocity overshoots are also predicted.

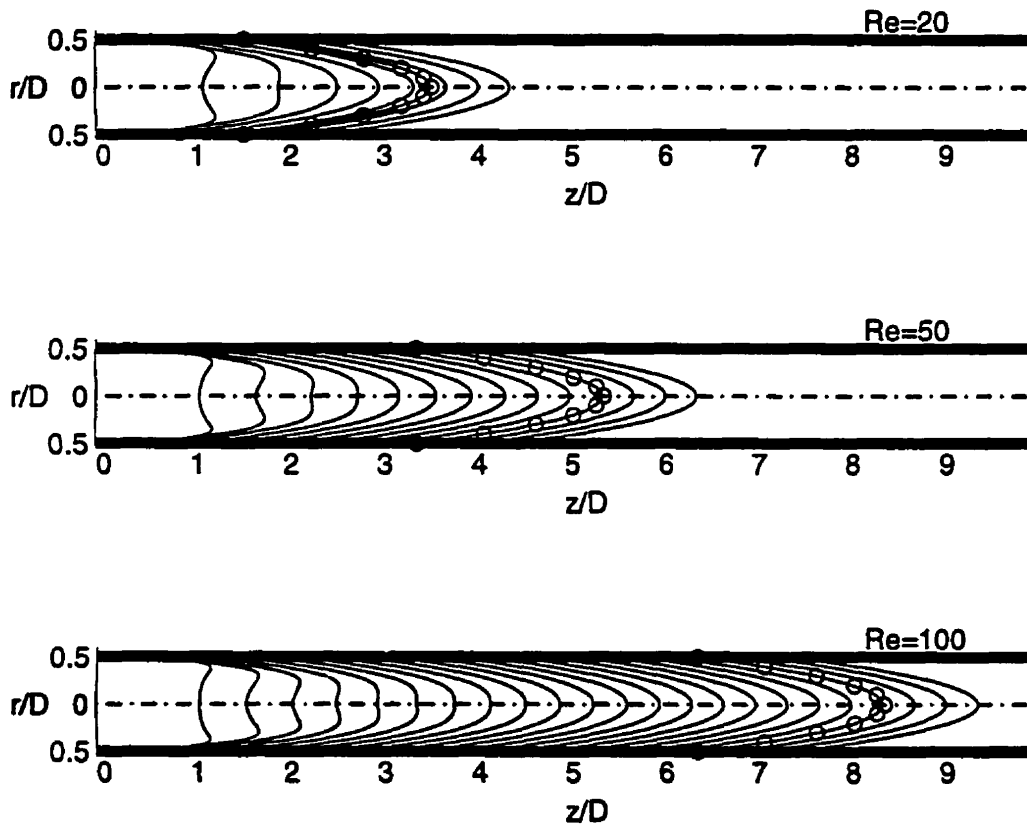


Figure D.7: Calculated and exact velocity profiles for the pipe flow test case

Pressure contours and centerline pressure drop along the pipe axis are shown in Figures D.8 and D.9, respectively. As shown in these figures, pres-

## D.2 Flow in Circular Pipes

---

sure drops linearly in the fully developed region and becomes uniform across the pipe at about  $z/D \approx 1$ .

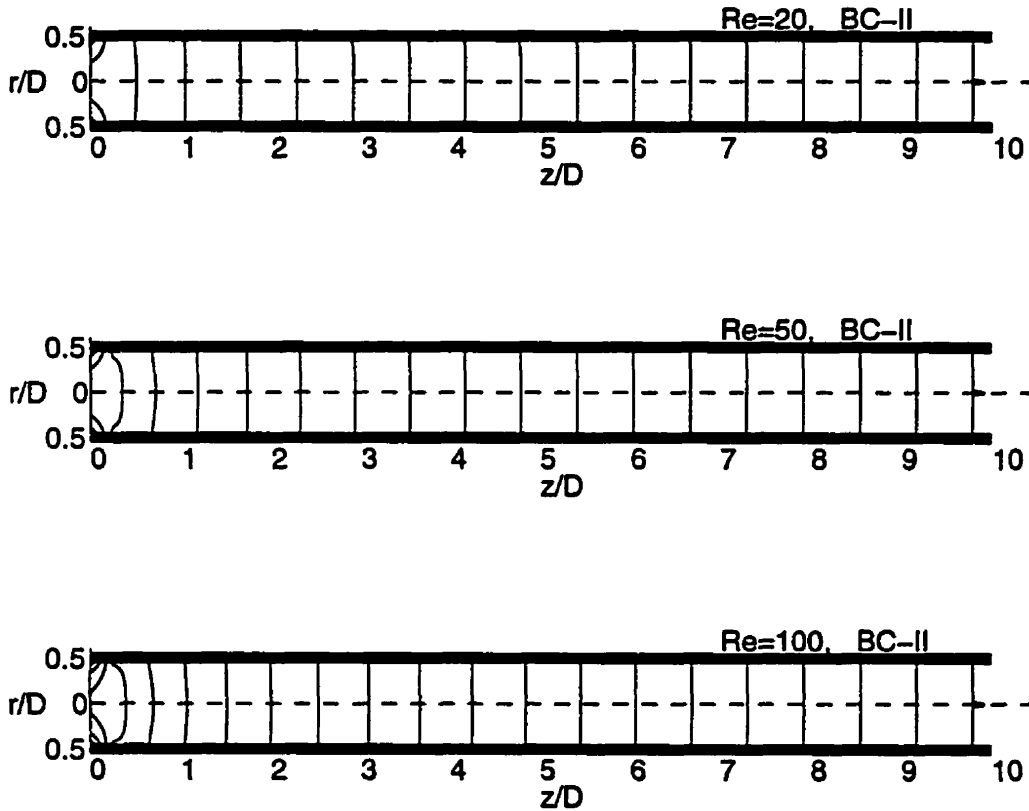


Figure D.8: Calculated centerline pressure variation for different  $Re$  numbers

The entrance length and friction coefficient for different Reynolds numbers have been calculated and are shown in Table D.3. Since the main purpose of these tests is to illustrate the validity of the solution for the hydrodynamic equations for axisymmetric flows, no attempt is made to obtain grid independent results for the calculated entrance length. However, numerical results in the fully developed region match with analytical solutions very accurately for the grid resolution used here.



## D.2 Flow in Circular Pipes

---

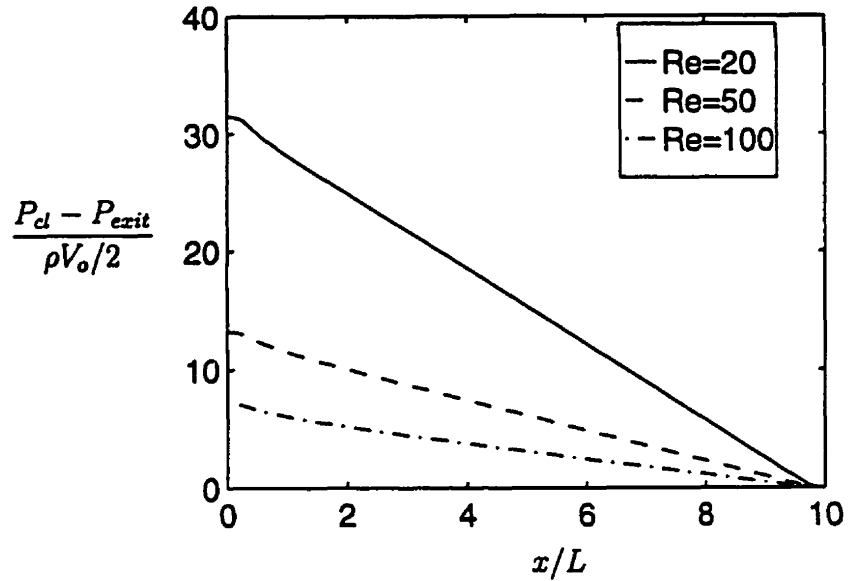


Figure D.9: Pressure contours along the pipe

Table D.3: Calculated results for flow in a circular pipe

| $Re$ | $L_e/D$ | $L_i/D$    | $\lambda$ | $\lambda_{th}$ |
|------|---------|------------|-----------|----------------|
| 20   | 1.583   | 0.583-0.75 | 3.195     | 3.2            |
| 50   | 3.417   | 1.083-1.25 | 1.279     | 1.28           |
| 100  | 6.417   | 2.08-2.25  | 0.6414    | 0.64           |

## D.3 Convection of a step profile

A popular test case used to compare the performance of different advection schemes is the solution of the convection of a step profile in a uniform flow oblique to grid lines. Figure D.10 shows a schematic of the geometry, flow direction and boundary conditions for this test case. As shown in the figure, the uniform  $\phi$  profile at the left boundary is convected into the domain by a uniform flow in the  $\theta$  direction. At the limit of zero diffusion, the exact solution yields a uniform value of  $\phi = \phi_0$  above the diagonal and  $\phi = 0$  below it, with a sharp step function across the diagonal.

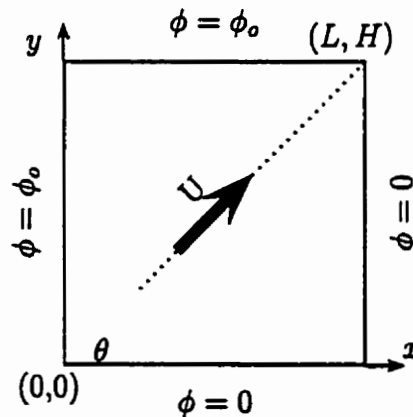


Figure D.10: Convection of a step profile in a uniform flow oblique to the grid lines

The calculations are done on three uniform grids with  $12 \times 12$ ,  $22 \times 22$  and  $42 \times 42$  nodes. The width and the height of the computational domain are set to unity ( $L = H = 1$ ) which yields  $\theta = 45^\circ$ . Figures D.11, D.12 and D.13 show the predicted  $\phi$  distribution along the horizontal mid-plane

### D.3 Convection of a step profile

---

of the computational domain obtained using the different advection schemes described in Section 4.2.2. Figure D.14 compares the results obtained using all three advection schemes on a  $42 \times 42$  node grid.

The UDS scheme (Figure D.11) introduces significant errors in predictions of the distribution of  $\phi$  due to false diffusion. The profiles are smeared and therefore UDS should not be used in prediction of similar flow situations. The HOUDS scheme (Figure D.12) captures the discontinuity much more accurately; however, it introduces overshoots and undershoots in the value of  $\phi$  which can be eliminated when limiters are used (Figure D.13). It was noticed that more iterations were needed to obtain the solution when the higher order advection scheme was used, and even more iterations were needed when limiters were required.

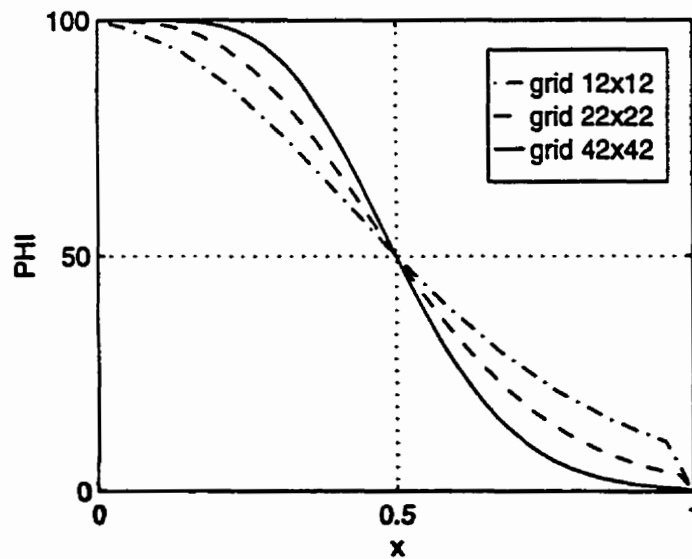


Figure D.11:  $\phi$  distribution along the horizontal mid-plane using UDS

### D.3 Convection of a step profile

---

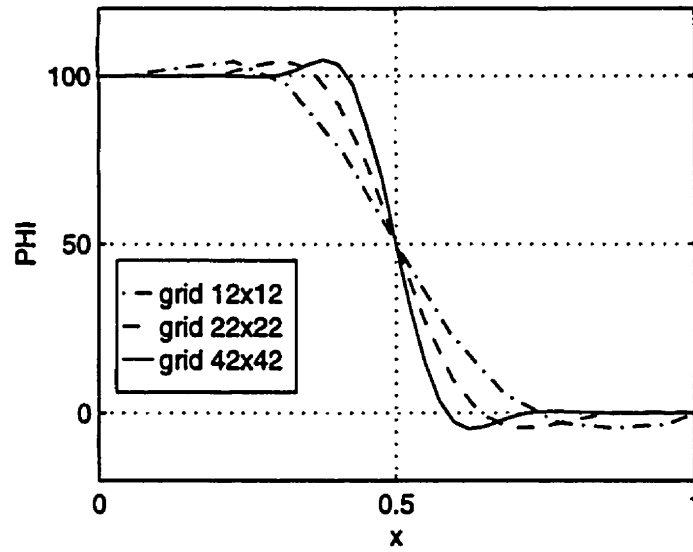


Figure D.12:  $\phi$  distribution along the horizontal mid-plane using HOUDS

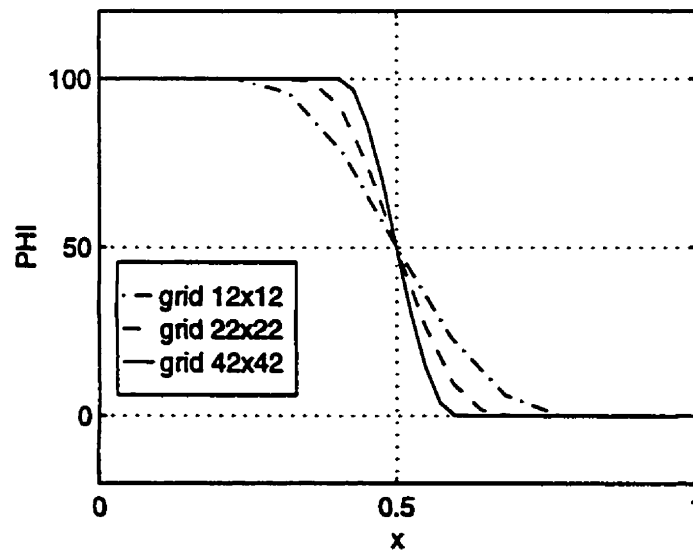


Figure D.13:  $\phi$  distribution along the horizontal mid-plane using HOUDS with limiters

### D.3 Convection of a step profile

---

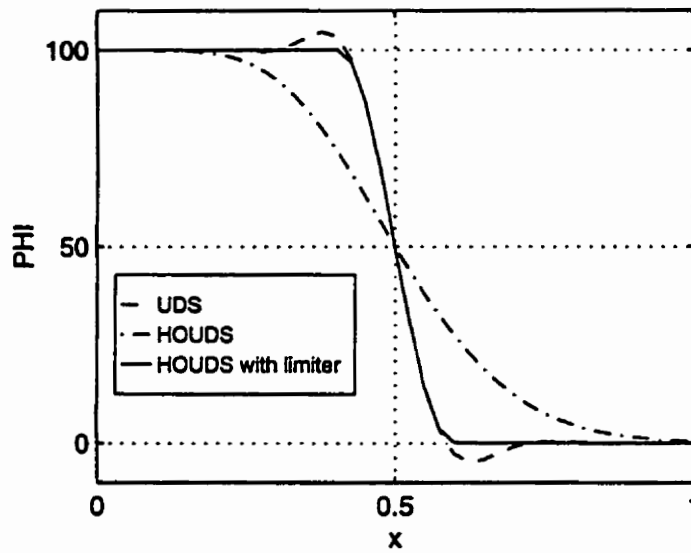


Figure D.14: Comparison of the results obtained from different advection schemes on the  $42 \times 42$  node grid

### D.4 Shear Driven Cavity Flow

Prediction of the shear driven cavity flow inside a square cavity whose top surface is moving in its plane with a uniform velocity, as depicted in Figure D.15, has been extensively used to evaluate numerical techniques. This problem exhibits different flow features (e.g. flow recirculation, oblique flow relative to the grid lines etc...) which makes it a suitable test case to examine the accuracy of a numerical model for fluid flow problems. Many researchers have solved this problem and therefore, a wealth of bench mark solutions are available in the literature (e.g. [117]) for different flow situations.

Here, the incompressible laminar cavity flow is solved for two Reynolds numbers,  $Re = 100, 1000$ , where  $Re$  is defined by  $Re = UL/\nu$ . The numerical simulations are performed on three uniform grids with  $10 \times 10$ ,  $20 \times 20$  and  $40 \times 40$  interior control volumes. The performance of two advection schemes (i.e. PEUDS and HOUDS) are compared. Simulations are started from a zero velocity field and steady state solutions are obtained using very large time steps. Usually 10 to 15 iterations are enough to reduce the maximum normalized residual to less than  $1 \times 10^{-3}$ .

The calculated results for the distribution of vertical and horizontal velocity along the horizontal and vertical cavity centerlines, respectively, are presented in Figures D.16 to D.19.

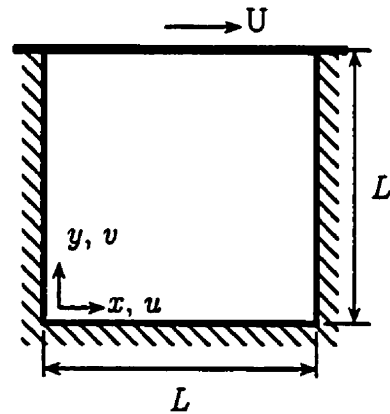


Figure D.15: Schematic of a square cavity with a moving lid

## D.4 Shear Driven Cavity Flow

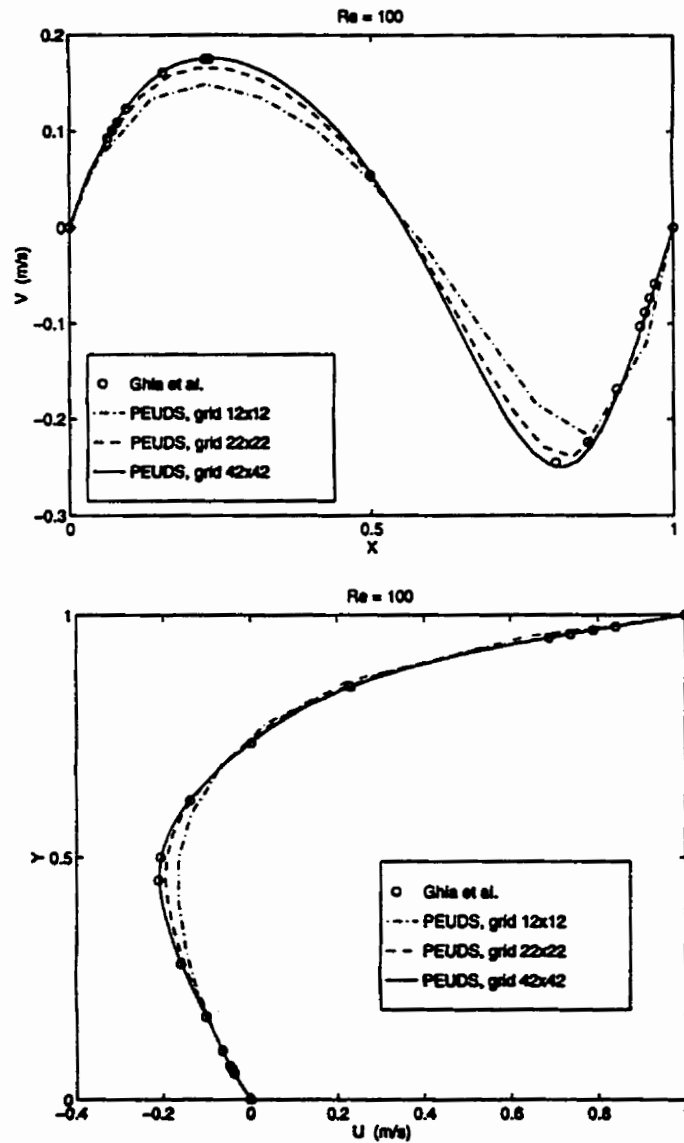


Figure D.16: Velocity distribution along the horizontal and vertical cavity centerlines,  $Re = 100$ , PEUDS

## D.4 Shear Driven Cavity Flow

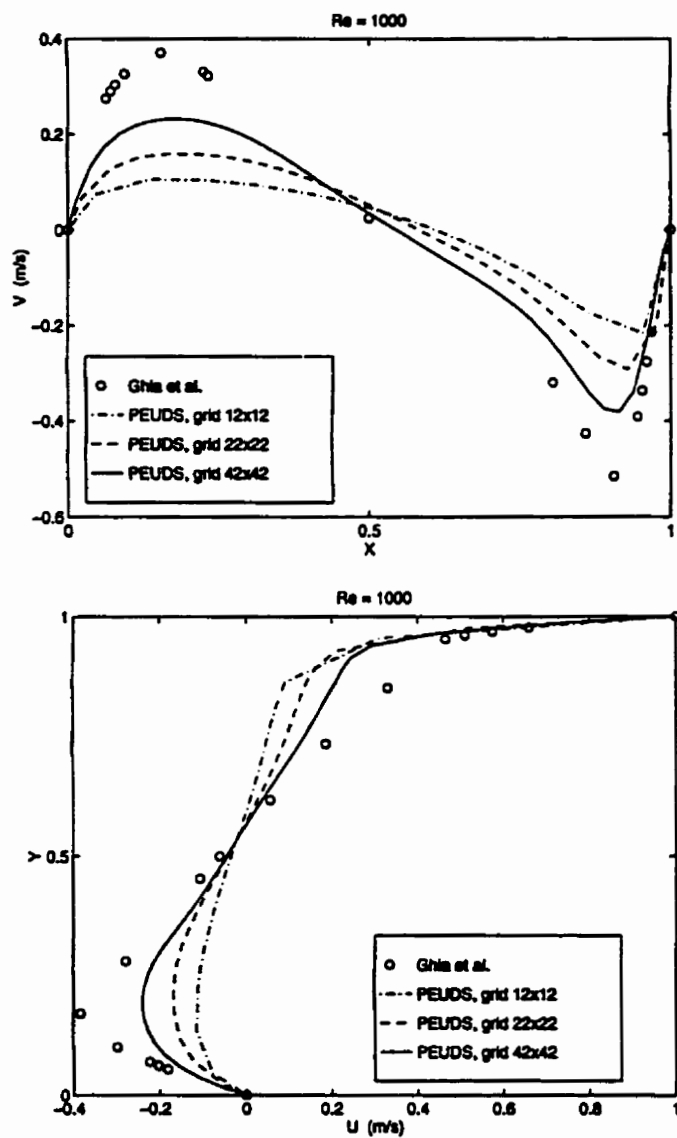


Figure D.17: Velocity distribution along the horizontal and vertical cavity centerlines,  $Re = 1000$ , PEUDS



## D.4 Shear Driven Cavity Flow

---

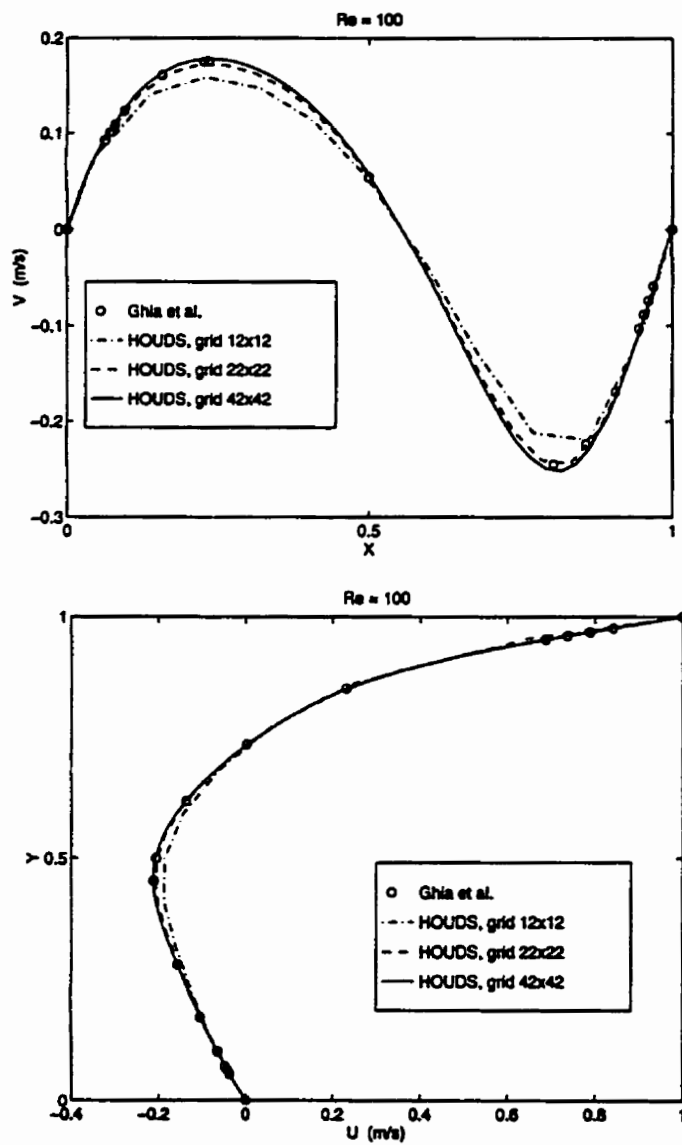


Figure D.18: Velocity distribution along the horizontal and vertical cavity centerlines,  $Re = 100$ , HOUDS

## D.4 Shear Driven Cavity Flow

---

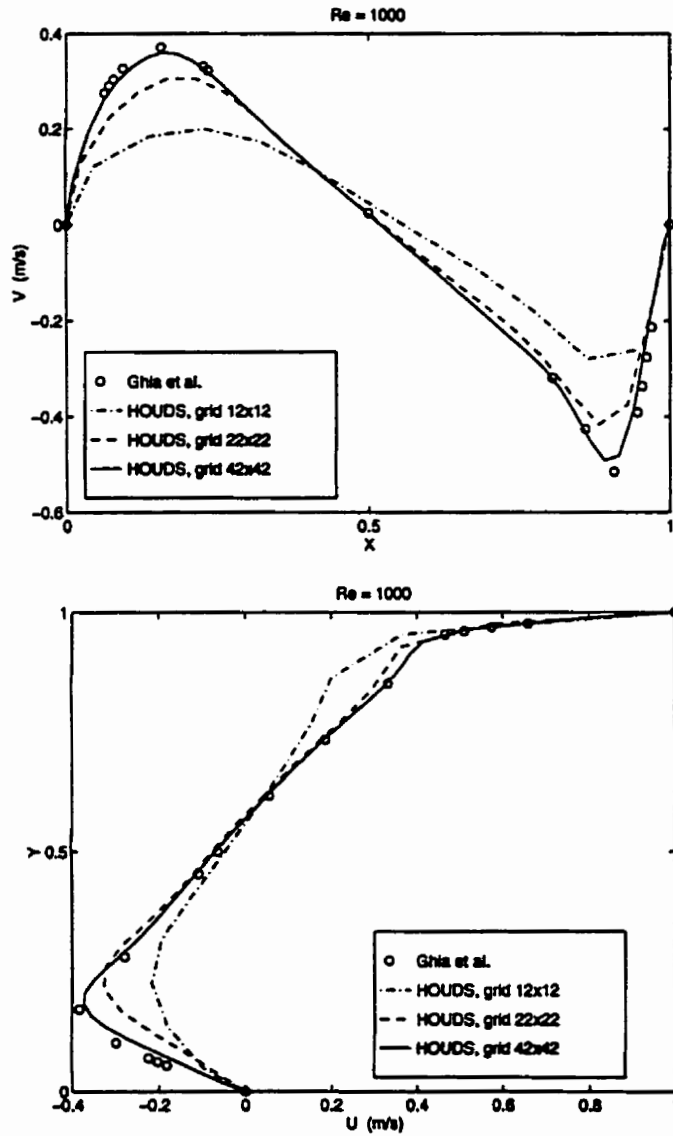


Figure D.19: Velocity distribution along the horizontal and vertical cavity centerlines,  $Re = 1000$ , HOUDS

## D.4 Shear Driven Cavity Flow

---

As shown in Figures D.16 and D.18 for  $Re = 100$  both advection schemes yield accurate results on the  $40 \times 40$  grid for this low  $Re$  number. Further, the solutions obtained using the HOUDS advection scheme approach the benchmark solution faster through refinement of the grid. On the other hand, for higher  $Re$ , shown in Figure D.17, the PEUDS which effectively becomes first order accurate, fails to accurately predict the velocity distributions. To improve the accuracy of these results much finer grids are required. For this case, when the HOUDS advection scheme is used (Figure D.19) the velocity field is still accurately predicted using a  $40 \times 40$  grid.

To further illustrate the accuracy of the model using HOUDS, the calculated streamline pattern and velocity vectors predicted for this flow geometry using a  $40 \times 40$  grid and HOUDS are shown in Figures D.20 and D.21. The secondary recirculating flows in the lower corners of the cavity are detected clearly. The results are in excellent agreement with those reported by Ghia et al. [117].

## D.4 Shear Driven Cavity Flow

---

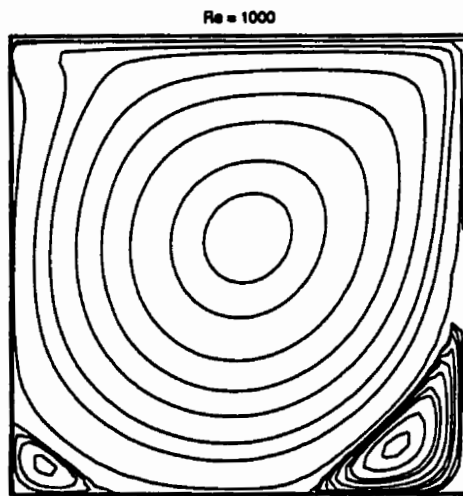


Figure D.20: Predicted stream lines inside the cavity,  $Re = 1000$ , HOUDS,  $40 \times 40$  grid

## D.4 Shear Driven Cavity Flow

---

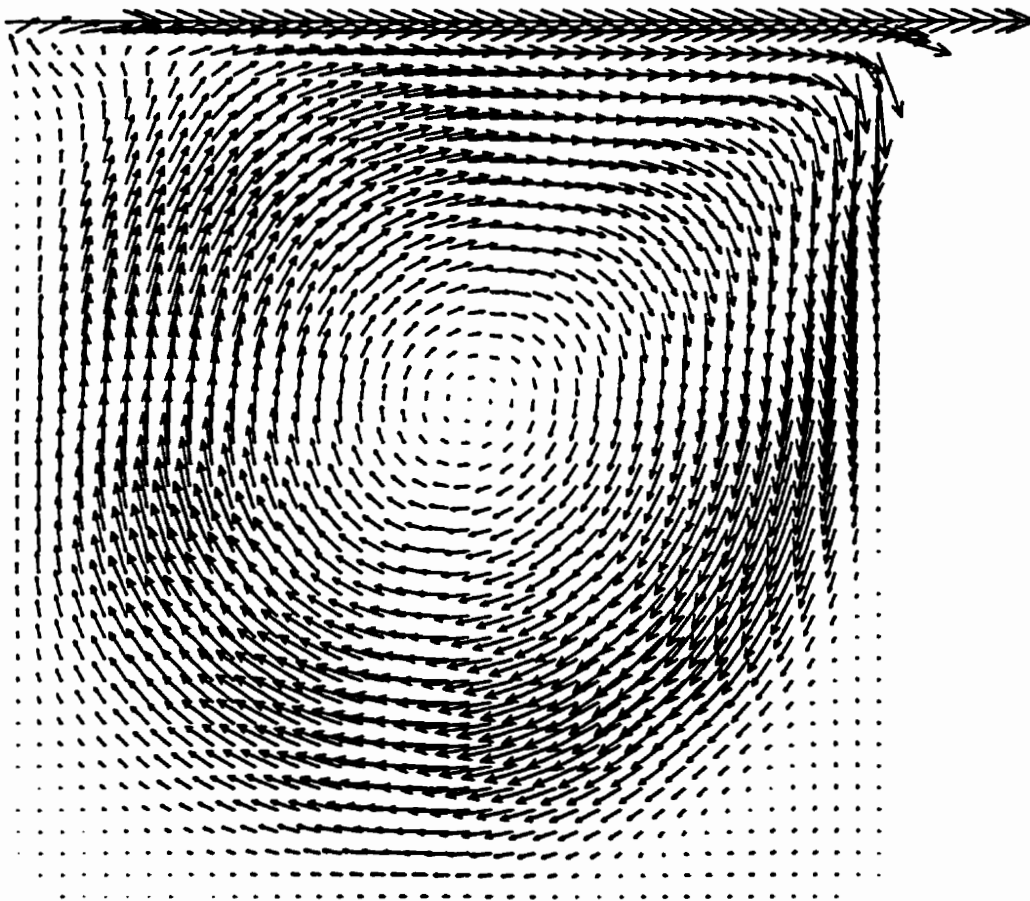


Figure D.21: Velocity vectors inside the cavity,  $Re = 1000$ , HOUDS.

## D.5 Natural Convection in a Square Cavity

---

### D.5 Natural Convection in a Square Cavity

The next test case for the present numerical model is prediction of the buoyancy driven flow inside a square cavity, with insulated surfaces top and bottom, and side walls at different temperatures. These predictions demonstrate the capability of the present model for predicting buoyancy driven flows. In addition, the performance of various upwind schemes in predicting such problems are compared.

The geometry of the cavity and the boundary conditions used for this test case are shown in Figure D.22. It should be noted that since the boundary conditions at both insulated walls are identical, they are only shown for the upper wall in this figure.

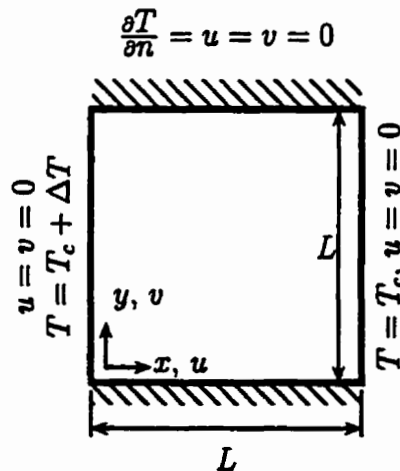


Figure D.22: Schematic of the heated square cavity and boundary conditions used for the calculations

Numerical simulations are carried out for  $Ra = 10^4$ ,  $10^5$  and  $10^6$  where

## D.5 Natural Convection in a Square Cavity

---

$Ra$  denotes the Rayleigh number and is defined by

$$Ra = \frac{g\beta L^3 \Delta T Pr}{\nu^2} \quad (D.3)$$

In this equation,  $g$  is the gravitational acceleration,  $L$  is the cavity dimension,  $\beta$  denotes the gas expansion coefficient,  $\Delta T$  is the temperature differential between the cavity side walls,  $Pr$  is the fluid Prandtl number and  $\nu$  denotes the kinematic viscosity of the fluid in the cavity. Table D.4 lists the numerical values of these quantities as used for the present test case.

Table D.4: property values for the heated cavity test case

| $\rho$ | $\mu$                  | $\beta$ | $Pr$ | $g$  |
|--------|------------------------|---------|------|------|
| 1.19   | $1.513 \times 10^{-5}$ | 0.00341 | 0.71 | 9.81 |

The value of  $\Delta T$  is 10 °C and is kept constant for all cases. Therefore, different values for the cavity dimension, as shown in Table D.5, are used to alter the Rayleigh number. In all the cases, uniform zero velocity and temperature fields are used to initialize the solution. For  $Ra = 10^4$  the steady-state solution can be obtained even with very large time steps. However, if a few iterations are done with a rather small time step at the start of the solution, the steady-state results can be quickly obtained by increasing the time step to a very large number. For higher  $Ra$  numbers, it was noticed that there is a limit for the time step. In this case, small time steps should be used to prevent divergence of the solution.

In Figures D.23 to D.25 are vector plots of the predicted velocity field for different values of Rayleigh number. As shown, when Rayleigh number is low

## D.5 Natural Convection in a Square Cavity

---

Table D.5: cavity size for different Rayleigh numbers

| $Ra$   | $L$ (m)  |
|--------|----------|
| $10^4$ | 0.021277 |
| $10^5$ | 0.045841 |
| $10^6$ | 0.098761 |

a single large vortex forms in the center of the cavity, but as Rayleigh number increases this vortex breaks down into two vortices which are positioned close to the cavity corners.

In order to compare the present numerical results with the bench mark solutions reported by Hortmann et al. [118], the following quantities are examined

- the maximum horizontal velocity component,  $U_{max}$ , in the vertical mid-plane  $x = L/2$  and its location,  $y_{max}$ .
- the maximum vertical velocity component,  $V_{max}$ , in the horizontal mid-plane  $y = L/2$  and its location,  $x_{max}$ .
- the maximum value of the local Nusselt number on the cold wall,  $Nu_{max}$ , and its position,  $y_{Nu}$
- the average Nusselt number,  $\overline{Nu}$ , defined by  $\overline{Nu} = Q/Q_c$  where  $Q$  is the calculated heat flux across the cavity and  $Q_c$  is the heat flux that would result from pure conduction

$$Q_c = k \frac{\Delta T}{L} L$$



## D.5 Natural Convection in a Square Cavity

---

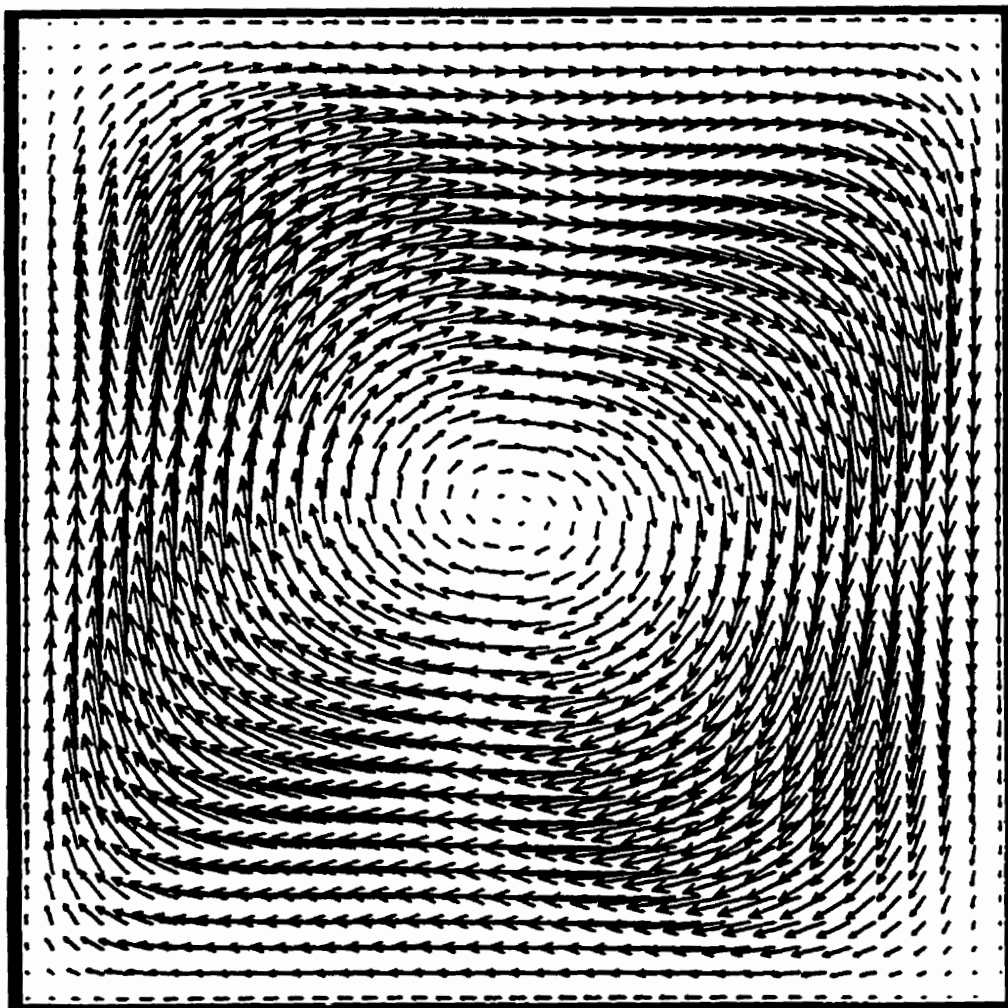


Figure D.23: Velocity vectors for the heated cavity,  $Ra = 10^4$

## D.5 Natural Convection in a Square Cavity

---

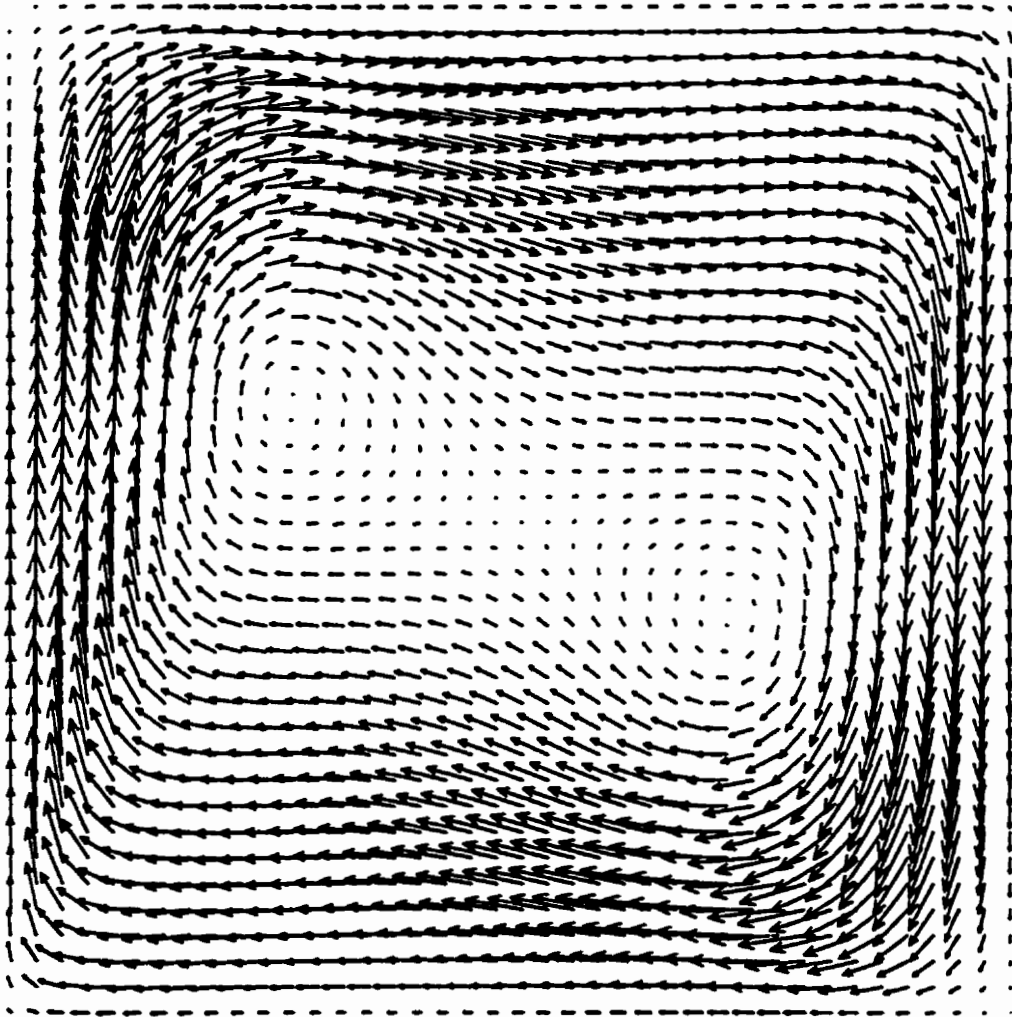


Figure D.24: Velocity vectors for the heated cavity,  $Ra = 10^5$

## D.5 Natural Convection in a Square Cavity

---

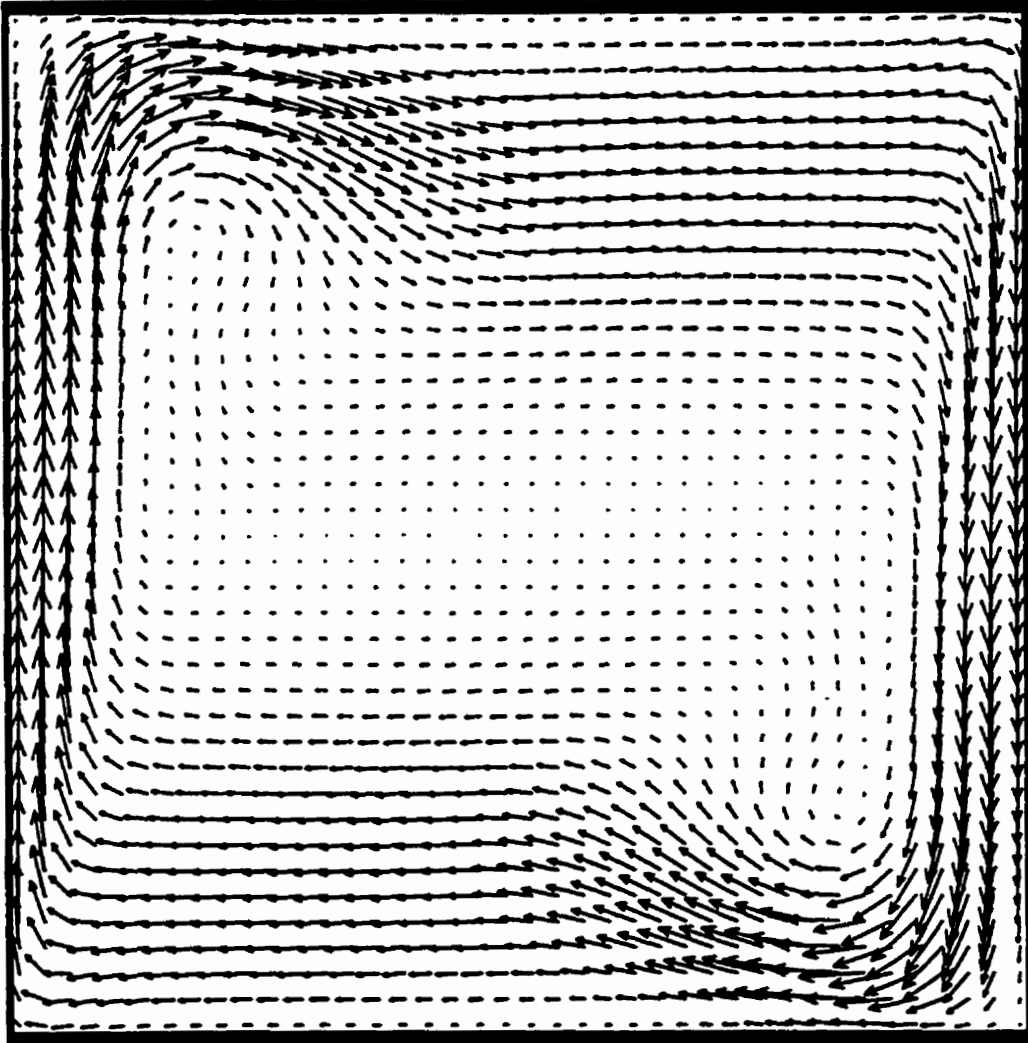


Figure D.25: Velocity vectors for the heated cavity,  $Ra = 10^6$

## D.5 Natural Convection in a Square Cavity

---

where  $k$  is the fluid conductivity and is set to 0.02553 (W/m/K) here.

Tables D.6 to D.8 summarize the numerical and benchmark results for different cases. The  $x$  and  $y$  coordinates are normalized with the cavity dimension,  $L$ , and all velocities are scaled with a diffusion velocity defined by

$$V_{\text{diff}} = \frac{\nu}{PrL}.$$

The validity and accuracy of the present results can be checked by comparing them with the reported benchmark solutions for the same grid resolution. As evident in Tables D.6 to D.8, the present results and the corresponding bench mark solutions are almost identical. Again, finer grids provide better accuracy in the results.

Despite the observed superiority of the HOUDS in accurately predicting the velocity profiles for the driven cavity flow, it is interesting to note that the accuracy of the results obtained by HOUDS and PEUDS advection schemes is not significantly different for these predictions. This is due to the fact that grid Peclet numbers are very low for these flows (max. Peclet number is about 1.). Therefore, the PEUDS approaches HOUDS as it becomes almost second order accurate.

Table D.6: Calculated results for the heated cavity test case,  $Ra = 10^4$ 

| grid size        | present model |         |              |         | bench mark results [118] |                |
|------------------|---------------|---------|--------------|---------|--------------------------|----------------|
|                  | 20 × 20 grid  |         | 40 × 40 grid |         | 40 × 40 grid             | 160 × 160 grid |
| advection scheme | PEUDS         | HOUDS   | PEUDS        | HOUDS   |                          |                |
| $U_{max}$        | 16.0772       | 16.2802 | 16.0955      | 16.1676 | 16.0955                  | 16.1759        |
| $y_{max}$        | 0.825         | 0.825   | 0.8125       | 0.8125  | 0.8125                   | 0.82551        |
| $V_{max}$        | 19.4503       | 19.5147 | 19.5303      | 19.6562 | 19.5303                  | 19.6242        |
| $x_{max}$        | 0.125         | 0.125   | 0.12779      | 0.1125  | 0.12779                  | 0.12009        |
| $Nu_m$           | 3.718         | 3.711   | 3.578        | 3.577   | 3.5373                   | 3.5313         |
| $y_{Nu}$         | 0.875         | 0.875   | 0.8625       | 0.8625  | 0.85108                  | 0.85399        |
| $\overline{Nu}$  | 2.292         | 2.293   | 2.257        | 2.257   | 2.2436                   | 2.24468        |

Table D.7: Calculated results for the heated cavity test case,  $Ra = 10^5$ 

| grid size        | present model |         |              |         | bench mark results [118] |                |
|------------------|---------------|---------|--------------|---------|--------------------------|----------------|
|                  | 20 × 20 grid  |         | 40 × 40 grid |         | 80 × 80 grid             | 320 × 320 grid |
| advection scheme | PEUDS         | HOUDS   | PEUDS        | HOUDS   |                          |                |
| $U_{max}$        | 36.3131       | 37.8104 | 34.7396      | 35.8028 | 34.7396                  | 34.7414        |
| $y_{max}$        | 0.875         | 0.875   | 0.8625       | 0.8625  | 0.8625                   | 0.85468        |
| $V_{max}$        | 65.8213       | 66.0238 | 68.8438      | 68.8845 | 68.8438                  | 68.6187        |
| $x_{max}$        | 0.075         | 0.075   | 0.0625       | 0.0625  | 0.0625                   | 0.06719        |
| $Nu_m$           | 9.013         | 8.948   | 8.158        | 8.142   | 8.1507                   | 7.7269         |
| $yNu$            | 0.925         | 0.925   | 0.9375       | 0.9375  | 0.9375                   | 0.91718        |
| $\overline{Nu}$  | 4.876         | 4.872   | 4.613        | 4.612   | 4.6165                   | 4.5231         |

**D.5 N**

---

---

## D.6 Simulation of a Turbulent Buoyant Plume

---

### D.6 Simulation of a Turbulent Buoyant Plume

The implementation of the  $k$ - $\epsilon$  turbulence model and also the buoyancy terms in both the momentum and turbulence equations are validated by simulating a round turbulent buoyant plume in a neutral environment. A description of the experimental facility and reported measurements for the mean velocity and temperature, as well as turbulence quantities, can be found in [119]. The buoyant plume is generated by heating air in a plume generator which is schematically shown in Figure D.26.

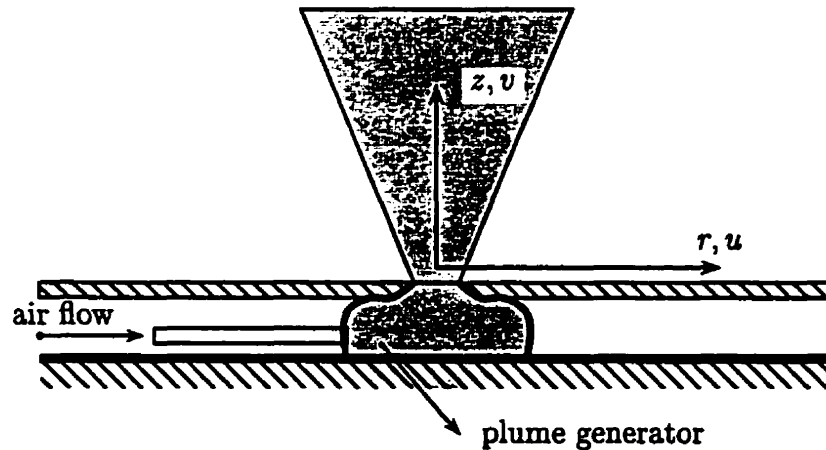


Figure D.26: Schematic of the buoyant plume

Steady-state operating conditions of the plume as reported in [119] are given in Table D.9, where subscript  $o$  denotes the source condition and  $I_o$  is the turbulence intensity at the source.



## D.6 Simulation of a Turbulent Buoyant Plume

---

Table D.9: Plume steady-state operating condition

| dia. (m) | $T_o$ (°C) | $V_o$ (m/s) | $T_{amb}$ (°C) | $I_o$ (%) |
|----------|------------|-------------|----------------|-----------|
| 0.0635   | 295        | 0.98        | 24.6-25.3      | 0.5       |

### The Computational Grid

The computational results which are presented in following pages are obtained on a grid whose specifications are given in Table D.10.

Table D.10: Grid specification for the buoyant plume

| no. of nodes<br>$N_r \times N_z$ | grid size<br>width $\times$ height | no. of nodes<br>across the source | grid spacing expansion factor |       |
|----------------------------------|------------------------------------|-----------------------------------|-------------------------------|-------|
|                                  |                                    |                                   | $E_r$                         | $E_z$ |
| 76 $\times$ 42                   | 150D $\times$ 100D                 | 5                                 | 1.05                          | 1.08  |

### Boundary Conditions

The boundary conditions used for the numerical simulation include:

- a velocity specified inlet at the plume source,
- a symmetry boundary condition along the plume axis,
- a no-slip wall boundary at the floor,
- a far field boundary, based on the ambient conditions, at the side of the computational domain, and

## D.6 Simulation of a Turbulent Buoyant Plume

- an exit boundary at the top face of the computational domain.

The numerical implementation of these boundary conditions is described in Figure D.27.

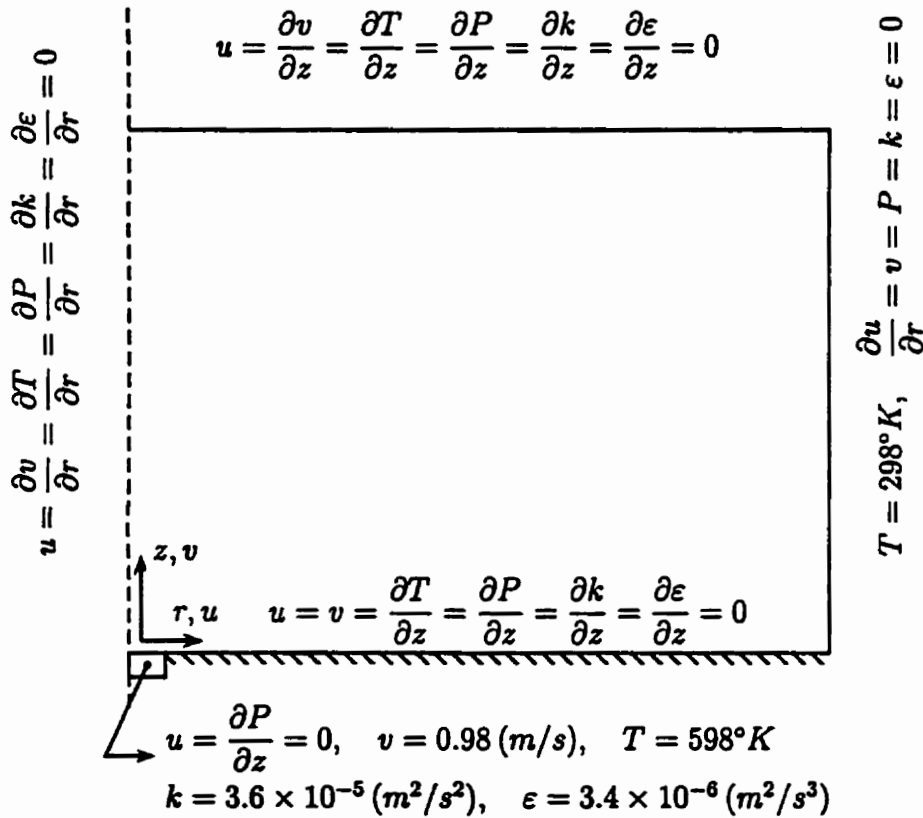


Figure D.27: Boundary conditions for the buoyant plume

As illustrated in Figure D.27, the normal gradient of  $k$  and  $\epsilon$  are set to zero at the solid wall which is not strictly correct. However, due to the minimal effect of such flow details in the vicinity of this boundary on main flow characteristics (e.g. plume decay and spread rates) and also, the relatively coarse grid resolution used near the wall, the additional complexity of using

## D.6 Simulation of a Turbulent Buoyant Plume

---

wall functions along with more realistic boundary conditions for  $k$  and  $\epsilon$  at the wall is not deemed necessary [120].

The value of  $k$  at the plume source is specified based on the source velocity,  $V_o = 0.98$  m/s, and the measured turbulence intensity,  $I_o = 0.5\%$ . The value of  $\epsilon$  at the source is approximated by  $\epsilon_o \approx k_o^{1.5}/D$  implying nearly homogeneous-isotropic flow at the source.

### Turbulence Model Constants

It is well known that the standard  $k$ - $\epsilon$  turbulence model does not provide accurate results in flow situations where buoyancy effects are significant [79, 121, 122]. In particular, the lateral spread of vertical plumes is underpredicted. To improve the accuracy of the results, a modified  $k$ - $\epsilon$  model which includes buoyancy production terms and incorporates a higher value of  $C_\mu$  is used for the present calculation. Other empirical coefficients in the turbulence model are the commonly used values listed in Table D.11.

Table D.11: Coefficients for the turbulence model

| $\sigma_t$ | $\sigma_k$ | $\sigma_\epsilon$ | $C_{\epsilon 1}$ | $C_{\epsilon 2}$ | $C_\mu$ |
|------------|------------|-------------------|------------------|------------------|---------|
| 0.7        | 1.0        | 1.3               | 1.44             | 1.92             | 0.11    |

The use of a value for  $C_\mu$  higher than that of 0.09 used in the standard  $k$ - $\epsilon$  model follows the recommendation of Hossain and Rodi [79] for buoyant flows. In addition, the application of a zero level Algebraic Stress Model (ASM) for turbulence along with the recommended constants by Hanjalic and Launder [123] results in  $C_\mu = 0.11$ .

## D.6 Simulation of a Turbulent Buoyant Plume

---

### Centerline Decay Rates

In cases where both momentum and buoyancy are added to the flow at the source, such as the present case, the flow behavior is initially like a buoyant jet and then, as the flow evolves, the buoyancy dominates and an asymptotic plume-like condition is reached. Experimental evidence shows that the plume-like condition is achieved for at least  $z/L_M > 5$ , where  $L_M$  is the Morton length scale defined by

$$L_M = M_o^{3/4} / F_o^{1/2}. \quad (D.4)$$

In this equation,  $M_o$  is the specific momentum and  $F_o$  denotes the specific buoyancy at the source. They are defined by

$$M_o = 2\pi \int_0^{D/2} V_o^2 r dr \quad (D.5)$$

and

$$F_o = 2\pi \int_0^{D/2} V_o g \frac{\rho_\infty - \rho_o}{\rho_o} r dr \quad (D.6)$$

According to experimental results [119, 124, 125], a plot of non-dimensional centerline temperature versus  $z/L_M$  should follow a  $-2/3$  slope and a plot of non-dimensional centerline velocity versus  $z/L_M$  should follow a  $2/3$  slope.

These plots are presented in Figures D.28 and D.29 where present calculations are compared with the best fit curve to the experimental data [119].

From Figure D.28, it appears that plume-like behavior is achieved at about  $z/L_M \approx 9$  which is well within the reported range of 6.5 to 16 for the present source condition [119]. In both cases, trends in the predicted decay rates follow those in the experimental data very closely.

## D.6 Simulation of a Turbulent Buoyant Plume

---

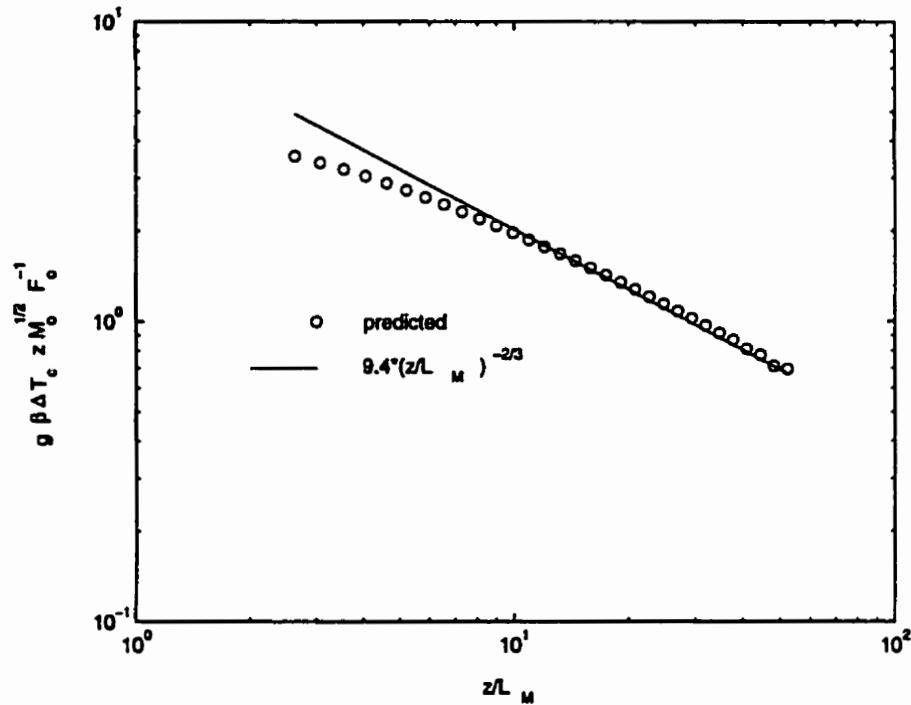


Figure D.28: Non-dimensional centerline temperature decay for a buoyant plume

### Plume Spread Rate

The plume spread rate calculated based on the plume half width<sup>1</sup> is compared with the experimental value in Figure D.30. As shown, after some initial distance the predicted spread rate reaches the experimental value and remains at that level. The variation of the plume half width with height, which is used to evaluate the spread rate, is also shown in the Figure.

---

<sup>1</sup>radius at which vertical velocity is half of the centerline velocity at the same height

## D.6 Simulation of a Turbulent Buoyant Plume

---

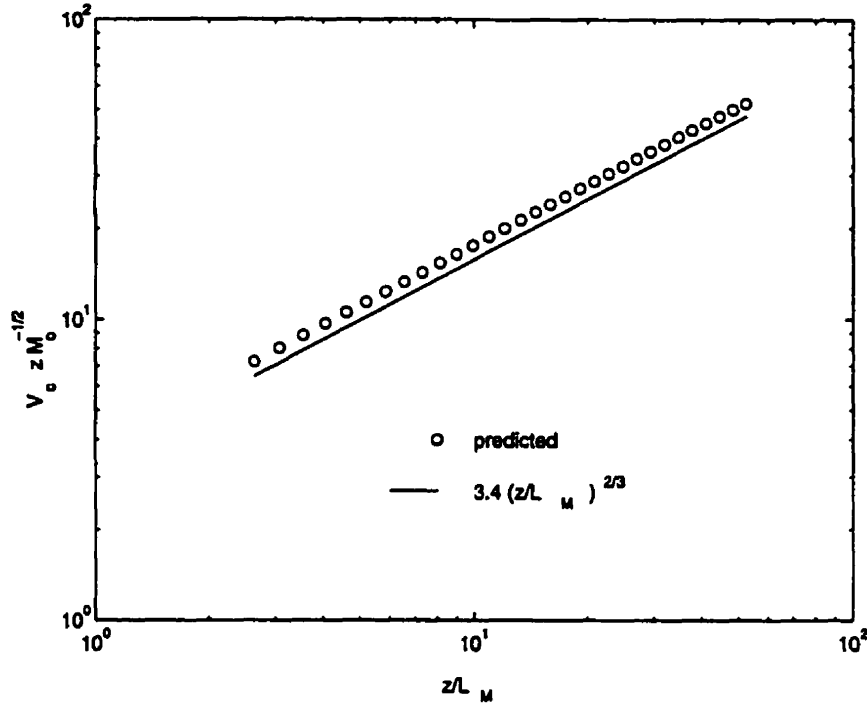


Figure D.29: Non-dimensional centerline velocity decay for a buoyant plume

### Radial Mean Flow Profiles

In flows such as that predicted here, the law of self similarity states that two dimensional, including axisymmetric, buoyant jets or plumes are considered self-similar when their time-averaged quantities (e.g. velocity and temperature) can be rendered dimensionless functions of only one non-dimensional geometric variable [124]. Therefore, non-dimensional radial profiles of a mean quantity at different non-dimensional heights should collapse onto a single profile.

Figure D.31 depicts such a plot for temperature distribution whereas,

## D.6 Simulation of a Turbulent Buoyant Plume

---

Figure D.32 shows the velocity profile. As shown in these figures, both experimental data and predictions confirm the existence of a self similar region for  $z/D > 10$ . The agreement between the predictions and measurements is excellent, except that the velocities close to the centerline are slightly over predicted.

### Turbulence Properties

The calculated normalized turbulence stresses are plotted against experimental values in Figures D.33, D.34 and D.35. The Reynolds stresses presented here, see Equation (3.33), are calculated based upon their full elliptic definition rather than the usual thin shear layer formulation.

The calculated turbulence shear stress,  $\overline{u'v'}$ , which is the only component of the Reynolds stresses considered in thin shear layer approximations, seems to agree very well with the data considering the scatter in the data itself. The radial normal stress,  $\overline{u'u'}$ , is also in good agreement with the data except in the vicinity of the centerline where the calculated values are up to 20% lower than the measurements. In contrast, the predicted vertical normal stress,  $\overline{v'v'}$ , seems to be about 50% lower than the measurements.

In general, the buoyancy modified version of the  $k$ - $\epsilon$  turbulence model, using a higher value of  $C_\mu$  (i.e.,  $C_\mu = 0.11$  instead of 0.09) seems to yield reasonably accurate results for mean flow properties in highly buoyancy driven flows.

## D.6 Simulation of a Turbulent Buoyant Plume

---

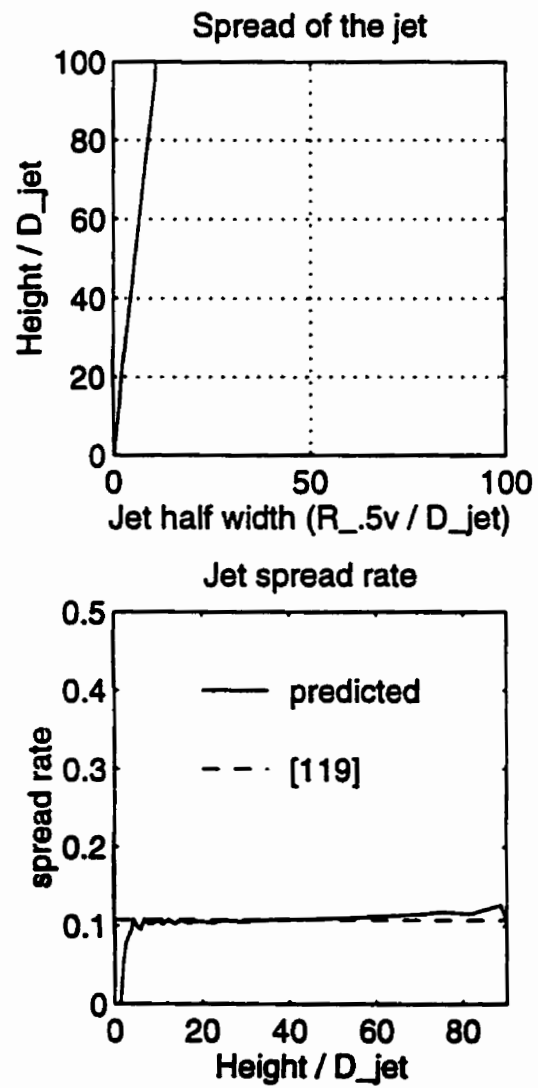


Figure D.30: plume spread rate



## D.6 Simulation of a Turbulent Buoyant Plume

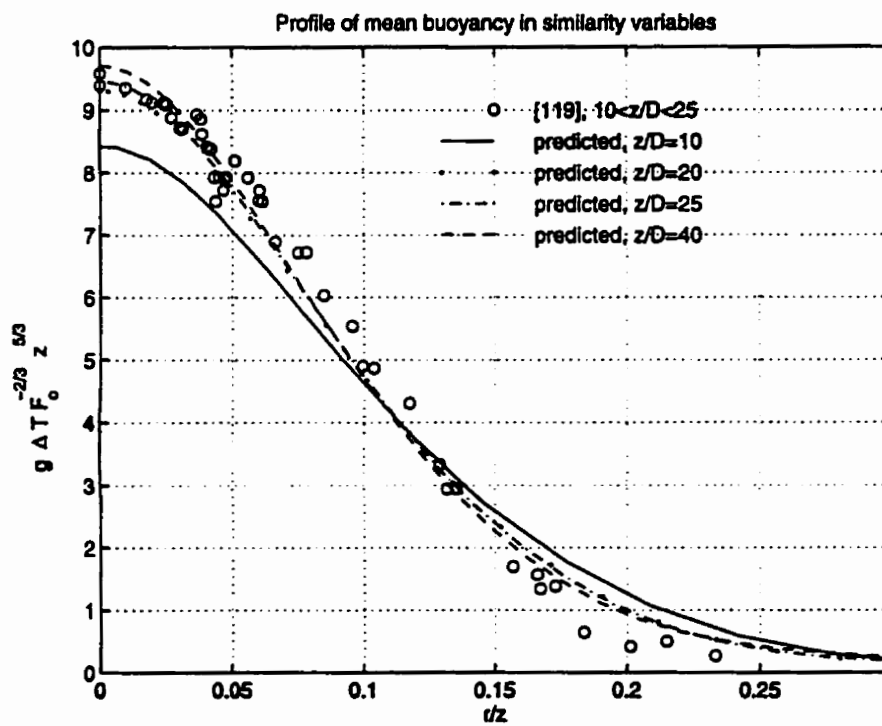


Figure D.31: Radial profiles of mean temperature for a buoyant plume

## D.6 Simulation of a Turbulent Buoyant Plume

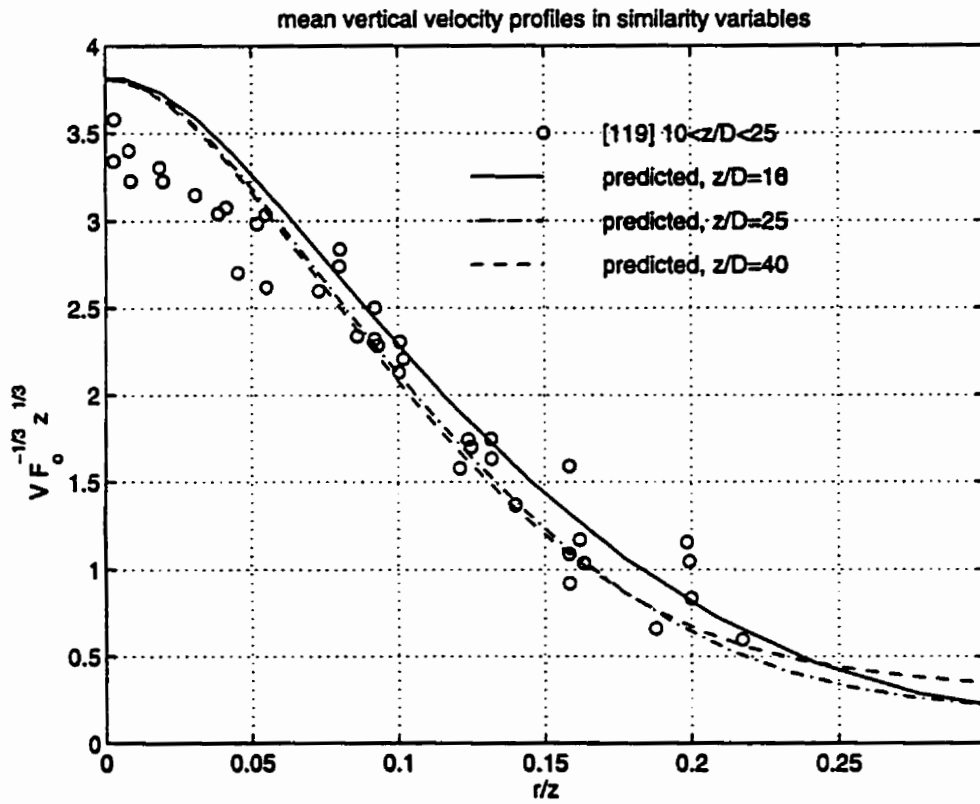


Figure D.32: Radial profiles of mean velocity for a buoyant plume

## D.6 Simulation of a Turbulent Buoyant Plume

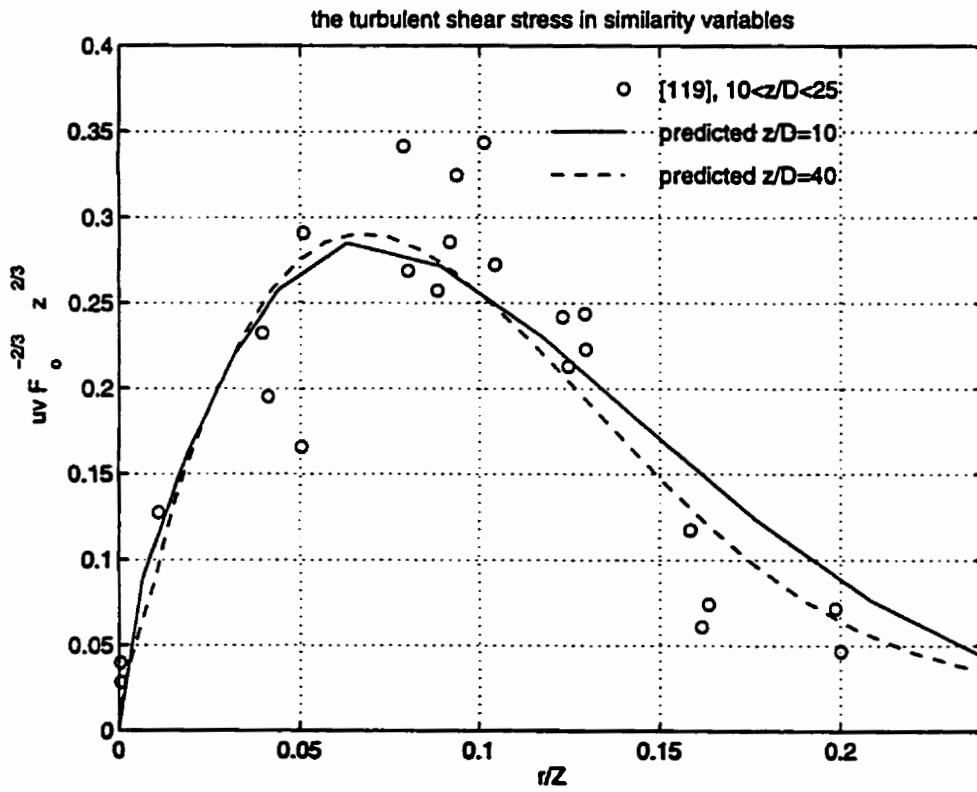


Figure D.33: Radial distribution of  $\overline{u'v'}$  for a buoyant plume

## D.6 Simulation of a Turbulent Buoyant Plume

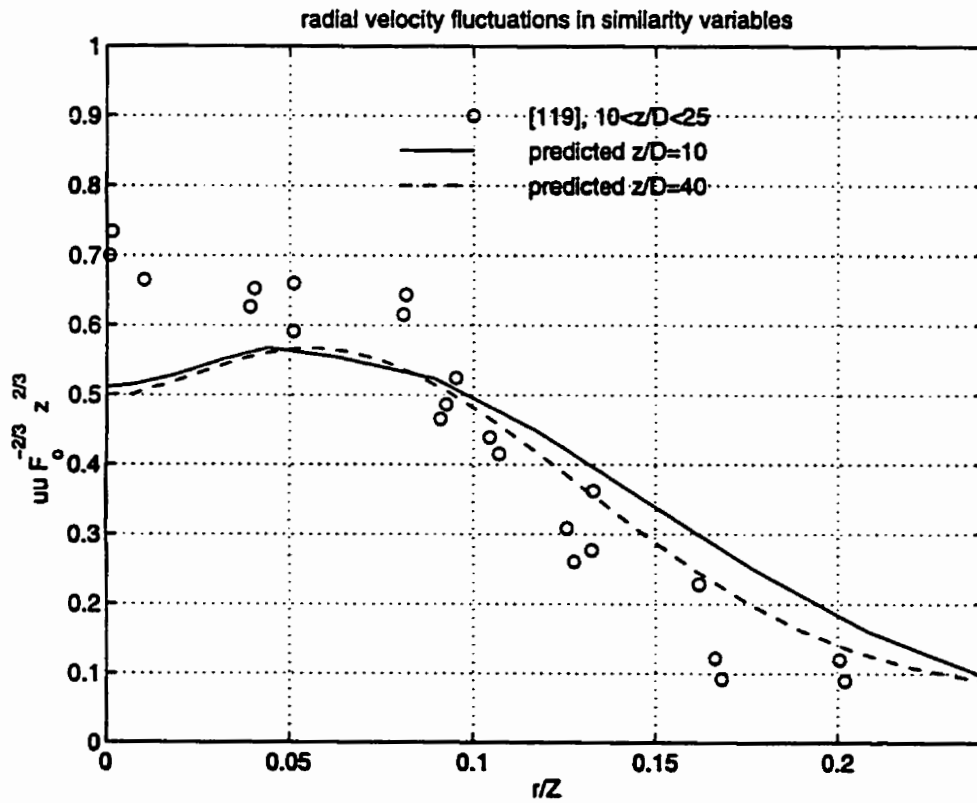


Figure D.34: Radial distribution of  $\overline{u'u'}$  for a buoyant plume

## D.6 Simulation of a Turbulent Buoyant Plume

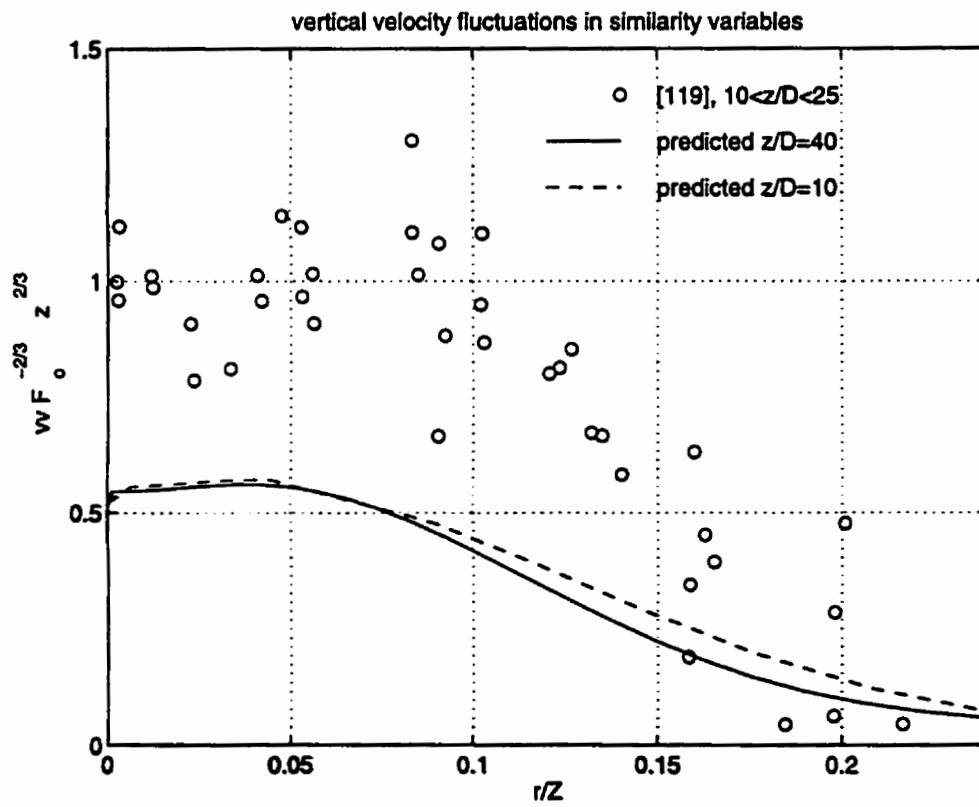


Figure D.35: Radial distribution of  $\overline{v'v'}$  for a buoyant plume



## An energy balance for the rectangular propane fire

$$\text{vel} := (2.092 \ 1.9298 \ 1.806 \ 1.6527 \ 1.3668 \ 1.0552 \ .8505 \ .3257)^T \cdot \frac{\text{m}}{\text{sec}}$$

$$\text{Xv} := (.00627 \ .01549 \ .02376 \ .04553 \ .06482 \ .08414 \ .1024 \ .1436)^T \cdot \text{m}$$

$$\text{temp} := (595.88 \ 552.36 \ 565.59 \ 549.64 \ 505.63 \ 462.79 \ 432.51 \ 392.82)^T \cdot \text{K}$$

$$\text{Xt} := (.008413 \ .01914 \ .02777 \ .04772 \ .06916 \ .08878 \ .10904 \ .1455)^T \cdot \text{m}$$

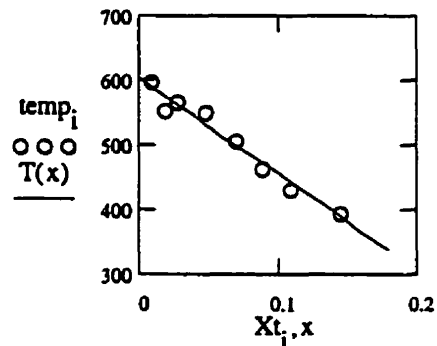
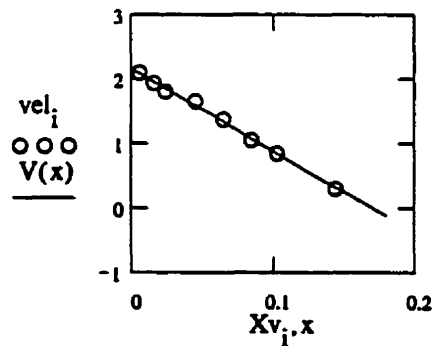
Now, we fit the data by linear functions,  $T(x)$  for temperature and  $V(x)$  for velocity and plot both the linear fit and the data in the following graphs:

$$T(x) := \text{slope}(\text{Xt}, \text{temp}) \cdot x + \text{intercept}(\text{Xt}, \text{temp})$$

$$V(x) := \text{slope}(\text{Xv}, \text{vel}) \cdot x + (\text{intercept}(\text{Xv}, \text{vel}))$$

$$i := 0..7$$

$$x := 0, .02.. .18 \cdot \text{m}$$



To conduct the energy balance, a control volume is setup around the flame as shown in the figure below:

## An energy balance for the rectangular propane fire

The following assumptions are made:

surrounding pressure  $P_{atm} := 101325 \cdot \text{Pa}$

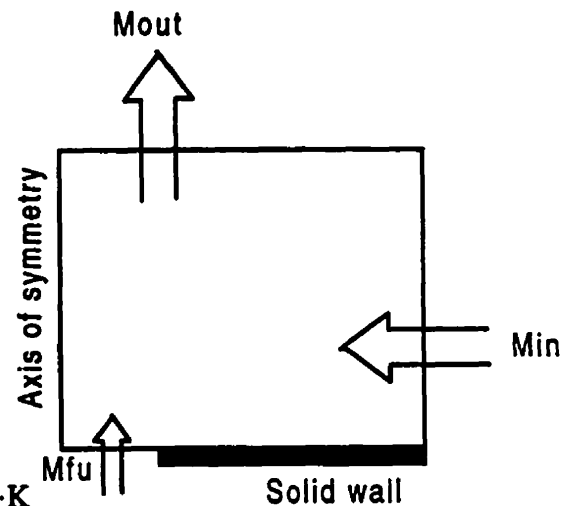
Heat capacity  $C_p := 1300 \cdot \frac{\text{joule}}{\text{kg} \cdot \text{K}}$

Gas constant  $R := 287 \cdot \frac{\text{joule}}{\text{kg} \cdot \text{K}}$

Perfect gas law  $\text{density}(x) := \frac{P_{atm}}{R \cdot T(x)}$

Gas temp. at the burner exit  $T_{fu} := 600 \cdot \text{K}$

Ambient temperature  $T_{inf} := 300 \cdot \text{K}$



From the linear fit to the measured velocities, we assume that velocity is zero for  $x > x_{lim}$ , where  $x_{lim}$  is the lateral location where extrapolated velocity is zero, that is

$$x_{lim} := \frac{-\text{intercept}(Xv, \text{vel})}{\text{slope}(Xv, \text{vel})} \quad x_{lim} = 0.17 \cdot \text{m}$$

$$T(x_{lim}) = 352.142 \cdot \text{K}$$

We now calculate the mass flow rate at  $z=0.46$ ,  $M_{out}$ , using the linear fits to the data

$$M_{out} := 2 \cdot \int_0^{x_{lim}} \text{density}(x) \cdot V(x) \cdot \text{depth} \, dx \quad M_{out} = 0.101 \cdot \text{kg} \cdot \text{sec}^{-1}$$



## An energy balance for the rectangular propane fire

The entrained mass flow rate,  $\dot{M}_{in}$ , can be calculated as follows;

$$\dot{M}_{in} := \dot{M}_{out} - \dot{M}_{fu} \cdot \text{width} \cdot \text{depth} \quad \dot{M}_{in} = 0.101 \cdot \text{kg} \cdot \text{sec}^{-1}$$

Also, convected energy leaving the control volume,  $\text{Convection}_{out}$ , is:

$$\text{Convection}_{out} := 2 \cdot \int_0^{x_{lim}} \text{density}(x) \cdot V(x) \cdot C_p \cdot T(x) \cdot \text{depth} \, dx$$
$$\text{Convection}_{out} = 6.719 \cdot 10^4 \text{ watt}$$

and the amount of energy entering the control volume can be calculated as follows:

$$\text{Convection}_{in} := \dot{M}_{fu} \cdot \text{depth} \cdot \text{width} \cdot C_p \cdot T_{fu} + \dot{M}_{in} \cdot C_p \cdot T_{in}$$
$$\text{Convection}_{in} = 3.962 \cdot 10^4 \text{ watt}$$

Amount of heat generated due to combustion;

$$\text{heat}_{generation} := \dot{M}_{fu} \cdot \text{depth} \cdot \text{width} \cdot H_c \quad \text{heat}_{generation} = 2.459 \cdot 10^4 \text{ watt}$$

and finally, a conservative estimation of the radiation heat loss becomes:

$$\text{percent}_{radiation} := \frac{(\text{heat}_{generation} + \text{Convection}_{in}) - \text{Convection}_{out}}{\text{heat}_{generation}} \cdot 100$$

$$\text{percent}_{radiation} = -12.141$$

This negative radiation heat loss, simply means that all the heat generated due to combustion is not enough to heat up the entrained air to the level that heat is convected out of the control volume considering all the assumptions made. If different values for the heat capacity is used, the calculated radiation heat loss changes and more physically justified values can be obtained. The following table shows the calculated radiation heat loss for different assumed  $C_p$  values.

## An energy balance for the rectangular propane fire

| <b>C<sub>p</sub> (J/kg.K)</b> | <b>radiation heat loss (%)</b> |
|-------------------------------|--------------------------------|
| 1300                          | -12.141                        |
| 1250                          | -7.828                         |
| 1200                          | -3.515                         |
| 1150                          | 0.798                          |
| 1100                          | 5.111                          |
| 1050                          | 9.424                          |
| 1000                          | 13.737                         |

# Bibliography

- [1] G. Cox. *Combustion Fundamentals of Fire*. Academic Press, 1995.
- [2] H. W. Emmons. Scientific progress on fire. *Annual Review of Fluid Mechanics*, 12:223–236, 1980.
- [3] H. W. Emmons. The prediction of fires in buildings. *17th Symposium (Int.) in Combustion, The Combustion Institute*, pages 1101–1111, 1978.
- [4] H. W. Emmons. The calculation of a fire in a large building. *Journal of Heat Transfer*, 105:151–158, 1983.
- [5] P. A. Tatem and F. W. Williams. Influence of complete enclosure on liquid pool fires. *Combustion Science and Technology*, 45:185–198, 1986.
- [6] C. C. Ndubizu, D. E. Ramaker, P. A. Tatem, and F. W. Williams. A model of freely burning pool fires. *Combustion Science and Technology*, 31:233–247, 1983.
- [7] R. Friedman. An international survey of computer models for fire and smoke. *Journal of Fire Protection Engineering*, 4:81–92, 1992.
- [8] T. Z. Harmathy and J. R. Mehaffy. Post-flashover compartment fires. *Fire Materials*, 7:49–61, 1983.
- [9] G. V. Hadjisophocleous and M. Cacambouras. Computer modeling of compartment fires. *Journal of Fire Protection Engineering*, 5(2):39–52, 1993.

- [10] R. W. Bilger. Computational field models in fire research and engineering. In *Fire Safety Science, proceedings of the fourth international symposium*, pages 95–110, 1994.
- [11] N. C. Markatos, M. R. Malin, and G. Cox. Mathematical modelling of bouyancy-induced smoke flow in enclosures. *International Journal of Heat and Mass Transfer*, 25(1):63–75, 1982.
- [12] G. Cox, S. Kumar, and Markatos N. C. Some field model validation studies. In *Fire Safety Science, Proceeding of the First International Symposium*, pages 159–171, 1985.
- [13] G. Cox and S. Kumar. Field modeling of fire in forced ventilated enclosures. *Combustion Science and Technology*, 52:7–23, 1987.
- [14] A. C. Ku, M. L. Doria, and J. R. Lloyd. Numerical modeling of unsteady buoyant flows generated by fire in a corridor. *16th Symposium (Int.) on Combustion, The Combustion Institute*, pages 1373–1384, 1976.
- [15] K. Satoh. A numerical study of ceiling jets based on T pattern flames. In *Fire Safety Science, Proceeding of the second international symposium*, pages 159–168. Hemisphere Publishing Corporation, 1989.
- [16] K. T. Yang, R. Lloyd, A. M. Kanury, and K. Satoh. Modeling of turbulent buoyant flows in aircraft cabins. *Combustion Science and Technology*, 39:107–118, 1984.
- [17] E. R. Galea and N. C. Markatos. Modeling of aircraft cabin fires. In *Fire Safety Science, Proceeding of the second international symposium*, pages 801–809. Hemisphere Publishing Corporation, 1989.
- [18] E. R. Galea and N. C. Markatos. A review of mathematical modeling of aircraft cabin fires. *Applied Mathematical Modeling*, 11:162–176, June 1987.
- [19] T. Joh, J. Mashige, T. Yoshikawa, and O. Sugawa. Numerical simulation of a compartment fire from burn-up to flashover. In *Fire Safety Science, Proceeding of the second international symposium*, pages 861–870, 1989.

- [20] B. F. Magnussen and J. Holen. Finite difference calculation of poolfires in enclosures. Technical report, SINTEF/NTH.
- [21] J. Holen, M. Brostrom, and B. F. Magnussen. Finite difference calculation of pool fires. *23rd Symposium (Int.) on Combustion, The Combustion Institute*, pages 1677–1683, 1990.
- [22] V. Chandrasekaran, G. H. Yeoh, and S. J. Grubits. A numerical prediction of fire in a large compartment. *Numerical Developments in CFD*, 215, 1995.
- [23] W. K. Chow and W. M. Leung. Solid-wall boundary effect on a building fire field model. *Combustion Science and Technology*, 71:77–93, 1990.
- [24] E. J. Weckman. *The Structure of the Flowfield Near the Base of a Medium-Scale Pool Fire*. PhD thesis, University of Waterloo, Waterloo, Ontario, Canada, 1987.
- [25] E. J. Weckman and C. S. McEwen. The time dependent structure of a medium-scale methanol pool fire. In *Proceeding of the Joint ASME/JSME National Heat Transfer Conference*, volume 5, page 269, 1991.
- [26] E. J. Weckman and A. B. Strong. Experimental investigation of the turbulent structure of medium-scale methanol pool fires. *Combustion and Flame*, 105(3):245–266, May 1996.
- [27] E. J. Weckman and A. Sobiesiak. The oscillatory behavior of medium-scale pool fires. *22nd Symposium (Int.) on Combustion, The Combustion Institute*, pages 1299–1310, 1988.
- [28] R. Kaazempur-Mofrad, E. J. Weckman, and A. B. Strong. The vorticity field in medium scale pool fires, 1993. NIST Annual Conference on Fire Research, Maryland.
- [29] B. J. McCaffrey. Momentum implications for buoyant diffusion flames. *Combustion and Flame*, 52:149–167, 1983.
- [30] H. S. Pergament and E. S. Fishburne. Influence of buoyancy on turbulent hydrogen/air diffusion flames. *Combustion Science and Technology*, 18:127–137, 1978.

- [31] R. W. Davis, E. F. Moore, W. M. Roquemore, L. D. Chen, V. Vilimpoc, and L. P. Goss. Preliminary results of a numerical-experimental study of the dynamic structure of a buoyant jet diffusion flame. *Combustion and Flame*, 83:263–270, 1991.
- [32] V. R. Katta, L. P. Goss, and W. M. Roquemore. Effect on nonunity Lewis number and finite-rate chemistry on the dynamics of a hydrogen-air jet diffusion flame. *Combustion and Flame*, 96:60–74, 1994.
- [33] A. F. Ghoniem, I. Lakkis, and M. Soteriou. Numerical simulation of the dynamics of large fires plumes and the phenomenon of puffing. *26th Symposium (Int.) on Combustion, The Combustion Institute*, 1996.
- [34] H. R. Baum. Large Eddy Simulation of fire phenomena. In *12th joint Panel Meeting of the UJNR Panel on Fire Research and Safety*, pages 67–74. Building Research Institute and Fire Research Institute, Oct. 1992.
- [35] W. Mell, K.B. McGratten, and H.R. Baum. Large Eddy Simulations of fire-driven flows. In *National Heat Transfer Conference, - Volume 2*, volume 304 of *HTD*, pages 73–77. ASME, 1995.
- [36] H.R. Baum, K.B. McGratten, and R.G. Rehm. Large Eddy Simulations of smoke movement in three dimensions. In C.A. Franks and S. Grayson, editors, *7th International Interflam Conference*, pages 189–198, London, England, Mar. 1996. Interscience Communications Ltd.
- [37] F. Tamanini. Reaction rates, air entrainment and reaction in turbulent fire plumes. *Combustion and Flame*, 30:85–101, 1977.
- [38] F. C. Lockwood and A. S. Naguib. The prediction of the fluctuations in the properties of free, round-jet, turbulent, diffusion flames. *Combustion and Flame*, 24:109–124, 1975.
- [39] G. H. Markstein. Scaling of radiative characteristic of turbulent diffusion flames. *16th Symposium (Int.) on Combustion, The Combustion Institute*, pages 1407–1419, 1977.
- [40] S. M. Jeng, L. D. Chen, and G. M. Faeth. The structure of buoyant methane and propane diffusion flames. *19th Symposium (Int.) in Combustion, The Combustion Institute*, pages 349–358, 1982.

- [41] C. J. Chen and C. H. Chen. On the prediction and unified correlation for decay of vertical buoyant jets. *Journal of Heat Transfer*, 101:532–537, Aug. 1979.
- [42] S. M. Jeng and G. M. Faeth. Species concentrations and turbulence properties in buoyant methane diffusion flames. *Journal of Heat Transfer*, 106:721–727, Nov. 1984.
- [43] H. Z. You and G. M. Faeth. Turbulent combustion, buoyant axisymmetric turbulent diffusion flames in still air. *Combustion and Flame*, 44:261–275, 1982.
- [44] E. Gengembre, P. Cambray, and J. C. Bellet. Turbulent diffusion flames with large buoyancy effects. *Combustion Science and Technology*, 41:55–67, 1984.
- [45] N. L. Crauford, S. K. Liew, and J. B. Moss. Experimental and numerical simulation of a buoyant fire. *Combustion and Flame*, 61:63–77, 1985.
- [46] K. C. Adiga, D. E. Ramaker, P. A. Tatem, and F. W. Williams. Modeling pool-like gas flames of propane. *Fire Safety Journal*, 14:241–250, 1989.
- [47] K. C. Adiga, D. E. Ramaker, P. A. Tatem, and F. W. Williams. Numerical predictions for a simulated methane fire. *Fire Safety Journal*, 16:443–458, 1990.
- [48] M. O. Annarumma, J. M. Most, and P. Joulain. On the numerical modeling of buoyancy-dominated turbulent vertical diffusion flames. *Combustion and Flame*, 85:403–415, 1991.
- [49] B. F. Magnussen, B. H. Hjertager, J. G. Olsen, and D. Bhaduri. Effects of turbulent structure and local concentrations on soot formation and combustion in  $C_2H_2$  diffusion flames. *17th Symposium (Int.) On Combustion*, The Combustion Institute, pages 1383–1393, 1978.
- [50] P. A. Tesner, T. D. Snegiriova, and V. G. Knorre. Kinetics of dispersed carbon formation. *Combustion and Flame*, 17:253–260, 1971.

- [51] A. D. Gosman and F. C. Lockwood. Incorporation of a flux model for radiation into a finite-difference procedure for furnace calculations. *14th Symposium (Int.) on Combustion, The Combustion Institute*, pages 661–671, 1973.
- [52] P. O. Annarumma. . PhD thesis, Universite de Poitiers, 1989.
- [53] M. Hertzberg, K. Cashdollar, C. Litton, and D. Burgess. The diffusion flame in free convection. Technical report, United States Department of Interior, Bureau of Mines, 1978. Report of investigation 8263.
- [54] J. D. Ris. Fire radiation-a review. *17th Symposium (Int.) on Combustion, The Combustion Institute*, pages 1003–1016, 1978.
- [55] R. W. Bilger. in *Turbulent Reacting Flows*, chapter 3. Springer-Verlag, 1980.
- [56] D. T. Pratt. in *Pulverized Coal Combustion and Gasification*, chapter 4. Plenum Press, 1979.
- [57] R. W. Bilger. Turbulent jet diffusion flames. *Progress in Energy and Combustion Science*, 1:87–109, 1976.
- [58] L. D. Smoot and P. J. Smith. *Coal Combustion and Gasification*. Plenum Press, 1985.
- [59] S. B. Pope. Pdf methods for turbulent reactive flows. *Progress in Energy and Combustion Science*, 11:119–192, 1985.
- [60] E. E. O'Brien. in *Turbulent Reacting Flows*, chapter 5. Springer-Verlag, 1980.
- [61] D. B. Spalding. Development of the eddy-brake-up model of turbulent combustion. *16th Symposium (Int.) on Combustion, The Combustion Institute*, pages 1657–1663, 1976.
- [62] B. F. Magnussen and B. H. Hjertager. On mathematical modelling of turbulent combustion with special emphasis on soot formation and combustion. *16th Symposium (Int.) on Combustion, The Combustion Institute*, pages 719–728, 1976.





- [75] P. F. Galpin and G. D. Raithby. Numerical solution of problems in incompressible fluid flow, Treatment of the temperature-velocity coupling. *Numerical Heat Transfer*, 10:105–129, 1986.
- [76] W. P. Jones and B. E. Launder. The prediction of laminarization with a two-equation model of turbulence. *International Journal of Heat and Mass Transfer*, 15:301–314, 1972.
- [77] D. C. Wilcox. *Turbulence Modeling for CFD*. DCW Industries, Inc., 1993.
- [78] Z. U. A. Warsi. *Fluid Dynamics Theoretical and Computational Approach*. CRC Press, 1992.
- [79] M. S. Hossain and W. Rodi. A turbulent model for buoyant flows and its application to vertical buoyant jets. In W. Rodi, editor, *Turbulent Buoyant Jets and Plumes*, number 6 in HMT, chapter 3. Pergamon Press, 1982.
- [80] K. N. C. Bray. Equations of turbulent combustion, I-fundamental equations of reacting turbulent flow. AASU Report 330, University of Southampton, Oct. 1973.
- [81] J. Janicka and W. Kollmann. The calculation of mean radical concentrations in turbulent diffusion flames. *Combustion and Flame*, 44:319–336, 1982.
- [82] P.N. Wild and O. Faltsi-Saravelou. Mathematical modeling of a 2.25 MW<sub>t</sub> swirling natural gas flame. Part 2: Conserved scalar approach for turbulent combustion. *Combustion Science and Technology*, 110:103–121, 1995.
- [83] C. K. Westbrook and F. L. Dryer. Chemical kinetic modeling of hydrocarbon combustion. *Progress in Engineering and Combustion Science*, 10:1, 1984.
- [84] B. F. Magnussen. The eddy dissipation concept for turbulent combustion modelling, its physical and practical implications. Technical report, Norwegian Institute of Technology, January 1990.

- [85] B. F. Magnussen. Modeling of reaction processes in turbulent flames with special emphasis on soot formation and combustion. In D. C. Siegla and G. W. Smith, editors, *Particulate Carbon Formation During Combustion*, pages 321–355. Plenum Press, 1981.
- [86] G. H. Markstein. Relationship between smoke point and radiant emission from buoyant turbulent and laminar diffusion flames. In *Twentieth Symposium (International) on Combustion*, pages 1055–1061. The Combustion Institute, 1984.
- [87] R. Siegel and J. R. Howell. *Thermal Radiation Heat Transfer*. HPC, third edition, 1992.
- [88] J. B. Moss. Turbulent diffusion flames. In G. Cox, editor, *Combustion Fundamentals of Fire*, chapter 4, pages 221–272. Academic Press, 1995.
- [89] T. F. Smith, Z. F. Shen, and J. N. Friedman. Evaluation of coefficients for the weighted sum of gray gases model. *Journal of Heat Transfer*, 104:602–608, Nov. 1982.
- [90] R. C. Reid, J. M. Prausnitz, and B. E. Poling. *The properties of gases and liquids*. McGraw-Hill, 4 edition, 1987.
- [91] R. E. Bolz and G. L. Tuve. *CRC Handbook of Tables for Applied Engineering Science*. CRC Press, 1973. 2nd Edition.
- [92] F. M. White. *Viscous Fluid Flow*. McGraw-Hill, 1974.
- [93] S. V. Patankar. *Numerical Heat Transfer and Fluid Flow*. Hemisphere Publishing Corporation, 1980.
- [94] J. H. Ferziger and M. Peric. *Computational Methods for Fluid Dynamics*. Springer, 1996.
- [95] G. Stubbley. Finite volume methods for fluid flow and heat transfer calculations. Dept. of Mech. Eng., University of Waterloo, Sep. 1991. ME780 course notes.
- [96] AEA Technology. *CFX-TASCflow Theory Documentation*. Version 2.7.2.

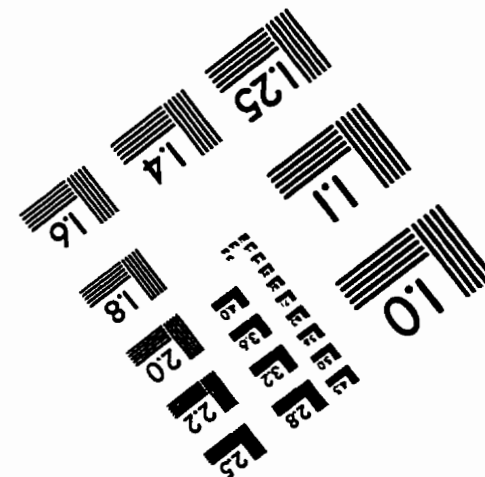
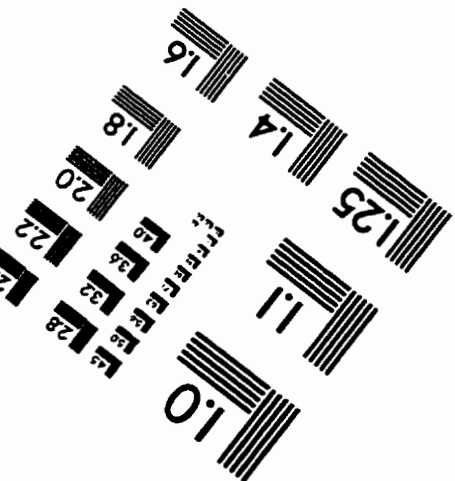
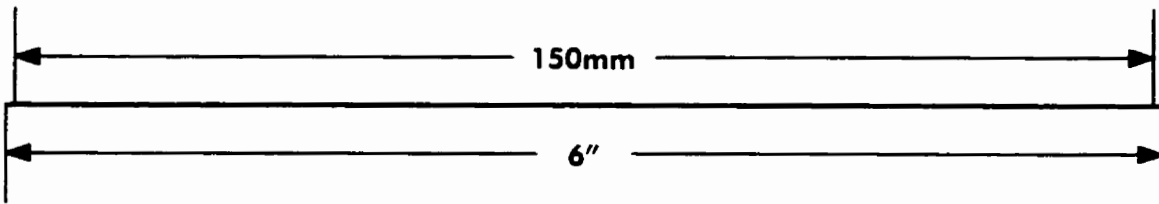
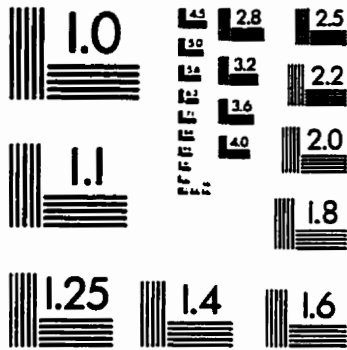
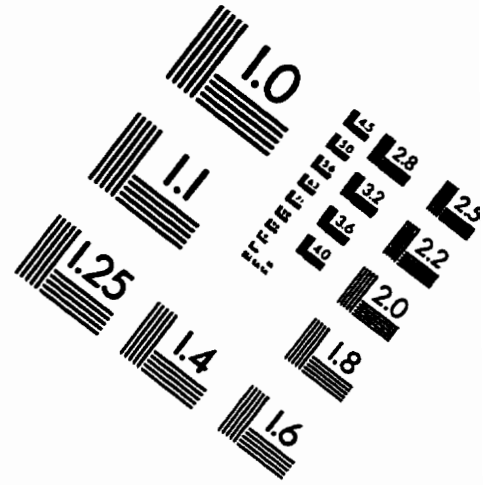
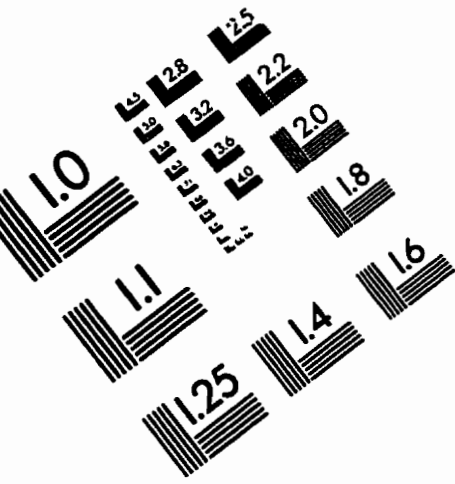
- [97] G. D. Raithby and K. E. Torrance. Upstream-weighted differencing schemes and their application to elliptic problems involving fluid flow. *Journal of Computational Fluids*, 8(12):191–206, 1974.
- [98] T.J. Barth and C. Jespersen. The design and application of upwind schemes on unstructured meshes. *AIAA, paper 89-0366*, 1989.
- [99] C. M. Rhie and W. L. Chow. Numerical study of the turbulent flow past an airfoil with trailing edge separation. *AIAA*, 21(11):1525–1532, 1983.
- [100] N. Z. Ince and B. E. Launder. On the computation of buoyancy-driven turbulent flows in rectangular enclosures. *International Journal of Heat and Fluid Flow*, 10(2):110–117, 1989.
- [101] E. Chu, A. George, J. Liu, and E. Ng. SPARSPAK: Waterloo Sparse Matrix Package. Research report cs-84-36, University of Waterloo, 1984.
- [102] J.E. VanderKwaak, P.A. Forsyth, K.T.B. MacQuarrie, and E.A. Sudicky. WatSolv Iterative Sparse Matrix Solver. Department of Earth Sciences, University of Waterloo, 1996. Version 2.12.
- [103] P.J. Pagni. Pool fire vortex shedding frequencies. In L.M. Trefethan and Panton, editors, *Some Unanswered Questions in Fluid Mechanics*, volume 43 of *Applied Mechanics Reviews*, pages 166–167. ASME, 1990.
- [104] M. Sibulkin and A. G. Hansen. Experimental study of flame spreading over a horizontal fuel surface. *Combustion Science and Technology*, 10:85–92, 1975.
- [105] E.E. Zukoski, B.M. Cetegen, and T. Kubota. Visible structure of buoyant diffusion flames. In *Twentieth Symposium (International) on Combustion*, pages 361–366. The Combustion Institute, 1984.
- [106] E. J. Weckman. Simplified calculation of total flux and entrainment using experimental results from a medium-scale pool fire, 1989. National Heat Transfer Conference, HTD-vol 106.
- [107] A. Bouhafid, J. P. Vantelon, and P. Joulain. On the flame structure at the base of a pool fire. *22nd Symposium (Int.) on Combustion*, The Combustion Institute, pages 1291–1298, 1988.

- [108] L.D. Chen, J.P. Seaba, W. M. Roquemore, and L.P. Goss. Buoyant diffusion flames. In *Twenty-Second Symposium (International) on Combustion*, pages 677–684. The Combustion Institute, 1989.
- [109] A. Hamins, J. C. Yang, and T. Kashiwagi. An experimental investigation of the pulsation frequency of flames. *24th Symposium (Int.) on Combustion*, The Combustion Institute, pages 1695–1702, 1992.
- [110] B. M. Cetegen and T. A. Ahmed. Experiments on the periodic instability of buoyant plumes and pool fires. *Combustion and Flame*, 93:157–184, 1993.
- [111] A. Bejan. Predicting the pool fire vortex shedding frequency. *Journal of Heat Transfer*, 113:261–263, 1991.
- [112] G. M. Byram and Jr. R. M. Nelson. The modeling of pulsating fires. *Fire Technology*, 6(2):102–110, 1970.
- [113] N.L. Crauford. *The Structure of an Unconfined Buoyant Diffusion Flame*. PhD thesis, University of Southampton, 1984.
- [114] A. B. Strong and E. J. Weckman. Comments on the use of the  $k - \epsilon$  model of turbulence for the prediction of pool fires. In *Spring Technical Meeting of the Combustion Institute, Canadian Section*, May 1994. Queen's University, Kingston, Ont., Canada.
- [115] M. Ashrafzaadeh, A. B. Strong, and E. Weckman. Velocity and temperature predictions in the developing region of a buoyancy-dominated turbulent diffusion flame. In *Proceedings of The Combustion Institute, Canadian Section, Spring Technical Meeting*, 1996.
- [116] B.J. McCaffrey. Some measurements of the radiative power output of diffusion flames. Paper WSS/C181-15, 1981. Western States Meeting of Combustion Institute, Puulman, Washington.
- [117] U. Ghia, K. N. Ghia, and C. T. Shin. High-Re solutions for incompressible flow using the Navier-Stokes equations and a multigrid methods. *Journal of Computational Physics*, 48:387–411, 1982.
- [118] M. Hortmann, M. Peric, and Scheuerer. Multigrid benchmark solutions for laminar natural convection flows in square cavities. In I. Celik and

C. J. Freitas, editors, *Benchmark Test Cases for Computational Fluid Dynamics*, volume 93 of *FED*, pages 1–6, 1990.

- [119] A. Shabbir and W. K. George. Experiments on a round turbulent buoyant plume. *Journal of Fluid Mechanics*, 275:1–32, 1994.
- [120] D. J. Bergstrom. *A Computational Study of Plane Buoyant Free Jets Using Algebraic Stress-Flux Models*. PhD thesis, University of Waterloo, 1987.
- [121] A. Shabbir and D. B. Taulbee. Evaluation of turbulence models for predicting buoyant flows. *Journal of Heat Transfer*, 112:945–951, November 1990.
- [122] L. Davidson. Second-order corrections of the  $k - \epsilon$  model to account for non-isotropic effects due to buoyancy. *International Journal of Heat and Mass Transfer*, 33(12):2599–2608, 1990.
- [123] K. Hanjalic and B. E. Launder. A Reynolds Stress Model of turbulence and its application to thin shear flows. *Journal of fluid Mechanics*, 52:609, 1972.
- [124] C. J. Chen and W. Rodi. *Vertical turbulent buoyant jets, a review of experimental data*. Pergamon Press, 1980. HMT-4.
- [125] N. E. Kotsovinos. Plane turbulent buoyant jets. *Journal of Fluid Mechanics*, 81:241–268, 1977.

# IMAGE EVALUATION TEST TARGET (QA-3)



**APPLIED IMAGE . Inc**  
 1653 East Main Street  
 Rochester, NY 14609 USA  
 Phone: 716/482-0300  
 Fax: 716/288-5989

© 1993, Applied image, Inc., All Rights Reserved